# Mesoscale Additively Manufactured Flow reactors for Synthetic, Crystallisation and Biocatalytic applications

*Obinna Okafor*

**Thesis** submitted to the University of Nottingham for the

degree of **Doctor of Philosophy**

**Department of Engineering**

2019

# Abstract

Mesoscale flow reactors are valuable tools for low volume experimental work for the development of new materials and drugs whilst utilising the benefits of continuous flow processes over batch. They represent a bridge between the microfluidic scale (where mixing is predominantly controlled by diffusion) and macroscale (where mixing is controlled by turbulent flow). The main challenge at the mesoscale is to optimise mixing under predominantly low flow rates, which correspond to low Reynolds numbers. Even though reactor designs exist which allow improved mass transport and heat transfer properties or added functionalities, there has been minimal application in the mesoscale due to manufacturing challenges. The use of additive manufacturing (AM) in the fabrication of mesoscale flow reactors with complex channel architectures, e.g. passive mixers, has received increased attention. Its use provides a valuable tool for rapid development of bespoke flow reactors for applications requiring precise mixing. It serves as a tool for producing complex 3D geometries which are challenging to achieve using other manufacturing techniques.

This work has investigated mesoscale flow reactors for chemical synthesis, crystallisation and bio-transformation applications. The flow reactors for these applications were manufactured using two low-cost (less than £5,000 machine cost) AM platforms based on vat polymerisation and material extrusion techniques.

A cost-effective methodology for the rapid development of low volume synthetic production using AM is presented. Production of Silver nanoparticles in a designed AM mesoscale continuous oscillatory baffled reactor showed a beneficial production of narrowly dispersed particles (5.0 nm ± 1.2 nm), stability of 200 min and reduced foiling compared to a conventional tubular reactor test. This was due to improved mass transport shown when running at increased oscillatory frequency and amplitude.

Continuous flow cooling crystallisation of Paracetamol by multi-component templating was carried out in a fully built AM mesoscale crystalliser. This demonstrated the utilisation of AM in the rapid design and manufacture of modular jacketed flow devices, where heat exchange can be modelled and controlled to generate efficient devices for applications in continuous-flow cooling crystallisation. The manufactured devices were effective to crystallise form II Paracetamol employing Metacetamol as the co-crystallising agent.

While benefiting from the advantages of carrying out reactions in continuous flow and at reduced scale, attachment of catalysts in the reactor walls for biocatalytic screening introduces a next generation in advancement. The first example of modified AM devices for the immobilization and application of ω-transaminase (ω-TA) enzymes in continuous-flow is presented. At a residence time of 50 min almost full conversion of the (R)-enantiomer was observed (>49 %) yielding the (S)-amine with an enantiomeric excess >99 % e.e. for a run time of 25 h dropping slightly when run for a further 78 hours.

# Dedication

*To mum and dad, for the unwavering love, support and*

*inspiration to pursue and complete this PhD.*

# Acknowledgements

# List of Publications

I. **Okafor, O.,** Weilhard, A., Fernandes, J.A., Karjalainen, E., Goodridge, R. and Sans, V., 2017. Advanced reactor engineering with 3D printing for the continuous-flow synthesis of silver nanoparticles. *Reaction Chemistry & Engineering*, *2*(2), pp.129-136. doi.org/10.1039/C6RE00210B

II. Peris, E., **Okafor, O.,** Kulcinskaja, E., Goodridge, R., Luis, S.V., Garcia-Verdugo, E., O'Reilly, E. and Sans, V., 2017. Tuneable 3D printed bioreactors for transaminations under continuous-flow. *Green Chemistry*, *19*(22), pp.5345-5349. doi.org/10.1039/C7GC02421E

III. **Okafor, O.,** Goodridge, R. and Sans, V., 2017. New trends in reactor engineering with additive manufacturing. *Chimica Oggi-Chemistry Today*, *35*(4), pp.4-6.

IV. Bracconi, M., Ambrosetti, M., **Okafor, O.,** Sans, V., Zhang, X., Ou, X., Da Fonte, C.P., Fan, X., Maestri, M., Groppi, G. and Tronconi, E., 2018. Investigation of pressure drop in 3D replicated open-cell foams: Coupling CFD with experimental data on additively manufactured foams. *Chemical Engineering Journal*. doi.org/10.1016/j.cej.2018.10.060

V.   **Okafor, O.,** Goodridge, R. and Sans, V., 2019 Additively manufactured advanced flow reactors for enhanced heat and mass transfer. *Flow Chemistry, RSC Ed.: Santiago V. Luis, Eduardo García-Verdugo*

VI.  **Okafor, O.,** Robertson K., Goodridge, R. and Sans, V., 2019 Continuous-flow crystallisation in 3D-printed compact devices. *Reaction Chemistry & Engineering* doi.org/10.1039/C9RE00188C

# Table of content

# List of Abbreviations

| | |
|---|---|
| ABS | Acrylonitrile butadiene styrene |
| API | Active Pharmaceutical Ingredients |
| AM | Additive Manufacture |
| ATIR | Attenuated Total Reflectance Fourier Transfer Infrared Spectroscopy |
| CT | Chiller Temperature |
| CFD | Computational Fluid Dynamics |
| CAD | Computer Aided Design |
| CFR | Continuous Flow Reactor |
| COBC | Continuous Oscillatory Baffled Crystalliser |
| COBR | Continuous Oscillatory Baffled Reactor |
| CSTR | Continuous Stirred Tank Reactor |
| CTR | Continuous Tubular Reactor |
| ºC | Degree Celsius |
| DLP | Digital Light Projector |
| EBM | Electron Beam Melting |
| FEP | Fluorinated Ethylene Propylene |
| FDM | Fused Deposition Modelling |
| g, Kg | Gram, Kilogram |
| Hz | Hertz |
| HPLC | High Performance Liquid Chromatography |

| | |
|---|---|
| IR | Infrared Spectroscopy |
| IPA | Isopropyl Alcohol |
| LS | Laser Sintering |
| MTPS | Magnetic Transient Plane Source |
| MJ | Material Jetting |
| MCOBR | Mesoscale continuous oscillatory baffled reactor |
| MTR | Mesoscale Tubular reactor |
| MCM | Metacetamol |
| mL, μL, nL, pL | millilitre, microlitre, nanolitre, picolitre: volumes |
| mm, μm, nm | millimetre, micrometre (micron), nanometre: lengths |
| NMR | Nuclear magnetic resonance spectroscopy |
| PC | Paracetamol |
| Pe | Peclet Number |
| PC | Polycarbonate |
| PDMS | Polydimethylsiloxane |
| PEI | Polyethylenimine |
| PLA | Polylactic Acid |
| PP | Polypropylene |
| PVA | Polyvinyl Alcohol |
| PVP | Polyvinylpyrrolidone |
| PXRD | Powder X-ray Diffraction |
| RTD | Residence Time Distribution |
| Re | Reynolds Number |
| RMS | Root Mean Square |
| SEM | Scanning Electron Microscopy |
| s | Second |
| SLM | Selective laser Melting |

| | |
|---|---|
| SLS | Selective Laser Sintering |
| Ag-NP | Silver Nanoparticle |
| SLA | Stereolithography |
| St | Strouhal Number |
| SPR | Surface Plasmon Resonance |
| TGA | Thermogravimetric Analysis |
| 3D | Three Dimension |
| TEM | Transmission electron microscopy |
| TR | Tubular Reactor |
| 2D | Two Dimension |
| UV-Vis | Ultraviolet-Visible spectroscopy |
| VP | Vat Polymerisation |

# Chapter 1 Introduction

## Background

Continuous flow processing, as opposed to batch processing, is especially beneficial for applications requiring precise mixing, rapid heat transfer and fast reactions [1]. Hence, processing in continuous flow can improve reaction yields, handling of reactants and allow control of physical properties of the products. Discovery of new materials or drugs require researchers to experiment at low volumes or material quantities under specific physical conditions. The experimentation may require the utilisation of specific reactor materials, mixing rates, temperature or residence time. As such, a bespoke reactor is mostly required to attain optimised process conditions for the specific application. Manufacturing a reactor for a specific application is time consuming and costly using conventional manufacturing techniques.

The ability to rapidly design and manufacture bespoke and cost-effective mesoscale flow reactors as needed for a specific reaction application would be valuable to both academic and industrial researchers. Processing in the mesoscale allows low volume process experimentation and lies between microscale and macroscale, relating to micro-litre and litres production volume. Micro and macro fluidics are fundamentally driven by different mixing mechanisms. Hence the diffusive based mixing in the microscale and advective dominated mixing characteristic of macroscale are not transferrable. In the microscale, flow tends to be laminar, characterised by a smooth and constant flow stream as opposed to chaotic patterns, eddies and vortices formed at

turbulence favouring rapid mixing [1]. Though meso-scale reactors offer the opportunity to bridge the divide, mixing can be enhanced by design.

To enhance mixing or heat transfer in the flow reactors, they are designed incorporating unique architectures called passive mixers. Passive mixers aim to increase the contact area between fluid layers by either splitting and combining the fluid or inducing vortex formation which creates multiple folds or turbulent mixing.

However, mesoscale flow reactors can be challenging and expensive to manufacture due to the complexity of the designs required for specific processes. In reactors having 3-dimensional channels, complex flow paths or internal structures such as baffles, it becomes highly laborious, costly or impossible to manufacture using conventional manufacturing techniques such as machining, injection moulding, and photolithography.

Additive manufacturing (AM) techniques provide a valuable tool for development of these complex devices. AM describes techniques that allow physical parts to be built directly from a 3D-model file, such as CAD, normally in a layer-by-layer fashion. Reactors can be designed for a specific purpose in a laboratory environment, rapidly manufactured and optimised to suit the process needs, whilst minimising the extensive use of computational methods, lead time for manufacturing and increased cost of one-off designs. Computational fluid dynamics (CFD) platforms are normally used in modelling fluid flow profiles, prior to reactor design. Although a valuable tool, CFD

analysis is highly complex and expensive to run. Additive manufacturing of flow reactors can allow the iterative optimisation of flow reactors for bespoke applications using residence time distribution studies. In this work, select AM methods suitable for cost-effective flow reactor manufacture were utilised in three novel applications:

- The production of Silver nanoparticles in a bespoke AM reactor with inline UV-Vis process monitoring.

- Paracetamol crystallisation in a bespoke AM crystalliser with inline heat transfer monitoring.

- A nylon AM reactor functionalised by immobilising enzymes on the wall of the flow path for the kinetic resolution of 1-methylbenzylamine

The applications aimed at demonstrating a methodology of developing a reaction process using AM, from reactor design to obtaining and monitoring the end product.

## Thesis outline

Chapter 2 consists of a literature review focused on AM advanced flow reactors for enhanced heat and mass transport. It provides an extensive discussion on the state-of-the-art in advanced continuous flow reactors (CFR). The utilisation of individual AM techniques in the development of flow reactors is also reviewed. The most current literature into the utilisation of AM in a number of unique chemical applications is presented. Chapter 2 is part of a recently published book chapter, (V) written by the author of this thesis.

Chapter 3 reports the investigation carried out into development of an AM flow reactor for synthesis applications. The fabrication of an oscillatory baffled reactor by vat polymerisation is presented. The methodology and results from synthesising Silver nanoparticles in a mesoscale AM advanced flow reactor is presented. Chapter 3 is part of a recently published work, which was carried out and written by the author of this thesis, (I).

A flexible and cost-effective methodology to develop compact AM crystallisers is presented in Chapter 4. The use of AM is demonstrated in the rapid design and manufacturing of meso-scale devices and efficient development of modular jacketed flow devices, where heat exchange can be modelled and controlled to generate efficient devices for applications in continuous-flow cooling crystallisation. The developed device is demonstrated in the crystallisation of paracetamol. Chapter 4 is part of a recently published work, which was carried out and written by the author of this thesis, (VI).

Chapter 5 reports the investigation carried out into the development of efficiently immobilising enzymes in an AM fabricated flow reactor creating added functionality. This involved a study into the fabrication of Nylon reactors using a cost-effective material extrusion platform. The development of a functional device enables the screening of reaction conditions for bespoke low volume biocatalytic applications. Chapter 5 is part of a recently published work (II). The development of the flow device was carried out by the thesis author, while the biocatalytic process described was carried out by collaborating authors.

Chapter 6 provides an overall discussion, conclusions and recommendations for future work.

# Chapter 2 Literature review

## 2.1 Introduction

Laboratory scale continuous tubular reactors (CTRs) have been increasingly studied over the past few decades. CTRs refer to the category of reactors in the continuous flow reactor (CFR) family, characterised by extended tubular channels in which synthetic processes are carried out. Across scales, CTRs are advantageous in safer handling of synthetic processes, minimisation of waste through efficient use of reactants and the isolation of compounds sensitive to air and/or moisture [1, 2]. Compared to stirred tank reactors, CTRs provide significant advantages in maintaining control of heat transfer, mass transport and application of extreme reaction conditions [2]. Hence, the amount of solvent and reagents utilised can be reduced whilst controlling the reaction temperature leading to the intensification of synthetic processes. CFRs have been shown to be advantageous for enhanced heat transfer in reaction applications of diazotization of aromatic amines, oxidation, electrophilic substitution of aromatics, organometallics, Paal-Knorr and reductions to name a few [1]. Enhanced mixing in CFRs has been demonstrated to be beneficial in the following areas: accelerated reaction rate in C-N bond formation, selectivity through precise ordering and contact of reagents in glycosylation, prevention of by-product formation in Moffatt-Swern type oxidation due to fast mixing and control of particle side distribution in silver nanoparticle formation [1]. CFRs also allow for the ease of utilisation of in process real time monitoring tools such as process analytical probes with optical turbidometrics, Fourier transform

infrared spectroscopy (FT-IR), UV-Vis spectrometer or focused beam reflectance measurement (FBRM) [3]. Examples of real reactors are presented in Figure 1.
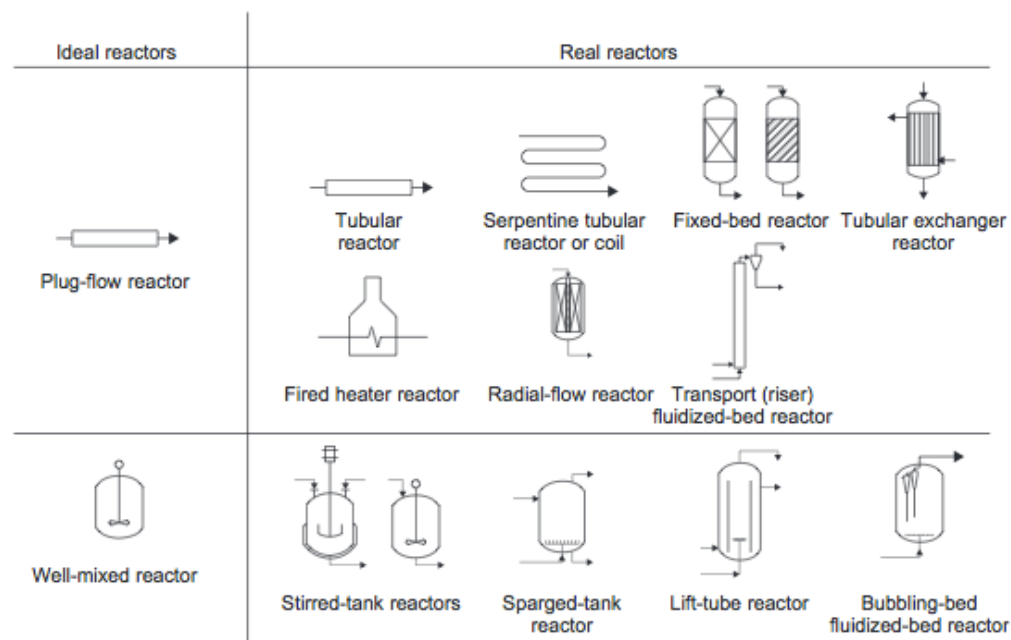


Figure 1: Ideal reactors and some examples of real reactors that approximate the same flow pattern.[4]

Lab-scale CTRs technologies have evolved from devices with simple flow paths to complex analytical systems allowing multiple functionalities [5, 6], resulting in significant process intensification [7]. Processing in lab-scale is highly beneficial for chemical and biological processes that require precise mixing and analysis of small volumes of rare, precious materials or multiple sequences. Such micro-scale analytical systems have been studied extensively as MicroTotal Analysis Systems (µTAS)[8] and lab on chip systems [9]. Microfluidic reactors are specifically beneficial for applications which require precise ordering and selective contact between reagents.

Laboratory scale CTRs are categorised dimensionally into micro-scale reactors and milli-scale reactors. Microscale flow reactors have a characteristic dimension below 1 mm. Mesoscale reactors lie in the range between microscale and macro-scale, and are normally operated at low flow rates (μl/min to ml/min) [10]. Mesoscale flow reactors lie at a unique interim position allowing for process scale up. Reactor design and selection utilises knowledge and experience in fluid mechanics, thermodynamics, chemical kinetics, mass and heat transfer, and economics [11]. In microfluidic reactors, flow tends to be laminar as the conditions correspond to low Reynolds. The Reynolds number (Re) is defined as the ratio of inertial forces to viscous forces, which for tubular reactors follows the formula: $\rho \cdot u \cdot L / \mu$, where $\rho$ is the density of the fluid, $u$ is the velocity of the fluid, $L$ is the characteristic length of the pipe and $\mu$ is the dynamic viscosity. At lower Reynolds, viscous forces are more dominant and is characterised by smooth and constant flow stream as opposed to mixing favouring chaotic patterns, eddies and vortices formed at higher Reynolds. A schematic of laminar, turbulent and plug flow is pictured in Figure 2. Reynolds closely relates to the Peclet number (Pe) and is the ratio of the advective transport to diffusive transport rate. Hence at low Reynolds, mixing is dependent on intermolecular diffusion due to the absence of turbulence.
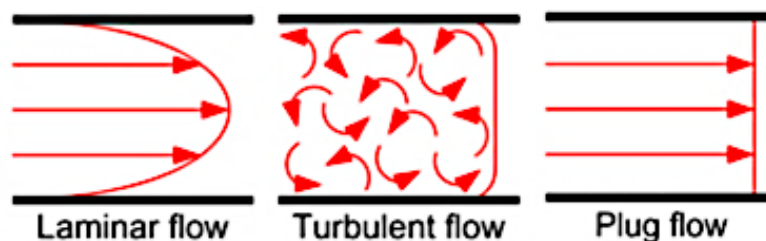


Figure 2: Schematic of Laminar, Turbulent and Plug flow conditions.[12]

Optimising diffusive mixing is dependent on maximising the diffusion coefficient, interfacial surface area and the concentration gradient i.e diffusive flux of a solute equals $D \cdot A \cdot \nabla c$. Enhancing the diffusion coefficient will require an appropriate increase in the temperature. Hence, several methods have been employed to maximise the interfacial surface area and concentration. An example of such a method includes splitting and re-combining the fluid to increase contact area. Other methods have been employed to enhance convection by inducing chaotic flow patterns [8]. These turbulent patterns are induced using mechanistic methods to agitate the fluid or embedded architectures in the flow path.

## 2.2 Enhancing mass transport in CFRs

To disrupt this smooth regular fluid motion in lab-scale, two categories of mixers commonly used are active and passive mixers. Both mixing categories which encompass different mixing techniques have been used in crystallisation, extraction, organic synthesis and polymerisation applications [13]. In CFRs passive mixers have become more popular than active mixers because they are simpler and easier to incorporate in lab-scale systems [14, 15]. Active mixers enhance mixing by using an external energy supply to agitate the fluid flow. They can be grouped into devices that have moving parts, i.e rotary and oscillatory motion, and without moving parts e.g. convection and electrokinetic instability [16]. They are also categorised by external disturbance effects: temperature [17], pressure [18], electrohydrodynamics, electrokinetics [19], magnetohydrodynamics [20], dielectrophoretics [21] and acoustics [22]. Active

mixers are less covered in the literature as even though their performance could outweigh passive mixers, their incorporation in fluidic devices can be challenging. They also require an additional power input to enhance mixing, making them more expensive to run [23]. Passive mixers are motionless, do not require moving parts or external forces. They are designed to effect mixing by diffusion or chaotic advection [23]. This is done by disrupting the laminar flow to give rise to the formation of vortices or eddies and by increasing fluid contact area resulting in increased diffusion time. Passive mixers are grouped by arrangement of the mixed phases: lamination (parallel & serial), injection, chaotic advection and droplet [20, 23]. Examples of mixing by parallel lamination include T-shape, Y-shaped mixers and multilamellar mixers, see Figure 3. The reactants are pumped into the reactor at multiple inlets after which they are combined and diffused along the channel length. Another example of a multi-lamination mixer is the circular mixer. Fluid flow from different entrants into the circular mixer creates an unbalanced force in the mixer resulting in the generation of a 3D vortex, which enhances mixing at low Reynolds [24]. A split-and-recombine design is commonly used to increase the fluid contact area. A split-and-recombine mixer is an example of serial lamination where three basic steps occur: fluid splitting, fluid recombination and fluid rearrangement [25, 26].
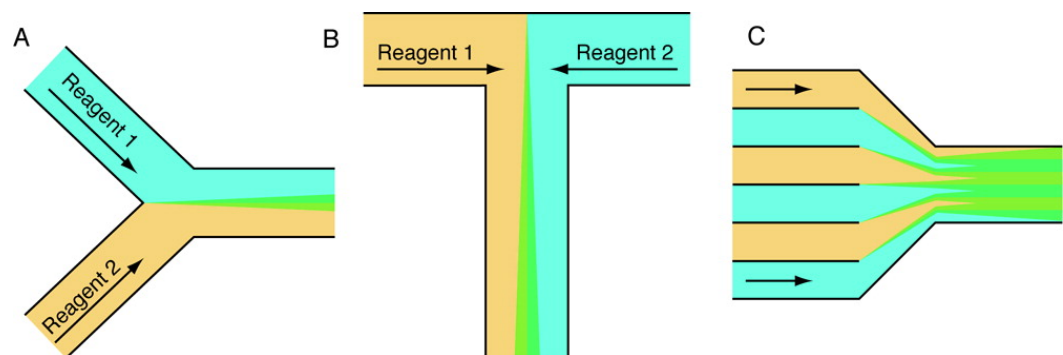
Figure 3: Schematic of different types of lamination mixers. (a) Y-shape mixer, (b) T-shape mixer and (c) multilamellar mixer [27].

Fluidic mixers based on chaotic advection vary in design but are similar in that the internal structure of the reactor enhances mixing by folding the fluid multiple times causing the formation of vortices and eddies. Baffled [28], herringbone[29-31], multi-orifice plates [32], zig-zag/meander channels[33] and helical mixers[34, 35] are some of the designs that allow optimised mixing. Static mixers have been established in the process industry dating back to the 1970s. They have been utilised for the unique heat transfer and mass transport benefits in industrial mixers such as Kenics mixer, SMV and SMX mixer, inliner series, Figure 4 [36].
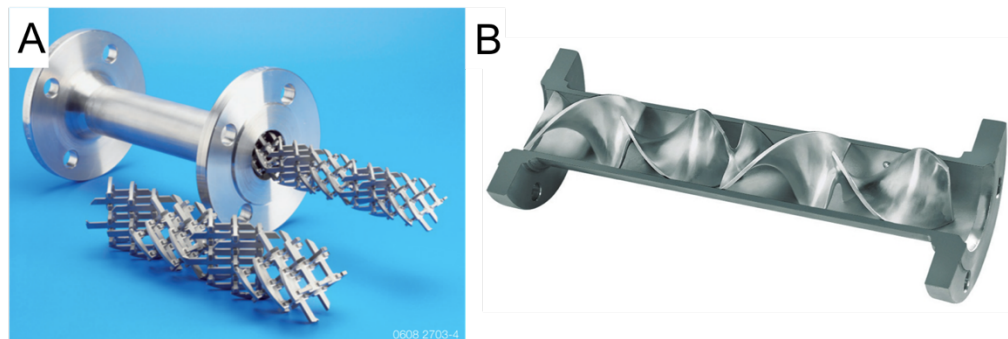


Figure 4: Industrial mixers. A) SMX mixer [37] B) Kenics KM mixer. [38]

Mixing in the different reactor designs is dependent on the geometrical properties of the embedded structures. Chaotic mixing effects can be created by either a continuous flow or oscillation of the fluid coupled with stationary embedded mixers in the flow path. In some cases, the embedded structures are oscillated or rotated with reference to the bulk fluid creating similar effects. Such cases are classified as a hybrid of both passive and active mixing, as they

involve the use of an external mechanism for moving baffles (MB)[39] or moving fluid (MF) [40] to create secondary flow patterns when coupled with stationary mixers.

Baffled reactors are common in literature and research areas involving fine chemical production. They comprise of the (i) single orifice[39] (ii) multi-orifice[32] and (ii) smooth periodic constrictions (see examples in Figure 5) [41]. Baffled reactors have been utilised in a number of applications including re-crystallisation of paracetamol [3, 42]. The mixing effects observed in baffled reactors are governed by physical dimensions including baffle thickness ($\delta$), spacing (L), orifice diameter ($D_o$), tube diameter ($D$) and open area ($\alpha = (D_o/D)^2$) [43, 44]. The effect of the geometrical parameters on the mixing effects have been studied and show distinct interrelationships [44]. For example, the space between baffles defines the shape and length of vortex formed. For uniform and effective mixing in inter-baffle zones an optimum gap is required for a complete vortex development. An under-developed vortex, resulting from sub-optimal distance, leads to collision with neighbouring baffles before expansion and undesired axial dispersion. In contrast, large baffle spacing leads to vortices that do not propagate across the inter-baffle zone resulting in stagnation areas. For tube diameters between 10 to 150mm, the optimum values are found to be: baffle spacing 1.5D, baffle thickness 2-3mm, baffle open area 20-22% and orifice diameter 0.45 to 0.50D [33, 43, 44]. The smooth periodic constriction baffles are designed such that dead/stagnation zones associated with the single and multi-orifice baffles can be eliminated, leading to a longer particle residence time. Flow in zig-zag and meandering channels provides breaking of the

continuous flow paths under laminar conditions. At corners, the fluid is stretched and compressed, changing the velocity profiles at each bend. With sharp edge corners, complex flow patterns are formed with the generation of eddies. Depending on the angles of the bend, sharpness of the corner and flow velocity a variation of eddies and patterns are formed [33].
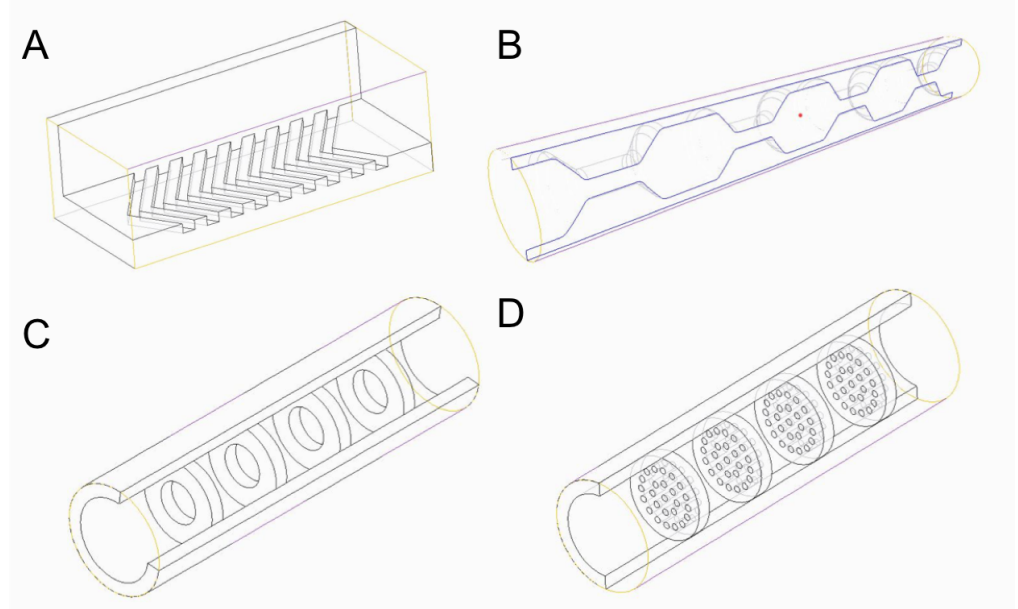


Figure 5: Examples of tailored design of static mixers for 3D-printing. A) herringbone mixer, B) smooth periodic constrictions (SPC) mixer C) single orifice mixer, and D) multi orifice mixer.

In the oscillatory flow regime, in addition to the Reynolds number Re $(\rho \cdot D \cdot u)/\mu$, an oscillatory Reynolds $Re_o$ $(\rho \cdot 2\pi f \cdot X_o \cdot D)/\mu$ is introduced. Other dimensionless groups of interest to characterise convective and diffusive mixing are the Strouhal number St $(D/4\pi \cdot X_o)$, Peclet number Pe $(uL/k)$ and velocity ratio $(\psi)$ $(Re_o/Re)$ [44]. The symbols are as follows; density $(\rho)$, frequency $(f)$, amplitude $(X_o)$, tube diameter $(D)$ fluid velocity $(u)$, dynamic viscosity $(\mu)$, characteristic length $(L)$, thermal diffusivity $(k)$. The Peclet number gives an indication of the

degree of axial dispersion. $Re_o$ relates to the mixing intensity and an increase is achieved by an increase in the frequency and amplitude. $Re_o$ can determine the nature of eddies whilst producing a range of mixing intensities coined soft mixing ($50 \leq Re_o \leq 500$) and hard mixing ($Re_o > 500$). The Strouhal is inversely proportional to the amplitude, hence it is a measure of the vortex propagation. Small Strouhal numbers relate to larger amplitudes and can result in desirable vortex formation.

## 2.3 Current production methods for CFRs

Reactors utilised in analytical chemistry, chemical engineering and process engineering have been manufactured using techniques including machining [45] etching [46, 47] to achieve the precision, channel size and surface roughness required. The reactor devices are commonly made using ceramics, polymers (Silicone, polypropylene, PEEK) or metals (Aluminium, steel). Large scale reactors are manufactured from extruded tubes of metals or plastics. These conventional techniques require large equipment and labour costs, specialised facilities and skill sets. Reactors with statics mixers are even more challenging to manufacture. Fabrication is normally from a single or multiple material as these complex internal structures are not easily manufacturable using one method. Material selection and manufacturing method is dependent on the scale of reactor required. Some more recent macro reactors are manufactured from glass tubes with plastic [3] or metal mixer inserts [10], however, they are limited to straight sections. Bespoke reactor manufacturing in glass can be very expensive as it requires specialist skill set and equipment.

Microreactors are commonly manufactured by etching, micromachining and laser ablation sections of the final reactor after which they are bonded by ultrasonic welding, laser welding or solution welding [48]. An example of a glass microreactor is present in Figure 6, where three layers of glass is milled, etched and fusion bonded together [49]. The first and third plates were manufactured using a micro milling machine (Micro-MC-2-Light, PMT Corporation, Japan) with diamond plated points (AD2104 [0.6 mm diameter at the top], and AD2211 [1 mm diameter at the top]. The second layer was fabricated by a combination of HF etching (by photo processing using micro-electro-mechanical system procedure) and milling. The three layers were then cleaned (using sulfuric acid and hydrogen perioxide), aligned manually, stacked and fusion bonded (5h bonding time) together. The process of manufacturing this fairly simplistic reactor design required expensive equipment and resources, skilled personnel and still provides room for errors in aligning the plates to form the device.
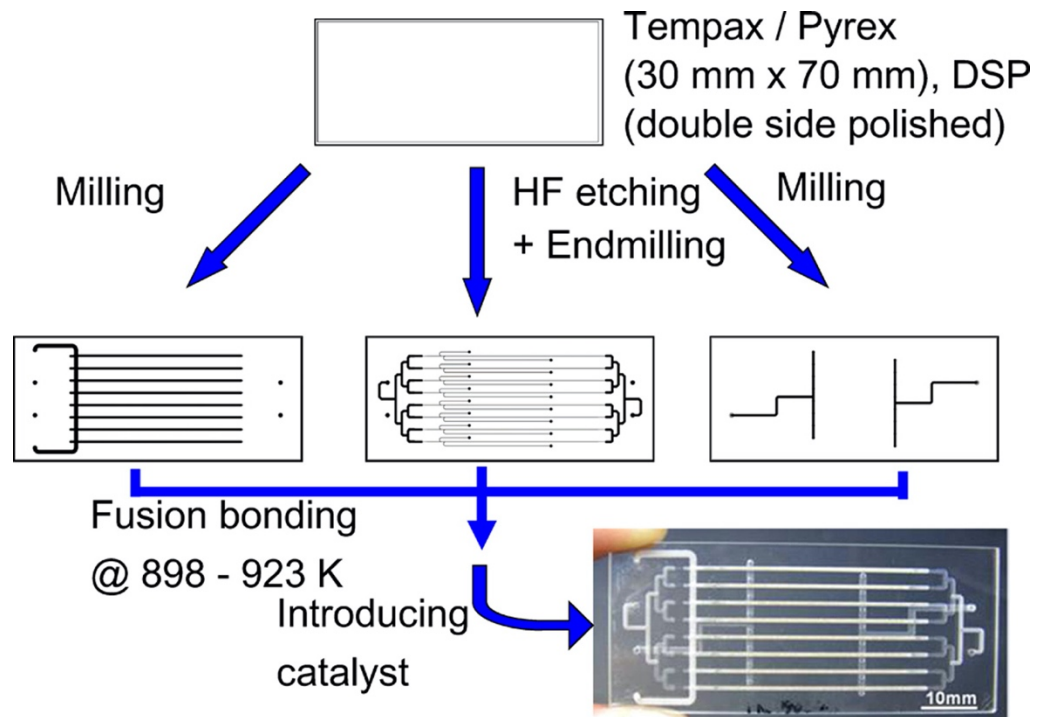
Figure 6: Fabrication process of a glass microreactor. Three glass layers required milling and etching before being fusion bonded [49].

Photolithography is a common technology in biomedical research for the manufacture of microfluidic devices. The process requires the production of channel architectures on silicon wafers which are then cast in PDMS. Although a key tool for microscale reactor manufacture, it requires cleanroom access, microfabrication tools, expensive reagents and extensive training. Fabricating 3D structures in photolithography creates challenges of precisely aligning layers. In multi-step lithography moreover, the extrusions produced are limited to 2D geometries [50]. PDMS reactors have low compatibility with organic solvents. Furthermore, the low temperature stability and mechanical strength when used in applications with elevated pressures and temperatures is a limitation [51].

Flow reactors can also be made by indirect manufacturing processes. In indirect manufacturing, the fabricated part serves as support or scaffold to a different process used to manufacture the flow device, e.g a resin flow reactor formed from a machined channel structure. All mentioned microreactor manufacturing techniques provide similar disadvantages, requiring specialised skill set and increased cost, and is prone to errors the smaller the scale [51]. Figure 7A shows a half section of a sinusoidal microchannel etched from stainless steel, while Figure 7B shows a stack of Poly(vinylidene fluoride) foils after a welding step. In this case, the welding was not carried out correctly, hence a gap can be observed in the middle of the structures. Similarly, incorrect alignment of the etched microstructure in Figure 7C when compared to Figure 7D resulted in non-elliptical microchannels after diffusion. The challenges in manufacturing lab-scale flow reactors with static mixers can be addressed by the use of Additive Manufacturing (AM).
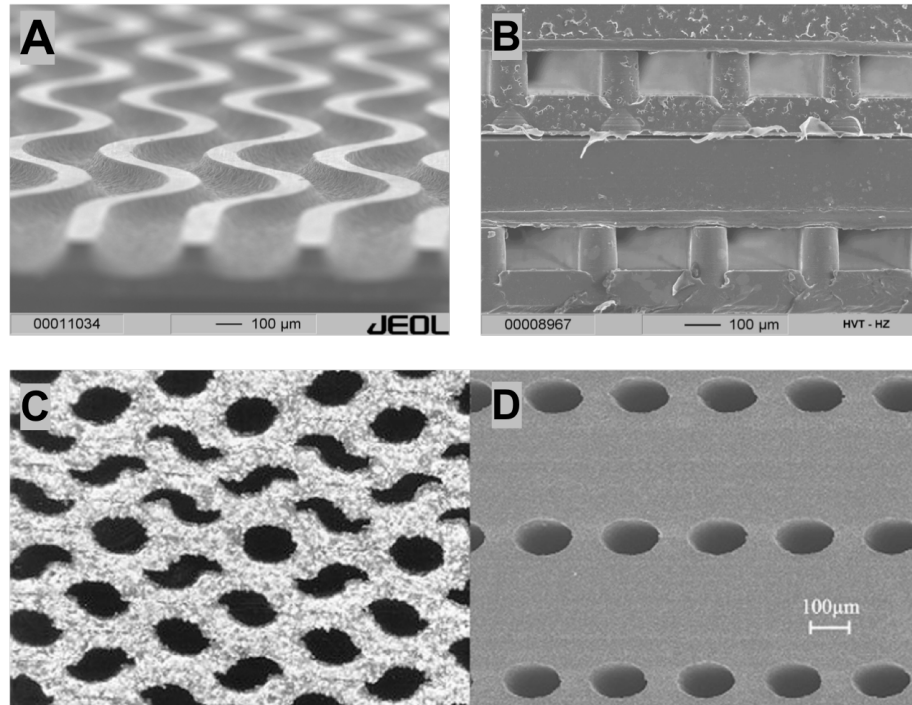
Figure 7: A) Stainless steel etched sinusoidal microchannels. B) Stack of Poly(vinylidene fluoride) foil after welding. C) Incorrect alignment of etched microstructure layers leading to non-elliptical channels after diffusion bonding D) Elliptical microchannels formed with correct alignment of microchannel layers [48].

## 2.4 Additive manufacturing of CFRs

In AM, also commonly referred to as 3D printing, parts are built directly from 3D model data, normally in a layer-by-layer fashion, in a variety of materials depending on the selected method. AM can serve as a valuable tool to manufacture millimetre-scale flow reactors with innovative internal architectures which were previously limited to microliter-scale microfluidic devices [52]. A search on Web of Science (WoS) on published articles with the topics '3D printed microfluidics', 'Additive manufactured flow reactors' and '3D printed flow reactors' from 2005 to 2018 show some interesting trends,

Figure 8. The plot shows a continuous increase in interest in the utilisation of AM for flow reactors in categories including nanotechnology, analytical chemistry and material science.
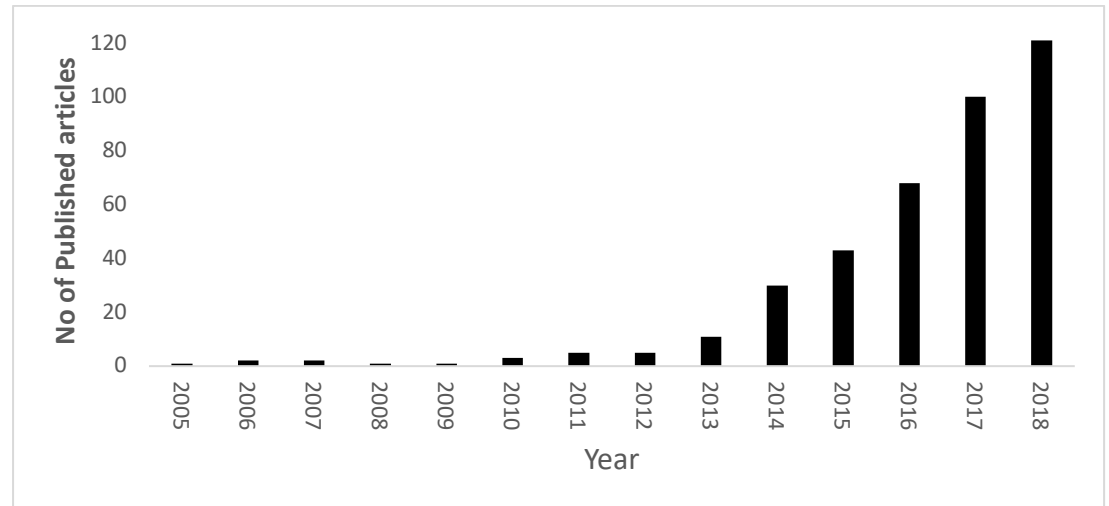


Figure 8: Published articles on web of science on the topics '3D printed microfluidics' 'Additive manufactured flow reactors' and '3D printed flow reactors' from 2005 to 2018.

AM processes can be grouped based on the deposition technique, form of the starting material or by the method of bonding and solidification [53]. AM processes have been categorized into 7 areas by ASTM F42: Material jetting (e.g Polyjet), Material extrusion (e.g. fused deposition modelling, FDM), Sheet lamination (e.g., ultrasonic consolidation), vat photopolymerisation (e.g., Stereolithography, SLA), Powder bed fusion (e.g selective laser melting, SLM), Direct energy deposition (e.g., laser cladding) and Binder jetting. Schematic representations for some of these techniques can be seen in Figure 9. In all AM techniques, the part fabrication starts from a designed 3D model, for example on a CAD platform such as Solidworks, Creo or open source options such as OpenSCAD and FreeCAD. The model is translated into commonly used

standard tessellation language (STL) or AM file formats, with subsequent slicing of the solid into defined layers and sequence of movements depending on the AM technique. For example, when building a part using a material extrusion technique, a component requiring some form of support for overhangs can be automatically generated in the platform's software. In the case of polymer powder bed fusion, where overhangs are supported by the surrounding unfused powder in the powder bed, support structures will not be relevant. Depending on the technique, the parts could be post-processed to improve the strength or surface quality. Several factors strongly influence the applicability of the different AM categories in fabricating flow reactors. The characteristic method of manufacture plays a major role.

## 2.4.1 Material Extrusion

AM platforms based on extrusion-based techniques are common and relatively inexpensive (see Figure 9D). Fused deposition modelling (FDM) is one of a number of extrusion-based methods and was patented by the company Stratasys. Parts are built up in a layer-by-layer fashion using a heated nozzle to extrude thermoplastic polymer in a pre-programmed pattern. Commonly utilised materials include Acrylonitrile Butadiene Styrene ABS, Polylactic acid PLA, Polypropylene PP, and Polycarbonate PC. Parts can be built with single or multiple materials with the option of a dual extruder nozzle on some platforms. Depending on the geometry of the part, a sacrificial material serves to support overhanging surfaces during fabrication. Extrusion based systems vary in the resolution and reproducibility between the low-cost DIY platforms and the industrial platforms. The more expensive systems include features such as

heated platforms, larger build volumes, humidity and temperature control, dual extruders and material specific programmes aiding improved quality of parts produced. The size of parts achievable is only restricted by the dimensions of the build platform and the robot gantry size. The resolution on FDM platforms, although dependent on materials and machine specification, ranges between 0.35 to 0.1mm at fabrication accuracy of around ±0.25 mm [52].

In Robocasting, another example of an extrusion-based method, paste-like suspensions of ceramics, metals or polymers can be deposited similarly to form solid parts after drying or firing. In this case, a resolution of 30 – 500 μm is normally achieved [54]. Although FDM has been used in a number of applications, it's use in developing flow reactors is challenging. The difficulty is in creating a good seal between the deposited polymer layers repeatedly along the channel path to prevent leaks. Typically, FDM parts have poorer physical properties perpendicular to the build plane as such leaks are normally projected between layers [52]. This can be challenging in reactors with smaller channel diameters and sharp corners due to the staircase effect created. Creating leak free reactors is dependent on a number of factors including selected material, reactor geometry, fabrication conditions and layer height.


### 2.4.2 Vat Photopolymerisation

Vat photolymerisation (VP) describes AM techniques where parts are built from a vat of liquid state photopolymer resin and cured in selective areas using a UV-light source, either a scanning laser or digital light projector. The process of fabrication in this method is by bat or bath configuration. In the bat

configuration, the part constrained to the platform is held above the vat of resin, allowing fabrication as the platform moves upwards at defined layer widths. The UV-light is projected from underneath the optically clear vat window, commonly made from FEP or PDMS. As the name implies, the part hangs from the platform bottom–up when completed, as shown in Figure 9E. This helps uncured resin from the surfaces to drip back into the vat before cleaning. In the bath configuration, the layers are photo-polymerised on the vat surface as the platform moves downwards towards the bottom of the platform. In this case, the light source and the scanning system are positioned on top of the vat whilst the part is fully submersed in the resin during the build. Disadvantages of this approach include the extensive cleaning process that is normally required, reactions with ambient air and resin waste [55]. As observed in Figure 9E, the size of the part is restricted by the size of the vat. In cases where the build fails and leads to particles of cured material in the vat, the waste will be costly. The bat system has several advantages over bath systems and is increasingly applied in vat photopolymerisation applications.
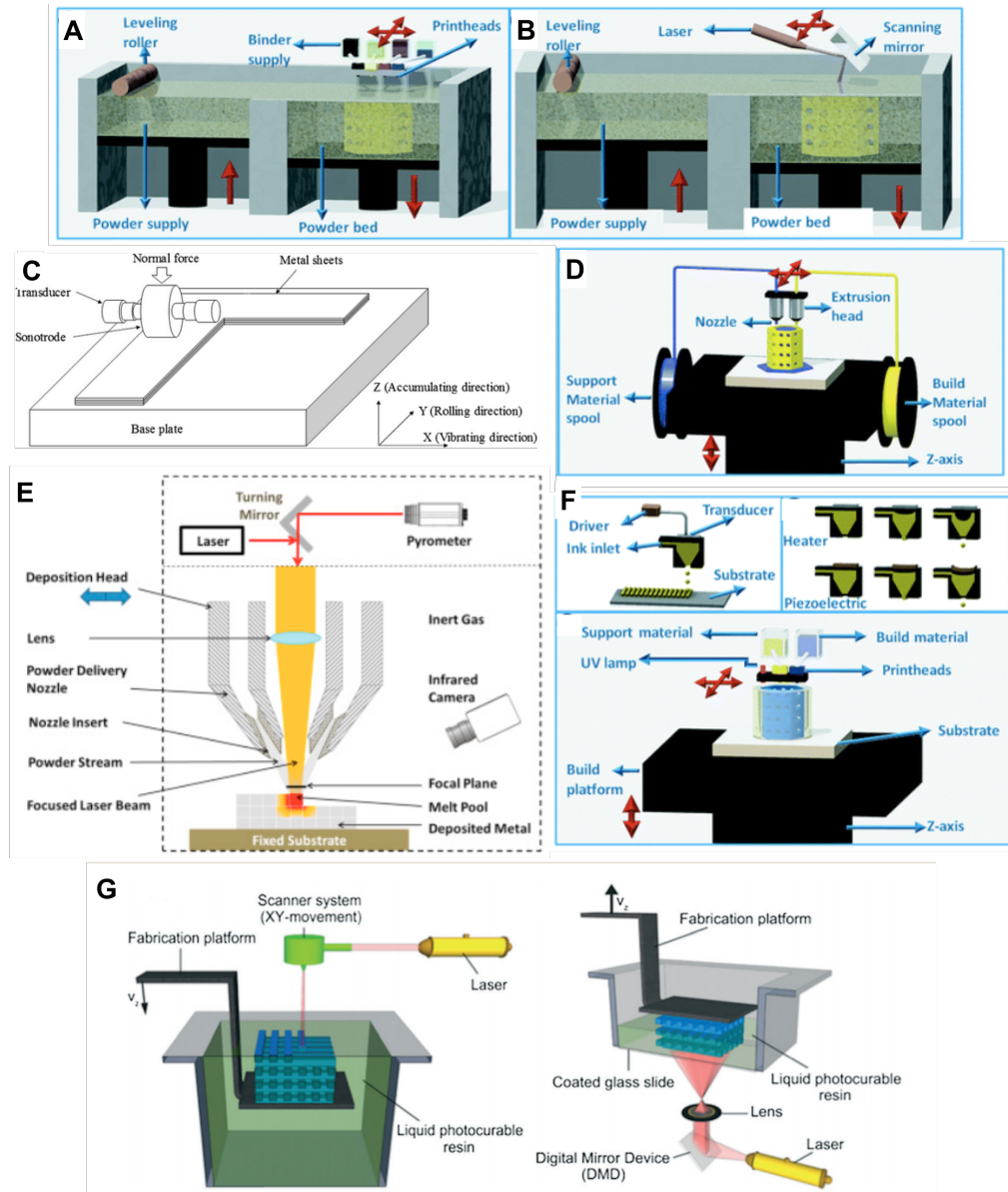
Figure 9: Summary of AM techniques: A) binder jetting; B) selective laser sintering (SLS) or melting (SLM); C) sheet lamination; D) fused deposition modelling (FDM); E) direct energy deposition; F) inkjet printing; G) vat photopolymerisation. Adapted with permission from references [54, 55].

Stereolithography (SLA), Stereolithography - Digital light processing (SLA-DLP) and Continuous Liquid Interface Production (CLIP) methods are common vat photopolymerisation techniques. In SLA, fully dense parts are produced using a laser which draws out the required 2-dimensional patterns on the optical

window at high speeds. Laser spot sizes are typically around 0.15 mm producing parts with layer thicknesses of as low as 25 μm to 150 μm. SLA-DLP utilises a DLP projector to flash an image of each layer at a time towards the optical window. The surface quality in parts produced by SLA-DLP is dependent on the size of the pixels in the projected voxel. The fabrication process is similar in SLA and SLA-DLP, after the UV-light source is projected (laser, projector or LED source) at a defined exposure time, the part is separated from the surface. A wiper mechanism then cleans out the window in preparation for the next layer build. CLIP technique is the most recent of the vat polymerisation methods and put forward by the company Carbon3D. CLIP is similar to SLA-DLP, as it uses a projector which sits underneath the vat of resin. However, fabrication is much faster than in traditional SLA as a part separation from the window and sweep action is not needed. In CLIP, an oxygen permeable window is used between the resin and projector. This creates a 'dead zone' at that region, inhibiting photopolymerisation and stopping the part from sticking to the surface. As such it is referred to as continuous printing. Most VP techniques can produce very good surface quality and dimensional accuracy although this is dependent on orientation, layer thickness, resin property and geometry [56]. VP platforms are typically limited to a narrow range of UV-curable polymers based on acrylates, urethanes and epoxides. When cured, the material will be densely cross-linked resulting in better mechanical properties. However, the polymer is still susceptible to swelling in some solvents. For flow reactors with these materials, their use is limited to a reduced range of solvents. TGA and IR showed changes to the degradation profile and chemical structure of Formlabs resin, Clear (FLGPCL02), soaked in Isopropanol (i-PrOH), Ethanol (EtOH) and Acetonitrile

(MeCN) at room temperature for 24 hours [40]. Significant swelling was also observed in VP parts made from Accura 60 resin, soaked for 24 hours in THF and dichloromethane [52]. However, research is on-going to develop materials for VP with better mechanical and chemical properties.

### 2.4.4 Material jetting

Material jetting (MJ) describes branded technologies including Polyjet and MultiJet Printing. In material jetting, a print head, similar to a standard inkjet printer head, is used to dispense materials in a continuous or drop on demand (DOD) approach onto a build platform. The materials are then hardened simultaneously with an UV-light source normally attached to the print head. A controlled XYZ gantry system, which the print head is attached to, allows parts to be built in a layer-by-layer fashion. Droplets are released on demand due to the pressure change in the nozzle by thermal or piezoelectric actuators. In piezoelectric print heads, the piezo element attached to a silicon plate contracts when a voltage is applied. This mechanical movement on the ink reservoir allows materials to be dispensed. In thermal systems droplets are formed from local evaporation of the ink solvent, creating a bubble in the reservoirs. The piezoelectric method allows a wider range of materials to be used. Materials used in MJ are similar to that of SL. They are normally acrylate-based photopolymer resins. Commercial MJ devices allow a layer resolution of 25 to 100 μm at deposition rates of 1 pL to 1 nL per droplet to be achieved [57]. Multiple nozzles which are individually controlled on the print head allow deposition of multiple materials in a single build. Sacrificial materials are used

as support structures alongside the functional materials and are normally removed on completion by water jetting or soaking in sodium hydroxide solution. Water jetting can be used to create smooth surfaces, although cleaning out channels with numerous corners and active mixers is challenging. The use of multiple materials makes it possible to achieve a matt or glossy finish, rigid or flexible and multi-coloured components. As a post processing step, MJ parts can be post cured under UV light to enhance their physical properties such as rigidity. MJ platforms enable narrow, complex channels to be manufactured accurately. Generally, the materials used in MJ UV-curable polymers based on acrylates, consequently the advantages and disadvantages for chemistry applications are similar [52]. With the development of new materials, compatible to a range of chemistry applications, the utilisation of AM-MJ for flow reactor manufacture will increase.

## 2.4.5 Powder bed fusion

In powder bed fusion (PBF), parts are built from fine layers of powder consolidated by heating. Powder based AM techniques include laser sintering (LS), selective laser melting (SLM) and electron beam melting (EBM). The listed techniques alongside SLA are well-established and are capable of producing superior resolution parts reproducibly when compared to other AM techniques. Although the resolution achievable is dependent on material, platform and the laser spot size, parts can be fabricated from polymers, ceramics and metals. Polymers are usually processed by LS and have the advantages that they do not require support structures as overhangs and isolated regions are

supported by un-fused powder in the build area. On LS platforms, the bed of powder is ideally heated close to the material melt temperature, and a laser is used to fuse layers, typically 0.1 mm or 0.15 mm, that make up a part. LS materials are usually based on polyamides (PA12 and PA11) with less frequent utilisation of PP, PEEK, TPEs and ceramics. Due to the high velocity of the laser scan over the powder surface, solid state sintering is not achieved with polymers, as the time for diffusion for solid state to occur is insufficient. As such, consolidation observed in LS is liquid phase sintering and/or partial melting although full melting can occur [58]. Parts can be heat treated to influence the physical and mechanical properties. However, this will lead to shrinkage of parts and should be taken in account at the design stage. Although highly precise parts can be produced in LS processes with materials with good solvent compatibility, clearing out the channels of powder is challenging. The heat generated during fabrication compacts the powder in the channels making it difficult to clear even by sonicating or jetting, more so in designs with narrow path and sharp bends [52]. As the polymer powder spends significant time close to its melting temperature, it often starts to degrade and has to be mixed with fresh, "virgin" powder [58].

Support structures are required for SLM of metals. With this technique the layers are fully melted to liquid state creating completely dense parts using a high-power fibre laser of 100 to 400W to produce thin layers of 0.02 to 0.1 mm. Commonly used materials in SLM are titanium, aluminium and stainless steel which are chemically stable to a broad range of conditions. A major advantage of metal reactors is the potential utilisation for high temperature applications.

Utilisation of SLM will be advantageous in flow reactors and heat exchanger applications. The remaining powder utilised in SLM can be fully reused without mixing with virgin powder, though un-melted material in the channels requires removal. EBM is another PBF method where materials are placed under vacuum and fused together by direct heating by an electron beam. In EBM, the powder is held at high temperatures (>870 K) during processing. Optimising the EBM process can be challenging as it involves more process parameters, which include beam scanning velocity, beam power, beam focus, plate temperature, pre-heat temperature (including the repetitions, speed, and power of the beam), beam diameter, beam line spacing, contour strategies, and scan strategy [59]. Common materials used in EBM are Ti grade 2, Ti6Al4V, Inconel 718, CoCrMo. Post processing in SLM and EBM requires separating un-fused powder from the fabricated part. The parts are further cleaned by air or powder jetting. Surface finish can be improved by computer numerical control (CNC) machining. Heat treatment can also be carried out to improve the density and strength of the parts.

**2.4.6 Other AM technologies**

Binder jetting (BJ) is similar to powder bed fusion methods as parts are built up from layers of powder but they are consolidated with a binder agent jetted on demand from a nozzle head. Parts from BJ normally compose of metal (including Al-based, Cu-based, Fe-based, etc.) or ceramic (including glass, sand, graphite, etc.) based material fused with adhesive. The manufacturing process is similar to other AM techniques; however, it requires several post processing steps [59]. These include de-powdering, curing, sintering, infiltration, annealing

and finishing. The binder-powder combination may however not be suitable for a wide range of solvents, and parts are generally much weaker. Directed energy deposition (DED) methods uses material in wire or powder form, coupled with laser, electron beam or plasma arc to build up layers. In sheet lamination, sheets of material are bonded together using an adhesive or welding and laser cut layer-by-layer to form a 3-dimensional part. The resolution on DED and sheet lamination platforms are not suitable for flow reactors as they will require post machining to achieve the surface finish and feature sizes required.

## 2.5 AM for Advanced flow reactor manufacture

Early work on additive manufactured flow reactors has predominantly utilised extrusion-based AM methods. This is presumably because it is an easily accessible, cost-effective method and offers a wide range of materials for researchers to explore. Although it has a relatively low resolution for AM platforms, reactors fabricated by extrusion-based methods have been utilised in a number of synthesis applications. Cronin and co-workers utilised polypropylene on a low-cost extrusion-based platform in manufacturing three 'reactionwares' having one, two and three inlet configurations [60]. The utility and versatility of utilising AM in the fabrication of reactors was demonstrated in organic (reductive amination and alkylation reactions), inorganic (large polyoxometalate synthesis) and material synthesis (gold nanoparticle synthesis) (see Figure 10). Similarly, FDM was employed in the fabrication of 0.54 mL and 0.51 mL reactors which were utilised in imine synthesis and imine reductions (see Figure 10) [61]. The reactors were connected to standard fittings

and tubing to syringe pumps and were monitored by inline ATR-IR. More recently, the same group has demonstrated the viability of this technique to manufacture miniaturised devices for automated synthetic set-ups [62].
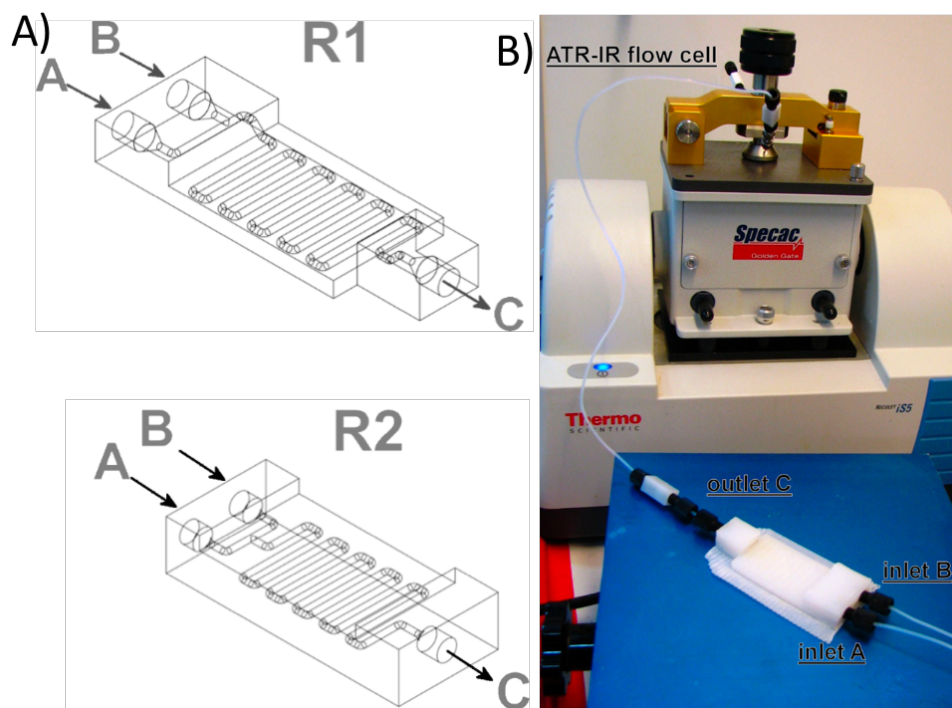


Figure 10: A) CAD design of flow reactors design for organic synthesis. B) 3D printed reactor in a continuous-flow set-up connected to an in-line ATR-IR detector. Adapted from reference [61].

Reactors fabricated on extrusion-based platforms are highly prone to leaks both between layers and across the areas on the deposited filament. Magnified images from a FDM reactor highlights unfilled areas in the reactor volume which suffered from leakage (see Figure 11) [63]. Although using a high fill density across the layer will fill the gaps, inter-layer leaks will depend on the cohesive bond between the polymer and the extrusion temperature. Another limitation of FDM, which is similar to other AM platforms with larger layer resolutions, is

the surface roughness. Utilisation of platforms or materials restricted to larger layer thicknesses will lead to flow devices with ridged or 'scalloped' patterns which, when used, may produce results that vary largely from the intended design. An example of this pattern is pictured in Figure 12 where a centrifugal microfluidic device fabricated in ABS material by FDM method was cast in PDMS. The surface effect is also shown which was collected using a contact profiler [64].
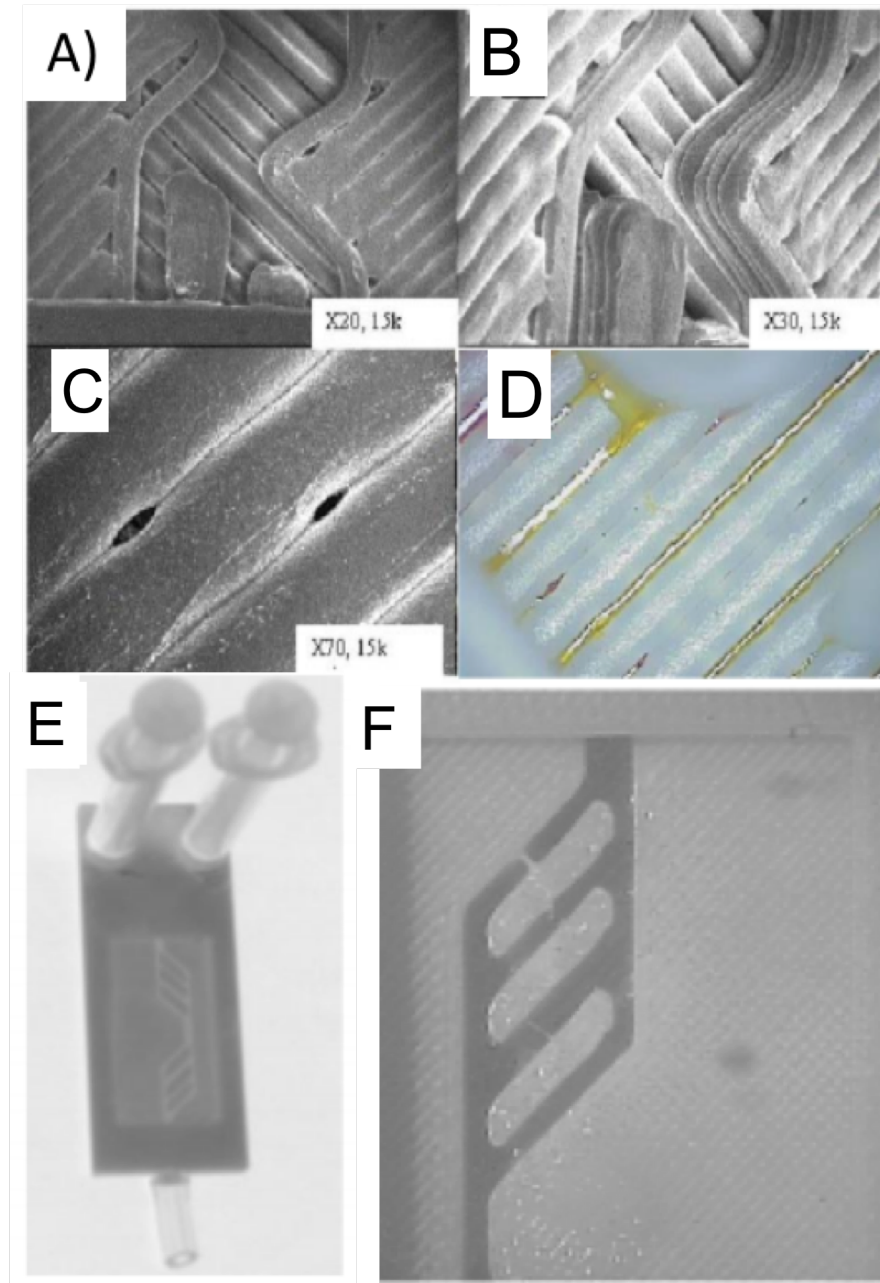
Figure 11: Close up images of microchannels on an FDM3000 fabricated microreactor at magnifications: A) X20 B) X30 C) X70. D) Image showing liquid flowing through the unsealed device using a CCD camera; E) FDM fabricated microfluidic device with channels and connectors F) close up view of the reactor channels. In the microfluidic device fabricated by material extrusion, unfilled cavities can be observed allowing for leaks to occur [63].

In a split-and-recombine device produced by Capel and colleagues [52], employing FDM with ABS filament, the devices were also found to leak in multiple regions at above 20 bar pressure. Extrusion based methods in flow reactor manufacture are valuable, although producing leak-free devices is challenging. More so with the requirements of advanced mixing capabilities, i.e active and passive mixing methods, which can improve heat and mass transfer.
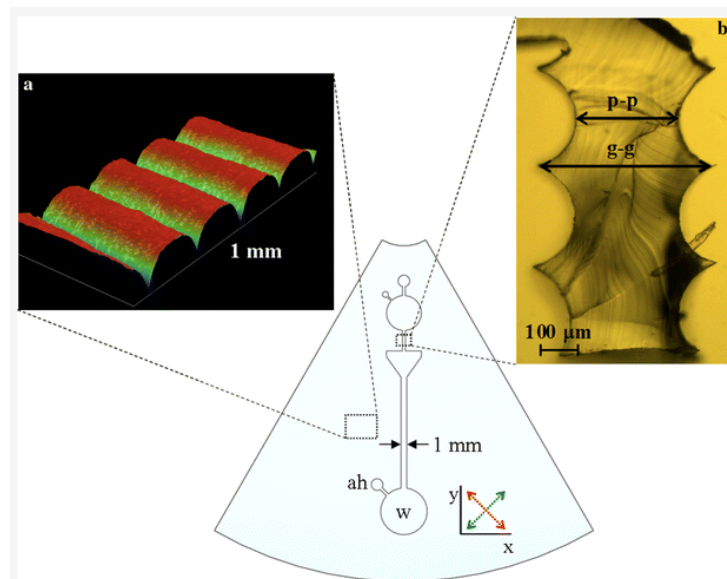


Figure 12: Top view schematic of a trapezoidal microfluidic reactor. a) surface profile of the device using a Dektak 8 contact profiler b) A slice of a channel section in the fabricated device cast in PDMS. Channel surface scalloping can be observed in the FDM device. [64].

Employing vat photopolymerisation (VP), Shallan et al. [65] fabricated a 3-dimensional mixer based on a split and recombine geometry, see Figure 13A. The geometry aimed at enhancing mixing by folding the fluid at the repeated 3D bends and re-combining at intervals, thus creating a larger area for fast-diffusion

45

based mixing. VP was highly beneficial in the reactor production as the 3D structure would be very difficult to manufacture by traditional methods. In other AM methods, achieving the required resolution and clearing the channels would be challenging. When compared to a similar tubular reactor using aqueous solutions of 0.1 μg/mL fluorescein (green) and 1 μg/mL rhodamine B (red) at similar flow rates the 3D mixers showed complete mixing indicating a better performance. Using the same materials and VP technique, a 3D gradient generator was also fabricated with three levels of combining, mixing and splitting, resulting in different dye ratios drop pure dyes in the peripheral units, Figure 13B.
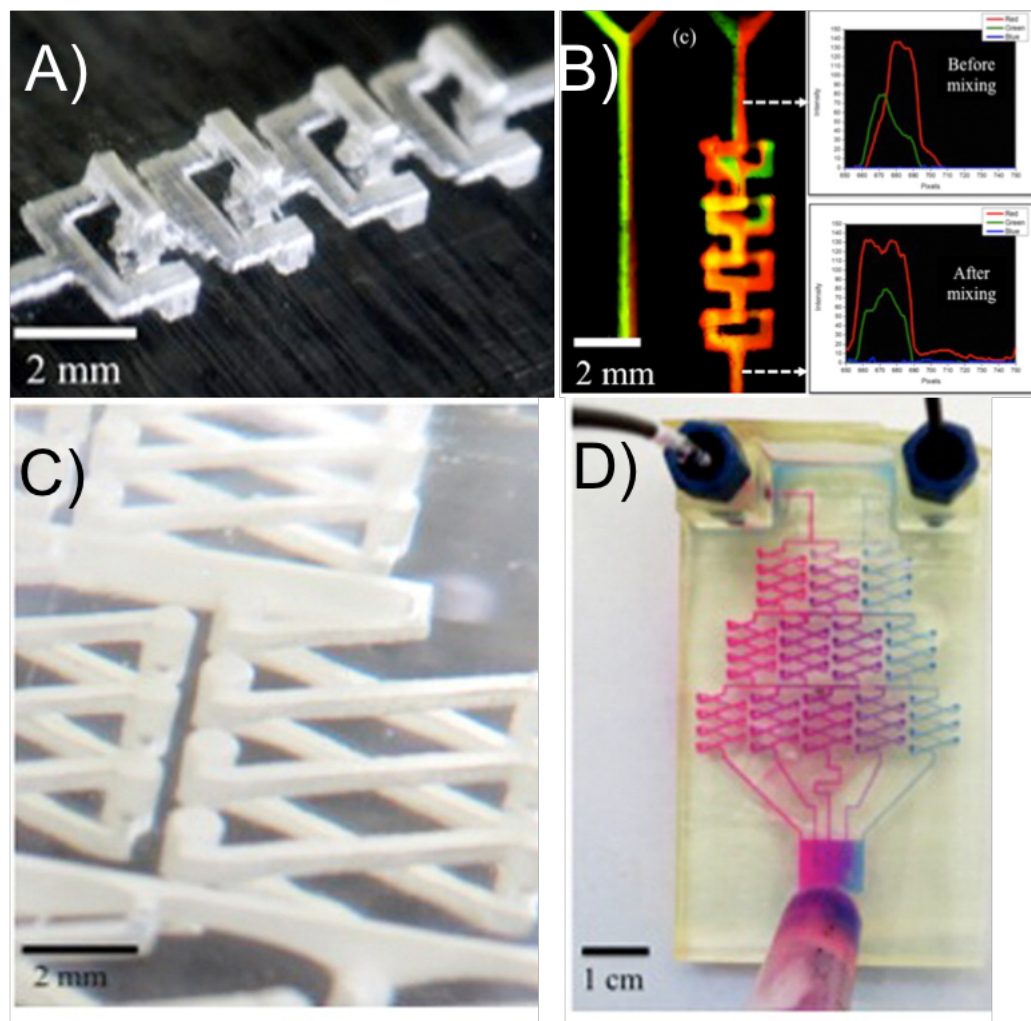
Figure 13: A) A 3D dimensional split-and-recombine micromixer. B) Fluorescent images of a comparison with straight channel with mixing results before and after mixing at a flow rate of 10μL/min. C) Detail of the AM fabricated unit of three stages of split-and-recombine microreactor. D) Gradient generation using two coloured dyes, bromothymol blue and rhodamine B. Reprinted with permission from reference [65].

An interesting bio-chemical application was demonstrated where the detection of pathogenic bacteria was carried out in a helical channel with a trapezoid cross-section using size based separation, see Figure 14 [66]. The researchers aimed to efficiently separate magnetic nanoparticle clusters (MNCs) and MNC-E. Coli complexes. The helical nature of the reactor results in secondary flow formation which consists of two generated vortices. The asymmetric nature of the trapezoidal channels results in the vortices to be larger at the outer wall reducing in size up to the smaller wall. This results in a size-sorting effect, where smaller materials migrate towards the outer channel wall leaving the larger materials at the narrower region. The solution of MNCs and MNC-EC were focused towards the outer wall of the reactor by Sheath flow at the inlet. On exiting the reactor, the MNC-EC was collected towards the inner wall, separating the free MNCs and collected at one of the two outlets.
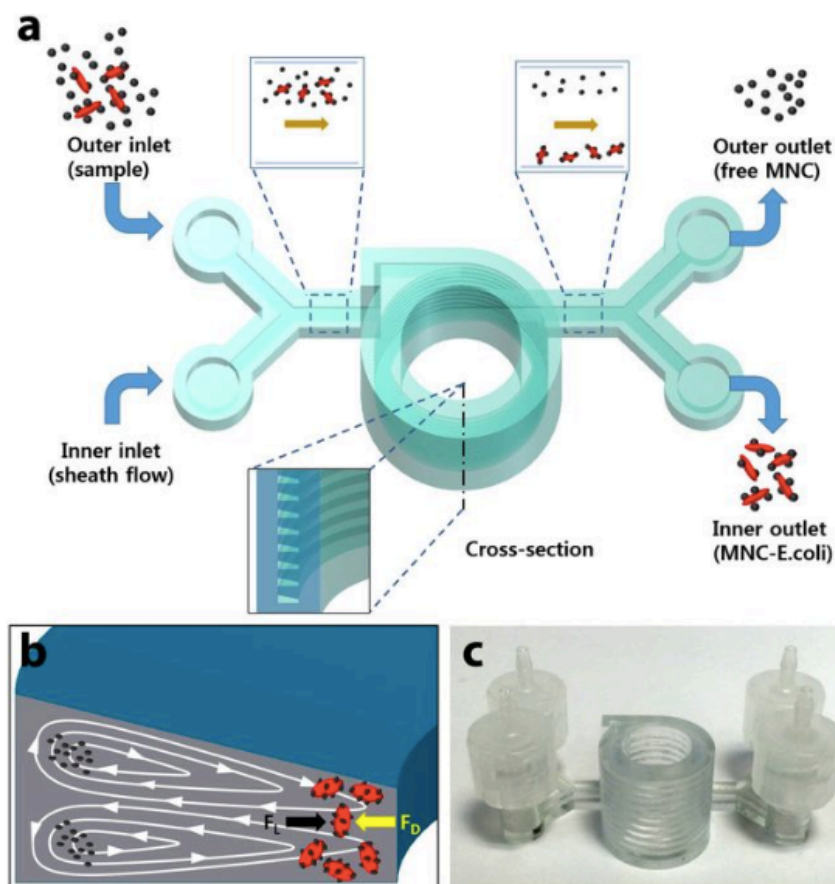
Figure 14: Dean flow based trapezoidal reactor for the separation of magnetic nanoclusters with and without bacteria. Reproduced from reference [66].

Capel and colleagues demonstrated the utilisation of VP and selective laser melting (SLM) to develop flow rectors with embedded analytical functionality for reaction optimisation [6]. The reactor device in Figure 15 was designed to be coupled with a light source and detector replacing the use of a flow cell. The set-up was trialled to optimise two reactions; a fused polycyclic heterocycle formation and a ketone functional group interconversion. The reactor device demonstrated the potential for the manufacture of bespoke flow devices for specific applications which can be designed to fit off-the-shelf components.

Figure 15: 123x67x47mm CAD model of VP flow reactor (left) Reactor device with sprung clip (centre) commercially available Agilent flow cell (right) [6]

However, the reaction required the reactor vessel to provide uniform temperature and optimal thermal conductivity to obtain the required yields which the polymer material could not. A second reactor manufactured by SLM in Ti-6AL-4V alloy opened up a much wider range of potential synthesis which will degrade the acrylate-based reactor. SLM provides the benefit of thermal stability in the reactor whilst heating at a wide range of temperatures [6].
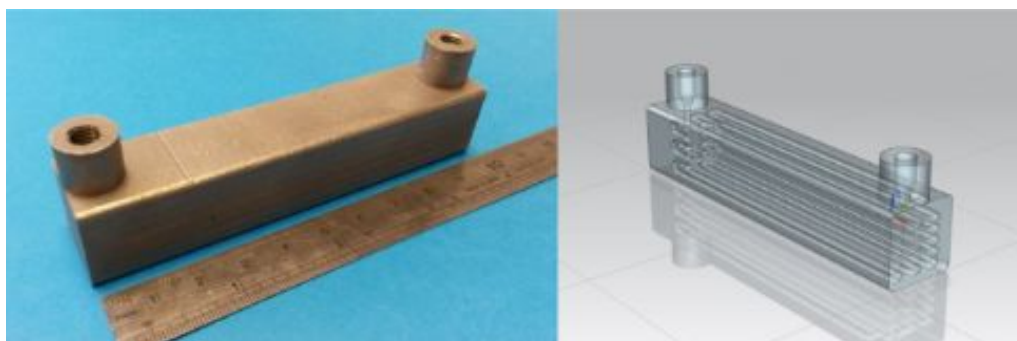


Figure 16: 100x20x20 mm SLM flow reactor (left) CAD model for flow reactor showing channel path (right) [6]

Using VP, comprehensive experimental work on open cell foams operating under low Reynolds number regime (Re < 50) has been presented by Bracconi et al, (Figure 17) [67]. Open-cell foams are considered promising candidates for structured catalyst supports for high throughput catalytic processes. They have a large surface area to impinge catalyst, which can also act as static mixers to enhance mass transport. AM enabled the fabrication of complex foam structures

with cell size of *ca.* 4 mm and porosity of 0.8, which was measured employing micro computed-tomography (μCT) scanning. The VP fabricated geometry was measured and compared to the CAD file. The deviation was as little as 1-5% depending on the strut size and foam porosity. The denser the packing, the more area for the un-polymerised resin to form a skin. Comparing experimental work on the foams and computation fluid dynamics data, the work aimed to close the gap between theoretical models and real structures. A close correlation was found between the pressure drop and cell diameter, porosity and strut geometry.
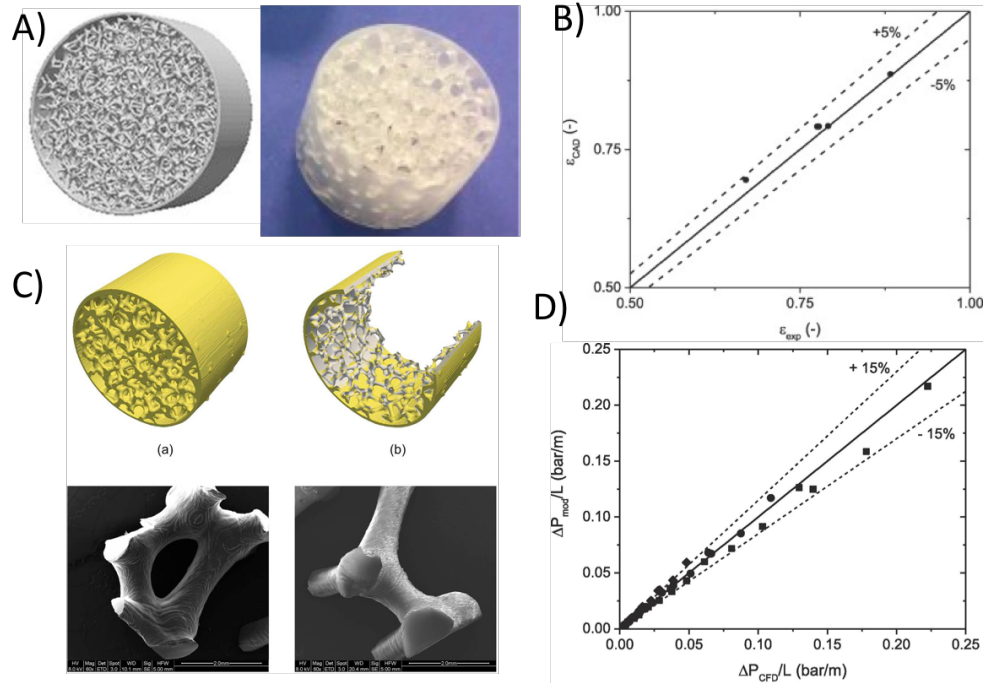


Figure 17: Additive manufacturing of structured open-cell foam packed reactor structures. A) Pictures of CAD design and AM developed part with SLA. B) Comparison of experimental vs. calculated porosity. C) μCT and SEM analysis of the printed devices. D) Pressure drop experimental vs. predicted in packed bed reactors based on the open cell foam structures manufactured. Adapted from reference [67].

Using electron beam melting EBM, a powder based AM method, a group of researchers developed bespoke catalytic static mixers (CSMs) (see Figure 18) [68]. The CSMs combined the improved mass transfer benefits of incorporating static mixers in the flow path with the functionality of the mixers serving as catalysts. The mixers were designed for specific synthetic processes and were coated with nickel or platinum catalyst after fabrication. The EBM based fabrication was made employing TiAl64V or cobalt-chrome powders which were cold sprayed or electroplated with the required catalysts.
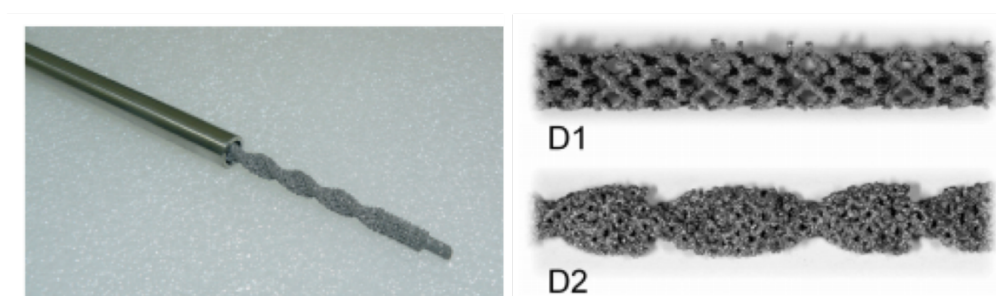


Figure 18: Structured catalytic static mixer generated with EBM for continuous flow hydrogenations. Reprinted from reference [68].

The AM catalytic flow reactor was evaluated in continuous flow hydrogenations of carbonyls and alkenes. Improvements were reported over current state of the art reactor systems using this approach. The benefit of utilising this approach is mainly due to the complex geometries generated in the 3D static mixers which enhance mass and heat transport while creating a large surface area for catalyst deposition. In this application, the researchers utilised a powder-based technique to manufacture static mixer inserts that fit into standard tubes. In a recent publication, selective laser melting SLM has been employed in manufacturing a complete synthetic flow reactor with heat exchanger functionality [51]. The reactor was designed and manufactured with multiple inlets tubes wrapped

around a heat exchanging tube. It was fabricated in stainless steel to ensure good heat transfer properties of the device. The fully fabricated device was used in the continuous synthesis of difluoromethyldiphenylactonitrile using fluoroform (see Figure 19).
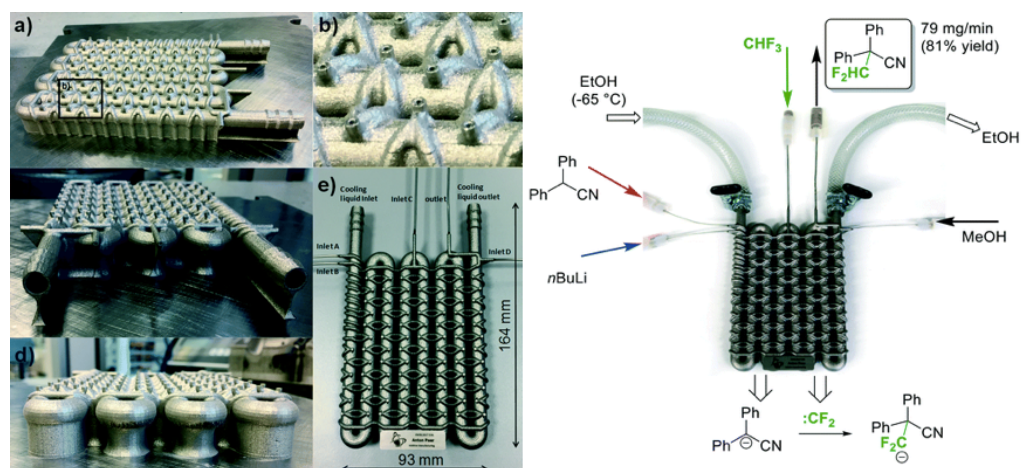


Figure 19: AM-based flow reactor fabricated in stainless steel by SLM. Left: Details from the manufactured reactor. Right: Scheme of the reaction performed with the flow reactor. [51].

## 2.6 Summary of literature and knowledge gaps

The employment of AM for the development of continuous-flow devices has experienced a rapid increase since the seminal work from Kitson *et al.* [60]. In recent years, increasingly sophisticated devices have been developed, aiming to offer advanced features to yield process advantages in terms of reducing heat and mass transfer limitations and improved mixing features. This has been possible due to the rapid development of the manufacturing techniques that allow cost-effective reproducible manufacturing at the required scales in a variety of materials. In the future, the development of even more sophisticated

devices, that allow not only chemical reactions, but other unit operations such as separations, electrochemical transformations or crystallisations under continuous-flow, are expected. Deductions from literature can be highlighted into the following points:

- Micro to mesoscale flow reactors are valuable for a number of mixing applications. The mass transport and heat transfer in the flow reactor is largely influenced with passive and active mixing methods, which is vital for applications requiring precise mixing.

- AM methods have been demonstrated to be valuable in the development of bespoke micro to mesoscale flow reactors which can be multi-functional and designed to fit off-the-shelf lab instruments and components.

- Select additive manufacturing methods are more beneficial for flow reactor development at their current stage. The barrier to utilisation of the methods relates to the capability to achieve the required precision, solvent resistivity of materials, thermal conductivity, manufacturing optimisation and ease of support material removal.

- AM flow reactors, presented in literature, are developing from standard tubular reactors to increasingly complex devices that allow enhanced mixing and heat transfer, and multi-functionality e.g coupling embedded analytics or catalytic functionality of the static mixer.

## 2.7 Research opportunities

The following research opportunities have been identified following review of literature in the AM flow reactor research area;

- Despite the demonstrated benefits of continuous oscillatory baffle reactor technology in applications involving fine chemical mixing at macroscale, this reactor design has not been demonstrated and utilised in the micro to mesoscale perhaps due to manufacturing challenges at this scale.

- There is a growing trend in demonstrating applications of multi-functional AM flow reactors and its benefits. There is a need to demonstrate bespoke AM devices in process applications involving inline temperature sensing and process optimisation. Specifically, in API crystallisation applications where the polymeric form of the material is influenced by the process parameters.

- The ability for these fully fabricated AM flow reactors to allow an added functionality e.g acting as a biocatalytic reactor is a unique position. Tailored modified catalytic reactors modules with unique characteristics can be developed and used for bespoke reaction processing.

## 2.8 Thesis Aim and Objectives

The overall aim of the research was to improve understanding of the utilisation of AM in the development of mesoscale flow reactors focusing on multi-functional devices for three different applications: material synthesis, crystallisation and biocatalysis. The following objectives were set for this research:

- To investigate the feasibility of producing a COBR using a low-cost AM method and determining the benefits by residence time distribution studies.

- To investigate the feasibility of producing a bespoke crystalliser device with inline process monitoring using a low-cost vat polymerisation platform.

- To investigate the feasibility of developing a AM modified continuous flow reactor for biocatalytic processes.

# Chapter 3 Additive manufacturing for the continuous-flow synthesis of nanostructured materials.

## 3.1 Introduction

Carrying out reactions in flow as opposed to batch has a number of advantages including safe handling of reagents [69] and improved reaction yields [12], though challenges of blockages and removal of fouling exists. Additionally, effluents can be characterised using spectroscopy techniques and real-time monitoring, allowing for enhanced control and optimisation of processes to be implemented [70, 71]. Mesoscale flow reactors have been of continual interest to researchers and are being developed for lab-scale processes. They are purposefully designed to scale-up to industrial scale or to be used in small scale production [10].

As the flow regime in microfluidics is laminar, mixing of reagents is dependent on intermolecular diffusion. As the channel size is increased towards the macroscale the length to diameter ratio reduces, resulting in longer residence time required for mixing to occur, thus reducing the mixing efficiency. The fluid flow at reactor scales can either be laminar or turbulent, depending on the flow rate and reactor design. Laminar flow is generally characterised by low Reynolds numbers (Re), while for higher Re values turbulent flow is observed. Laminar flow regime is characterised by high momentum diffusion and low momentum convection [8]. Turbulent flow on the other hand results in lateral mixing and formation of eddies. At the scale and flow conditions studied in this

chapter, less than 5 mm inner diameter and flow rate of 10ml/min, laminar flow is normally observed.

Hence, methods to improve mixing in mesoscale reactors and the manufacturability has to be explored. Active and passive mixers have been utilised by researchers to induce efficient mixing under laminar conditions with each having its benefits and drawbacks [14, 15]. An effective method of enhancing mixing in mesoscale, explored in this chapter, is the continuous oscillatory baffle reactor (COBR) technology shown in Figure 20 [72-74].

The COBR is a combination of the passive and active mixing method. It comprises of even spaced baffles in the flow channels coupled with an additional oscillatory device to force the bulk fluid to create unique mixing patterns [72]. The combination of the baffles with the fluid movement lead to the formation of vortex rings during the forward and backward stroke [75]. In this way, near complete mixing in the radial direction and minimal back mixing can be achieved because of the even velocity profile developed in the channel. Baffled cells can be envisioned as a number of continuous stirred tank reactors (CSTRs) in series.
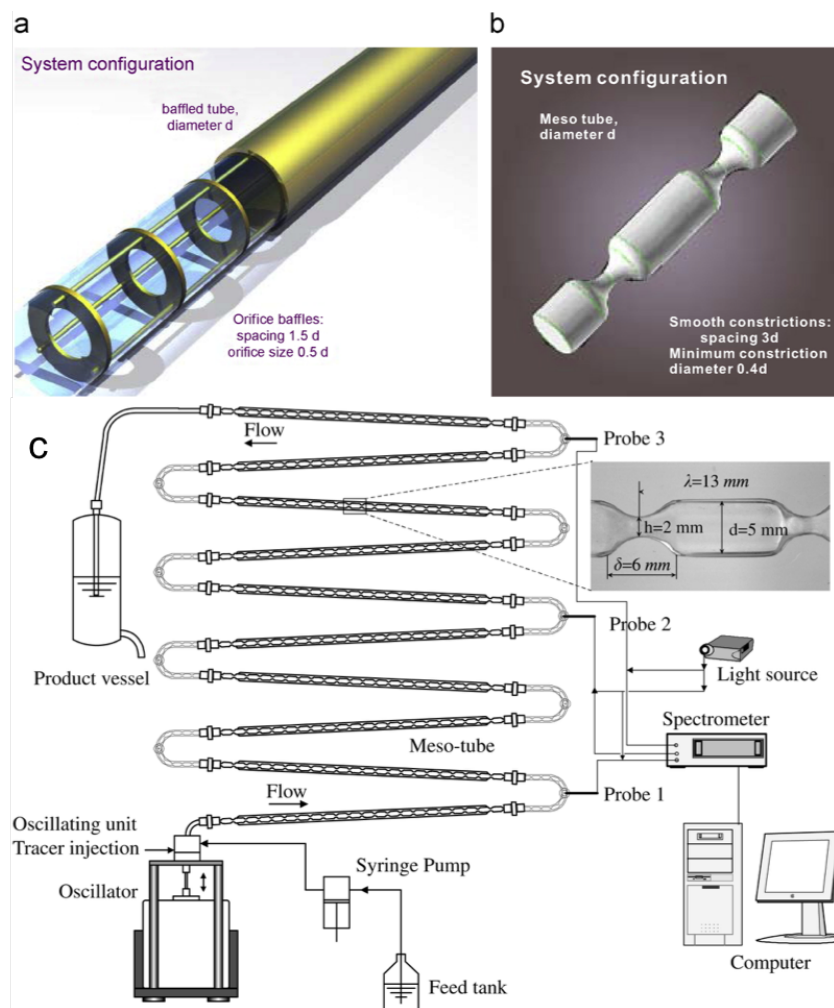
Figure 20: Continuous oscillatory baffled reactor (COBR) configurations: (a) baffled type and (b) smooth periodic constriction. (c) schematic of COBR including oscillator and setup for residence time distribution studies [74].

COBRs have been demonstrated in several synthesis applications including production of biodiesel [73, 76] and continuous-flow crystallization [3, 12]. Improved mixing, facile handling of solids and reduced fouling have been reported as process advantages compared to tubular reactors. COBRs and other advanced reactor designs can provide a tool for discovery to manufacturing of chemicals and materials. This requires the ability to be able to configure the reactors across the scales from laboratory, to pilot and up to industrial scale.

However, an important limitation in the uptake of this technology is the difficulty to configure and manufacture the reactors employing conventional techniques. The down-scale of the reactor geometries is particularly challenging. In the macroscale, the COBRs can be easily manufactured in glass or metal. However, with reduced feature sizes of the channel internal structures, e.g baffles, manufacturability becomes a challenge. Generally, with the reduction in reactor volume, conventional manufacturing techniques become unsuitable. At micro to mesoscale, more precise and technically challenging fabrication methods are required.

As stated in Chapter 1, AM is potentially a valuable tool for developing complex geometries with high precision and repeatability, and therefore AM was selected for the fabrication and research into mesoscale continuous oscillatory baffle reactors (mCOBR) for synthesis applications [40]. A wider review of AM for mesoscale flow reactors and key geometrical parameters for COBRs were presented in Chapter 2. For the work in this chapter, the dimensions used were in close range to effective geometry demonstrated in literature of 1.5Do baffle spacing and 16 per cent open baffle area [44]. Processing at such optimal range has been found to lead to increased vortex width, promoting advection and minimised mixing time. Thinner baffle thicknesses ($\delta$) are recommended, as larger baffles lead to longer 'cling time' and reduced flow separation [44].

### *Silver Nano-particles (Ag-NPs)*

Silver nanoparticle synthesis was proposed to be used for experimentation as its reduction has been adequately studied and its behavior during processing is well known. Processing Silver Ag-NPs in flow can provide similar insight and

changes with a range or nanostructured materials. Silver nanoparticles (Ag-NPs) are of major interest for a manifold of applications such as photovoltaics [77], biological [78] and chemical catalysis [79] due to their unique optical [80], chemical [81] and electronical [82] properties. Consequently, the synthesis of Ag-NPs in continuous flow is an area of high interest [83]. Ag-NPs plasmons can be tuned from between 400nm (Violet light) to 530nm(green light) depending on the shape and size (between 1 to 100nm) of the particle [84]. When excited by light at a specific wavelength, the conductive electrons on the surface of the metal collectively oscillate. This phenomenon is known as surface plasmon resonance (SPR). The oscillation at the surface result in strong scattering and absorption properties. Hence, 60nm Ag-NPs, when illuminated by white light, produce a bright blue colour peaking at 450nm due to the LSPR effect. Synthesis of silver NPs can be carried out by physical, chemical and photochemical methods which includes techniques such as, laser ablation, electron irradiation, gamma irradiation, chemical reduction, photochemical methods, biological synthetic methods and microwave processing. The most common chemical method of synthesis of silver nanoparticles is chemical reduction by organic and inorganic reducing agents [85]. Reducing agents such as Ascorbate, sodium citrate, sodium borohydride ($NaBH_4$), polyol process and elemental hydrogen are used in the reduction of silver ions ($Ag^+$) in aqueous or non-aqueous form. The metallic silver ($Ag^0$) formed from the reduction process subsequently agglomerates in oligomeric clusters (Equation 3.1.1).

$$Ag^+ + BH_4^- + 3.H_2O \rightarrow Ag^0 + B(OH)_3 + 3.5.H_2 \qquad \textit{Equation 3.1.1}$$

Processing of Ag-NPs brings about challenges during manufacture due to the tendency to agglomerate, leading to deposition on the reactor walls [86]. Polymeric compounds such as poly(vinylpyrrolidone), poly(ethylene glycol), poly(methacrylic acid), polymethylmethacrylate and poly(vinylalcohol) have been reported to serve as protective agents effective in stabilising NPs [85].

In large batch reactors, the fouling of the walls is not as hazardous, because continuous flow processes are carried out in tubes which are prone to blocking. Nevertheless, with agglomerates, there will exist unwanted differential in the size of the particles. Under continuous flow conditions this causes a constant change in the nature of the reactor walls, which prevents a controlled and stable formation of nanoparticles under steady state. Furthermore, the formation of Ag-NPs is strongly dependent on chemical and physical properties such as temperature, pH, stabilizer, all of them influencing the different kinetic processes typically responsible for this type of synthesis [87-89]. Hence, it is very challenging to generate monodisperse solutions of NPs with controlled size [90, 91]. The improved mixing observed in the AM fabricated mCOBRs should foster the generation of small nanoparticles with a narrow size distribution in a stable controlled and reproducible fashion. In this chapter, the feasibility of fabricating an AM-mCOBR, its comparison with a convectional tubular reactor, the effect of the flow parameters on the mixing performance and its effectiveness in the synthesis of Silver nanoparticles is presented.

*Residence time distribution (RTD)*

Residence time distribution (RTD) studies were employed to explore the behavior of the mCOBR and to test them against a tubular reactor as a benchmark. RTD has been employed as a valuable tool for understanding the quality of mixing, mean residence time of materials and to model the flow within a reactor vessel [92]. It allows for the preservation of selected flow patterns during the reactor design and serves as a quantifiable measure of the degree of back mixing in a flow system [93]. RTD describes the quantity of time fluid elements have spent in the reactor in a flow system [94]. Therefore, the RTD of a continuous reactor is influenced by the rate of diffusion, the flow dynamics and internal geometry of the tubular reactor, e.g. baffles. RTD studies are also particularly important in making comparisons between reactors of different architectures and dimensions. A thorough understanding of the nature of mixing in the reactor can aid in scale-up. RTD experiments involve injecting a tracer, an inert species, into the reactor at a recorded time and measuring the effluent stream as a function of time [95]. It is important that the non-reactive species have similar physical properties with the base mixture and do not absorb at the walls of the reactor [96]. Lithium salts [97] and toluene [98] have been used to conduct tracer experiments. Pulse and step input are two main methods of tracer injection. In pulse input, the tracer is instantaneously injected into the flow stream in the minimal possible time. The concentration of the outlet stream is then measured with respect to time. In the step input the tracer is constantly introduced over time and measured as in the case with the pulse input [95]. Figure 21 shows a graph of tracer concentration at the injection inlet and outlet measurement in the step and pulse input methods.
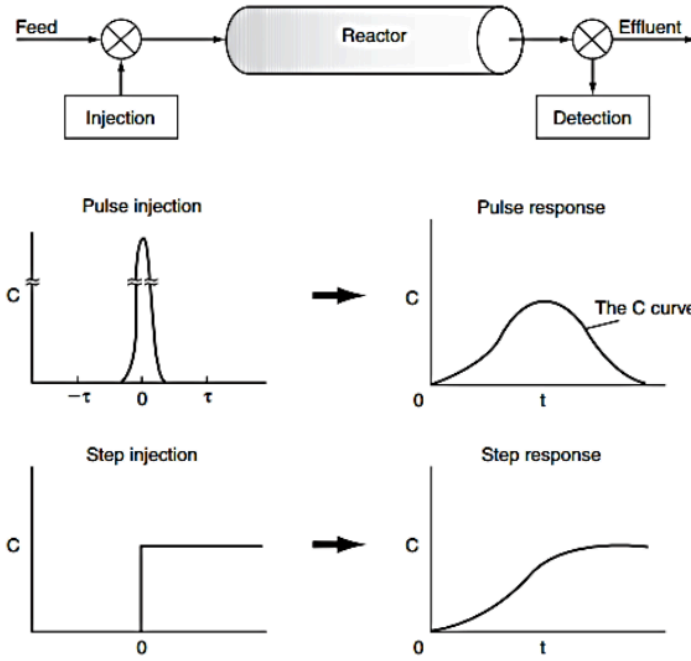
Figure 21: Residence time distribution measurements at the tracer inlet and outlet in a PFR [95].

Pulse input methods are more often used in RTD study. This is because numerical errors which are associated with step input, resulting from data differentiation is avoided [94]. The RTD of fluid elements is defined by E(t). The residence time of a fraction of fluid elements, in the vessel, in the range dt about time t is defined by Equation 3.1.2. Where E(t) is a probability function and meets the normalisation condition.

$$\int_0^\infty E(t) \, dt = 1 \qquad \text{Equation 3.1.2}$$

In RTD study by pulse method, a small amount of tracer $m_o$ is injected into the flow stream at a uniform concentration, which is then recorded with respect to time, $C_t$(pulse). At constant volumetric flow rate $\dot{v}$, the differential fraction of the tracers exiting the reactor at a given time is given by:

$$\frac{dm}{m_0} = \frac{\dot{v} C_t \, dt}{m_0} \qquad \text{Equation 3.1.3}$$

Therefore:

$$E(t)dt = \frac{dm}{m_0} = \frac{\dot{v}}{m_0}C_t dt \qquad \text{Equation 3.1.4}$$

The E(t) can be derived from normalisation of C(t) in a pulse experiment knowing the total mass $m_0$ of the injected tracer:

$$E(t) = \frac{C_t}{\int_0^\infty C_t\, dt} \qquad \text{Equation 3.1.5}$$

The mean residence time tm and variance are obtained by:

$$t_m = \int_0^\infty t.E(t)dt \qquad \text{Equation 3.1.6}$$

$$\sigma^2 = \frac{\int_0^\infty (t-t_m)^2.C(t)dt}{\int_0^\infty C(t)dt} \qquad \text{Equation 3.1.7}$$

Mixing performance in flow systems of varying sizes can be compared by using the normalised RTD function E(θ) and the dimensionless time θ:

$$E(\theta) = t_m.E(t) \qquad \text{Equation 3.1.8}$$

$$\theta = \frac{t}{t_m} \qquad \text{Equation 3.1.9}$$

RTD studies employs a similar set up illustrated in Figure 22. Pumps are used to drive the fluid to towards the reactor coupled with a HPLC valve that produces a pulse tracer input into the flow path. A detector is stationed at the inlet and outlet regions of reactor which collate tracer absorbance measurements. Some analytical methods for RTD studies utilise, pH, conductance, UV-vis/IR Spectroscopy or radioactive tracers. Use of in-situ conductive measurements and UV-vis spectroscopy are the most conducive techniques as the instruments can be located close to the microfluidic device and can detect small liquid volumes [99]. Using UV-vis spectroscopy, the tube at the entrance of the reactor is placed into in the meandered channel of the tube cuvette and fastened, which prevents

external light interference. Employing commercial transparent FEP tubing

transmittance, measurements can be obtained from the effect of the coloured
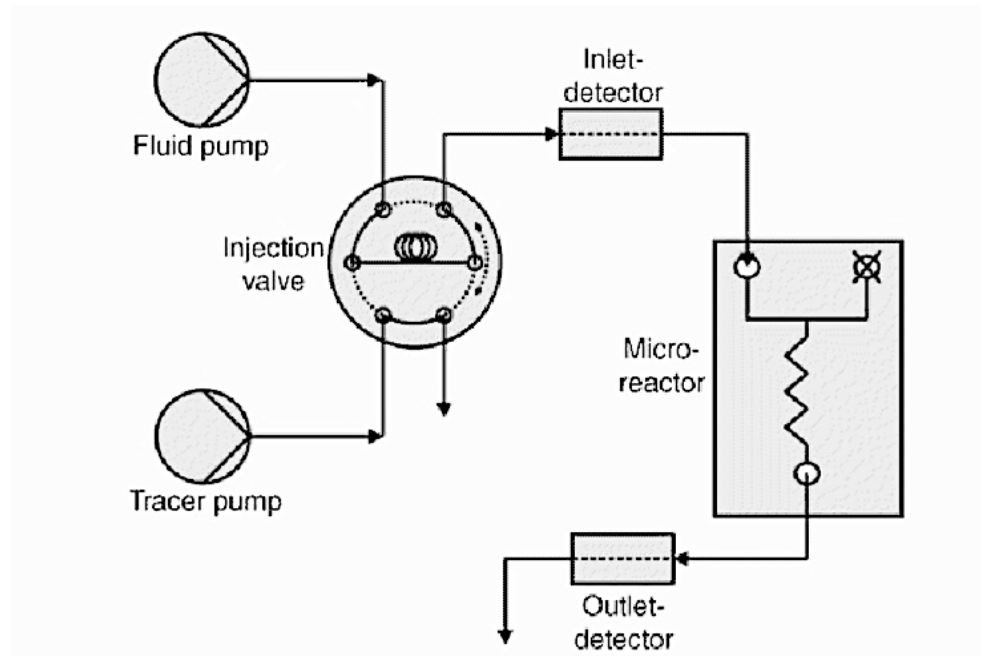
tracer.



Figure 22: Schematic of the experimental setup comprising of syringe pumps,

capillary, HPLC-valve, inlet and outlet detectors connected to a micromixer

[99].

Theoretical models used to characterise reactors are based on the ideal assumption of plug flow or perfect mixing [100]. They are useful in representing flows in manufactured reactors, for scale up and in diagnosing poor flow conditions [92]. However, neither model assumptions fully match real flow systems. Two common models are the axial dispersion and Tank-in-series model.

Axial dispersion model or "open" dispersion model assumes the movement of the fluid is made of the convective component, as a result of the bulk motion, and the diffusive component arising from random motion of the fluid elements [101]. The dispersion model satisfactorily describes flows that do not deviate largely from plug flow. From Fick's Law, molecular diffusion in the x-direction can be expressed mathematically as;

$$\frac{\partial C}{\partial t} = D \frac{\partial^2 C}{\partial x^2} \qquad \text{Equation 3.1.10}$$

Where D is the axial or longitudinal dispersion coefficient, which characterises the degree of back mixing in the flow. In dimensionless form, the differential equation of the dispersion model is as follows:

$$\frac{\partial C}{\partial \theta} = \left(\frac{D}{uL}\right)\frac{\partial^2 C}{\partial z^2} - \frac{\partial C}{\partial z} \qquad \text{Equation 3.1.11}$$

Where the dimensionless group, $\left(\frac{D}{uL}\right)$, the vessel dispersion number represents the extent of axial dispersion. The inverse of the dimensionless group is quantified by the Peclet number, Pe, where u is the fluid velocity, and L is the length of the reactor. For ideal mixed flow, the Peclet number is 0 and infinity for an ideal plug-flow.

$\frac{D}{uL} = \frac{1}{Pe} \rightarrow 0$   Minimal dispersion, therefore approaching plug-flow

$\frac{D}{uL} = \frac{1}{Pe} \to \infty$ Large dispersion, therefore approaching mixed flow

"Open" boundary condition is achieved if the flow is undisturbed at the inlet and outlet of the vessel. In this case the D is same at the boundaries. In the "closed" case, there is a change in flow pattern at the boundaries. The inlet to the reactor is an idealised plug flow, which transforms to a dispersed flow in the reactor and back to plug flow at the reactor exit [92, 101]. The mathematical solution for Equation 3.1.11, "open" boundary conditions is given by:

$$C = \frac{1}{2\sqrt{\pi\left(\frac{D}{uL}\right)}} exp\left[-\frac{(1-\theta)^2}{4\left(\frac{D}{uL}\right)}\right] \qquad \text{Equation 3.1.12}$$

This represents a family of gaussian curves and therefore:

$$E(\theta) = t_m.E(t) = \frac{1}{2}\sqrt{\frac{Pe}{\pi\theta}}e^{\frac{-Pe(1-\theta)^2}{4\theta}} \qquad \text{Equation 3.1.13}$$
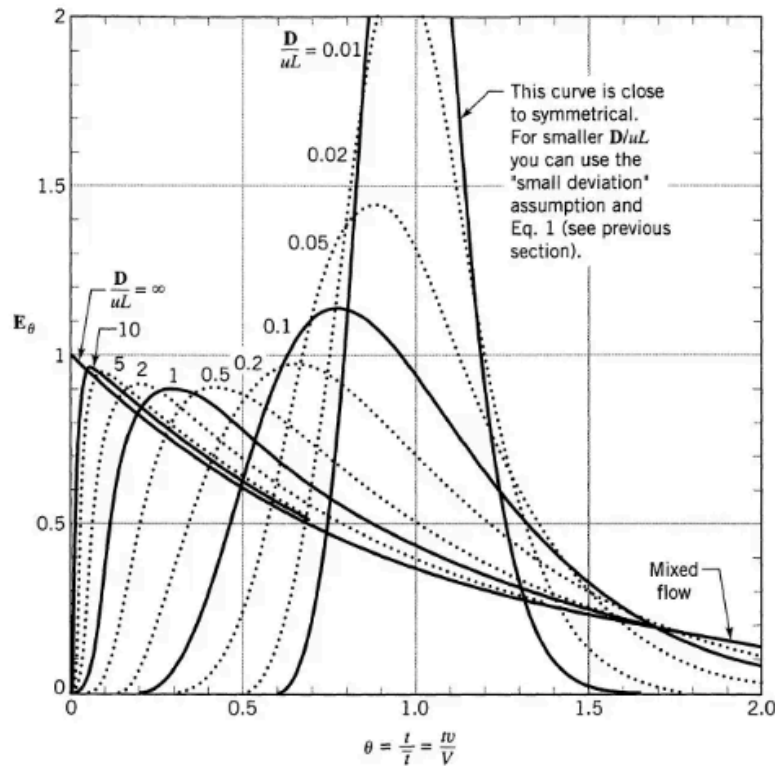


Figure 23:E($\theta$) curves of tracer responses in "open" vessels. Large to small deviation to plug flow is shown [92].

Similar RTD studies employing pulse tracer experiments and an axial dispersion models have been employed in highlighting the difference in the nature and shape of polymeric material used in packed bed reactors [98]. Similarly numerical and experimental studies have also been carried out in T-junction channels [94].

In Tank-in-series model, the reactor is modelled as a series of equally sized perfectly mixed stirred tanks, N. Level of mixing in this model is altered from plug flow($N \rightarrow 1$) at plug flow to $(N \rightarrow \infty)$ for complete mixing. Compartment models are obtained from a combination of change in configurations for ideal PFR and CSTRs. Compartment models are less frequently employed for analysis therefore it will not be covered in detail.

## 3.2 Objectives

The aim of the research carried out in this chapter was to improve the understanding of utilising AM in the development of advanced mesoscale flow reactors with improved mass transport properties. This research comprised of studying the feasibility of manufacturing near net shape mesoscale continuous baffle reactors using vat polymerisation, residence time distribution studies to characterise mixing in the reactors and continuous Silver nanoparticle synthesis in the developed device. The objectives of the research included:

- To study the feasibility of manufacturing near net shape mesoscale flow reactors with static mixers on a selected low cost (< £5,000) AM platform.

- To manufacture a mesoscale continuous oscillatory baffle reactor (mCOBR) by AM for both flow characterisation and chemical synthesis.

- To develop a test rig and acquisition methodology for characterising the mixing in the reactor.

- To characterise the mixing efficiency of the manufactured reactor by pulse injection method residence time distribution study.

- To carry out continuous synthesis of Silver nanoparticle utilising the mCOBR AM device.

- To carry out inline and offline characterisation of the nanoparticles in the mCOBR and bench mark against a standard tubular reactor.

## 3.3 Methodology

The experimental study reported in this chapter covers the AM material solvent compatibility, fabrication of flow channels on a selected vat polymerisation platform, residence time distribution study in a fabricated mCOBR under varying oscillatory conditions and a study in the continuous flow synthesis of silver nanoparticles in the reactor.

### 3.3.1 Material solvent compatibility test

The solvent compatibility of the AM resin used in the vat polymerisation process (Formlabs Clear – FLGPCL02) was characterised, as the reactors will be used in a range of solvents and it is important that the reactor doesn't degrade. Cured films of the polymerised material were measured using TGA and IR to monitor changes in the material when exposed to different solvents. The films were exposed to isopropanol (i-PrOH), ethanol (EtOH), water and acetonitrile (MeCN). The solvents tested were selected as they to be used in the reactor for production of Ag-NP though the acrylate-based VP material is known to swell and degrade with strong solvents.

*Thermo Gravimetric analysis (TGA)*

Thermogravimetric analysis (TGA) is a technique used to evaluate the thermal stability of a material. The mass of a material is measured over time at a constant temperature change. TGA was used for a comparative study as changes in the material properties, due to exposure to select solvent, can be reflected in the thermal profile [44]. A typical TGA comprises of a precision balance fitting a

sample pan and a temperature-controlled furnace. The thermogravimetric data is then collected at a prescribed temperature increase. The data is typically recorded as a plot of the percentage weight of the initial mass on the y-axis against temperature on the x-axis.

### *ATR-IR spectroscopy*

Infrared spectroscopy is an analytical technique used commonly in determining structures of a compound. It takes advantage of the vibrational transitions of molecule when exposed to infrared radiation for identification. Attenuated total reflection (ATR) is normally used in conjunction with IR for liquid and solid characterisation. The use of ATR-IR is advantageous over transmission IR as the problems of strong attenuation are avoided. Since ATR uses a principle of total internal reflection, an evanescent effect is created when an optical material with higher reflative index is coupled. In this way the sample penetration depth will only be 0.5 to 2 micrometers into the sample, depending on the wavelength of light. ATR-IR spectroscopy was used to monitor changes in the polymer as a result of exposure to select solvents.

### *Experimental procedure*

A film of FLGPCL02 Formlabs Clear resin was deposited on tygaflor backed petri dishes. The tygaflor was used to minimise cracking during detachment of cured material. The sample was then placed under UV-lamps for a minimum of 1min to completely cure. The cured films were cut to about 3mm strips. The films were either soaked in vials containing isopropanol (i-PrOH), ethanol (EtOH), water and acetonitrile (MeCN) at room temperature for 24 hours. Subsequently, the films were filtered out from the solvent and dried at 50°C

under high vacuum overnight. TGA and IR measurements were then carried out on the dry samples.

Thermogravimetric analysis (TGA) was conducted under nitrogen atmosphere with a PerkinElmer TGA 4000. The samples were stabilized at 30 °C for 5 minutes and then heated to 900 °C at the rate of 10 °C/min. Infrared (IR) spectra were measured with a Bruker Alpha-spectrometer using 24 scans with resolution of 4 cm$^{-1}$.

### 3.3.2 Additive manufacturing of reactors

Fabrication of the mCORs and test components on a vat polymerisation platform was carried out in three stages. The pre-fabrication stage, which encompassed the designing of the parts and iterative stages of design for manufacture. Subsequently, the fabrication stage involved the building up of the part on the AM platform, while the later post fabrication stage involved cleaning and preparing of the reactor for utilisation.

*Experimental Procedure*

*Pre-fabrication*

The parts were designed in Creo Parametric to the required parameters and saved as a part file. The CAD models in .PRT (Creo Parametric part format), were then converted to .STL format, commonly used on AM platforms. Formlabs-PreForm software was used in interfacing the created part files by converting it into defined slices for manufacture on the platform. On PreForm, a proprietary algorithm detects surfaces close to the base plate and overhanging surfaces more

than ±45 degrees to the build bed. Thin support structures were then generated to attach the build to the build plate.

PreForm allows the user to select between an automatic and manual mode. In automatic mode, the parts to be built are arranged to fit the build base and are rotated to software defined angles in the XZ direction and XY. The positioning of the parts is done to minimise the layer area being built in one laser pass. In manual mode, the orientation of the model can be adjusted to minimise overhangs and for support addition. The density and point size of the supports can also be adjusted to suit. Generally, a larger support point size and density was selected when fabricating larger structures as it holds the build in place. The generated fabrication program was then run on the AM platform.

*Fabrication*

A Formlabs Form 2 vat polymerisation platform was selected for the manufacture of the reactor devices and the initial characterisation studies. On completion of model pre-processing on Preform, the file was uploaded to the Form 2 device for fabrication. It was equipped with a 140 μm beam-width 250mW laser for photo-polymerisation of Formlabs Clear (FLGPCL02) resin. This allows for a fine layer thickness of 25-100 μm to be achieved in a large build volume of 145×145×175mm. Thus, multiple flow reactors were fabricated at the same time. On this platform the intended structure was built from the bottom-up with the initial layers requiring longer layer exposure to ensure adhesion on the aluminium build plate. The solid layers were formed from laser exposure unto the transparent Polydimethylsiloxane (PDMS) layer of the resin tank during fabrication. Each layer formation was followed by a peel and sweep

mechanism which removed the component from the PDMS optical window. The process was then repeated until the part is completed. Resin was automatically topped up automatically during the build process from the resin cartridge.

*Post fabrication*

On completion of fabrication, the build was detached from the device and the build bed. The surfaces were then removed and washed in IPA to remove excess resin form the surfaces. In some cases, the parts were sonicated in a bath of IPA for up to 30 min. In the case of the mesoscale flow reactors, they were immediately connected to Luer fittings and flushed to get rid of resin in the channels. This was done to prevent polymerisation, when the device is removed from the platform. Fabricated parts were also further cured under an UV lamp to improve the strength and transparency of the parts.

*Optical microscopy*

An Olympus BX51 optical microscope coupled with a 5X magnification lens was utilised in producing high resolution images for evaluating the produced channels. An inexpensive desktop camera was used to collect low resolution to check for blockages. The low resolution images were utilised to inspect the parts for blockages while higher resolution was used to measure and monitor deviation between the designed and the actual build of the unblocked channels.

### 3.3.3 Residence time distribution study

Residence time distribution studies were utilised in monitoring the behaviour of the mCOBRs under a range of oscillatory conditions. They served to benchmark

the mCOBR with respect to a mTR whilst evaluating a range of oscillatory parameters. The schematic of the rig setup is presented in Figure 24. The setup comprised of two C3000 Tricontinent programmable syringe pumps equipped with 5ml syringes. One pump controlled the net flow of fluid into the reactor, in this case distilled water, while the other pump was used to oscillate the incoming fluid by high frequency extraction and plunging movements, Figure 25. The mTR setup required one pump connected to the single inlet as oscillation was not required. The oscillating fluid used was silicon oil to prevent back mixing. The silicon oil stopped before the inlet of the bulk fluid and was not allowed to travel through the reactor.
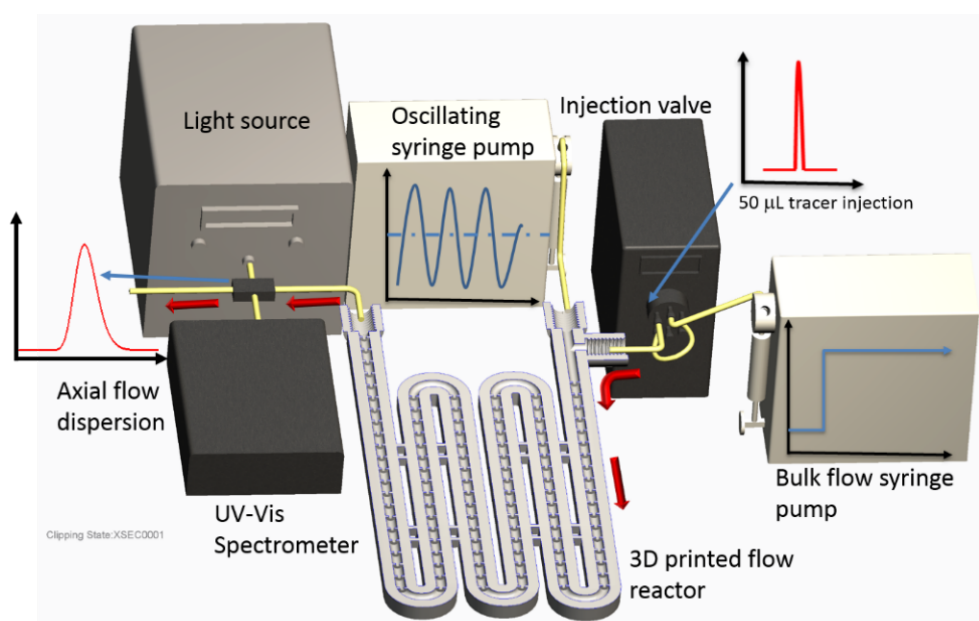


Figure 24: Modelled designed setup for residence time distribution studies, comprising of two syringe pumps (one for continuous flow and the other for oscillation), a Rheodyne valve, flow cell, and an UV-VIS.
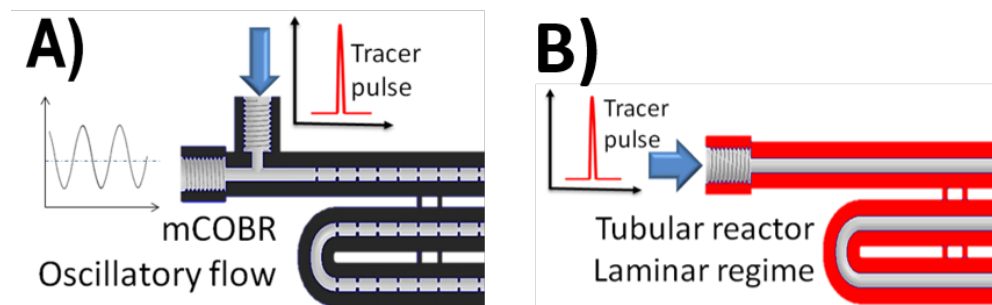
Figure 25: Schematic for RTD testing for TR and mCOBR a) mCOBR with oscillating flow and bulk flow b) bulk fluid flow only.

A programmable 6-way Rheodyne injection valve equipped with a 50 μL loop was utilised for controlled pulse injection of the tracer when initiated. Methylene blue served as the tracer and was monitored with an Avaspec UV/Vis spectrometer, coupled with a flow cell and an Avantes DH-2000 light source. A pulse injection method was utilised for the residence time distribution studies. This involved the injection of a 1mM pulse of aqueous solution Methylene blue in the flow path of distilled water under set oscillatory frequency. The fluid and injected tracer was then transported into the reactor. On exiting, the effluent was monitored by UV-vis spectrometer. The observed light spectra was collated and analysed over specified time intervals with an in-house developed programme built on Labview visual programming platform. A screenshot of the developed user interface is presented in Figure 26.
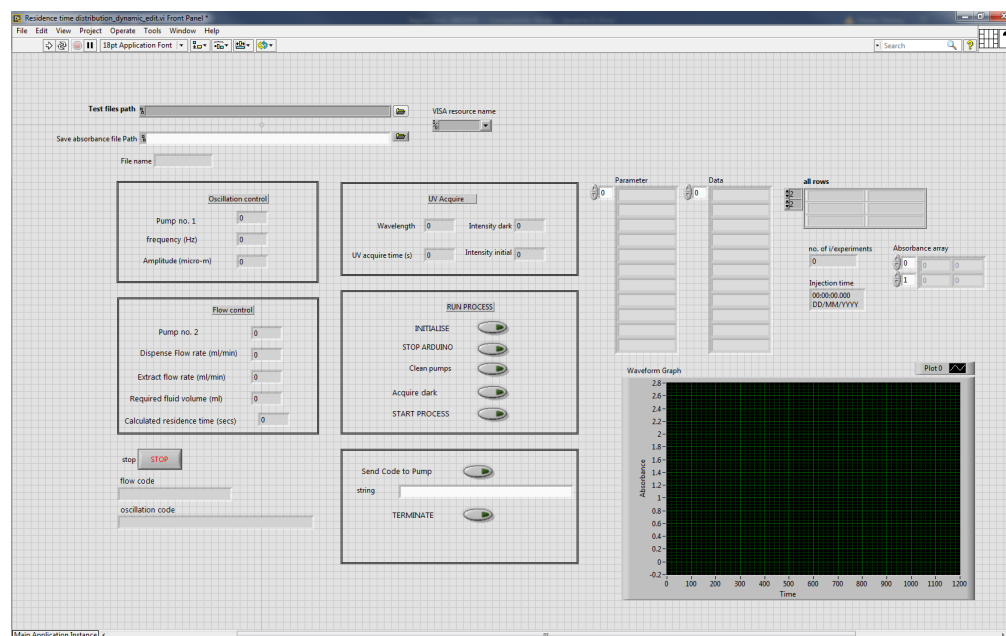
Figure 26: Graphical user interface for residence time distribution RTD experimentation. It was designed on Labview and used to control the pumps valve and data acquisition.

## *Experimental setup and procedure*

The experimental process was automated using a Labview development environment. The programme was designed to allow automated running of experiments without user inputs. Experiments were designed to compare the TR and mCOBR under several oscillating conditions. RTD data was collected for the TR and mCOBR at varying flow rates. The mCOBR was further tested at several oscillating frequencies and amplitudes. Experiments were automated by setting up required parameters in a format recognised by the developed Labview programme. An example parameter text file will have the file name of the saved data and parameters for the pumps such as the oscillating frequency and amplitude, dispense and extract flow rate, UV acquisition intervals and the peak wavelength of the tracer (665nm for Methylene blue).

Communication and control of the C3000 Tricontinent syringe pumps for oscillation control and net flow were carried out on Labview using manufacturer designed strings. A simplified example string to extract fluid from the pump inlet and dispense is as follows: /1V1200IP24000V1200OA0R, where V represents the velocity I, E and O relate to three valve ports and P, A and D relate to the position of the pump. Hence programs can be designed to utilise these commands and convert flow rates or amplitudes from requirements of the user. The oscillation of the pump was carried out by converting the required frequency and amplitude into positive and negative movements of the syringe plunger. Initiation of the Rheodyne valve switch mechanism for tracer inject was also carried out on Labview, although connected using an Arduino Uno and a relay. The Arduino programme was called up on the Labview when required during the experimental process. The injection of the tracer followed when the flow had attained steady state. The switch changes the position of the 6-way valve to allow the already primed 50 μm methylene blue into the flow path.

The Arduino code for switching the valve is as follows:

```
void setup() {
// initialize digital pin 13 as an output.
pinMode(2, OUTPUT);}
// the loop function runs repeatedly
void loop() {
digitalWrite(2, HIGH);   // turn the LED on (HIGH is the voltage level)
delay(500);           // wait for a second
digitalWrite(2, LOW);    // turn the LED off by making the voltage LOW
delay(5000);            // wait for a second}
```

The UV-Vis spectrometer was also initiated on Labview simultaneously recording time at intervals until the end of the experiment. The light source was switched on 5 minutes before experimentation to allow for warm up. The control

user interface for communicating with the rig, collecting parameters, carrying out the set procedure, storing data and analysis is pictured in Figure 26.

Automation of the experiments were carried out out in the following process flow:

*User:*
Insert required parameter file and Initialise the experiment.

*LabVIEW automated Protocol:*
1. Initialise platforms
    a. Initialise Arduino controller for Rheodyne valve
    b. Initialise UV-Vis spectrometer
    c. Initialise oscillation pump and net flow pump
2. Collect procedure file and convert into pump commands
3. Start flow pump from prescribed parameter
4. Start oscillation pump from prescribed data
5. Wait for steady state
6. Start UV-Vis measurement
7. Activate injection valve
8. Collect UV-Vis spectra at prescribed time interval
9. End of experiment
10. Collate and analyse data
11. Save data in prescribed text file
12. Clean pumps and reactor
13. Reinitialise and Restart process for next experiment
14. End process

The data analysis process step involves negating the effects of the initial intensity and collating the absorbance over time at the peak wavelength of methylene blue, 665nm. The resulting curve is the concentration of the effluent over time. With further integration steps described in the section 3.1 (RTD theory), the non-dimensional time and $E(\theta)$ curve is then obtained and used in comparing different conditions and reactor vessels.

### 3.3.4 Silver nanoparticle synthesis in mCOBR

To study the synthesis of nanostructured materials in additive manufactured mCOBRs, silver nanoparticle formation was selected. The formation of silver nanoparticles was carried out by flow using two solutions at a similar flow rate into the AM reactor. A 0.25 mM solution of silver nitrate $AgNO_3$ in acetonitrile ($CH_3CN$) and 0.75 mM solution of sodium borohydride ($NaBH_4$) with 0.7 g of Polyvinylpyrrolidone (PVP) in $CH_3CN$ (Equation 3.1). The PVP served to stabilise the particles. The formation was carried out in a continuous process using two programmable pumps at specified flow rates.

$$AgNO_3 \ + \ NaBH_4 \ \xrightarrow{\ PVP + CH_3CN\ } \ Ag.\,Np \qquad\qquad \text{Equation 3.1}$$

*Experimental setup and procedure*

To carry out the synthesis of Ag-NPs in the mCOBR and mTR in a continuous, controlled and monitored fashion, the setup in Figure 27 was used. This comprised of two HPLC pumps which were used to achieve continuous flow of $AgNO_3$ and the $NaBH_4$ solutions, while a Tricontinent C3000 5ml syringe pump was used for fluid oscillation. A back-pressure regulator was used to control and maintain the system pressure throughout the experimentation. Monitoring of the Ag-Np was carried out using in-line UV-Vis spectroscopy with a flow cell, Avantes DH-2000 light source and an Avaspec UV-Vis spectrometer. The entire process was automated, similar to the residence time distribution study, using an in-house developed programme coded in Labview.
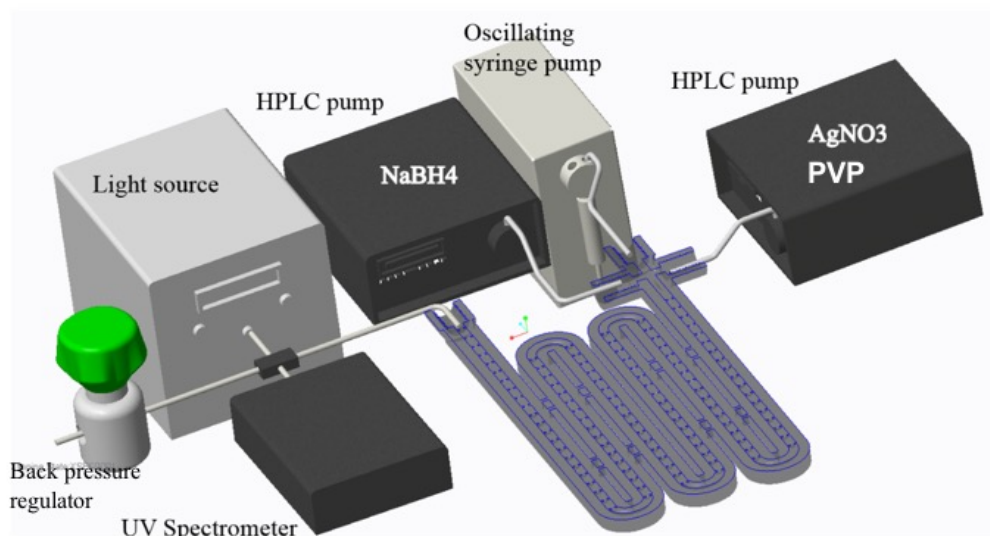
Figure 27: Designed experimental schematic of continuous silver nanoparticle synthesis in the mTR and mCOBR. This comprises of two HPLC pumps employed to pump NaBH$_4$ and AgNO$_3$:PVP solution, a syringe pump for fluid oscillation, a flow cell, light source and UV-Vis spectrometer for flow monitoring and a back-pressure regulator.

The two HPLC pumps were primed with acetonitrile and set to run for 10min while oscillating with the syringe pump. This was done to flush the system of impurities and air bubbles. The solution of NaBH$_4$ and AgNO$_3$ were then attached and the experimentation was quickly initialised.

The automated process for the Ag-Np formation was as follows;

*User:*
Insert required parameter file and initialise the experiment.

*LabVIEW automated Protocol:*
1. Initialise platforms using CH$_3$CN
    a. Initialise UV-Vis spectrometer
    b. Initialise oscillation pump and net flow pump
2. Collect procedure file and convert into pump commands
3. Start flow pump from prescribed parameter
4. Start oscillation pump from prescribed data
5. Wait for steady state
6. Start UV-Vis measurement

7. Switch CH$_3$CN to NaBH$_4$ and AgNO$_3$:PVP solutions
8. Collect UV-Vis spectra at prescribed time interval
9. End of experiment
10. Collate and analyse data
11. Save data in prescribed text file
12. Clean pumps and reactor
13. Reinitialise and Restart process for next experiment
14. End process

At the end of the process, the collected UV-spectra was collated and analysed to subtract the initial and dark intensity using Beer-Lambert absorbance equation $(A = \ log_{10} \left(\frac{I_o}{I}\right))$. The time series of the spectra was then plotted and presented.

### 3.3.5 Transmission electron microscopy TEM

Transmission electron microscopy (TEM) was used to measure the size of the silver nanoparticles produced from the mCOBRs. TEM is a microscopy technique that uses discharged beam of electrons which are transmitted through a specimen to form representative images [102]. The collected samples from the synthesis were prepared by diluting a drop of the freshly collected reaction mixture in acetone. A drop of the diluted reaction mixture was dropped onto a carbon-coated copper grid. The prepared samples were measured in a JEOL 2000FX operated at 200kV. The produced images were then analysed to obtain the particle size distribution under the tested conditions.

## 3.4 Design of Experiments

### 3.4.1 AM Build Characterisation

Experiments were designed to understand the effect of the build parameters on the produced geometry and minimum channel size reproducible on the Formlabs platform. These covered the design variables: mesh size, length of channel, wall thickness surrounding the void and fabricating parameters, build angle and layer thickness.

The following study was setup to understand the minimum channel feasible in the manufacture of the mesoscale flow reactors on the specific VP-AM platform:

i. Channel length (L)– 3x9mm blocks with varying heights of 6, 10 and 14mm and evenly spaced channel diameters of 1.2, 1.0, 0.8, 0.6 and 0.4mm were designed, Figure 28, and fabricated at 25, 50 and 100 µm layer thickness. The channels were positioned perpendicular to the build base during fabrication as per Figure 29.
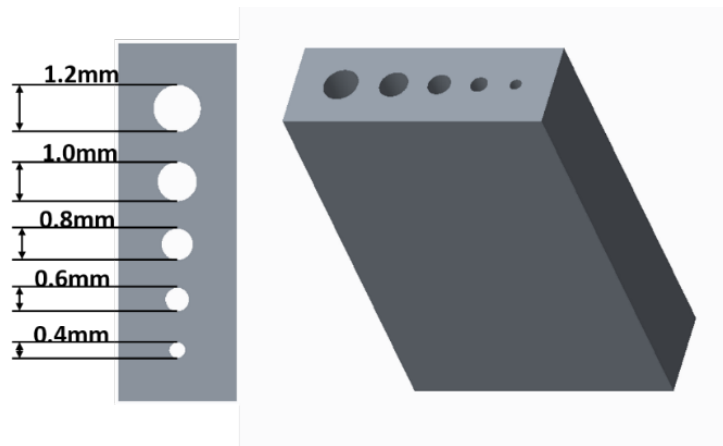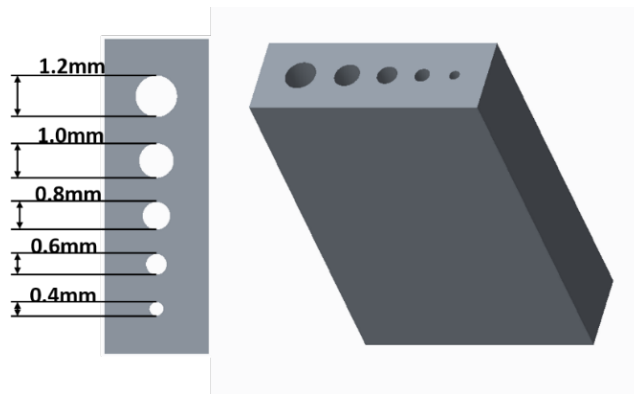


Figure 28: 3x9x14mm part designed with channels 1.2, 1.0, 0.8, 0.6 and 0.4mm
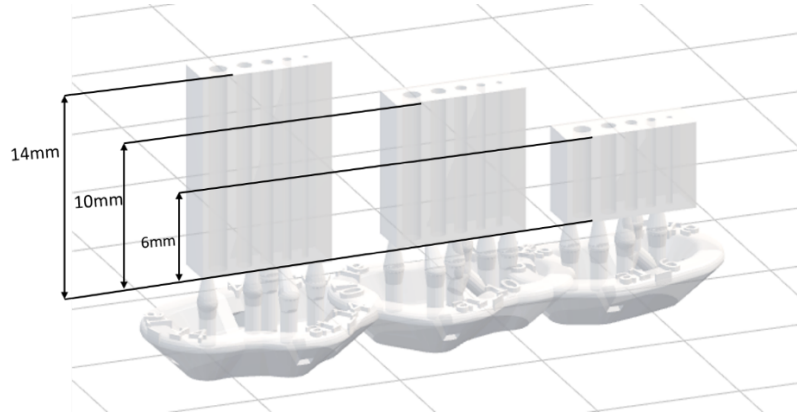
Figure 29: Study A parts prepared for fabrication on PreForm. The parts have channel widths of 1.2, 1, 0.8, 0.6 and 0.4 mm built at 90° to the optical window. The cross-sectional dimensions of the part are 3x9mm with varying lengths of 14, 10 and 6mm.

ii. Wall thickness (D) – 20mm blocks with varying square cross sections of 3, 5, 9 and 13 mm with a diameter of 1.2mm were designed, Figure 30, and fabricated at 25, 50 and 100 μm layer thickness. The channels were positioned perpendicular to the build base during fabrication as per Figure 31.
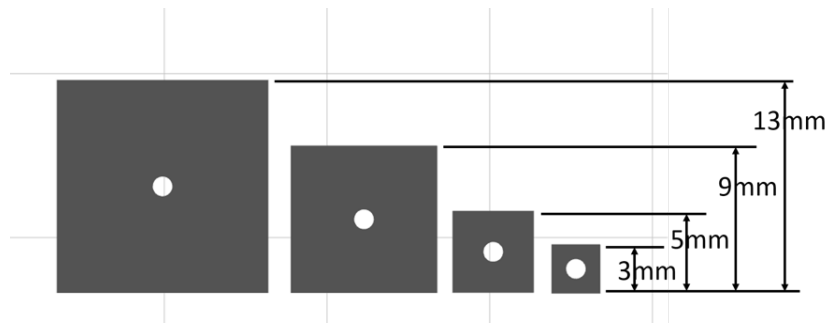


Figure 30: Designed 20mm part with 1.2mm channel diameter and varying square cross section of 3, 5, 9 and 13 mm.
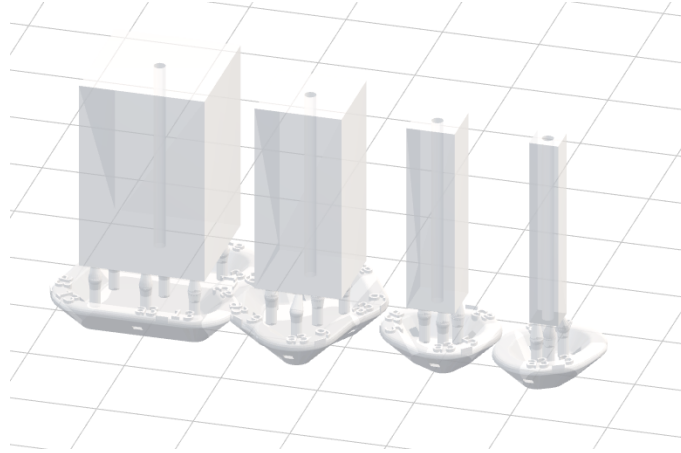
Figure 31: 20mm part with 1.2mm channel diameter and varying square cross section of 3, 5, 9 and 13 mm processed for fabrication on the Formlabs.

iii. Build angle (Z)– 3x9x14mm blocks with channel diameters of 1.2, 1.0, 0.8, 0.6, 0.4mm were designed, Figure 32, and fabricated at 25, 50 and 100 µm layer thickness. The channels were positioned at varying angles of 90º,45º and 0º to the build base during fabrication as per Figure 33.



Figure 32: 3x9x14mm part designed with channels 1.2, 1.0, 0.8, 0.6 and 0.4mm
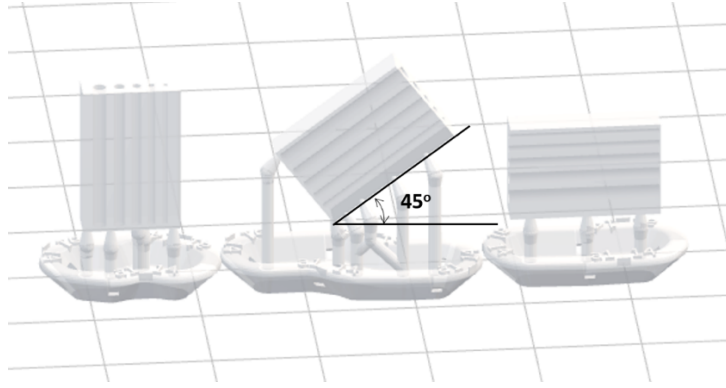
Figure 33: Study C parts prepared for fabrication on PreForm. The parts have channels of 1.2, 1, 0.8, 0.6 and 0.4 and were fabricated at 90º, 45º and 0º to the build plate. The part dimension is 3x9x14mm.

The studies in all 3 cases aimed to give an indication of the disparities between the designed and fabricated size at the range of layer thickness. Study i aimed to explore the dependency of the channel diameter of the fabricated part and the length of the part. Study ii aimed to understand the effect of the surround part thickness on the size and shape of the channels. Study iii aimed to understand the effect of build angle for subsequent part fabrication.

**3.4.2 mCOBR fabrication**

The mCOBR device was designed with reference to a scaled down version of a macro-scale COBR demonstrated by Harvey and colleagues [44]. At the scale studied by the authors, the geometry of the baffles and the position are critical in the development of eddies required to enhance mass transfer. The mCOBRs were designed following the schematic in Figure 34 and the dimensions in Table 1, with a baffles thickness of 0.5 mm, baffles spacing of 4 mm, inner and outer baffle diameter of 1 mm and 2.5mm.
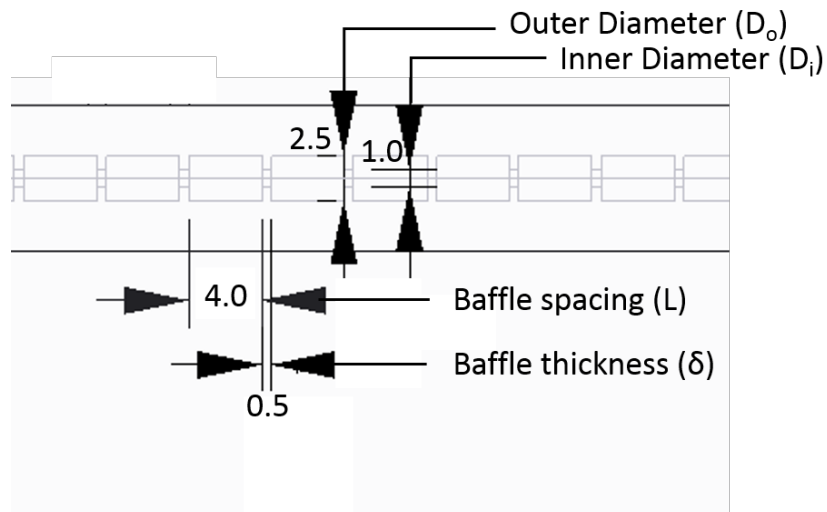
Figure 34: Schematic of mesoscale continuous oscillatory baffle reactor. Detail of dimensions corresponding to baffle thickness, baffle spacing, Outer diameter and inner diameter.

Table 1: mesoscale continuous oscillatory baffle reactor design parameters, symbols and value.

| Parameter | Symbol | Value |
|---|---|---|
| Baffle thickness | $\Delta$ | 0.5mm |
| Baffle spacing | L | 4mm |
| Inner baffle diameter | $D_i$ | 1mm |
| Outer baffle diameter | $D_o$ | 2.5mm |

The mCOBR was designed in two configurations: i) two inlet and one outlet for the residence time distribution study and ii) three inlet and one outlet for the Silver nanoparticles study. For comparison with the mCOBRs, a mesoscale tubular reactor (mTR) was designed. This was designed with the same geometry as the mCOBR, but without the baffles to represent a conventional tubular reactor. The mTR was designed having an internal volume of 2.7ml, whilst the mCOBR was 2.5ml due to the presence of the baffles in the channel. Standard

1/16'' connector fittings were employed to transport the fluid from the pumps to the reactor.

The mTR and mCOBR were designed on Creo Parametric, a 3D CAD solid modelling platform. In all cases, the parts were fabricated at 45° to the build plate and at layer resolution of 100μm. The pre-fabrication and post-fabrication carried out was similar to the description in experimental procedure (section 3.4.2). The rationale behind the number of inlet connectors are further explained in Figure 35 to Figure 38. A single inlet-outlet configuration design represents a tubular reactor used in the RTD studies, dual inlet and a single outlet represents an mCOBR used for the RTD studies while the triple inlet designs were used for the silver nanoparticle synthesis study.
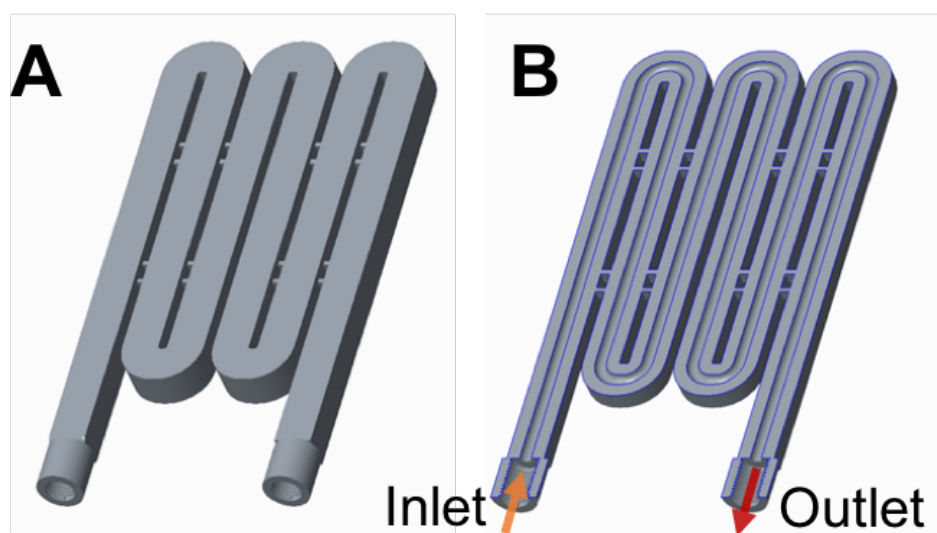


Figure 35: CAD model of a mesoscale tubular reactor (mTR) utilised for residence time distribution studies. A single inlet-outlet was designed as oscillation was not required. a) mTR model b) Sectioned view of the mTR model.
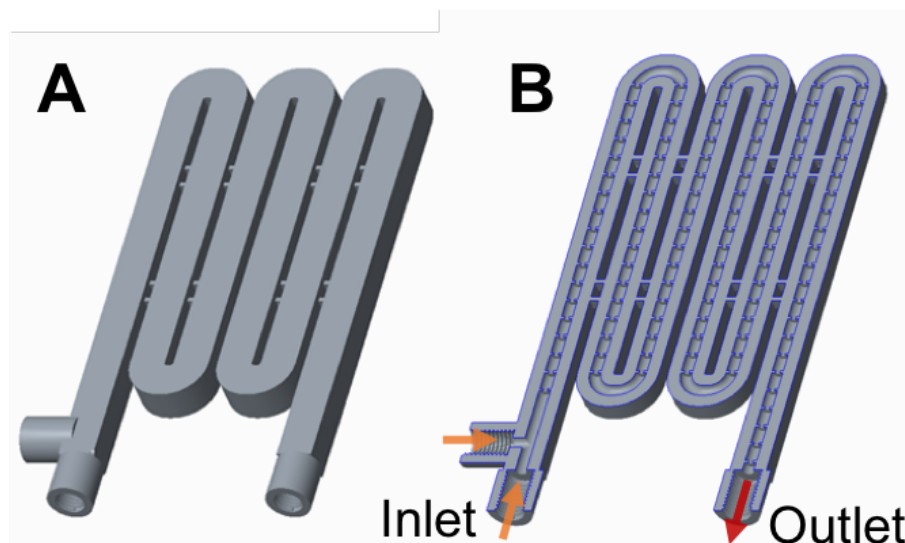
Figure 36: CAD model of a mesoscale continuous oscillatory baffled reactor (mCOBR) utilised for residence time distribution studies. Two inlets and one outlet were required. The perpendicular inlet was used in transporting the bulk fluid through the reactor while the parallel inlet allowed continuous fluid oscillation. a) mCOBR model b) Sectioned view of the mCOBR model.
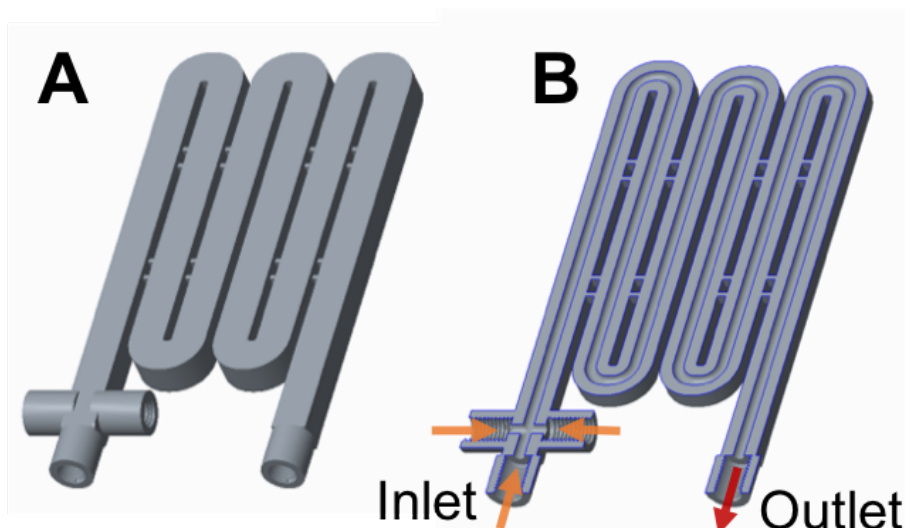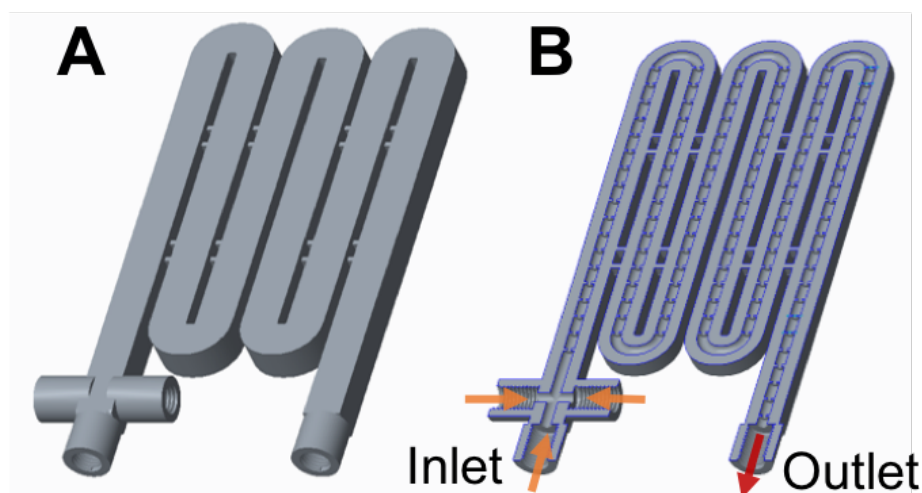


Figure 37: CAD model of a mesoscale continuous oscillatory baffled reactor (mTR) utilised for silver nanoparticle synthesis. Three inlets and one outlet were required. The two perpendicular inlets were utilised in transporting the bulk fluid

through the reactor while the parallel inlet allowed continuous fluid oscillation. a) mTR model b) Sectioned view of the mTR model.



Figure 38: CAD model of mesoscale continuous oscillatory baffled reactor (mCOBR) utilised for silver nanoparticle synthesis. Three inlets and one outlet were required. The two perpendicular inlets were utilised in transporting the bulk fluid, through the reactor while the parallel inlet allowed continuous fluid oscillation. a) mCOBR model b) Sectioned view of the mCOBR model.

### 3.4.3 Residence time distribution study

Experiments were designed to monitor the flow behaviour in the mTR and mCOBR under varying oscillatory conditions with respect to time. The following RTD studies were carried out in the reactors:

i.     RTD measurements in the mTR and mCOBR at flow rates between 0.5mL/min to 8mL/min, Table 2.

ii.     RTD measurements in the mCOBR at a constant flow rate and amplitude with varying frequency between 0.5 to 80Hz, Table 3.

iii.    RTD measurements in the mCOBR at a constant flow rate and frequency with varying amplitude between 0.18 to 5.4mm, Table 4.

In all experiments, the extraction flow rate was set to 15 ml/min. The UV acquisition interval was 0.1s whilst compiling the intensity related to the tracer (665nm for methylene blue).

Table 2: Residence time distribution studies in the mCOBR and mTR. The mCOBR was studied at a constant frequency and amplitude whilst varying the flow rate. In the mTR study, the fluid was not oscillated.

| | | | **Bulk fluid - flow rate (ml/min)** | | | |
|---|---|---|---|---|---|---|
| **mCOBR** | Frequency | 24Hz | 0.5 | 1.0 | 4.0 | 8.0 |
| | Amplitude | 2.16mm | | | | |
| **mTR** | Frequency | 0Hz | 0.5 | 1.0 | 4.0 | 8.0 |
| | Amplitude | 0mm | | | | |

Table 3: RTD studies in the mCOBR at varying oscillatory frequency with a constant flowrate and amplitude.

| | | | **Oscillatory frequency (Hz)** | | | | | | |
|---|---|---|---|---|---|---|---|---|---|
| **mCOBR** | Flow rate | 1ml/min | 0.5 | 1.6 | 2.4 | 4.0 | 12 | 24 | 40 |
| | Amplitude | 2mm | | | | | | | |

Table 4: RTD studies in the mCOBR at varying oscillatory amplitude with a constant flowrate and frequency.

| | | | **Oscillatory amplitude (mm)** | | | | | |
|---|---|---|---|---|---|---|---|---|
| **mCOBR** | Flow rate | 1ml/min | 0.18 | 0.54 | 1.08 | 1.80 | 2.88 | 3.60 |

| | Frequency | 24Hz | | | | | | |
|---|---|---|---|---|---|---|---|---|
| | | | | | | | | |

### 3.4.4 Silver nanoparticle production

An experiment was designed to compare the mTR and mCOBR in the synthesis of Ag-NP. With the mCOBR experiment, the oscillation on the pump was programmed to a peak-to-peak amplitude of 0.1mm and a frequency of 40Hz. All the experiments were performed at room temperature and at a controlled pressure of 4 bar using a back-pressure regulator BPR connector at the outlet of the reactor. The continuous synthesis was run for 100 minutes, with the spectra collected at 10 second intervals. The pumps were set to dispense the reactants at individual flow rates of 1ml/min each with a cumulative flow of 2ml/min through the reactor. In the mCOBR the middle inlet allowed for oscillation to be imposed on the flowing reagents. The intended characterisation methods were by inline UV-Vis spectroscopy and offline Transmission electron microscopy (TEM). The TEM images served to analyse and quantify the particle size distribution in both reactors. For this purpose, samples were put in vials 10 min and 90 min after start-up, while the rest of the synthesized Ag-NP solution was collected in a Duran flask. UV-Vis spectroscopy was used to characterise in the real time the materials being produced and the stability of the process.

## 3.5 Results and Discussion

### 3.5.1 AM Build Characterisation

The low-resolution images collected as per experiments 3.5.1.i, ii and iii (blocks with various channel diameters, fabricated at select length, wall thickness and build orientation) were utilised to inspect the parts for blockages, while the higher resolution images were used to measure and monitor deviation between the designed and actual build of the unblocked channels. The low-resolution images are presented in Figure 39-Figure 41.
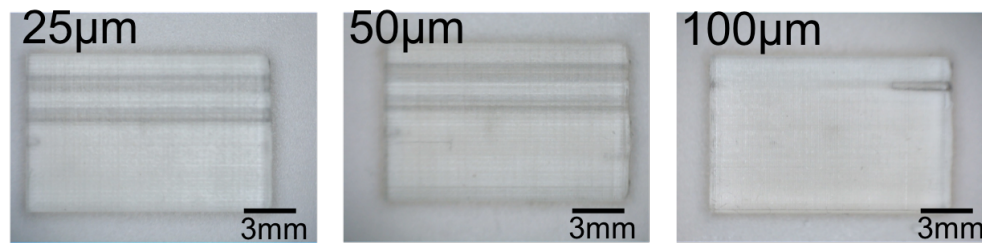


Figure 39: 3x9x14mm parts with channel diameters of 1.2, 1, 0.8, 0.6 and 0.4mm (top to bottom as in Figure 28) fabricated at 90º to the build bed at a layer thickness of 25 μm, 50 μm and 100 μm.
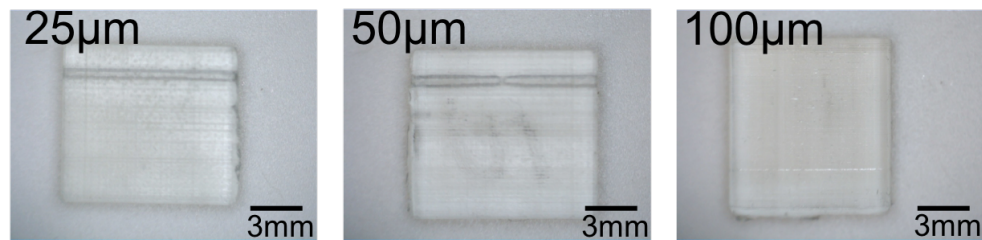


Figure 40:3x9x10mm parts with channel diameters of 1.2, 1, 0.8, 0.6 and 0.4mm (top to bottom as in Figure 28) fabricated at 90º to the build bed at a layer thickness of 25 μm, 50 μm and 100 μm.
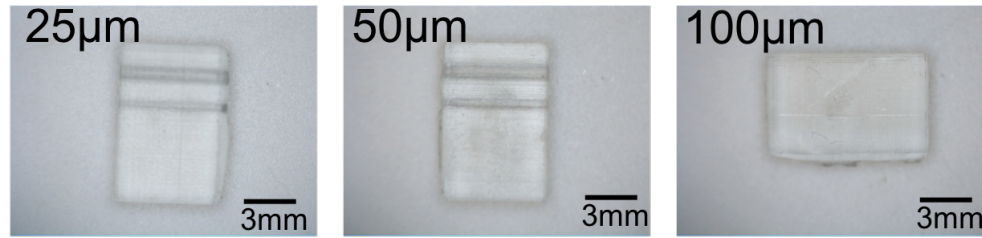
Figure 41: 3x9x6mm parts with channel diameters of 1.2, 1, 0.8, 0.6 and 0.4mm (top to bottom as in Figure 28) fabricated at 90º to the build bed at a layer thickness of 25 µm 50 µm and 100 µm.

In the longer 14 mm part, the 1.2 mm and 1mm channels are seen to be clear at 25 µm and 50 µm layer thicknesses. In the case of the 100 µm layer thickness, the part can be seen to be blocked and this is similar at all part heights of 6, 10 and 14 mm. In the 10 mm part only the 1.2 mm channel in the 25 and 50 µm prints were unblocked, while in the shorter 6 mm print the 1.2 and 1mm channels are seen to be clear. The rationale behind the varying length was to investigate if the smaller diameter channels could be fabricated at shorter lengths but could get blocked with increasing lengths.

Although the images give an indication of the blocked channels, they do not allow a distinct comparison of 25 and 50 µm layer thickness setting and the degree of deviation from the designed dimension. The parts fabricated at 25 and 50 µm were further analysed by optical microscopy as all the 100 µm parts had blocked channels.

Table 5: Optical microscopy images of parts fabricated at 25 µm showing the measured channels and blocked channels 1.2mm, 1mm, 0.8mm, 0.6mm and 0.4mm. Dimensions: 3x9 mm at heights of A) 14mm B) 10mm and C) 6mm.
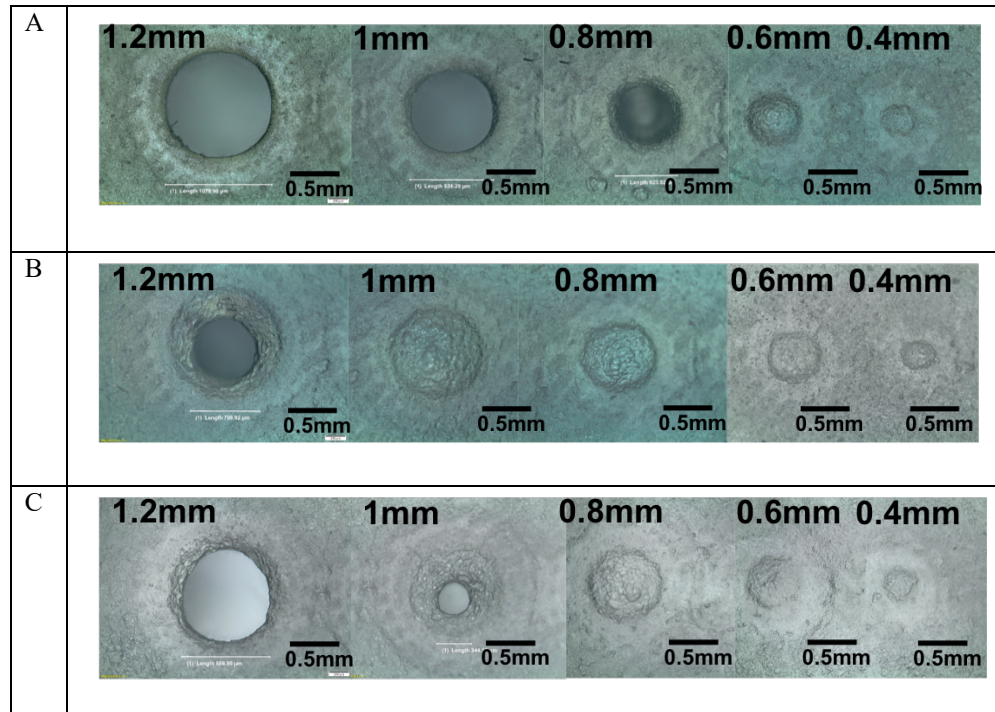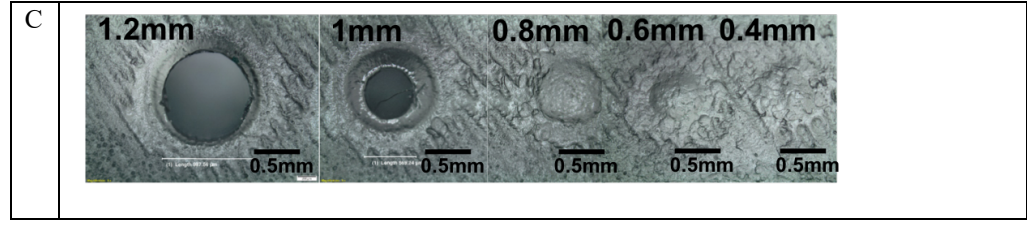


Table 6: Optical microscopy images of parts fabricated at 50 µm showing the measured channels and blocked channels 1.2mm, 1mm, 0.8mm, 0.6mm and 0.4mm. Dimensions: 3x9 mm at heights of A) 14mm B) 10mm and C) 6mm.
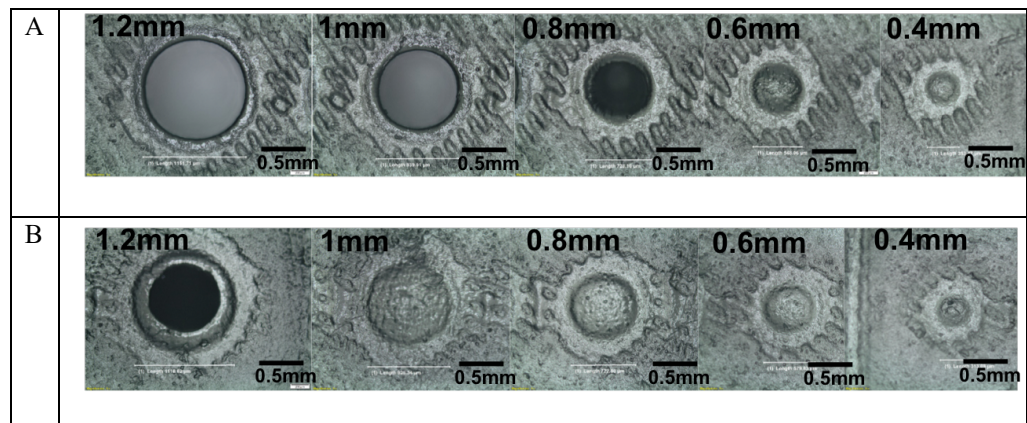
Table 7: Channel measurements for 6, 10 and 14 mm blocks at 25, 50 and 100 µm layer thickness, where D is the deviation from the specified dimension and PLR is the platform layer resolution. The greyed cells signify the blocked channels, where channel diameters were not obtained.

| | 1200 (µm) | D (µm) | 1000 (µm) | D (µm) | 800 (µm) | 600 (µm) | 400 (µm) | PLR |
|---|---|---|---|---|---|---|---|---|
| 6mm | 886.95 | 313.05 | 344.19 | 655.81 | - | - | - | 25µm |
| 10mm | 706.92 | 493.08 | - | - | - | - | - | 25µm |
| 14mm | 1078.9 | 121.1 | 839.29 | 160.71 | - | - | - | 25µm |
| 6mm | 987.56 | 212.44 | 569.24 | 430.76 | - | - | - | 50µm |
| 10mm | 1118.62 | 81.38 | - | - | - | - | - | 50µm |
| 14mm | 1151.71 | 48.29 | 939.91 | 60.09 | - | - | - | 50µm |
| 6mm | - | - | - | - | - | - | - | 100µm |
| 10mm | - | - | - | - | - | - | - | 100µm |
| 14mm | - | - | - | - | - | - | - | 100µm |

The images Table 5- Table 6 show the fabricated and blocked channels in the 25 and 50 µm builds. In the 25 µm builds at 1.2mm the channel deviation was between 121 – 313 µm from the original design compared to 160 - 655 µm for the 1mm build, Table 7. In the 50 µm build, the deviation was between 48 - 212 µm at 1.2mm and 60 – 430mm at 1mm. The 25 µm did not produce an improved result compared to the 50 µm layer thickness. On the other hand, the 50 µm part showed reduced deviation.

To investigate the impact of a larger wall thickness on the dimension of the channel, parts were fabricated with the channels at 90º to the optical window in

layer thickness of 25, 50 and 100 µm (experiment 3.5.1.ii). The prefabrication and post fabrication processes carried out were similar to previous parts.
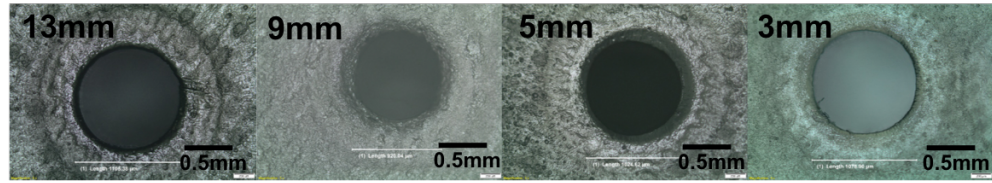


Figure 42: Optical microscopy images of 20mm part fabricated at a layer thickness of 25 µm with a channel diameter of 1.2mm and square cross section of 13mm, 9mm, 5mm and 3mm.
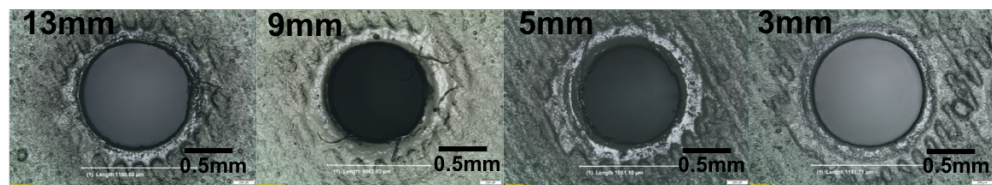


Figure 43: Optical microscopy images of 20mm part fabricated at a layer thickness of 50 µm with a channel diameter of 1.2mm and square cross section of 13mm, 9mm, 5mm and 3mm.

Similar to the previous study, the 4 parts fabricated at 100 µm were found to be blocked, hence were not measured. As presented in Table 8, the deviation in diameter of the parts fabricated at 25 µm and 50 µm were between 94 – 280 µm and 19 – 149 µm respectively. The minimum deviation was in the part fabricated at a square cross section of 13mm at both layer thicknesses. There was no clear indication of a relationship between the build area and the channel diameter. However, similar to experiment 3.5.1.i, a minimised deviation was observed at the 50 µm layer thickness compared to the 25 µm case.

Table 8: Channel measurements and deviation for 3, 5, 9 and 13mm measurements at 25 and 50 µm layer thickness setting (LTS) for a 1.2mm diameter

|  | 25 (µm) | D (µm) | 50 (µm) | D (µm) |
|---|---|---|---|---|
| 13mm | 1105.38 | 94.62 | 1180.83 | 19.17 |
| 9mm | 920.04 | 279.96 | 1063.03 | 136.97 |
| 5mm | 1024.62 | 175.38 | 1051.1 | 148.9 |
| 3mm | 1078.9 | 121.1 | 1151.71 | 48.29 |

To investigate the effect of the build orientation on the geometry and dimension of the channel, parts were fabricated as per experiment 3.5.1.iii. The design, fabrication and post fabrication process were carried out similar to the previous experiments. All parts in the varied build orientations were fabricated at a layer thickness of 25, 50 and 100 µm.

From the low-resolution images in Figure 44-Figure 46, blocked and unblocked channels can be identified. Firstly, the parts fabricated at 100 µm showed the poorest results of the LTS as most of the channels were blocked. Initiation of the channels can be observed at either end of some of the blocked parts. The parts fabricated at 0° produced the poorest of the orientations. The parts fabricated at 25 and 50 µm at 45° to build plate were observed to produce the best result (Figure 44, Table 9A and Table 10A). The 1.2 and 1mm channels were unblocked in both cases while the 0.8mm was completely unblocked in the 50 µm part and halfway blocked with the 25 µm build. The 90° build was also unblocked in the 1.2 and 1mm case, leaving the rest of the channels blocked. With the build in the 0° orientation, bowing of the channels could be observed

stemming from a normal phenomenon that occurs at the interface between the support branches and the initial layers of the build.
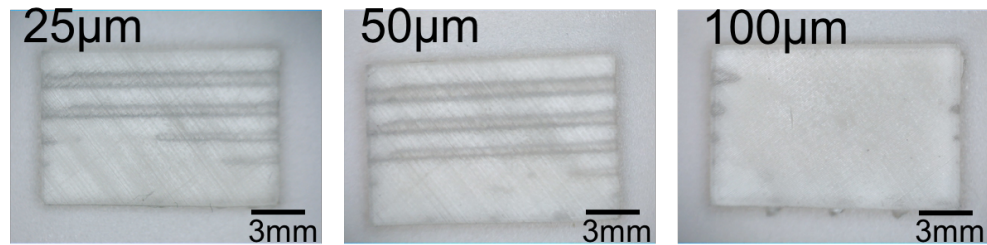


Figure 44: 3x9x14mm parts with channel diameters of 1.2, 1, 0.8, 0.6 and 0.4mm (top to bottom as in Figure 32) fabricated at 45º to the build bed at a layer thickness of 25 µm, 50 µm and 100 µm.
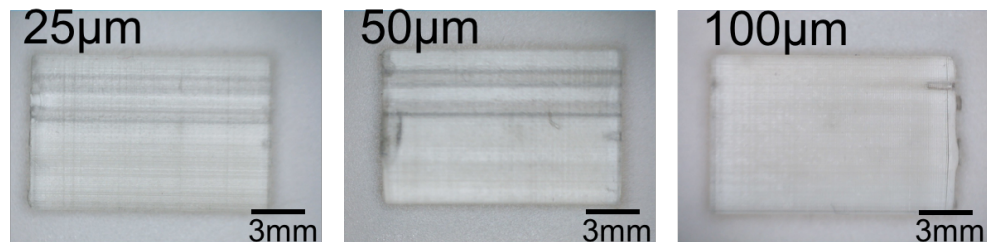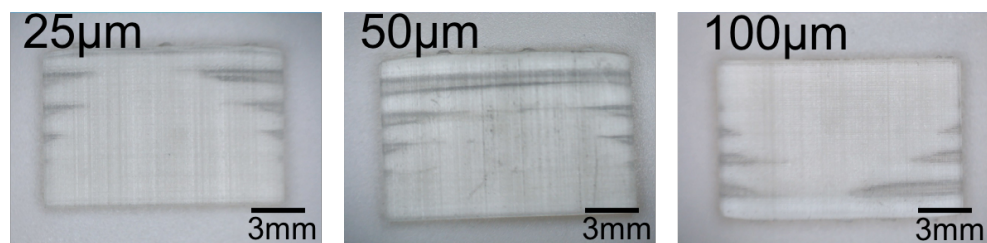


Figure 45: 3x9x14mm parts with channel diameters of 1.2, 1, 0.8, 0.6 and 0.4mm (top to bottom as in Figure 32) fabricated at 90º to the build bed at a layer thickness of 25 µm, 50 µm and 100 µm.



Figure 46: 3x9x14mm parts with channel diameters of 1.2, 1, 0.8, 0.6 and 0.4mm. fabricated at 0º to the build bed at a layer thickness of 25 µm, 50 µm and 100 µm.

Table 9: Optical microscopy images of 3x9x14mm parts fabricated at A) 45º B) 90º C) 0º to the build bed and layer thickness setting at 25 µm showing the measured channels and blocked channels 1.2mm, 1mm. 0.8mm, 0.6mm and 0.4mm
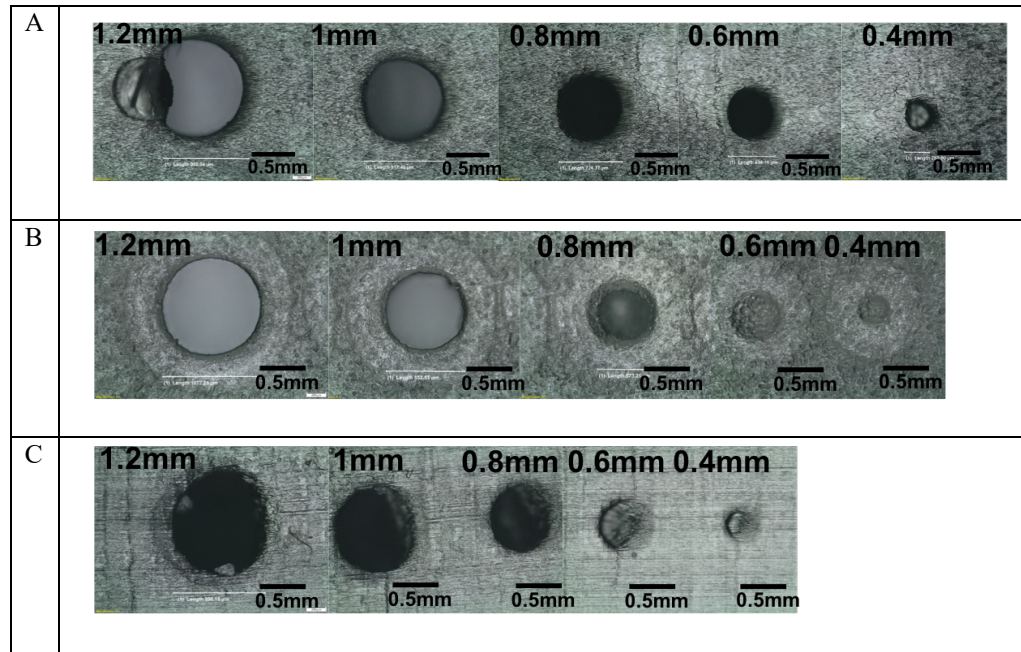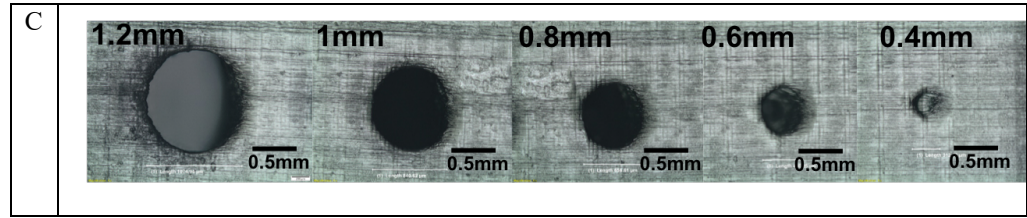


Table 10: Optical microscopy images of 3x9x14mm parts fabricated at A) 45º B) 90º C) 0º to the build bed and layer thickness setting at 50 µm showing the measured channels and blocked channels, 1.2mm, 1mm, 0.8mm, 0.6mm and 0.4mm
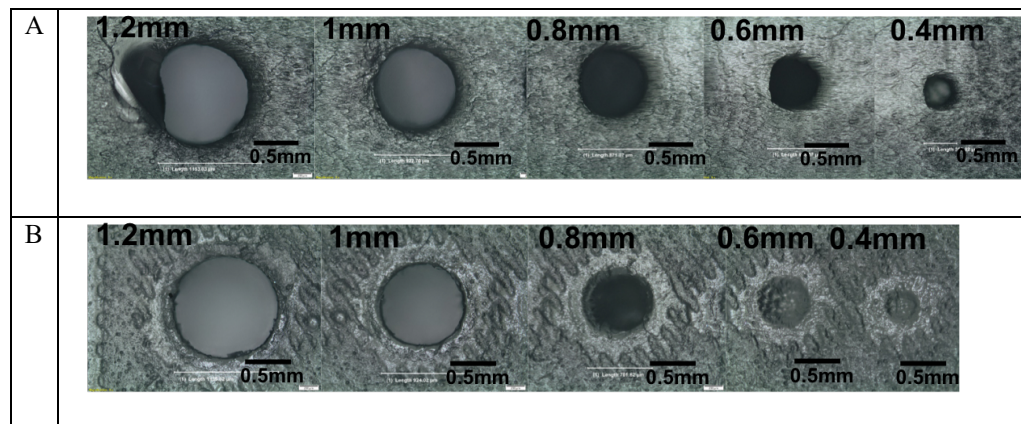
Table 11: Channel measurements and deviation for the 90º, 45ºand 0º fabrication angle with channel diameters of 0.4mm to 1.2mm. The greyed cells represent areas with blocked channels.

| | 1200 (µm) | D (µm) | 1000 (µm) | D (µm) | 800 (µm) | D (µm) | 600 (µm) | 400 (µm) | PTY |
|---|---|---|---|---|---|---|---|---|---|
| 90º | 1072.28 | 127.72 | 852.53 | 147.47 | - | - | - | - | 25µm |
| 45º | 980.94 | 219.06 | 917.40 | 82.60 | - | - | - | - | 25µm |
| 0º | - | - | - | - | - | - | - | - | 25µm |
| 90º | 1135.82 | 64.18 | 924.02 | 75.98 | - | - | - | - | 50µm |
| 45º | 1153.03 | 46.97 | 922.70 | 77.30 | 871.07 | 71.07 | - | - | 50µm |
| 0º | 1074.94 | 125.06 | - | - | - | - | - | - | 50µm |
| 90º | - | - | - | - | - | - | - | - | 100µm |
| 45º | - | - | - | - | - | - | - | - | 100µm |
| 0º | - | - | - | - | - | - | - | - | 100µm |

From the optical microscopy images collected and measurements complied in Table 11, a comparison can be made between the 25 and 50 µm builds for the 0º, 45º and 90º orientation. The best fabricating orientation was found to be at 45º, as channels 1.2, 1 and 0.8mm are observed to be unblocked with a deviation of between to 47-77 µm at 50 µm.

*Discussion*

The rationale behind varying the part length was to investigate if the smaller diameter channels could be fabricated at shorter lengths but block with increasing lengths. This understanding will allow for the final reactor design to include varying channel lengths, with larger channels in areas more prone to blockages. Perhaps, with increasing channel length there is a deviation in the Z-arm of the device. Also, with the swipe and peel mechanism of the technique there could be movement of the parts in relation to the attached bed. Such movements have been observed when parts are under supported, creating a stepped surface due to shift in layers. Hence, the possibility of having unblocked channels with shorter tube lengths was envisaged. However, from the parts fabricated the relationship was not observed. The 14mm and 6mm parts were clear at only 2 channel dimensions leaving the 10mm channel blocked at the 1mm for the 25 and 50 μm layer thickness. It is important to highlight that the parts were fabricated together at the same position on the build plate at every resolution. Perhaps, the blockages observed at the 1mm diameter channels on the 10mm could relate to the position on the build plate. Poor part resolution on build areas could be as a result of wear from extended fabrication on specific areas of the optical window.

There is a clear indication that at this range of diameters, the 100 μm layer thickness is not suitable to achieve channel diameters less than 1.2mm. The higher resolution images and results showed that although a better understanding of all the factors affecting the build need to be investigated, the 25 μm did not produce an improved dimensional accuracy compared to the 50 μm thickness.

On the other hand, the 50 μm part showed reduced deviation. This could be have resulted from longer exposure of the laser as twice as many layers were produced in the 25 μm case. Longer laser exposure will result in undesirable curing of the resin in the internal channels and will lead to a reduced channel size and blockages in some cases.

The experiment designed to build channels at a varying wall thickness was intended to understand the dependency of the thickness of the walls on the channel diameter. With a larger wall thickness this will equate to larger exposure of the laser to the part. It was presumed that this could result in lengthy exposure of the material in the channel, hence blocking the part. However, this was not shown in the data collected. Perhaps, this results from the laser traces being perpendicular to the parts as they were built vertically. The data however showed a similar result of a minimised deviation at the 50 μm layer thickness compared to the 25 μm case.

The later experiment studied the effect of the build orientation on the channel dimension produced. The most desirable build orientation was found to be at 45° to the build plate, with the worst case being the parallel case. At 45° a larger oval trace is stacked layer by layer, allowing for reduced contact with the internal channels. When the parts are fabricated parallel to the plate, the laser traces perpendicular to the channel, resulting in the stepped formation of the void. When the top of the channel is being formed the Laser pattern passes over the void of uncured material, resulting in undesirable polymerisation. This will lead to blockages or reduction in channel diameter which was observed in the results.

The studies served to give an understanding of the limitation of the selected vat polymerisation platform (Form 2), although the tolerances may vary on devices. It highlights the process parameters of the technique and it's effect on the channel diameter and final build. This study feeds into the design for manufacture of mesoscale flow devices to enhance reproducibility and prevent blockages. In conclusion, the studies show that reactors can be manufactured using this technique up to channel diameters of 0.8mm. Deviation of the channel diameter can be minimised by positioning at 45° to the build bed and at 50 μm layer thickness on the Form 2 machine. The challenge of fabricating voids parallel to the build bed is that when the laser crosses the void path, surrounding material is polymerised and can cause blocking. This is more so in channels less than 1mm in diameter. There was a significant difference fabricating at 100 μm compared to 25 and 50 μm as coarse surface roughness and blockages were observed. However, the best fabricating condition for applications requiring channel diameters up to 1.2mm was found to be 50 μm. The 25 μm measurements for the printed parts did not show improvements to the blockage issues and dimensional variation.

**Defects and surface roughness**

A less mentioned topic in vat polymerisation technique is the defects and inconsistencies that arise from fabrication. The main source of the inconsistencies arises from the build vat's optical window. With continuous use, the PDMS surface degrades. This was visible during inspection as the mid region of the optical window, which is used more often, turns milky showing traces of build layers, see Figure 47.
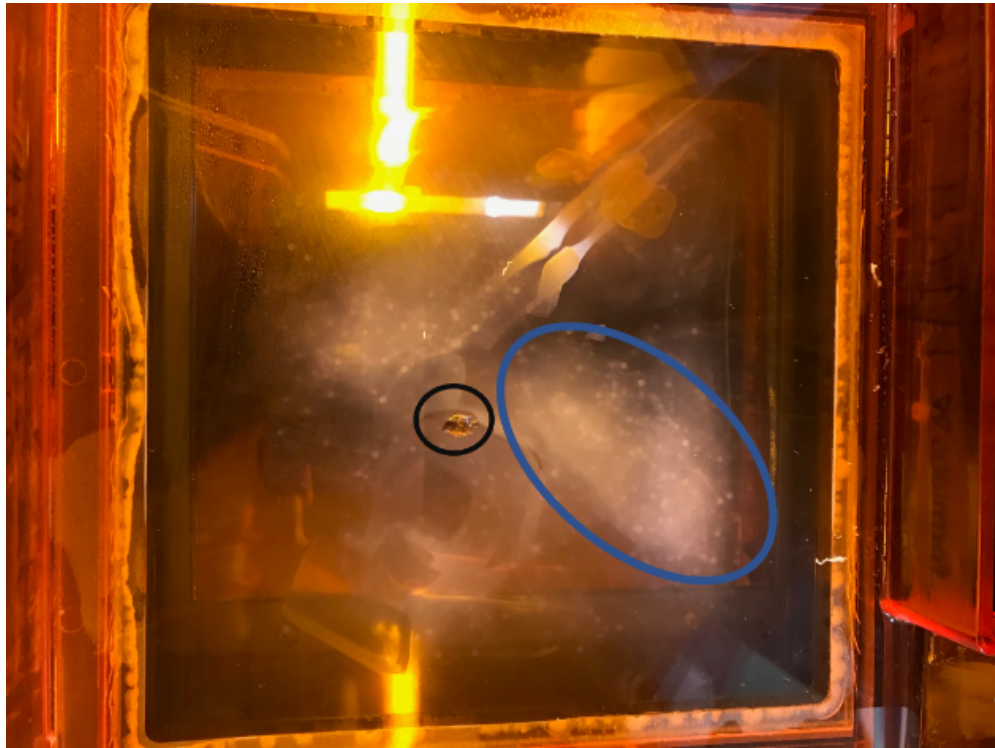
Figure 47: A picture of the optical window of the Formlabs with defects arising. The blue circle shows an area of extended use which starts to turn milky. Small circles in that area can be seen showing traces of supports previously built. The black circle shows a defect in the optical window. Parts positioned in this region will have holes as a result.

Changing the physical properties of the optical window will adversely affect the refractive index of the material and surface quality. Hence, the parts fabricated will also be affected. Figure 48A-C show optical images from the surface of parts fabricated at layer thickness 25, 50 and 100 μm. A clear distinction can be observed between the surfaces as the 100 μm part has a coarser surface finish while the 25 μm build has the finest.
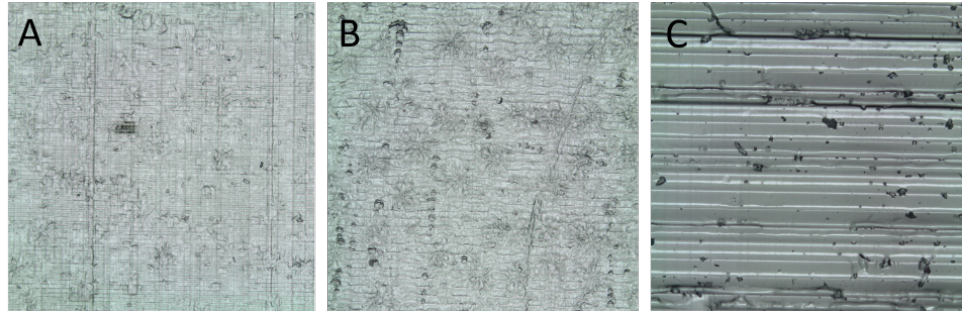
Figure 48: Optical microscopy images of surfaces of parts fabricated on the Form 2 platform at layer thickness of A) 25 μm B) 50 μm and C) 100 μm

Additionally, a difference in the surface finish was also observed on the surface of two parts built at 100μm, see Figure 49. Although the change is not understood, this could be likened to a change in the processing condition. This includes changes to the quality of the optical window, fabrication temperature, effecting the viscosity of the polymer; Laser source intensity, changes to the vat refractive index and nature of the resin as new material is auto refilled over pre-existing material in the vat.
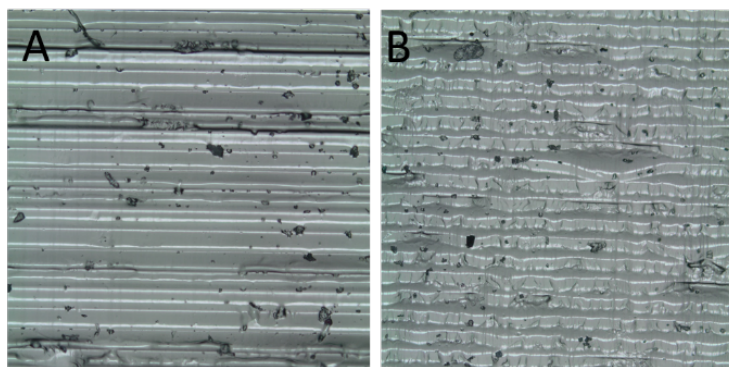


Figure 49: Optical microscopy images of a part fabricated at 100 μm with varying surface characteristics.

As the parts fabricated are intended for flow reactors, control of the quality of the surface is important as it influences the flow dynamics. Hence, an understanding and a follow up optimisation of the process parameters is essential. Parts not adequately supported to the build base were also been observed to show deviation in the build layers. This is because after each layer, the peel mechanism exerts a shear force on the interface between the part and the PDMS layer. In the case of inadequately supported parts, this results in slight movement of the part. The degradation of the optical window, obstacles in the laser path from particles or polymerised material from previous build will result in deviation from the required design. In some cases, this could lead to pronounced defects as seen in Figure 50. This defect was consistent in several parts produced in the same location on the build bed.
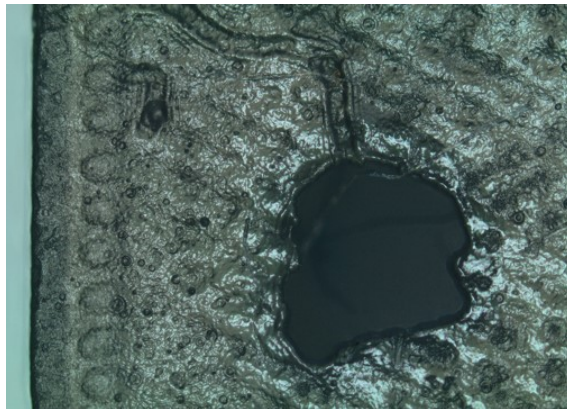
Figure 50: Defect in part fabricated by vat polymerisation

In general, vat polymerisation on a low-cost platform like the Form2 allows the fabrication of mesoscale flow reactors, where the channels can be easily cleared by flushing with IPA. As discussed in Chapter 2, clearing the channels in other AM processes, such as powder bed fusion, will be more challenging. An added benefit of utilising the vat polymerisation technique coupled with a Formlabs

Clear resin is that it allows for visual transparency of the part with post processing. Figure 51 presents one of the parts fabricated for experiment 3.5.1. It was sprayed with RS Pro Clear Acrylic Lacquer and allowed to dry for 30min. For best results, the fabricated part is normally finely polished, minimising the surface roughness, cleaned and spray coated with clear acrylic lacquer. This allows for inspection of the channels if blockages occur whilst in use. It can also be utilised in inline flow monitoring applications.
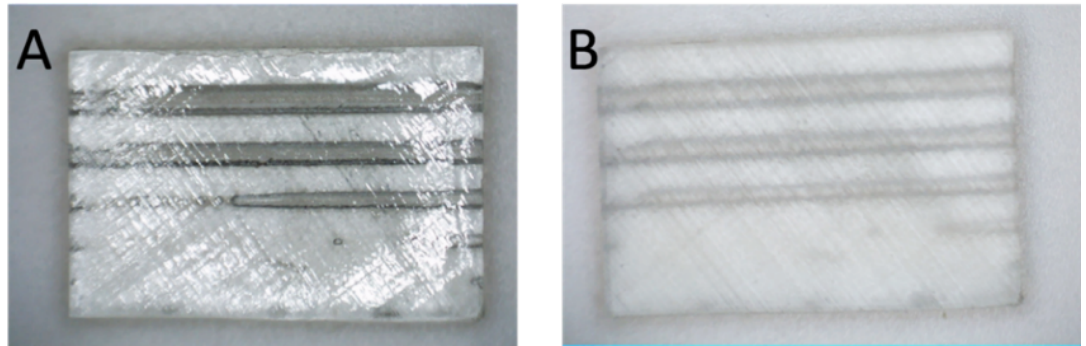


Figure 51: Images of a fabricated part from the experiment in 3.5.1. Spraying with clear lacquer will allow visual transparency for inspection and inline flow monitoring A) sprayed with RS Clear Lacquer B) Unsprayed.

### 3.5.2 mCOBR and mTR fabrication

A number of mCOBRs and mTRs were fabricated for subsequent studies. Figure 52(left) shows two completed flow reactors hanging from the build plate attached to support structures, while Figure 52B shows post processed reactors for utilisation.
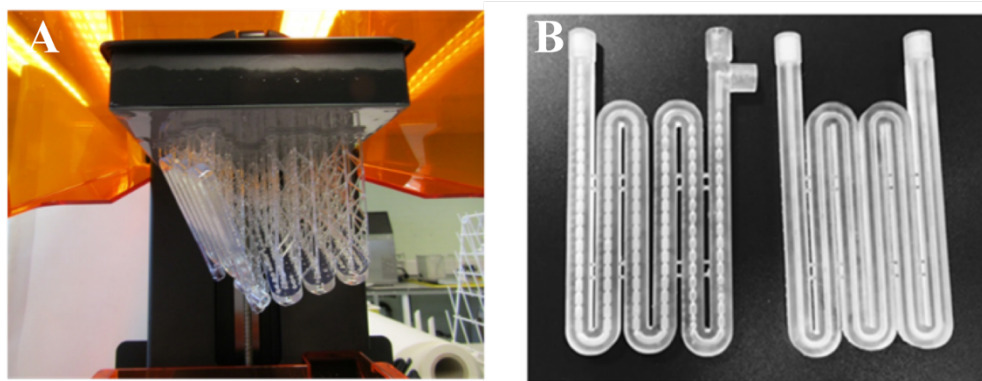


Figure 52: Images of fabricated mTR and mCOBR in Form2 vat polymerisation platform. A) Parts as built and attached to the build plate via support structures. B) fabricated mTR and mCOBR with supports removed and cleaned

As presented in Table 12, the mTR was produced at a slightly quicker time of 4hrs 53min compared to 5hrs 2min for the mCOBR at layer thickness of 100 μm. The 100 μm setting was selected as the diameter requirement for the following studies was larger than 1.2mm. At above 1.2mm and positioned at 45° to the build plate blockages and large dimensional deviations were unexpected. For example, a 3-inlet mCOBR will require 5hrs 53min to complete at 100 μm but will take 15hrs 42min at 25microns on the Form2. Device run time can be minimised by fabricating multiple parts in a build. Although a single 3-inlet mCOBR requires a completion time of 5hrs 53min, two devices can be

manufactured in 8hrs 54min, saving running costs and time. The material cost of the mTR and mCOBR devices works out to £7.74 and £8.84 respectively.

Table 12: A comparison of resin volume, fabrication time and material cost for the mesoscale tubular reactor (mTR) and mesoscale oscillatory baffled reactor (mCOBR)

| Parameter | mTR | mCOBR |
|---|---|---|
| Reactor Volume | 2.7mL | 2.5mL |
| Diameter | 2.5mm | 2.5mm |
| Resin volume | 51.67mL | 54.9mL |
| Fabrication time | 4hrs 53min | 5hrs 2min |
| Material Cost | £7.74 | £8.24 |

When fabricated at the prescribed orientation and print conditions, there were no issues with blockage of the reactor. With the devices fabricated parallel to the build bed, blockages occurred, more so when the devices were flushed more than 24hrs after build completion.

Although the preliminary study serves to simplify the understanding of fabricating with SLA and creates concrete understanding of the possibilities enabled by the FormLabs 2, more complex geometries bring forward other challenges. The mCOBR is an example of such complex geometries as it features curved channels, overhanging periodically spaced baffles and thin screw connector threads for interfacing with pumps. Although the straight channels can be positioned at between 45-90º to the build bed, to minimise blockage, the curved regions of the reactor lie below 45º to the plate. This region

creates the opportunity for blockages to occur. The PreForm software may also create internal supports, depending on the fabricating angle, which limits the removal of the resin in the channels. Hence thorough checks were carried out before fabrication. The screw fittings which had fine threads also had a high efficacy at the prescribed conditions. Though, when positioned with the connectors closer to the build plate and supports are attached, fastening to a tube fitting becomes more difficult or in some cases loose. In such cases, leaks arose at the connector with higher flow rate or increased pressure.

The reactor devices were pressure tested to ascertain the quality and durability of the fabricated connectors. This was carried out by connecting the reactor device using connector fittings to a HPLC pump coupled with a pressure transducer. It was pressurised using water to 85 bars without any leaks or ruptures observed. Polishing and spraying with RS clear lacquer aided visual monitoring of the build to check for leaks. The external surface roughness of the fabricated devices was obtained to 1.2 µm root mean square. This is pictured in Figure 53, the layers can be observed running across the image. This aimed to serve as an estimate of the internal surface roughness of the channels, as it was inaccessible to be measured using available techniques.
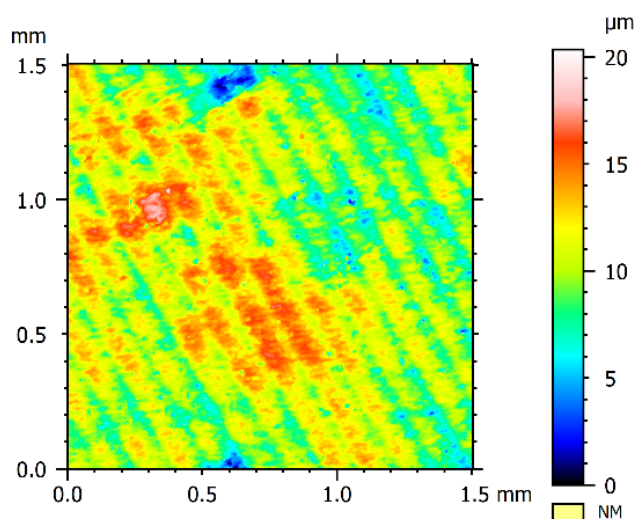
Figure 53: Surface roughness characterisation of a fabricated flow reactor. The room mean square roughness was 1.2 μm. The layers can be seen across the image.

3.5.2.1 AM material characterisation

The TGA results of the AM material sample display a slight change in the thermal decomposition behaviour of the samples (Figure 54 A). The samples tested decomposed in two steps (Figure 54 B). According to the manufacturer, the resin consists of Methacrylates and Polymethcrylates. Thus, first mass loss starting at 200 °C can be attributed to partial loss of the side groups and the second one at 400 °C to depolymerization of the polymer. Water increases the relative importance of the second decomposition step, which can be attributed to partial hydrolysis of the side groups. The decrease in thermal stability caused by organic solvents could be due to extraction of stabilizers from the resin. However, all changes are minor and the IR-spectra are indistinguishable (Figure 54 C), indicating that the bulk of the material remains essentially the same.
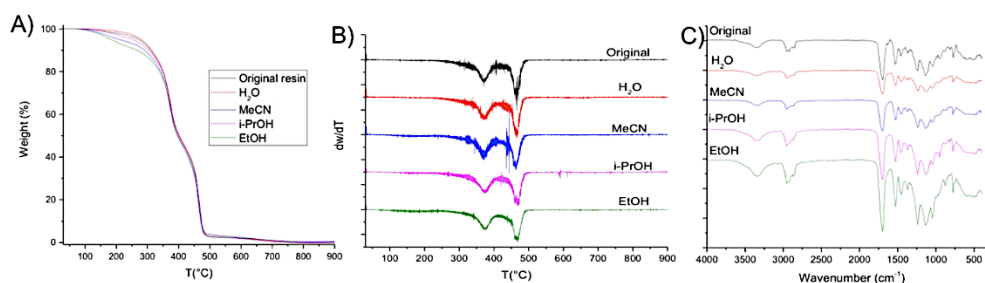
Figure 54: A) TGA-curves for the resins. B) Derivatives of the TGA-curves. Data has been vertically shifted for clarity. C) IR spectra of the solvent soaked pieces of resin. The curves have been vertically shifted for clarity

### 3.5.3 Residence time distribution study

The experimental rig for the residence time distribution study is pictured in Figure 55. At the start of the experimentation, the degree of backing mixing of the fluid with the oscillating fluid was questioned. Carrying out the initial test to ensure smooth running of the setup, the extent of back mixing of the fluid was not spotted. With injection of the methylene blue tracer towards the flow direction, the back flow and mixing with the oscillating fluid could be observed at the T-mixing interface. The tracer colouring could be observed incrementally changing the colour of the water in the fluid syringe. This effect was increased with larger oscillating amplitude and lower frequency. The resulting effect can also be explained on the E($\theta$) curves, as the back flow resulted in the tracer having a longer residence time in the reactor. This results in long tail on the trailing end of the distribution. Silicon oil was replaced as the oscillating fluid, as it is immiscible with water, see Figure 56. Silicon oil worked well as the oscillating fluid allowing a continuous flow of the bulk fluid while oscillating and avoiding a dead volume in the reactor.
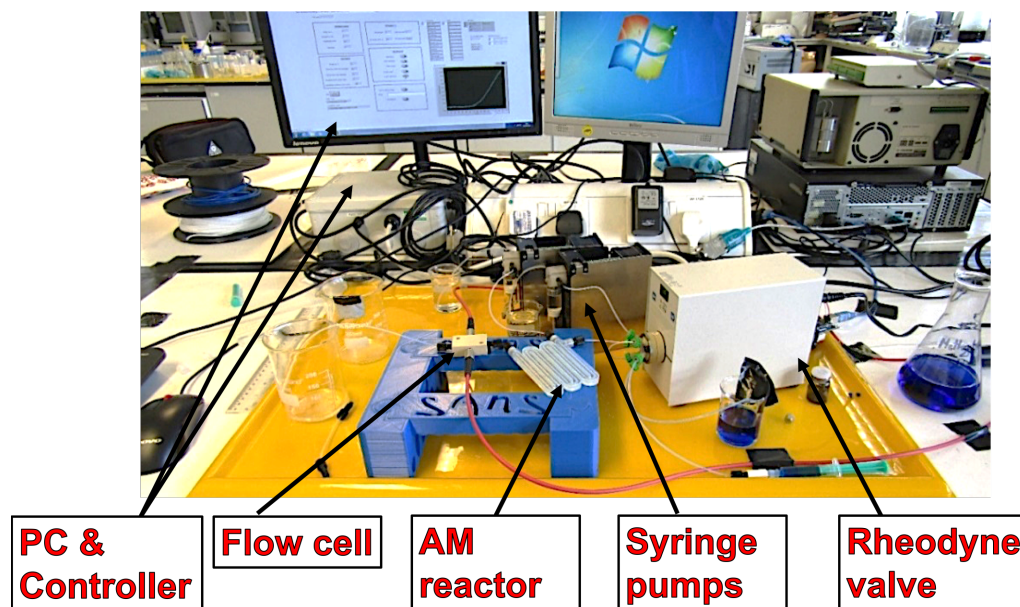
Figure 55: Experimental setup for residence time distribution studies. Comprising of two syringe pumps, one for continuous flow and the other for oscillation, a Rheodyne valve, flow cell, UV-VIS spectrometer and a light source coupled by tubes and 1/16" connector fittings
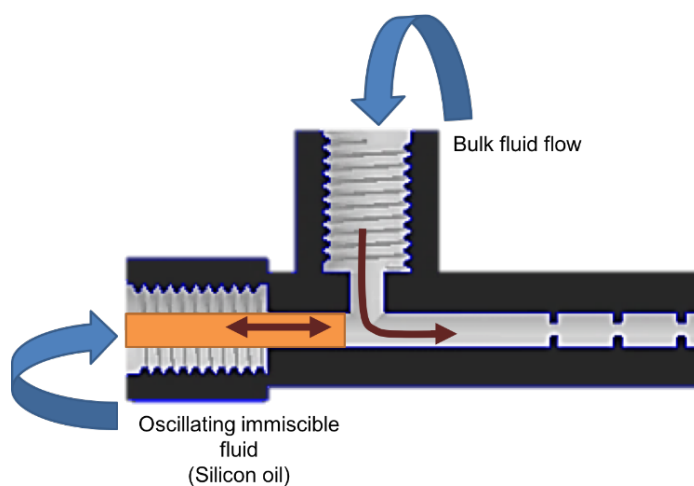


Figure 56: Schematic of the oscillation of fluid in the mCOBR using silicon oil to prevent back mixing with the bulk fluid (distilled water).

The RTD curves for the experiment 3.5.3.i, are presented in Figure 57 and Figure 58. From the RTD curves of the experiment using the tubular reactor presented in Figure 57, the development of the injected tracer pulse can be analysed. The

curves indicate an un-even residence time of the fluid in the reactor. A larger volume of the fluid exited the reactor at a dimensionless time of 0.5 -1.0. At all flow rates, a long trailing edge and a skewed curve was observed. In the range of flow rates, there was no improvement in the residence time distribution.
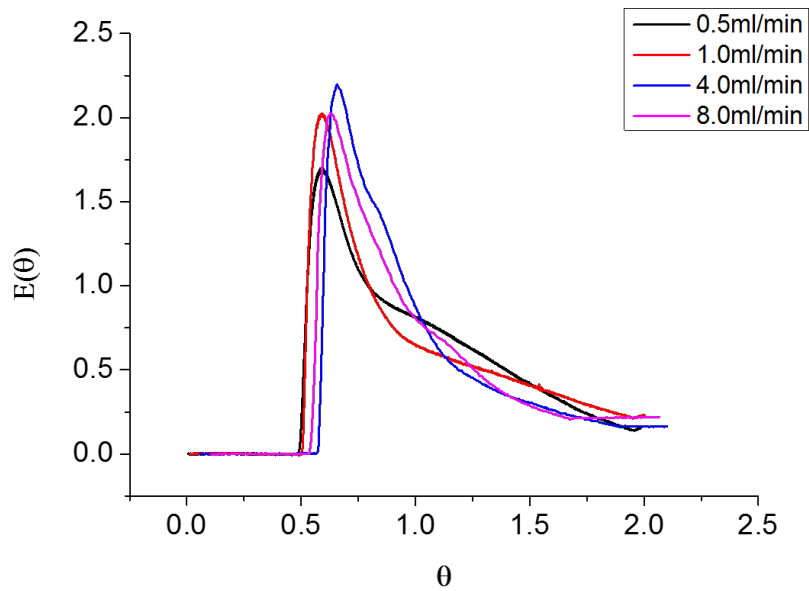


Figure 57: Residence time distribution curves for experiments carried out in the fabricated TR. The range of flow rates explored was between 0.5-8ml/min.

During the experimentation, the tracer flow was visually monitored. The fluid could be observed with a higher velocity at the mid region of the channel in a deep parabolic shape. This flow pattern is characteristic of laminar flow through a channel under such low Reynolds.
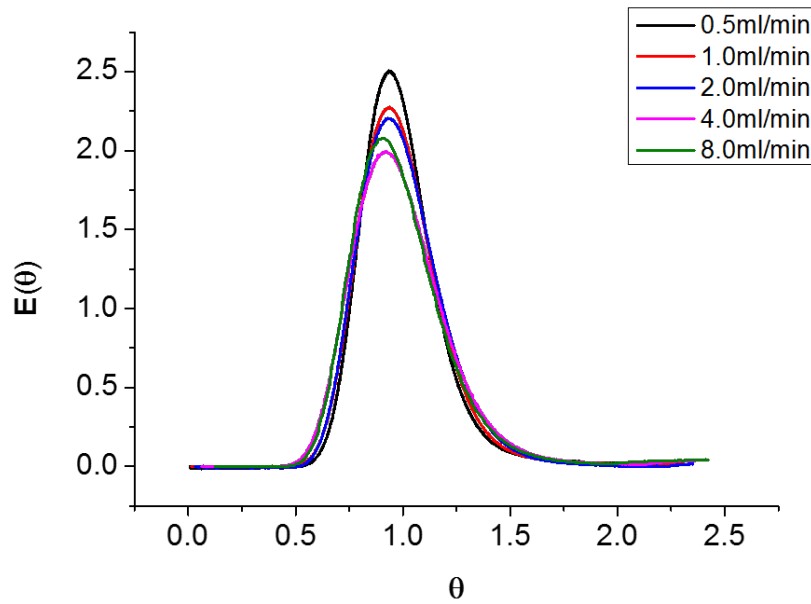
Figure 58: Residence time distribution curves for experiments carried out in the fabricated mCOBR. The tested range of flow rates between 0.5-8ml/min at oscillatory frequency and amplitude of 24Hz and 2.16mm respectively.

The RTD curves in the mCOBR under similar flow rate conditions showed a different result. With the oscillatory conditions in the mCOBR, the RTD curves showed enhanced symmetry. The curves presented in Figure 58 indicate a less dispersed, uniform flow of fluid through the reactor. A shorter tail end of the curves compared to that of the TR is also observed. The results also indicate a lower degree of back mixing approaching plug flow conditions. As the distribution was converted to dimensionless values, a comparison of the distribution at a flow rate of 1ml/min was presented in Figure 59. A clear difference of qualitative improvements in the distribution can be observed.
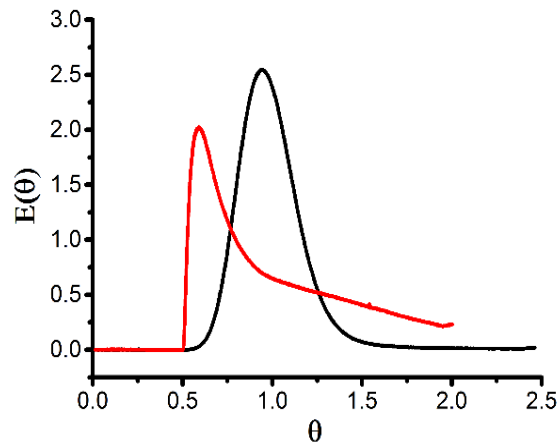
Figure 59: Comparison of RTD curve in a TR (red) and mCOBR (black) at a similar flow rate of 1ml/min. Qualitative improvements can be observed using an mCOBR

This shows a controlled residence time and improved mixing efficiencies observed in the mCOBR. With an increase in flow rate, the width of the curve increased, and length reduced from 0.5 to 4ml/min, after which it reversed at 8ml/min. This is because as the flow rate increases, the effect of the oscillation is increasingly suppressed. Hence, the velocity ratio ($\psi = Re_o/Re_n$) minimises and starts approaching zero. The velocity ratio is key in COBR design. A value of 1 and greater represents an increase, resulting in beneficial domination of the oscillatory effects on the fluid flow.

The acquired spectra were then fitted to the to the axial dispersion model described in the chapter 3 introduction utilising the formulae. The RTD obtained fit well with the axial dispersion model. The axial dispersion model effectively describes flow conditions close to plug flow. Using a solver, the Peclet numbers were computed from the axial dispersion model fit.
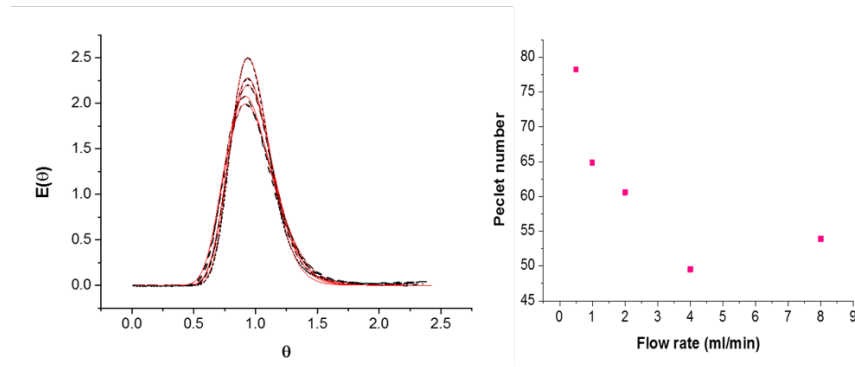
Figure 60: Fit of the residence time distribution curves to the axial dispersion model for experiments done in the mCOBR at oscillatory amplitude and frequency of 2.16mm and 24Hz at flow rates ranging between 0.5ml/min to 8ml/min. (left). The computed Peclet numbers from the model is calculated presented as a function of the flow rate (right).

Peclet number, is a non-dimensional number used in bench marking flow conditions. It is the ratio of rate of advection to the rate of diffusion. Hence, a higher Peclet number signifies a prevalence of advective mixing and closeness to plug flow conditions. The Peclet numbers of the curves obtained and presented in Figure 60, can be seen to decrease with increase in flow rate. For the tested range in experiment two the Pe (N tanks-in-series = Pe/2) was between 50 to 80.

Experiment 3.5.3.ii aimed to explore a range of oscillatory frequency in the mCOBR. Using a fixed oscillation peak-to-peak amplitude of 2mm and flow rate of 1ml/min, a range of frequencies between 0.5 to 80Hz were tested. UV acquisition time and dispense rate were kept constant as in experiment 3.5.3.i. The resulting RTD curves are presented in Figure 61.
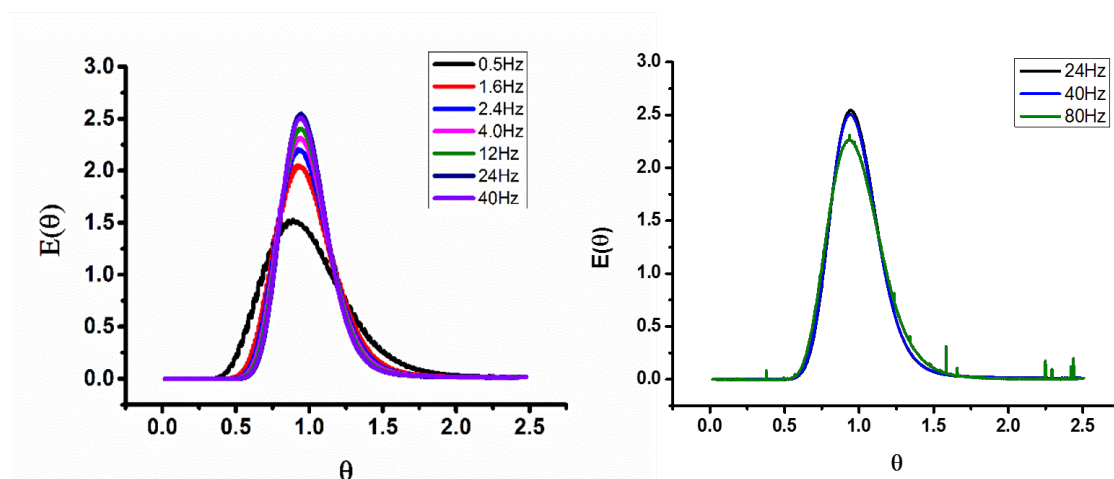
Figure 61: Residence time distribution curves for experiments carried out in the fabricated mCOBR. The tested range of frequencies between 0.5-80Hz at flow rate of 1ml/min and peak-to-peak amplitude of 2mm.(left) The RTD curves under similar conditions and at frequency of 24-80Hz are presented separately to show peaks found in the distribution(right).

From the RTD curve in Figure 61A a broad distribution is observed at the lowest frequency of 0.5Hz and this decreased as the frequency increased. Qualitative improvements were observed from the RTD curves from 0.5 – 24Hz. This indicates that with increase in frequency, the data matches the expectation of approaching to plug flow conditions. Hence, a domination of oscillatory conditions over the bulk fluid flow. With further increase in the frequency, this effect was reduced. At frequencies greater than 24Hz, small peaks were noticed in the data, as seen in Figure 61B. On close investigation during operation, the cause was attributed to the silicon oil passing though the reactor and the flow cell. The setup was designed to have the silicon oil just before the inlet of the bulk fluid. However, with higher frequencies, the silicon oil which was used for oscillating and to prevent back mixing with water was found to split and enter

the reactor. As a result, plugs of oil was found in the reactor, creating dead volumes and causing flow channelling.
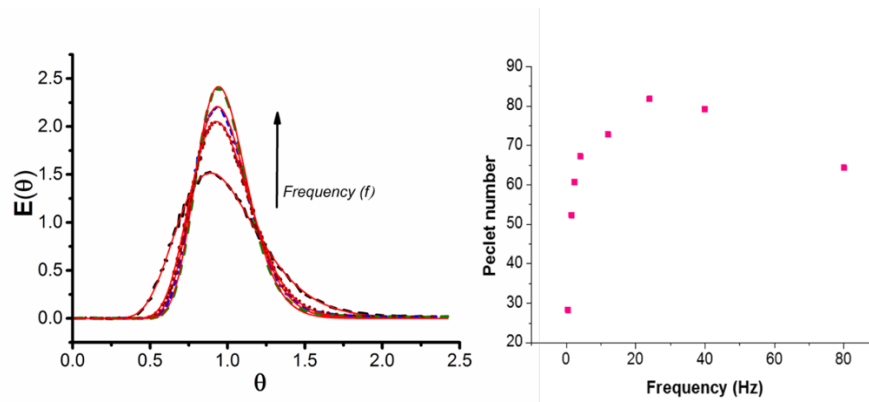


Figure 62: Examples of the axial model fit of the residence time distribution curves for experiments done in the mCOBR at oscillatory amplitude and constant flow rate of 2mm and 24Hz at a flow rate of 1ml/min, with varying flow rates of 0-80Hz. (left). The computed Peclet numbers from the model is calculated presented for the varying flow rates(right).

Similar to experiment 3.5.3.i, the axial dispersion model fitted well with the collected data. Example plots at 4 frequencies are presented in Figure 62. The Peclet number (Pe) obtained in experiment 3.5.3.ii also indicate the influence of the oscillation. With increase in frequency the Peclet number also increased up to 24Hz after which it reduced due issues resulting from the silicon separation. The range of Pe (N tanks-in-series = Pe/2) obtained was between 28 at the lowest frequency to 82 at 24Hz.

Experiment 3.5.3.iii was designed to understand the influence of the oscillatory amplitude on the fluid flow in the mCOBR. A fixed frequency and flow rate of 24 Hz and 1 ml/min at an amplitude range of 0.18 to 5.4mm were tested. The processing and acquisition parameters were kept constant as in experiments 3.5.3.i and ii. The obtained RTD curves are presented in Figure 63A and Figure 63B.
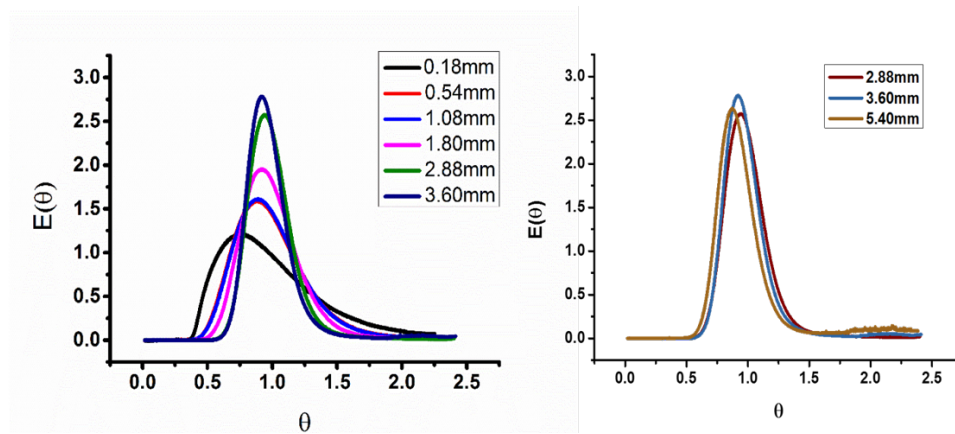


Figure 63: Residence time distribution curves for experiments carried out in the fabricated mCOBR.(left) The tested range of peak-to-peak amplitudes ranged between 0.18 – 5.4 mm at a flow rate of 1ml/min and frequency of 24 Hz . (right) The RTD curves under similar conditions and at frequency of 2.88-5.40 mm are presented separately for comparison.

Similar to the results in the lower frequency range, the amplitude range between 0.18 to 1.8mm resulted in a broad distribution of the RTD curve. Narrower RTD curves were obtained with increasing oscillator amplitude. The improvements observed with increase in the frequency and amplitude measurements, indicates a relationship between both parameters. Interestingly, at amplitudes of 3.6 mm and 5.4 mm, a deviation from the ideal curve shape was observed at the trailing

end of the distribution, as shown in Figure 63. It is worth also mentioning the relationship between the oscillatory amplitude of the fluid and the reactor and the reactor design. The inter-baffle spacing is at 4mm, hence closer to 4mm amplitude it is expected that the formation of the eddies will be disrupted negating the enhanced effects. It also became obvious after close monitoring that increasing the amplitude of the oscillation created issues in the setup. As the oscillatory amplitude was further increased, the silicon oil goes over the bulk fluid inlet, obstructing it from continuous fluid flow. This led to the splitting of the silicon oil as the bulk fluid was forced through the reactor. Comparable to the high frequency issues, plugs of silicon oil were found in the flow path and towards the flow cell. In this way, the best conditions in the mCOBR setup maximising the oscillating frequency and amplitude to operating conditions below 24Hz and 3.6 mm. It is worth noting that the concrete values are a function of the flow rates and reactor geometry.
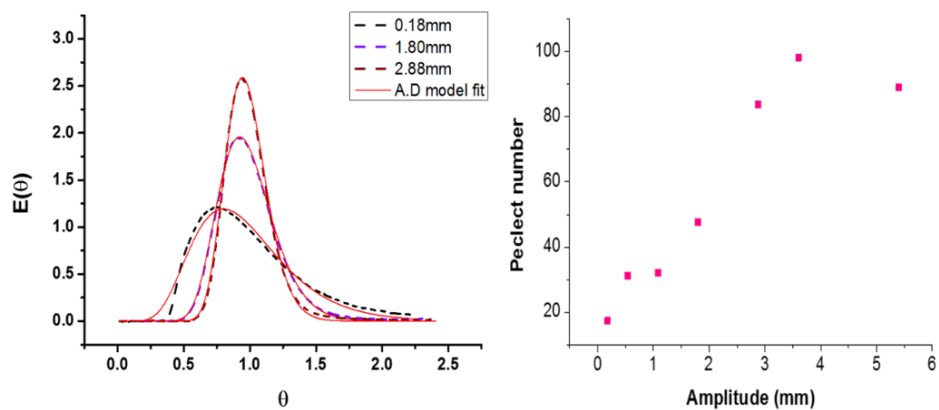


Figure 64: Residence time distribution curves for experiments carried out in the mCOBR at oscillatory frequency and constant fow rate of 2 mm and 24 Hz at a flow rate of 1ml/min, with varying amplitudes of 0.18-5.4mm (left). The calculated Peclet numbers from the model as a function of the flow rate (right).

The axial dispersion model fit for the varying amplitudes also showed good fit with the experimental data. Example axial dispersion model fitting for the change in amplitude study is presented in Figure 64. Deviation from the axial model can be seen at 0.18mm amplitude, where the curve is broad and have a skewed shape. The axial dispersion model best fits and describe conditions close to plug flow so this disparity is not surprising. The computed Peclet can be seen to linearly increase with increase in amplitude from 17 to 99. The increase in Peclet presented in Figure 64B can be seen to peak at 3.6mm and drops to 89 at 5.4mm amplitude due to the issues explained with the oscillating fluid. The dispersion effect from the peripherals was reduced by minimising the length of the tubes between the pumps, flow cell and Rheodyne valves.

As demonstrated in literature at macroscale, the RTD study carried out here showed similar effects can be achieved in the mesoscale. In other words, the parabolic flow pattern, high flow velocity at the mid regions reducing towards the walls, associated with laminar flow in a traditional tubular reactor can be affected using a reactor with a combination of the baffles and oscillation. The oscillation of the fluid and interaction with the baffles create beneficial chaotic flow patterns under laminar condition. Such that mixing eddies are created at both sides of each baffle with an upward and downward movement of the fluid. This macro mixing breaks the wall viscous effects in a tube creating even flow through the channel and achieving close to plug flow conditions. 'Soft mixing' and 'hard mixing' effects [44] can be achieved by adjusting the oscillatory parameters, frequency and amplitude as a factor flow rate, as well as the

geometry of the baffles. Using this mCOBR technology, precise mixing can be achieved in applications requiring fine processing.

### 3.5.4 Silver nanoparticle production

The rig setup for the synthesis of Ag-Np is presented in Figure 65, where the fabricated reactor was coupled with HPLC pumps, UV-Vis Spectrometer, reactants and a back pressure regulator, whilst absorbance data was being collated. The Absorbance spectra as a function of time, carried out in the mCOBR and mTR, is presented in Figure 66. Using a contour graph, the experiment time vs the wavelength spectra is also presented.
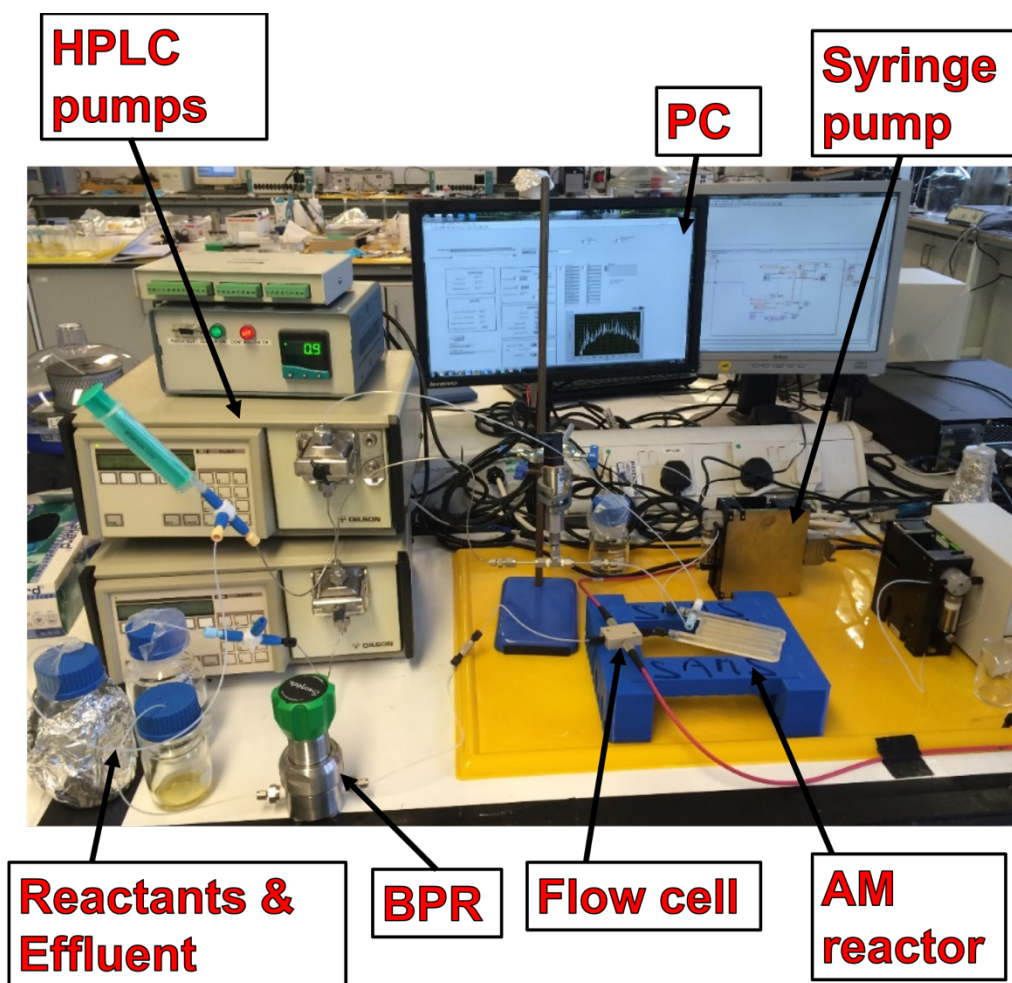


Figure 65: Experimental setup of continuous silver nanoparticle synthesis in the mTR and mCOBR. This comprised of two HPLC pumps employed to pump NaBH4 and AgNO3, a syringe pump for fluid oscillation, a flow cell, light

source and UV-Vis spectrometer for flow monitoring and a back-pressure regulator.
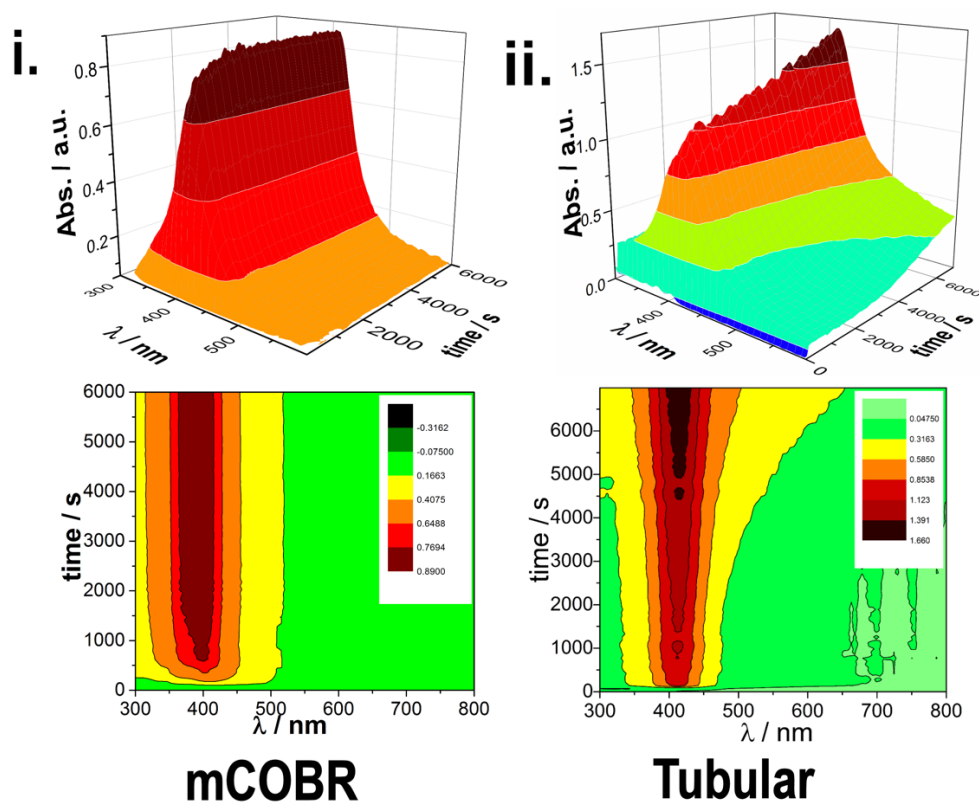


Figure 66: Time series extinction UV-Vis spectra collected at 10 secs intervals for 10min. Side view (above) and Top view (below) are presented for i) the mCOBR ii) mTR

From the time series spectra of the mCOBR under oscillatory conditions, a sharp peak wavelength of around 400nm could be observed. This indicated the presence of silver nanoparticles, as its surface plasmon resonance peak wavelength ranged from 400nm to 530nm depending on its size. When the process achieved steady state, around 25 min, the shape of the curve can be seen to be very stable up to 100 min. The spectra of the mTR, on the other hand, can be seen to continuously broaden and increase in absorbance. The broadening is

a clear signal of scattering from the nanoparticles due to the increase in the particle size over time. This points to agglomeration of the particles in this reactor. Steady state was not achieved in this reactor. For further insight, the spectra were analysed in more detail.

The spectra were modelled with a Lorentzian type function (Equation 3.6.1), as it is known to fit UV/Vis spectra of Ag, Au and Cu nanoparticles. The width describes the distribution size, the concentration of the NPs is described by the intensity and the maximum absorption the average size.

$$L_{(x)} = \frac{1}{\pi} \frac{\frac{1}{2}\Gamma}{(x-x_0)^2 + \left(\frac{1}{2}\Gamma\right)^2} \qquad \text{Equation 3.5.4.1}$$

Where $x_o$ is the centre and $\Gamma$ specifies the width of the curve.

An example of an SPR spectra collected in the mCOBR, fitted to the Lorentzian function is presented in Figure 67(i). The entire time series was fitted to the Lorentzian function and the wavelength and absorbance of the peaks were plotted with time. The full width at half maximum (FWHM) of the spectra was also plotted for the series for comparison between the mCOBR and mTR, see Figure 67(ii-iv).
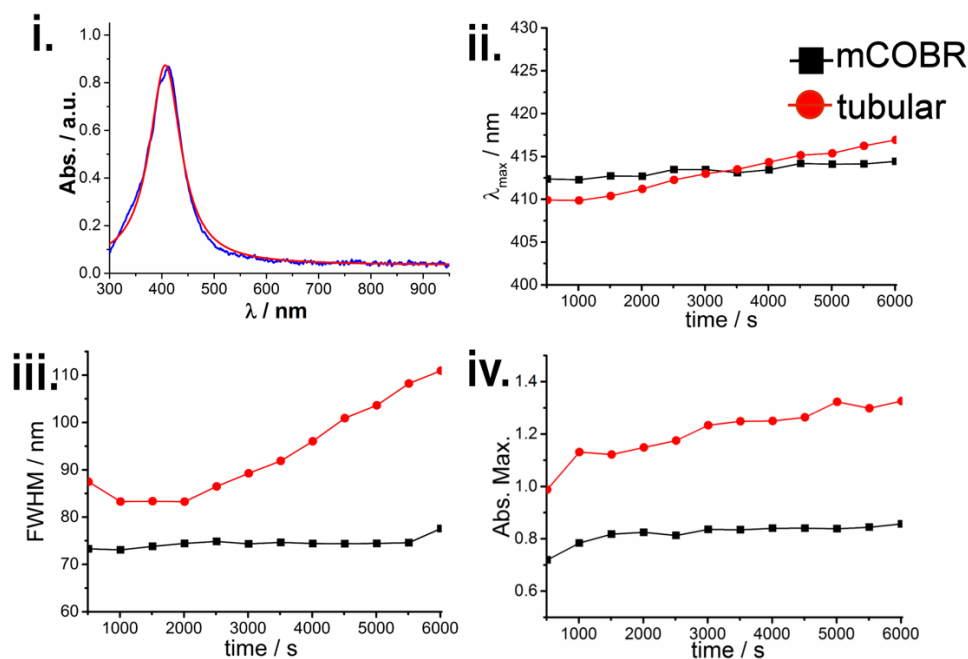
Figure 67: Comparison of the surface plasmon resonance profiles as a function of time in the mCOBR and mTR. i) An example of an absorbance spectra (blue) fitted to a Lorentzian function (red). The Lorentzian fit was then produced for the time series for the mCOBR (black square) and mTR (red circle) at 500s time intervals and analysed to produce ii) Peak wavelength iii) full width half maximum (FWHM) and iv) Maximum absorbance as a function of time.

From the presented data, the collected spectra fit well with the Lorentzian function. It is important to mention that under oscillatory conditions a smaller peak was observed at 385nm, Figure 67i, although being less pronounced in the tubular reactor. This could be due to solvent polarisation or dipole-dipole interaction of NPs. The synthesis in the mCOBR showed a remarkable stability which can be observed Figure 67i-iv. On achieving steady state around 2000s, A stable plasmon resonance can be observed at approximately 413nm, with a constant FWHM value of around 75nm and a maximum absorbance of 0.8. With

the mTR, the peak wavelength increased from 410nm to 417nm, while an almost linear shift from 83nm to 110nm of the FWHM can be observed. Similarly, the maximum absorbance increased from 1.15 to 1.35.

This supports the assumption of an increase in particle size and distribution over time, while a more stable particle size in the mCOBR. The increase in absorbance in the mTR is associated with the increase in particle size, broader particle size distribution and less regular particle geometry. The improved conditions reported in the mCOBR process can be associated to the enhanced mixing conditions previously demonstrated in the RTD data. As the process is running close to plug flow conditions, the reactants will be evenly mixed in the radial direction and have similar residence time in the reactor. This will lead to reduced fouling, more stable conditions in the reactor over time and in the controlled production of monodispersed particles.

A visual analysis of the reactors pictured in Figure 68 indicates a much-reduced fouling in mCOBR under optimised conditions compared to the mTR. It is also important to note that at conditions where the effect of the oscillation is small compared to the flow rate, the mCOBR will have an opposite effect. In such a case, the baffles will create dead zones in the reactor causing the materials to spend extended times at un-even flow concentrations.
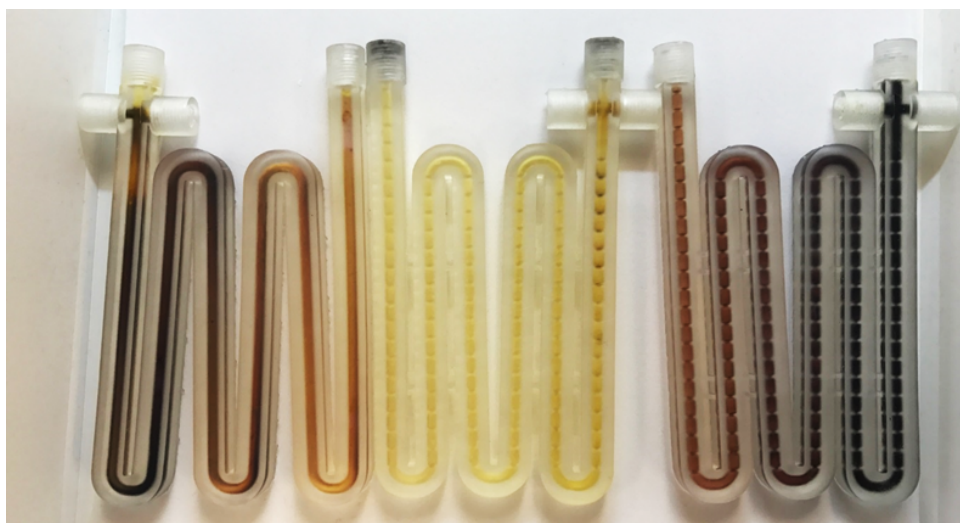
Figure 68: Visual observation of the fouling of AgNPs in AM fabricated mCOBRs and mTR. i) mTR (left) ii) mCOBR under oscillatory conditions (middle) iii) mCOBR under unoptimized oscillatory condition (right). Significant reduction of fouling can be achieved at optimised conditions in the mCOBR compared to the mTR.

This will result in fouling similar to the mTR. An example of such a case can be seen in the reactor in Figure 68(right). Under enhanced conditions in the mCOBR, silver nanoparticle production was run for a further 100 min to assess its long-term stability. The spectra obtained was consistent with the previous time series, with any apparent change after steady state was reached. There was also no visible continuous deposition on the walls of the channels.

TEM images were obtained for the samples collected at 10 min (Figure 69) and 90 min (Figure 70) after the commencement of the production process in the two reactors. The resolution of the images allowed for analysis and counting of the nanoparticles. Particle size distribution histograms of the Ag-NPs were also produced for the images shown in Figure 63.
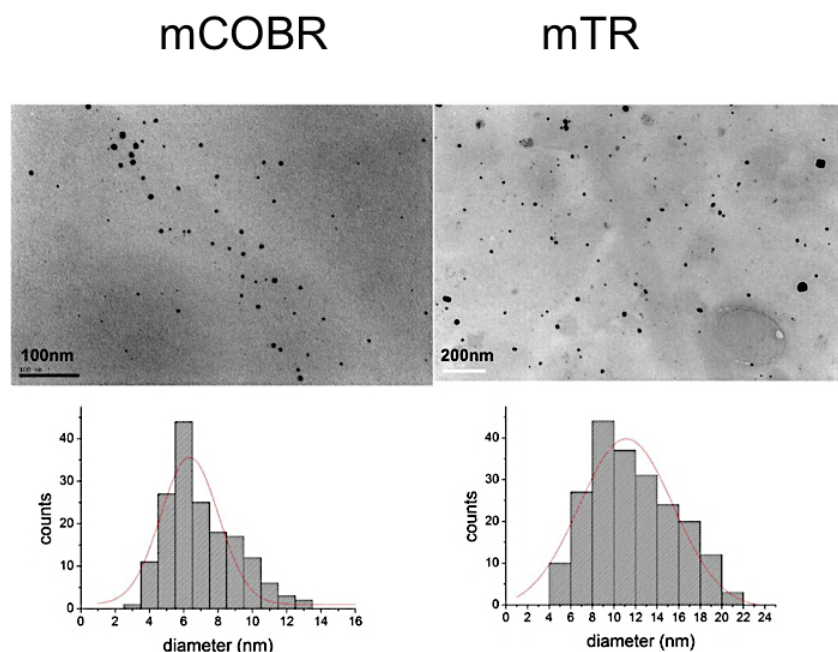
Figure 69: TEM images and histograms showing particle size distribution of the silver nanoparticles produced in the AM fabricated mCOBR (left) and mTR (right) at 10min after process initialisation.

TEM images displayed a particle size of about 4nm to 22nm diameter of Ag-NPs in the mCOBR and around 2nm to 14nm in the mTR when collected at 10 min after starting to pump the solutions. The analyses of the UV-Vis spectra as a function of time suggests that the production had not yet achieved steady state, as time series spectra in both cases showed this was achieved at 2000secs. Hence, it was expected that a broad distribution will be obtained, and qualitative improvements should be seen in the images produced at 90 min.
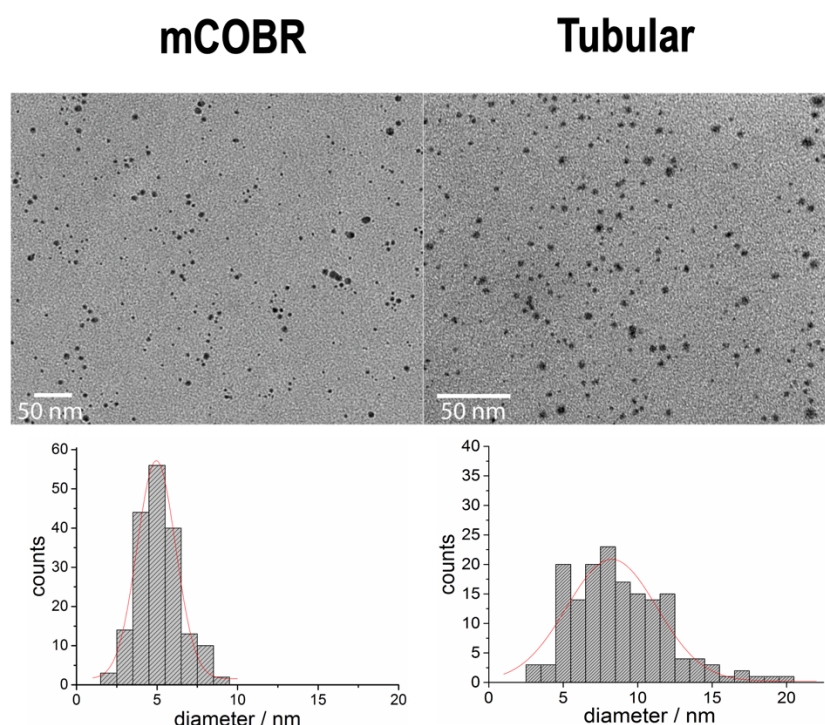
**mCOBR** **Tubular**

Figure 70: TEM images and histograms showing particle size distribution of the silver nanoparticles produced un the AM fabricated mCOBR (left) and mTR (right) at 90min after process initialisation.

The TEM images presented in Figure 70 at 90 min in the mCOBR showed improvements in the particle size distribution of the NPs but not in the mTR. TEM images displayed a narrow distribution of the Ag-NP with a particle size distribution of 5.0 nm $\pm$ 1.2nm, (mean particle size and standard deviation of the mean) when carried out under oscillatory conditions. The NPs was observed to have an evenly spherical structure with small amounts of agglomerates. However, under traditional conditions in the mTR, the NPs size was calculated to 8.3nm $\pm$ 3.0nm. In this case, larger polydispersed particles were formed with a greater portion of agglomerates. The particles obtained from the mTR were not of uniform spherical structure as seen in Figure 71.
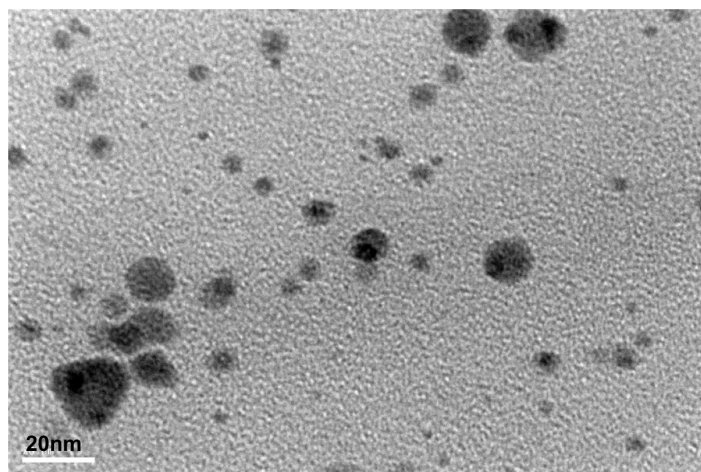
Figure 71: Pronounced TEM image of Ag-NPs produced in the mTR. Irregular particle morphologies can be observed.

Infact, the narrowly dispersed silver nanoparticle size obtained was as a result of the enhanced micro and macro mixing effects created by the interaction between the baffles and the oscillating fluid. This resulted in the controlled and stable production of small monodispersed particles and reduced fouling in the reactor. The oscillation of the fluid plays a vital role in the beneficial results obtained in the mCOBR. This was evident when the synthesis was repeated in the mCOBR without oscillating the fluid. Under these conditions, the colour of the collected sample changed to a darker brown colour, producing unstable Ag-NPs, see Figure 72. This is because the baffle will create dead zones resulting in uneven residence times without the fluid oscillation.
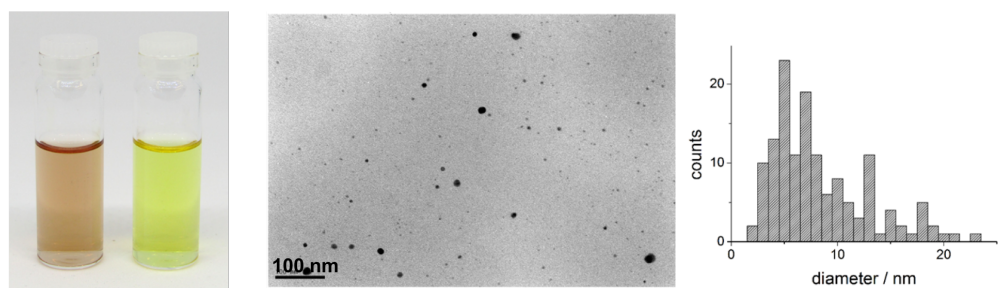
Figure 72: Ag-NPs produced in the mCOBR without oscillation. A) Collected Ag-NPs samples of produced in the mCOBR without oscillation (left) and under oscillatory conditions (right) B) TEM image of Ag-NPs produced in the mCOBR without oscillation C) Histogram of the particle size distribution in the mCOBR without oscillation.

The fouling caused a modification to the nature of the wall surface and reduction in the reactor inner diameter. Modifying the wall surface changes the nucleation points for NPs, thus resulting in uncontrolled growth in the particle size. As such, a method of cleaning the reactors for reuse was investigated. Careful flushing of the reactor with Aqua Regia, a strong acid, was found the remove the deposited silver particles. This was followed by extensive washing of the reactor with deionised water. The washing process recovered the reactor to its original physical appearance. However, when the reactor was reutilised in the synthesis of Ag-NPs, a shift of the plasmon resonance was observed to 425nm, Figure 73. This is presumably due to the modification of the polymer surface of the reactor wall.
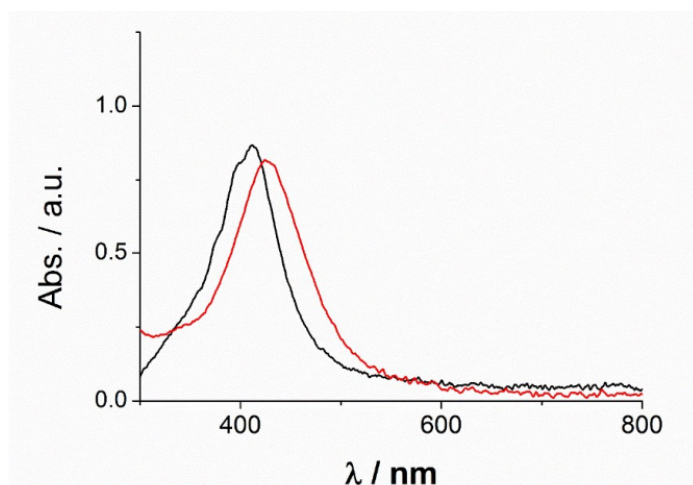
Figure 73:UV-VIS spectra of Ag-NP produced in a fresh mCOBR(black) compared to one which was reused by washing with aqua regia (red).

## 3.6 Summary

The development of an AM mesoscale continuous oscillatory baffled reactor with enhanced mass transport was demonstrated in this chapter. An AM technique, vat polymerisation, aided the low-cost (less than £5,000 equipment cost, mCOBR material cost: £8.24) fabrication of mesoscale flow reactors with complex structures in the flow path. The benefits of the continuous oscillatory baffle technology in the mesoscale was shown using residence time distribution studies. These benefits were further demonstrated in the continuous formation of silver nanoparticles. The enhanced mass transport presented will be valuable in various applications involving fine controlled processing of chemicals and nanostructured materials. This was reported as the first example of a miniaturised continuous oscillatory baffled reactor manufactured by a vat Polymerisation AM platform. The scale of reactors presented in this chapter bridges an important gap between industrial scale and microfluidic laboratory scale, speeding up the discovery to manufacturing utilising AM. The simplicity, continuous development and adoption of AM techniques, will foster the development of a plethora of advanced reactor engineering applications in continuous advanced material manufacturing process.

The following conclusions have been made from the research work carried out in this chapter:

- Vat polymerisation (VP) AM method on the tested platform served as valuable tool to manufacture 3-dimensionally complex flow reactors.

- Fabricating near net shape flow channels without blockages by vat polymerisation is influenced by process parameters such as build

orientation, layer resolution, channel diameter and the quality of the optical window.

- The most suitable conditions for fabricating flow devices on the Form 2 platform was at a layer resolution of 50 μm and 45º to 90º to the build bed. Using these parameters and under conditions demonstrated in this chapter, flow devices as low as 0.8mm ± 77 μm inner channel diameter were achieved. In this way, there is also minimal contact of the laser in the channel thus minimising polymerisation of loose material in the channel.

- Although it is known that the specifically designed baffles coupled with the oscillatory flow had improved benefits, the effects was demonstrated for the first time at this scale (2.5mm diameter) using AM.

- Using the flow setup presented, the best conditions near plug flow, at flow rate of 1ml/min, was at frequency and amplitude of 24Hz and 3.6mm, although this will change with respect to flow rate.

- TEM studies showed small and narrowly dispersed particles (5.0 nm ± 1.2nm) were produced in the mCOBR with good stability of up to 200 min from collected UV/Vis spectra, compared to the test in a conventional tubular reactor.

- Fouling in the reactor was visually largely reduced due to micro and macro mixing created in the reactor by the oscillatory effects.

# Chapter 4 Continuous-flow crystallisation in AM mesoscale flow reactor.

## 4.1 Introduction

Crystallisation is a key unit operation in the pharmaceutical industry and other high added value industrial processes [103]. The synthesis of reproducible and highly controlled crystals is critical for polymorphism and processability [104]. Polymorphic forms can display markedly different physicochemical properties such as density, chemical stability, solubility, hardness, melting point, rate of dissolution, hygroscopicity and interaction with biological systems [105]. Polymorphism in drug development is an important area of study as it contributes to the variability in active pharmaceutical ingredients (APIs), posing a challenge to scientists. Statistically, 50% of APIs have multiple forms, while 85% exhibit (pseudo)polymorphism [105], which opens challenges to the engineering of 'tailor made' properties of an API. General selection criteria during an API development process aim for polymorphs with thermodynamic stability, good solubility and dissolution rate, non-hygroscopic and block-like habits for ease of manufacturing [105, 106]. Current knowledge on nucleation and crystal growth mechanisms and process are still insufficient to ensure precise control of formation and polymorph disappearance or phase transformation [107].

Paracetamol (PC) is a widely used analgesic and antipyretic, which is commonly used to relieve aches and pains. It makes up part of cold and flu remedies and has been extensively studied in its solid state [108]. PC crystallises in three

different polymorphs: Stable form I (monoclinic), metastable form II (orthorhombic) and unstable form III. Two other polymorphic forms are only accessed at high pressure. The layered structure of form II and the notably well-defined slip planes facilitate compressibility facilitating tableting and packaging, and increased solubility which improves bioavailability [109, 110]. There have been extensive studies in the production of both forms of paracetamol in both batch [110, 111] and continuous crystallisers: COBC [42] and MSMPR [112-114]. Studied routes for the selective crystallisation of form II paracetamol include swift cooling [115], reaction coupling [114], enforcing Ostwald's rule of stages [116], heterogenous nucleation [117], use of polymer additives [118, 119], separation in gel matrix [120] and multicomponent templating [109, 121]. Wilson *et al*. [121] demonstrated a new multi-component crystallisation route to selectively produce polymorphic form II by using auxiliary molecules, including benzoic acid derivatives and metacetamol (MCM), to perturb the solution environment encouraging its formation. Although the effect and mechanism of templating agents on the crystallisation process is not completely understood, it is proposed that the MCM affects the solution mediated phase transformation (form II to form I) that occurs during cooling [109]. It is also noted that the presence of the templating agent, MCM, has the effect of widening the metastable zone width of PC crystallisation.

Traditionally, batch crystallisation is the methodology most widely employed. However, batch to batch variability and mixing inefficiencies are important limitations. Continuous crystallisation offers rapid heat transfer and mass transfer benefits, as well as eliminating down time between batches [3, 42].

Continuous crystallisation processes can improve control of product properties and save production costs by up to 40 % [122].

There are important studies of continuous-crystallisers at the macroscale [123, 124]. However, the requirements for intensified mesoscale devices able to combine scalability and flexibility are very important for the development of industry 4.0 applications. Mesoscale devices might suffer from poor mixing as the dimensions are too large to ensure efficient mixing by diffusion and the crystalliser volumes are too low to enable residence times required for crystallisation at the high flow rates required to generate turbulent flow. Hence, the utilisation of advanced strategies to induce turbulent mixing at low flow rates represents a key requirement to develop efficient processing. However, the employment of traditional manufacturing techniques to generate necessary advanced features, such as baffles, is complicated.

The application of AM to manufacture continuous-flow devices has attracted a great deal of interest in recent years [60, 125]. AM can be employed to generate advanced meso-scale continuous-oscillatory baffled reactors for the controlled synthesis of nanoparticles, as demonstrated in Chapter 3 and the associated recent publication [40]. It was hypothesised that AM can be employed to generate advanced flow crystallisers. AM has two main potential benefits in mesoscale crystallisation process: i. enhanced mass transport with complex mixing architectures; ii. controlled heat transfer properties by designing the geometry of the crystalliser and the materials of construction. For instance, polymer materials have intrinsically low heat transfer coefficients which can

allow gentle heating and cooling profiles. In this chapter, the first example of utilising an AM vat polymerisation technique to develop advanced devices with applications in continuous-flow crystallisers is presented. The crystallisation of paracetamol is demonstrated as a benchmark.

### *Crystallisation: Nucleation and Growth*

Nucleation and growth of crystals are driven by supersaturation. On dissolution of chemicals in a solvent, the solution must be supersaturated for nucleation to occur. Supersaturation ratio $\beta$ is the ratio of the concentration of the solute in solution $C_i$ and its saturated concentration $C_s$. Hence $\beta > 1$ indicates crystal growth, $\beta = 1$ shows that crystals and solvent are in equilibrium, and $\beta < 1$ shows that the crystals are dissolving. Nucleation is the prerequisite for crystal growth to occur. If a solution reaches a state of supersaturation, nuclei are formed in the bulk solution. Homogenous nucleation occurs when the nuclei are formed in the solution, while for a heterogeneous case, the nuclei are formed from substrates such as reactor walls or solid particles. Secondary nucleation on the contrary, occurs in the presence of existing crystals. The rate of solid formation in a supersaturated solution is dependent on external growth conditions such as temperature, hydrodynamics, degree of saturation and solvent medium; and internal factors such as structure bonds and defects [126]. Sharp steps between each temperature-controlled zone can lead to spikes in supersaturation resulting in unwanted nucleation and variation of the products. The solubility of the material in the solvent also plays an important role, as the higher the solubility, the higher the growth rate. The growth rate slows down as the solvent is adsorbed by the crystal faces. The rate of growth is also dependent on the

141

hydrodynamics of the system as in a still solution, the face grows at the slow rate of diffusion of the solute towards the crystal. Control of the crystal formation can allow the control of the crystal size distribution and polymorphs in the product stream.

*Polymorphism in APIs*

Polymorphism refers to the different structural forms a chemical substance can exist. It is defined as the ability of a molecule to exist in more than one crystalline form having different packing arrangement or conformation of its lattice structure [127]. The various polymorphs display marked physicochemical properties such as density, chemical stability, solubility, hardness, melting point, rate of dissolution, hygroscopicity and interaction with biological systems [105]. Polymorphism in drug development is an area of important study as it has contributed to the variability in APIs, posing a challenge to scientists. Statistically, 50% of APIs have multiple forms, which opens challenges to the engineering of 'tailor made' properties of an API. Though APIs should ideally exist in a single form i.e monomorphic, this is not the case. Important pharmaceutical compounds that have been studied for polymorphism include: Aspirin, Acetominophen, Atorvastatin, Ritonavir and Axitinib. A popular example is the case of the anti-HIV drug, Ritonavir, where two conformation polymorphic forms were later discovered having significantly different solubility properties. Although the form II has a more stable packing arrangement, it was only coincidentally discovered due to a highly supersaturated solution (400%) with the presence of a nucleation enhancer [128]. Hence, the understanding of particular solid state of a molecule at all

process stages, is specifically important in API development. This can be achieved by the knowledge of the thermokinetics and thermodynamic stability of the compound coupled with the understanding of the transformation process and time required [129]. General selection criteria during API development process aim for polymorphs with thermodynamical stability, good solubility and dissolution rate, non-hygroscopic, compact morphology and ease of manufacturing. More often, the production of polymorphs bring about challenges, such as 'disappearing' polymorphs and variation in properties of polymorphs from similar batches [105, 106]. Polymorph phase transformation, which accounts for the disappearing and complex transformation, make distinguishing, detecting and monitoring difficult. Since the most stable polymorph has the lowest solubility, a basic method to differentiate between polymorphs is to measure their solubility in a similar solvent. Dimorphic (two polymorph) systems can be enantiotrophic, where the solubility curves cross each other at a lower temperature than the melt temperature of the two polymorphs. This represents the transition temp (Tr). The stability of the polymorph is dependent on being either before or after the transition temperature, as seen in Figure 74.
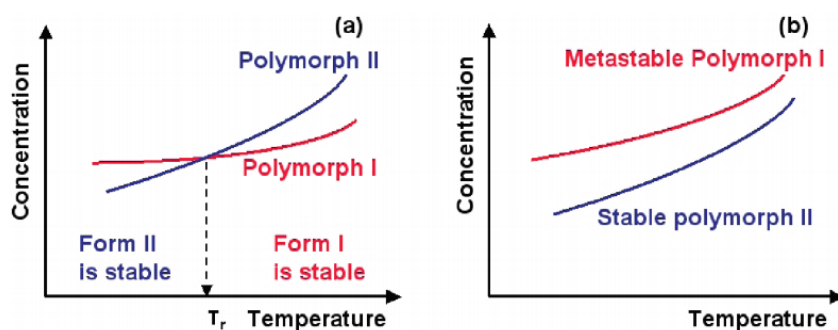


Figure 74: Solubility curves for form I and II polymorphs, a) Enantiotropic b) monotropic [126]

The polymorphs are considered to be related monotropically if the solubility curves of the polymorphs do not cross. In this case, the polymorph II is more stable than I. At a specific temperature, form II is more stable than form I, while having the lowest free energy. Understanding the relationship between polymorphs will allow the selective production of a pure form of a single form. Using swift cooling technique, Sudha and Srinivasn (2013) demonstrated that the induction period of all three polymorphs decreases with an increase in the degree of supersaturation of the solution, with the unstable (form III) having the shortest period [106, 115]. The report also showed that the range of supersaturation played a role in the percentage nucleation of the different polymorphs. PC mono (form I) was observed to have 100% nucleation at a lower supersaturation range of 0.10-0.83 which suddenly decreased. At s = 0.92-1.25 the nucleation was observed to yield 100% for Ortho (form II), which later dropped with rise to similar yields in the unstable polymorph from 1.28, Figure 75.

Understanding the behaviour of these polymorphs under different degrees of supersaturation, temperature and in solution with other materials can allow the selective production of a desired polymorph allowing the engineering of required properties.
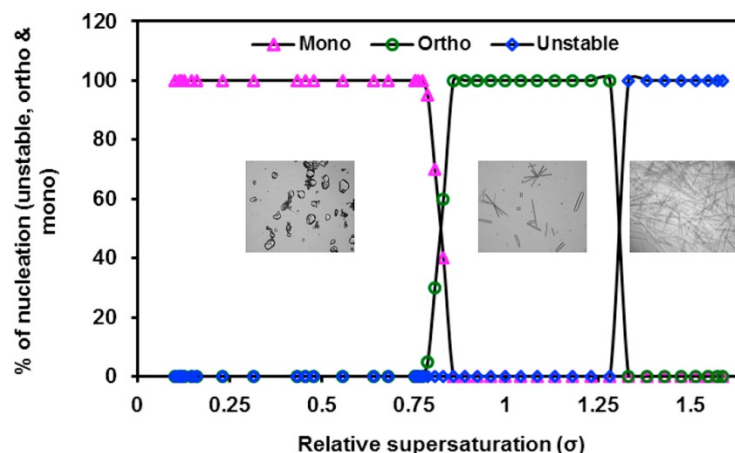
Figure 75: Percentage variation of nucleation with relative supersaturation. [106]

*Multicomponent templating*

In the multicomponent templating process, a different polymeric form is obtained by using a co-molecule to perturb the solution environment encouraging its growth [121]. An API, in this case Paracetamol, is mixed in solution with a templating agent and then crystallised. In this way, the templating agent, a molecule included in the crystallisation process, forces the adoption of a different polymorph without being present in the crystal structure of the final product, Figure 76 [42].
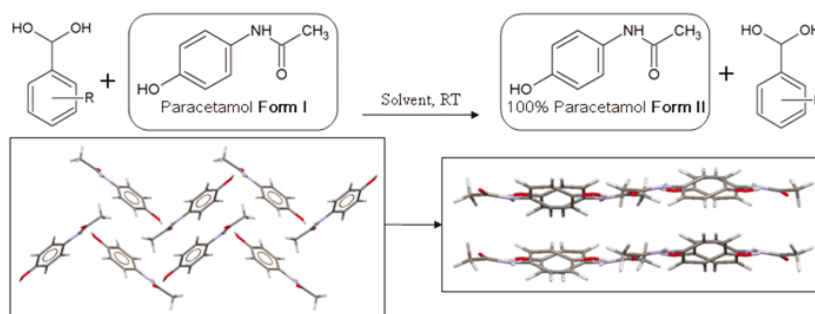


Figure 76: Multi-component templating of paracetamol for the conversion of form I to form II

It is understood that for 100% purity to be achieved using such an approach, the selected solvent and co-former play an important role. Wilson and colleagues work presented a detailed exploration of co-crystallisation of Paracetamol in a range of co-formers: Benzoic acid and halo-substituted benzoic acids (4-BrBA, 4-ClBA, 4-FBA, 3-BrBA, 3-ClBA, 3-FBA, 2-BrBA, 2-FBA) and solvents: Ethanol, Methanol, Acetone, Acetonitrile and Isopropanol [121]. The authors found that increased ratios, 1:1 of 4-substituted benzoic acid to paracetamol, produced the most repeatable production of form II at 100% purity. The importance of producing 100% pure form II was highlighted, as samples collected with a mixture of polymorphs all converted to form I after a period of time. Although high yields of form II was obtained using BA in the co-crystallisation process, utilising higher wt% of the co-former will lead to a further separation step. A more recent paper by Wilson demonstrates the utilisation of Metacetomol (MCM) $C_8H_9NO_2$ in the crystallization process where the co-former is not present in the collected product [109]. This is because MCM displays a much higher solubility in the chosen system, hence higher concentration can be used aiding system scale-up, without the need for further separation processes. Change in the crystal shape of pure PC has also been reported using small amount of MCM from tabular to column habit [130]. An increased dissolution rate with a positive benefit on drug delivery was also reported alongside. This means that the rate of drug release will be faster, enhancing bioavailability. Although the effect and mechanism of templating agent on the crystallisation process is unknown, it is proposed that the MCM affects the solution mediated phase transformation (form II to form I) that occurs during cooling [109]. It is also suggested that the presence of the templating

agent, MCM, has the effect of widening the metastable zone width of Paracetamol.

### *Crystallisation process monitoring*

A key issue with many pharmaceutical crystallisation processes is relatively poor reproducibility. In 2004, the US Food and Drug Administration (FDA) initiated the process analytical technology (PAT) concept to encourage the drive towards and implementation of real-time quality testing as opposed to off-line methods [131]. New monitoring technologies has been shown to minimise issues with reproducibility while allowing precise control. Extensive studies on inline/online measurements using bespoke analytical tools have also been shown in monitoring PC polymorphs. Inline process analytical technologies (PAT) have been utilised in monitoring paracetamol production, with a combination of focused beam reflectance measurements (FBRM) and infrared (IR). FBRM is a powerful tool in the crystallisation process as it provides information on the shape and size of crystals produced in-line. Rousseau (2008) demonstrated the tracking of chord lengths using FBRM in a batch cooling crystallisation process to show solution-mediated phase transformation (SMPT) from PC form II (needles) to form I (octahedral) [132]. A recent publication by Wilson (2017) shows the utilisation of FBRM and Raman in two reactors: mixed-suspension, mixed product removal (MSMPR) and continuous oscillation baffled reactor (COBR) for Paracetamol cooling crystallisation. In their report, the authors showed the use of these two characterisation techniques in the selective production of form II. Analysis of important peaks in the Raman spectra, serving as individual polymorph finger print, was utilised in the in-line monitoring [42].

On the other hand, Wang (2015) studied the batch cooling crystallisation process of paracetamol using in-line NIR spectroscopy [110], while Braatz (2002) utilised Laser back scattering and attenuated total reflection (ATR)- Fourier transform infrared (FTIR) in identifying SMPT [111]. Using these technologies can allow the real time control of process flow rate, concentration or temperature to achieve desired product yields. PAT probes can however be expensive and challenging to setup and optimise. Moreover, current PAT probes will require extensive modification to be used in mesoscale flow reactor applications. A major challenge in inline measurement with PAT probes is fouling during crystallisation processes. Mechanical wipers and brushes have been widely used to counteract fouling and deposits on the optical window. Figure 77 shows a mechanical wiper fitted to a commercial ParticleTrack FBRM C35 probe and an Infinity CLW fluorescence/turbidity/temperature immersion probe [133]. Such mechanical cleaning methods will be difficult to implement in smaller scale probes required for mesoscale reactors. Hence, inline monitoring of mesoscale crystallisation processes can be challenging.



Figure 77: (left) Mechanical scrapper at the tip of a commercial ParticleTrack FBRM C35 probe and an Infinity CLW fluorescence/turbidity/temperature probe [133].

Characterisation of paracetamol polymorphs in their solid state is normally carried out by powder X-ray diffraction (PXRD), single crystal X-ray diffraction, differential scanning calorimetry (DSC), thermogravimetric analysis (TGA) and FT-IR [108, 134]. PXRD serves as the 'Gold' standard for phase identification and it usually shows clear distinctions between polymorphs. Single crystals can be prepared and individually identified using a single crystal x-ray diffractometer. This technique measures the distinct crystal structure of individual crystals. DSC, TGA and IR data aid to complement PXRD information. DSC can provide information on thermodynamic relationships, TGA provides information on the stoichiometry of solvates/hydrates while IR [135] can serve as a complementary phase identification method by observing the molecular interactions. The degree of crystallinity of the collected samples is usually measured by computing the ratio of the melt enthalpy to the enthalpy of a reference standard [118].

### Batch and continuous crystallisers

In the pharmaceutical industry, the crystallisation process has traditionally and more frequently been performed in batches. Regulations have driven the crystallisation processes towards batch mode, as it has simply been run the same way for decades [122]. Also, batch production allows quality verification to be carried out for a single batch of product made before further processing, whereas in a continuous process the 'batch' is not contained similarly [136]. However, with the technological developments in process analytical tools (PAT), real-time quality checks can be carried out in continuous production systems. Moreover, although batch crystallisation has been extensively studied, batch to batch

variability and process inefficiencies still exist. Continuous crystallisation offers rapid heat transfer and mass transfer benefits, as well as a reduced down time between batches [3, 42]. Continuous crystallisation processes can improve control of product properties and save production costs by up to 40% [122]. Continuous crystallisers are divided into two main types: mixed-suspension, mixed-product removal (MSMPR) and continuous tubular crystalliser [137]. A schematic of the two crystallisers is presented in Figure 78, while examples of continuous crystallisers is presented in Figure 79. MSMPR comprises of vessels connected in series, where the mother liquor stream is recycled to the system, allowing the residence time for the mother liquor to be longer than the solids [138]. Conversely, a continuous tubular crystalliser, comprises of tubular channels where controlled nucleation and crystallisation is stimulated.
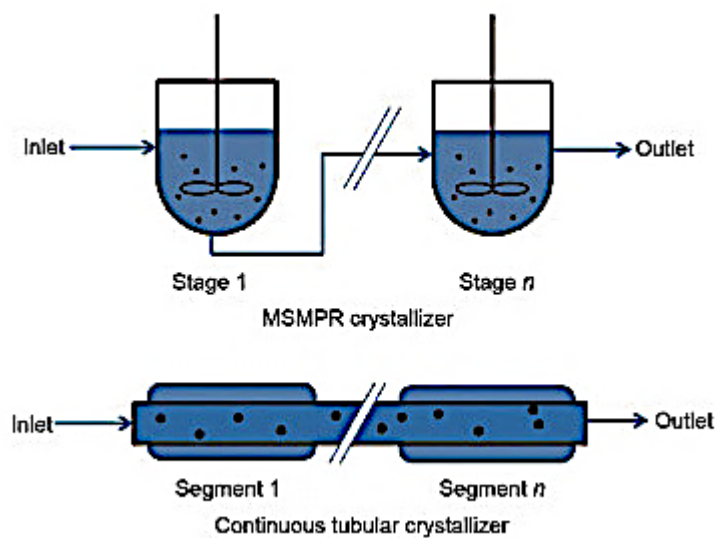


Figure 78: Schematic of a MSMPR crystalliser and a continuous tubular reactor [137].

Advantages of a MSMPR include low cost of simpler equipment and ease of maintenance, while a tubular crystalliser allows for higher efficiencies to be

achieved, narrower residence time distribution and ease of scale up [139]. Tubular crystallisers are more beneficial for processes requiring short residence time and high conversions. Although tubular reactors can generally be highly beneficial for application requiring precise mixing, their use in crystallisation applications can be challenging. These challenges include process control difficulties and blockages as a result of crystal growth and fouling. Hence, several techniques have been explored to enhance control of crystal growth and minimise blockages. This includes segmented flow, which has been shown to narrow residence distribution, therefore resulting in narrow crystal size distribution [140]. In segmented crystallisers, slugs are created by controlled flow of slurry and an immiscible fluid or air. As the slurry in each slug flows through the reactor, this leads to a mixing vortex formed in each cell [141]. This leads to complete mixing in each cell and control of residence time in the crystalliser as even residence time is achieved in each slug [142]. A continuous oscillatory baffle crystalliser (COBC) is a modification of a tubular crystalliser that allows enhanced mass transfer and heat transfer [42]. COBCs are plug flow crystallisers that consist of a series of jacketed tubes with baffles periodically spaced. The interaction between the baffles and the oscillation of the fluid create eddies, which aids advection [123]. The oscillatory effect suspends crystals during growth as it flows through the reactor. Mixing effects generated by the oscillation can be controlled by changing a combination of the oscillatory frequency and amplitude. Varying the oscillatory conditions can lead to a range mixing conditions effecting the nature and size of crystals produced [123]. Other tubular crystalliser designs exist with varying internal structures: helical mixer [124] smooth periodic constrictions (SPC), multi-orifice baffle [123].
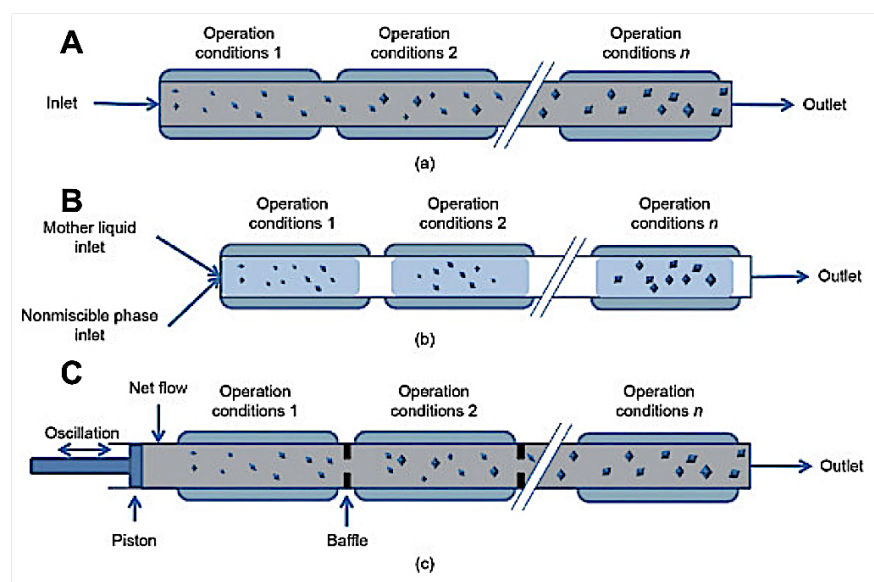
Figure 79: A) Tubular crystalliser B) Segmented flow crystalliser C) Oscillatory baffled crystalliser [137]

*AM for mesoscale crystallisation*

As discussed in previous chapters, manufacturing flow reactors with static mixers is highly complicated and, in most cases, impossible using conventional manufacturing techniques. AM can aid the fabrication of such complex structures. The previous chapter has shown the first example of a mesoscale advanced flow reactor. The reactor was utilised in the synthesis of Silver nanoparticles (Ag-NP) and the studies found that the oscillatory effects enhanced mass transport through the reactor improving the Ag-NP size distribution. Accordingly, similar improvements can be achieved in a crystallisation process. AM has two main potential benefits in mesoscale crystallisation process: i. Enhanced mass transport with complex mixing architectures e.g oscillation in baffled flow path induces advection and suspension of particles ii. Fabrication of crystallisers in a wide range of materials. e.g polymer crystallisers allow a slower rate of heat transfer, hence a

152

less steep cooling gradient can be achieved for crystallisation processes. To the best of my knowledge, development of AM crystallisers has not been previously explored.

## 4.2 Objectives

The aim of this chapter is to demonstrate the feasibility of utilising AM to develop advanced devices for continuous-flow crystallisation. The key hypothesis is that AM can be employed to generate a flow crystalliser with the potential benefits of enhanced mass transport and heat transfer which can be incorporated with the introduction of complex mixing architectures. As a proof of principle, the formation of Paracetamol crystals using in-line and off-line techniques in the uniquely fabricated crystalliser under varying cooling profiles was investigated. The objectives included:

- To study the feasibility to design and fabricate an AM mesoscale crystalliser allowing for in-situ temperature and process monitoring.

- To develop a test rig and acquisition methodology to characterise the heat transfer in the AM mesoscale crystalliser.

- To develop a test rig for in-situ temperature monitoring of the cooling crystallisation process of Paracetamol.

- To model and characterise the heat transfer in the manufactured reactor at varying process conditions.

- To characterise the crystallisation of Paracetamol under varying process conditions by in-line and off-line techniques.

## 4.3 Methodology

Experimentation in this chapter investigates the development of a mesoscale crystalliser by AM for the production of Paracetamol crystals. Firstly, the fabrication of a crystalliser by AM was studied. Then, heat transfer studies in the crystalliser were carried out using a designed set up. Finally, paracetamol crystallisation studies at varying process conditions were performed using both in-line and offline techniques.

### 4.3.1 Design and fabrication of an AM crystalliser

*Design process*

To explore the feasibility of manufacturing an AM cooling crystalliser device for paracetamol crystallisation, a systematic approach was implemented. It was crucial to follow the design flow process, Figure 80, in order to obtain a fully functional reactor to meet the intended requirements. The reactor design was based on the volume to achieve required residence time, wall thickness, connector sizing and configuration, cooling chamber volume and number of temperature sensing ports. The dimensions of the parameters are listed in Table 13. The final design was then configured for manufacturing on the AM platform using the process parameters explored in the previous chapter. The thickness of the reactor wall impacts the rate of heat transfer to the reacting fluid. A large chamber volume ensures there is a minimal drop in temperature due to heat loss to the fluid. Different inlet-outlet connector configurations were trialled for the heat transfer studies and crystallisation.
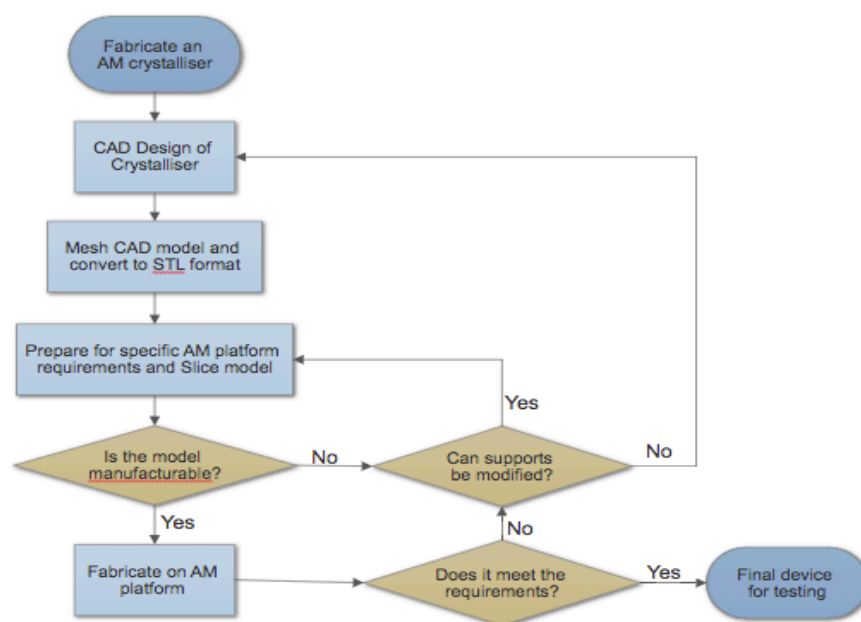
Figure 80: Design flow to achieve desired reactor geometry

Table 13: Reactor design parameters

| Parameter | Units | AMC-I | AMC-II |
|---|---|---|---|
| Reactor Volume | mL | 2.08 | 2.95 |
| Inner diameter $D_i$ | mm | 2.1 | 2.5 |
| Outer diameter $D_o$ | mm | 9.0 | 9.0 |
| Wall thickness | mm | 3.45 | 3.25 |
| Cooling jacket $V$ | mL | 158 | 170 |
| Reactor dimensions | mm | 155x118x32 | 165x118x32 |
| Thermocouple ports | ZEA | 14 | 4 |

Similar to the AM reactor in Chapter 4, the reactor was designed on Creo Parametric, a Computer-aided design software. The reactors used for characterisation varied between 2 and 3mL. A STL file of the designed model was then sliced on PreForm software to prepare for fabrication. The designed

reactor was orientated at 45º to the build plate and sliced to be fabricated at 50 micro-meter layers per scan. The reactors were produced on a Formlabs Form2 vat Polymerisation platform using proprietary Clear resin RS-F2-GPCL-04.

The crystallisers were designed for modularity. Hence, several crystallisers can be stacked in series to increase the residence time if required. It was also designed to allow for safely locking several crystallisers in place to avoid movement. Several ports (14) were also designed to allow for temperature monitoring along the length of the tube, Figure 81 and Figure 82.
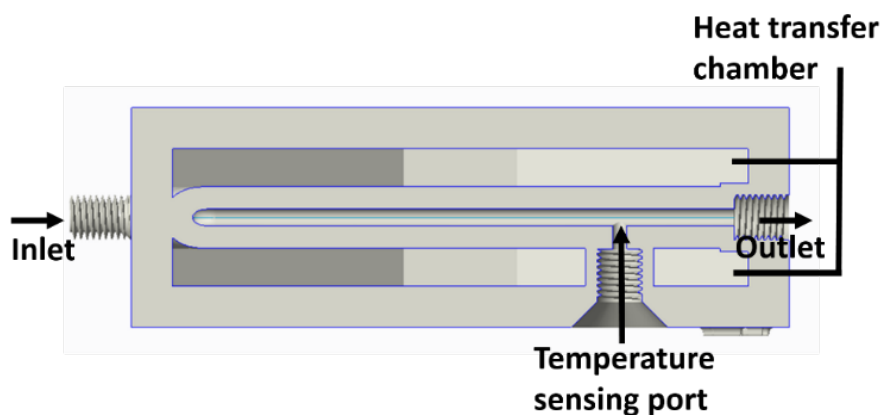


Figure 81: Crystalliser design features
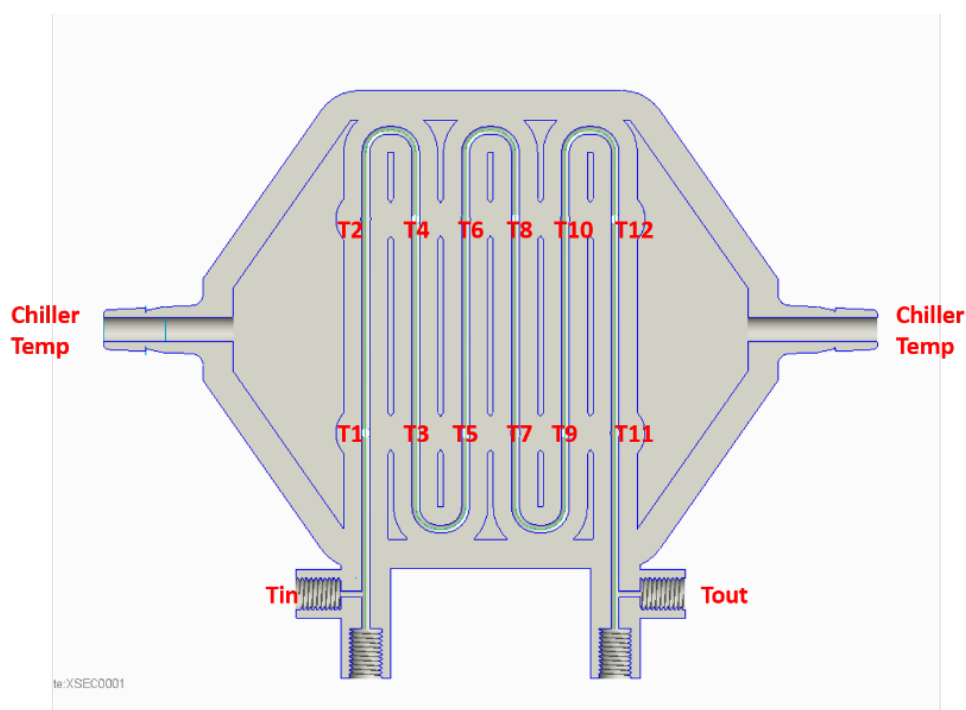
Figure 82: Designed temperature monitoring ports evenly spaced along the crystalliser channel and ports to allow for heating/cooling by a recirculating chiller.

Two reactor designs were used in the crystalliser study. For the heat transfer experiments, a 2.1mm (ID) crystalliser, AMC-I, Figure 83, was designed with 14 temperature points, reactor volume of 2.08mL, inner and outer diameter of 2.1 mm and 9 mm respectively, a heat transfer chamber of 158.52mL with 1/16" connector inlet and outlet ports. The 14 thermocouples were placed at regular intervals (46 mm, equivalent to 0.16 mL) spanning from the inlet to the outlet of tubular channels. The thermocouple connectors were designed to be in constant contact with the fluid flowing into the crystalliser at room temperature whilst monitoring the heat transfer as an effect of the jacketed fluid.
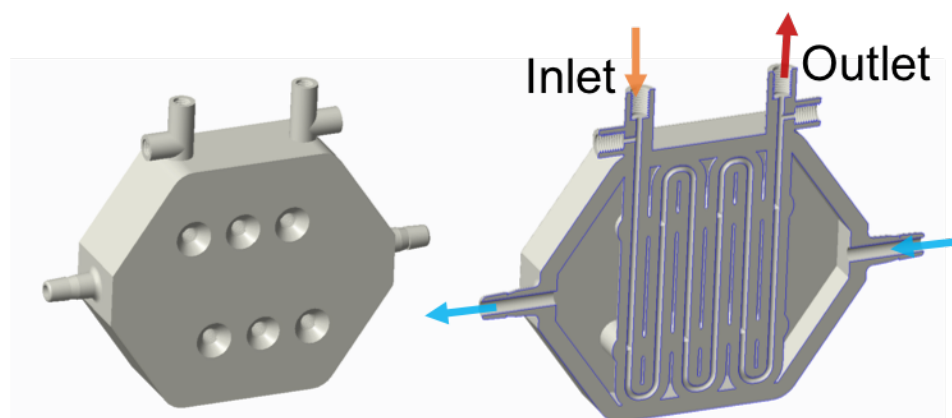


Figure 83: Designed mesoscale crystalliser for heat transfer characterisation AMC-I. Orange and Red arrows indicate flow through the reactor, while blue arrow shows flow path in the heating chamber.

As longer residence times were required for the crystallisation study, a modified version of the AMC-II was designed. The later design allowed for modularity as several devices can be interconnected allowing for longer residence times to be achieved. Also, this allowed for each device to be fitted with a single chiller in series or different chillers which could operate at different required temperatures. The geometry of AMC-II, Figure 84, was differentiated by the number of temperature sensing ports (4), inner diameter (2.5mm), slightly larger chamber and the male-female 1/16'' ports on opposite sides of the device.
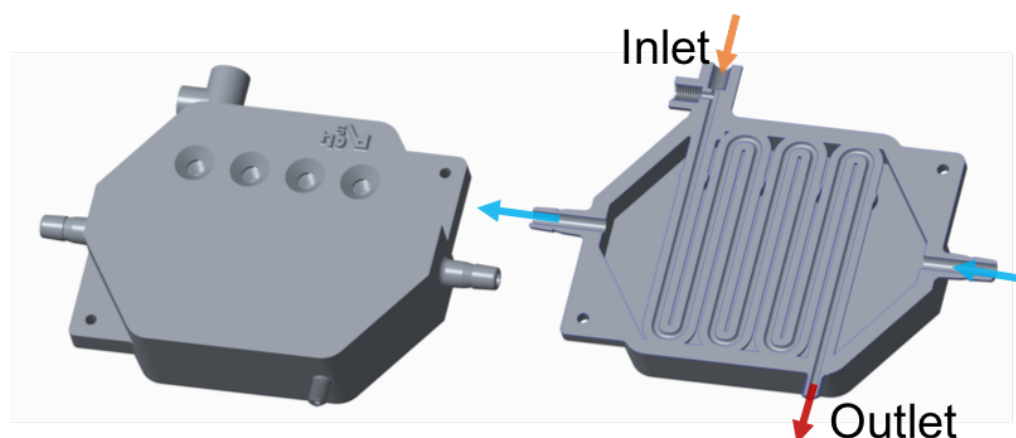


Figure 84: Modular crystalliser designed for paracetamol cooling crystallisation study. Orange and Red arrows indicate flow through the reactor, while blue arrow shows flow path in the heating chamber.

Using the Formlabs Form 2 vat polymerisation platform with Formlabs Clear resin, the crystallisers were fabricated at 50μm layer width. On completion, the build was detached from the platform and washed in a bath of Isopropyl alcohol and left to sonicate for 30min consequently removing the excess resin on the part. It was also flushed immediately to clear the channels of resin as it could solidify and block the channels. Supports were finally removed with a knife.

### 4.3.2 Heat transfer characterisation

The rate of heat transfer in the crystalliser was characterised. It was important to measure the temperature at different points in the crystalliser as this will allow for modelling of the reactor behaviour. For this purpose, a rig was set up consisting of a Gilson 307 HPLC pump connect via 1/16" PTPE tubing and tube connectors to the crystalliser, while a Julabo F250 recirculating chiller was connected in a counter-flow direction to the device via tubing (Figure 85).
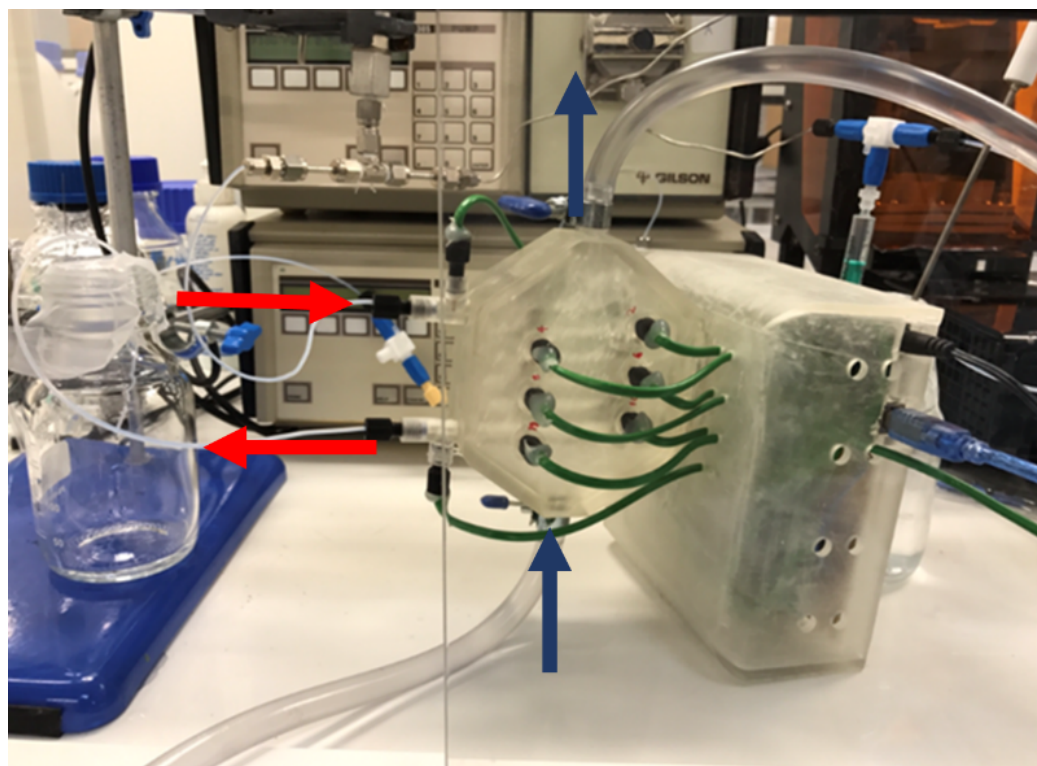


Figure 85: Rig setup for heat transfer characterisation in the AM crystalliser. The setup comprises of a recirculating chiller, HPLC pump and temperature sensors connected to the crystallisers. Red arrow represents flow direction through the reactor, while blue arrow indicates direction of heating fluid in surrounding chamber.

An acquisition system for in-situ monitoring of the temperature in flow was designed. This served as a cost-effective method of monitoring the temperature at different points in the reactor. K-type thermocouples (*ca.* 2mm diameter) were attached to 1/16" tube connectors with araldite glue. The thermocouples were then coupled with a MAX6675 thermocouple sensor module which was linked to an Arduino mega micro-controller. Temperature was collected every second. The schematic and setup of the temperature acquisition system is presented in Figure 86. Labview was used to compile the data received from the Arduino software linked to the micro-controller.
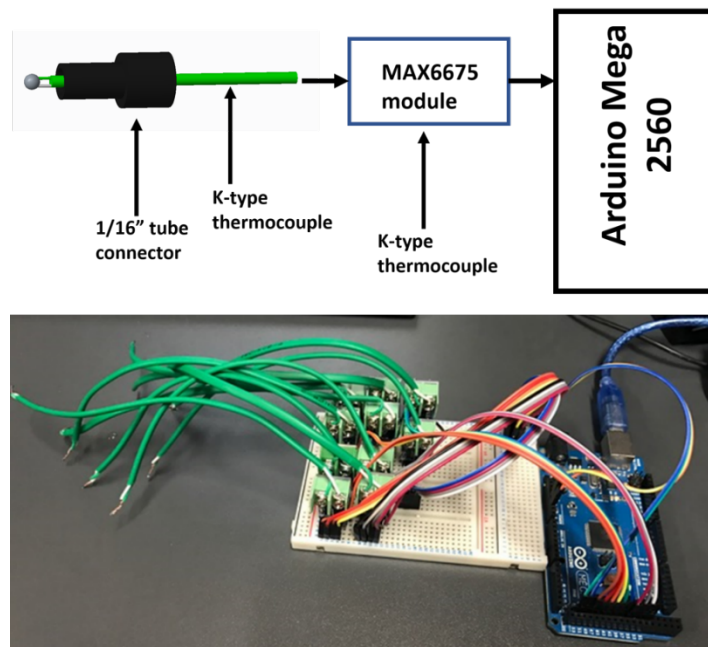


Figure 86: (Top) Schematic of inline temperature acquisition system and (below) actual setup

*Modelling*

The modelling carried out in this work was simplified by assuming the following:

- Temperature at the internal wall surface was assumed constant across the tube length. This was not the case however, because some parts of the tube wall were attached to the wall of the crystalliser. Also, some of the support structure was densely populated at the lower regions of the crystalliser, which will result in an unevenly distributed flow across the tubes.

- There was no loss or drop in temperature in the heat transfer chamber. However, it was expected that there will be a drop-in temperature to the surroundings of the recirculating fluid from the inlet to the outlet.

- The flow rate of both fluids was assumed to be constant.

- The temperature sensors are positioned in the flow path of the fluid without any dead zones.

- The temperature of the circulating fluid was constant during each experiment.

- Steady state was achieved before data was collected.

Modelling of the collected data was carried out using the following heat transfer equation:

$$\frac{T_s - T_{m,o}}{T_s - T_{m,i}} = exp\left[-\frac{PLU}{mcp}\right]$$

$$U = \left(\frac{1}{h_i} + \frac{1}{h_o}\right)^{-1}$$

$$h = \frac{Nu\,k}{L}; \quad Nu = 0.023.\,Re^{0.8}\left(\frac{\mu c_p}{k}\right)^{0.3}$$

where $T_s$ is the temperature at the tube internal surface, $T_{m,i}$ and $T_{m,o}$ represents the temperature at the middle inlet and outlet of the tube. P is the perimeter, L is

the tube length, m is the mass flow rate, μ is the dynamic viscosity, k is the thermal conductivity, Re is the Reynold number, $D_h$ is the hydraulic diameter, A is the correction factor U is the overall heat transfer coefficient, $c_p$ is the heat capacity of the fluid, $h_i$ and $h_o$ are the convective heat transfer coefficient of the internal and external fluid. Nu corresponds to the Nusselt number. A Nu value of 3.66 was used for the $h_i$ calculation, an approximation for fully developed laminar flow, while the Nu equation was used for $Nu_o$ calculation. For modelling purposes, the equation was simplified by assuming a linear relation between the outside temperature in the heat transfer chamber, T, and the internal surface temperature. The constant noise in the signal was smoothed employing a 5-point fast Fourier transform (FFT) algorithm (Equation 4.3.2).

$$T_{m,o} = A.T_\infty - [A.T_\infty - T_{m,i}].exp\left[-\frac{PLU}{mcp}\right] \qquad \text{Equation 4.3.2}$$

### 4.3.3 Thermal conductivity measurement

The thermal conductivity of the solid-state material used in the manufacture of the reactors was characterised. The thermal conductivity measurement allowed the quantifying of the heat transfer rate between the chiller and the reactant fluid. The thermal conductivity measurements were carried out on a TCi Thermal Conductivity Analyzer utilising a Modified transient plane source (MTPS) sensor. The device employs a one-sided interfacial heat sensor that applies a heat to the sample and measures the thermal conductivity of the material. This is done by inducing a one-dimensional heating to the sensor and material resulting in a rise in temperature by an applied current. The applied current induces a change in the voltage drop in the sensor. Heat generated dissipates into the sample and

the rate depends on the transport properties of the material. The rate of increase in voltage, which is calibrated to the temperature, is inversely proportional to the thermal conductivity. Hence, the slope for highly conductive materials will be flatter, while steeper in materials with lower conductivity.

### 4.3.4 Paracetamol (Acetaminophen) crystallisation in AM reactor

A multi-component cooling crystallisation route to obtain paracetamol was explored in the AMC. This was achieved through recrystallisation of an aqueous Isopropyl alcohol solution (IPA) of purchased Paracetamol form I, with a high concentration of Metacetamol (MCM) to assist the crystallisation. MCM served as an additive which was to be retained in the effluent as MCM-hydrate. The AM reactor aims to provide conditions in which the metastable orthorhombic polymorph (PC II) is produced over the monoclinic form (PC I), (Figure 76).

*Chemicals utilised*

The following chemicals were used for this study: Paracetamol (PC, $C_8H_9NO_2$, Acetaminophen, 4'-hydroxyacetanilide) CAS: 103-90-3, Metacetamol (MCM $C_8H_9NO_2$, 3'-Acetamidophenol, 3'-Hydroxyacetanilide) CAS: 621-42-1 and solvents: Isopropyl alcohol (IPA, $(CH_3)_2CHOH$) and Laboratory grade distilled water. All chemicals and solvents were purchased from Sigma-Aldrich.

PC concentration of 300mg/g with 25 wt % of MCM was dissolved in aqueous IPA of 60:40 $H_2O$/IPA (v/v). The solution of PC, MCM and aqueous IPA was stirred for 60min at 70°C before the recrystallization process. The recrystallization process was designed to allow for a controlled cooling of the

solution in the crystalliser. The set up comprised of a hot plate, Tricontinent C3000 syringe pump, Julabo F250 recirculating chiller, the fabricated crystalliser and for monitoring, Arduino Mega connected to temperature sensors, Avaspec UV/Vis spectrometer, coupled with in a flow cell and an Avantes DH-2000 light source. The PC filtration was done with a filter paper, Buchner funnel and flask connected to an extractor pump.

The HPLC pump used in the heat transfer study was not suitable as the aluminium tube allowed for quick loss of heat. As a result, crystals were formed in the small tubes resulting in clogging. To control the temperature and to allow for ease of cleaning, the 5mL syringe of the Tricontinent pump was jacketed with a heating mat. The jacket temperature was modulated with a PID controller coupled with a thermocouple. The control and monitoring of the system were carried on Labview. The designed rig is pictured in Figure 87
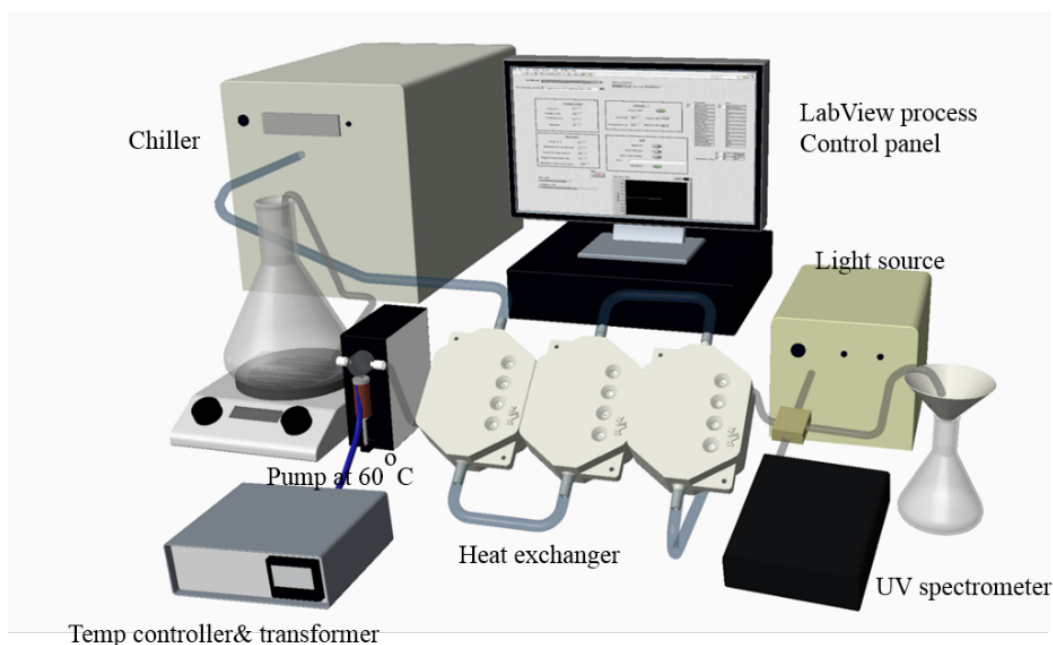


Figure 87: Designed Rig setup for cooling recrystallization of Paracetamol. It comprised a chiller, temperature controller, AM fabricated crystalliser, UV-Vis spectrometer, flow cell, lamp, hot plate and pump.

Two hot plates were used for the recrystallization process and kept at 70°C. The first was the solution of aqueous IPA, PC and MCM while the other was aqueous IPA of similar ratio without solute. For all the experiments, the solution was kept at 70°C and the pump jacket at 60°C, while the chiller temperature was changed for different sets of experiment. When the devices had achieved steady state, aqueous IPA was pumped through the system for 30min at 0.5ml/min after which the PC solution was switched. The switch of the PC solution marked the start of temperature and UV-spectra collection using Arduino and Labview. The temperature sensors were positioned at the inlet and 2.25mL into the crystalliser while the flow cell was positioned at a short distance after the outlet port. Temperature data and UV spectra were accumulated every second. The filter papers and Buchner funnels were changed every 20-30min to avoid clogging. To study the effect of the process conditions on the recrystallization of PC, a range of cooling temperatures from 30°C to 0°C were utilised.

### 4.3.5 Inline UV-Vis spectroscopy for nucleation

An Avantes flow cell coupled to an Avaspec UV/Vis spectrometer and an Avantes DH-2000 light source was connected to the outlet of the crystalliser. This was done to attempt to monitor, in real time, the nucleation and crystallisation of Paracetamol formation from the crystalliser. Paracetamol in solution has a peak at 244nm in the UV range, and is visually colourless (Near UV range: 200-400nm, Vis: 400 -750nm). [143] MCM on the other hand is beige

colour in solution. The UV-vis spectra was collected every second for experimentation time of 20 to 60min. The data was accumulated on Labview.

### 4.3.6 Crystal characterisation

Crystal characterisation was carried out to qualify the nature of the materials formed in the crystalliser and to allow for comparison, optical microscopy images were obtained along-side DSC and PXRD.

### Optical microscopy characterisation

High resolution images were collected with Olympus BX51 optical microscope coupled with a 5X and 10X magnification lenses with a polariser filter attached to demonstrate the formation of crystals. The collected samples were spread on glass slides for monitoring.

### Powder X-ray diffraction characterisation

Powder X-ray diffraction (PXRD) patterns were collected using a Panalytical MPD X-ray diffractometer with primary monochromatic radiation (Cu-K$\alpha$1, $\lambda$ = 1.5406A). The X-ray generator was run at 40 kV and 40 mA. The samples were mounted on brass plates and exposed over the range of 5$^\circ$ to 70$^\circ$ 2$\theta$ for 10.5 minutes per sample (continuous scan rate of 0.103 per sec).

### Differential scanning calorimetry characterisation

DSC was used to measure the heat flow into and out of a material as a function of temperature or time. Heat flow patterns of materials can be compared to highlight changes in the material properties. DSC was carried out using TA

167

instruments Discovery DSC equipped with an auto sampler. DSC aluminium pans with lids were filled with the samples and queued for testing. The heat profiles were collected against a reference DSC pan at a heating rate of 5°C/min over a temperature range of 20°C to 200°C.

## 4.4 Design of Experiments

### 4.4.1 Heat transfer characterisation

Measuring the change in temperature across the reactor, from the inlet to outlet, is crucial as this will allow the modelling of the thermal behaviour of the device. As the designed device will also behave uniquely at different flow rates, temperatures and dissimilar materials, experiments were carried out enveloping the varying parameter changes. The following heat transfer experiments were carried out on the crystalliser AMC-I:

- Heating of the heat transfer chamber between 40°C to 25°C at a constant flow rate of 0.5ml/min at inlet temperature of 23°C to 25°C.

- Heating of the heat transfer chamber between 20°C to 5°C at a constant flow rate of 0.5ml/min and inlet temperature of 23°C to 24°C.

- Flow rate change of the reactor chamber between 0.25ml/min to 2ml/min at a constant chiller temperature of 5°C and inlet temperature of 24°C.

- Flow rate change of the reactor chamber between 0.1ml/min to 3ml/min at a constant chiller temperature of 40°C and inlet temperature of 24°C.

Table 14: Design of experiments to characterise heat transfer in AMC-I at varying flow rates and chiller temperature.

| Code | Reactor flow rate | Chiller Temp. | Comments |
|------|-------------------|---------------|----------|
| H1 | 0.5ml/min | 25°C | Heating at constant flow rate. |
| H2 | 0.5ml/min | 30°C | Heating at constant flow rate. |
| H3 | 0.5ml/min | 35°C | Heating at constant flow rate. |
| H4 | 0.5ml/min | 40°C | Heating at constant flow rate. |
| C1 | 0.5ml/min | 23°C | Cooling at constant flow rate. |
| C2 | 0.5ml/min | 20°C | Cooling at constant flow rate. |
| C3 | 0.5ml/min | 15°C | Cooling at constant flow rate. |
| C4 | 0.5ml/min | 10°C | Cooling at constant flow rate. |
| C5 | 0.5ml/min | 5°C | Cooling at constant flow rate. |
| FC1 | 2.0ml/min | 5°C | Varying flow rates at constant cooling. |

| FC2 | 1.5ml/min | 5°C | Varying flow rates at constant cooling. |
|------|-----------|------|------------------------------------------|
| FC3 | 1.0ml/min | 5°C | Varying flow rates at constant cooling. |
| FC4 | 0.5ml/min | 5°C | Varying flow rates at constant cooling. |
| FC5 | 0.25ml/min | 5°C | Varying flow rates at constant cooling. |
| FH1 | 3.0ml/min | 40°C | Varying flow rates at constant heating. |
| FH2 | 2.0ml/min | 40°C | Varying flow rates at constant heating. |
| FH3 | 1.5ml/min | 40°C | Varying flow rates at constant heating. |
| FH4 | 0.5ml/min | 40°C | Varying flow rates at constant heating. |
| FH5 | 0.5ml/min | 40°C | Varying flow rates at constant heating. |
| FH6 | 0.5ml/min | 40°C | Varying flow rates at constant heating. |
| FH7 | 0.5ml/min | 40°C | Varying flow rates at constant heating. |

## 4.4.2 Paracetamol (Acetaminophen) crystallisation in AM reactor

The control and monitoring of the system was carried out on with Labview. The experiment sequence involved pumping the heated aqueous IPA at 70 °C, with the syringe pump jacket at 60 °C through the fabricated crystalliser and then switching to the PC solution when conditions reached steady state. The time required to refill the pump was kept to a minimum with a high extraction rate (15 ml min$^{-1}$), which refilled the 5 ml syringe in 20 seconds. Further increase in the extraction rate resulted in cavitation. The experiments were run at a flow rate of 0.5ml/min resulting in a residence time of 5.9min.

The first set of experiments (PC-07, 5°C, PC-06, 10°C, PC-05, 15°C, PC-04, 30°C, PC-03, 25°C, PC-02, 20°C) which ran for 20min each were carried out with the flow cell and UV-Vis spectrometer connected, Table 15. These were

done at varying chiller temperatures of 5°C to 30°C. Subsequent experiments (AT10, 10°C 10min, AT30, 10°C 30 min, AT60, 10°C 60 min, BT10, 0°C 10 min, BT30, 0°C 30 min, BT60, 0°C 60 min, CT10, 5°C 10 min, CT30, 5°C 30 min, CT60, 5°C 60 min) were carried without the flow cell and with a larger outlet tubing of 1/8'' ID. This set was run for 60min at lower temperatures of 0°C, 5°C and 10°C and the filter paper and Buchner funnel were changes at intervals of 10 min, 30 min and 60 min. This was done to test the stability of the system at longer runs.

Table 15: Paracetamol cooling crystallisation experimentation

| Exp. Code | Temperature /°C | Collection time /min |
|-----------|-----------------|----------------------|
| PC-07 | 5°C | 20 |
| PC-06 | 10°C | 20 |
| PC-05 | 15°C | 20 |
| PC-04 | 30°C | 20 |
| PC-03 | 25°C | 20 |
| PC-02 | 20°C | 20 |
| AT10 | 10°C | 10 |
| AT30 | 10°C | 30 |
| AT60 | 10°C | 60 |
| BT10 | 0°C | 10 |
| BT30 | 0°C | 30 |
| BT60 | 0°C | 60 |
| CT10 | 5°C | 10 |
| CT30 | 5°C | 30 |
| CT60 | 5°C | 60 |

## 4.5 Results and Discussion

### 4.5.1 Fabrication of AM crystalliser

The fabrication time of an individual crystalliser was 17hrs 32min at 100μm layers though a finer resolution of 25 μm can be utilised with increased fabrication time. Reduced time can be achieved when fabricating multiple devices at a time as a bulk of the time is spent on the sweep and peeling mechanism with less time on laser tracing. An example fabrication of AMC-I is presented in Figure 88, with supports to hold over-hanging structures. Table 16 shows the resin volume required for fabrication and the calculated material cost of £30 for producing a crystalliser. At the internal diameters used for the studies, 2.1-2.5mm, there were no issues with blocking during fabrication when staying within the recommended process parameters and post processing procedures, i.e build orientation and cleaning in warm IPA shortly after building.
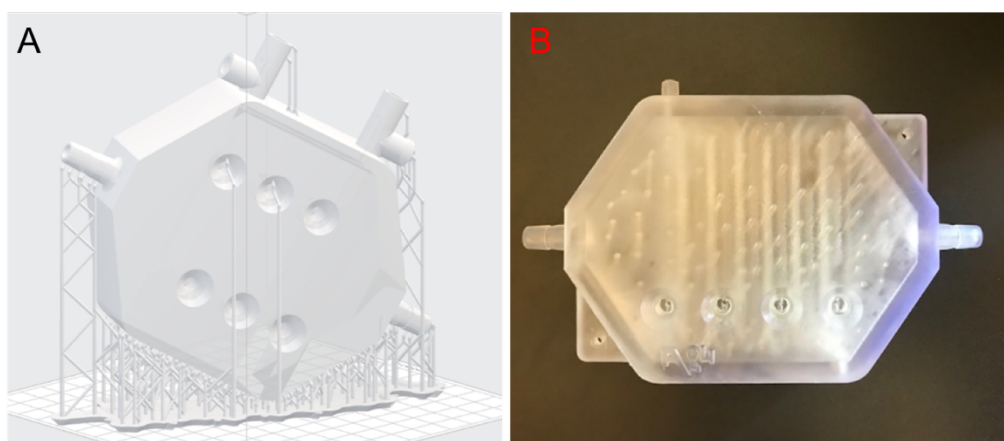


Figure 88: A) Designed crystalliser and supports attaching overhanging structures to the base of the reactor B) A fabricated crystalliser.

Table 16: Material, print layer thickness, Resin volume, fabrication time and material cost required for the fabrication of the AMC-I crystalliser used for heat transfer characterisation.

| Parameter | AMC-I |
|---|---|
| Fabrication Platform | Form 2 |
| Material | Formlabs Clear resin |
| Print layer thickness | 50 $\mu$m |
| Resin volume | 209mL |
| Fabrication time | 17hrs 32min |
| Device material cost | £30 |

## 4.5.2 Thermal conductivity measurements

To measure the thermal conductivity of the polymerised material, three 15mm outer diameter (OD) cylinders with varying thicknesses of 3, 4 and 5mm were fabricated on the Form 2 device. Two of each of the three-cylinder thicknesses were fabricated and tested. The measurements were collected for each of the samples.

Table 17:Effusivity and thermal conductivity (k) values collected for AM fabricated cylinders with outer diameter of 15mm and 3, 4 and 5mm width.

| | | Effusivity (W s$^{½}$ m$^{-2}$ K$^{-1}$) | k (W m$^{-1}$ K$^{-1}$) |
|---|---|---|---|
| 5mm | 1 | 744.76 | 0.37 |
| | 2 | 770.22 | 0.39 |
| 4mm | 1 | 797.25 | 0.42 |
| | 2 | 895.61 | 0.52 |
| 3mm | 1 | 854.05 | 0.47 |
| | 2 | 917.96 | 0.54 |

Although the MTPS measurement is a surface technique and the thermal conductivity of the material should not relate to the thickness of the material, variations in the measurement were found. This could be either due to the uneven

density of the fabricated material or errors in the measuring devices. Variations can also arise for surface roughness variation of the materials resulting in varying contact surfaces or the packing structure of the polymer. The measurements were however found to be in the range of $\pm$ 0.09W/mK at a mean thermal conductivity of 0.45 W/mK. The thermal conductivity measurement was plugged into the heat transfer model to predict the effect of change in thickness of the material.

### 4.5.3 Heat transfer study in AM Crystalliser

In all cases, the chiller was allowed to reach steady state before the flow process was initialised. The HPLC pump was then run for 10min to ensure steady state was achieved at different conditions. The constant noise in the signal was smoothed employing a 5-point fast Fourier transform (FFT) algorithm. An example of a raw compiled data of the temperature profile collected at steady state is present in Figure 89.
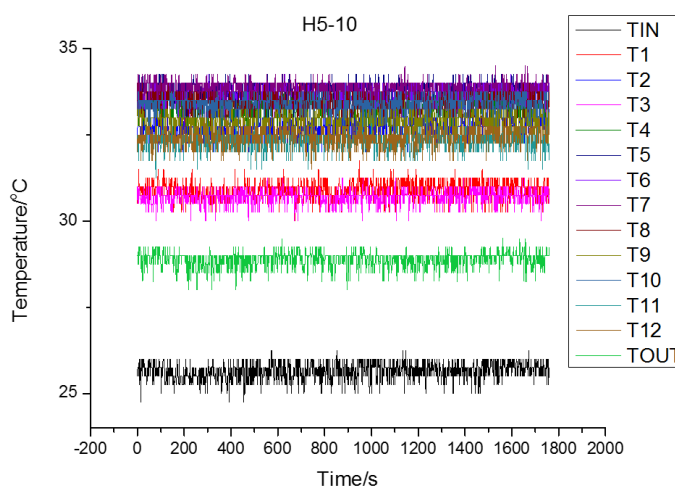


Figure 89: Example of collected data along the length of the crystalliser.

To quantify and study the heat transfer to the reactant fluid, a series of experiments were carried between 25°C to 40°C (heating) and 5°C to 23°C (cooling) at a flow rate of 0.5ml/min. Collected temperature vs time data at the evenly spaced sensing ports on the reactor was analysed and presented with reference to the position along the reactor length. The heating and cooling profiles are presented in Figure 90. Distinct changes can be observed in both graphs presented. As the chiller temperature was lowered to 5°C in one of the experiments, the temperature of the fluid in the crystalliser dropped around 10°C at 60 µL volume into the reactor. The steepness of the curve from the inlet to 60 µL was more pronounced with an increase or decrease in temperature.
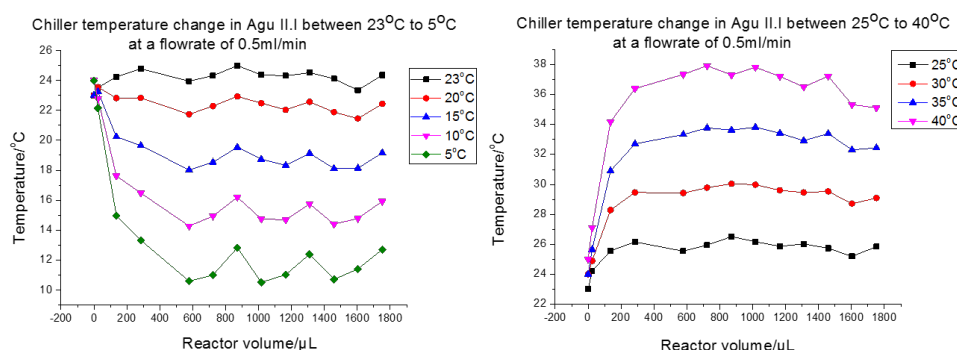


Figure 90: Temperature profile in the AM crystalliser at different recirculating temperatures, 5°C to 40°C and a constant flow rate of 0.5ml/min.

After 60 µL, the temperature seemed to flatten until towards the end where it reduced. A similar pattern could also be observed in the heating profile. Dips in the temperature profile could be observed at 900 and 1300 µL points in the profile. This was due to the inaccurate production of the temperature sensors. If the thermocouple tips were not sitting directly in contact with the fluid, there was a degree of error to the result. Hence, the temperature measurement collected was slightly off as it was in contact with the dead zone above the fluid

path. The temperature can also be seen to converge towards the end of the outlet of the crystalliser and this is observed in both profiles. This was assumed to be due to heat loss to the surroundings. Perhaps this effect can be minimised by insulating the surrounding surfaces of the crystalliser or increasing the thickness of the walls. Collected experimental data was applied to the heat transfer model presented in the modelling section. The model fit well with experimental data, Figure 91, although the data points discussed can be seen to show the largest variation from the ideal curve. The model describes the ideal behaviour of the crystalliser without the errors such as those associated with the position of the temperature sensors. It however describes the ideal temperature profile without heat losses to the environment, which can be observed from the dips in temperature from 1400 µL towards the outlet.
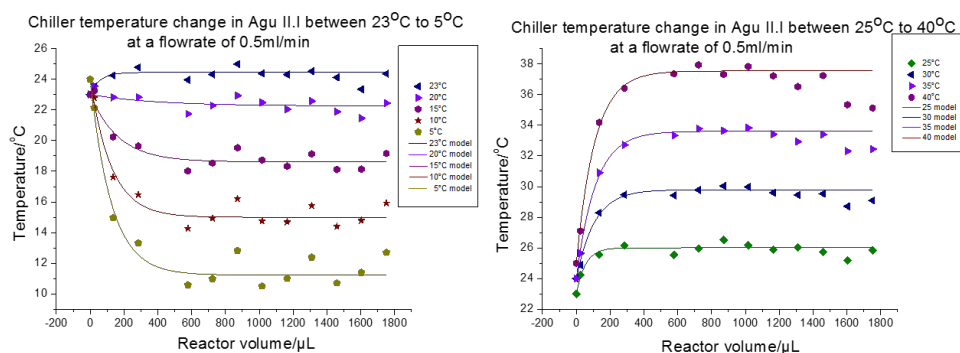


Figure 91: Temperature profile in the AM crystalliser at different recirculating temperatures, 5°C to 40°C and a constant flow rate of 0.5ml/min with the modelled data. (left) 23°C to 5°C (right) 25°C to 40°C.

Change in the recirculating temperature showed a marked change to the temperature profile in the crystalliser. Studying the effect of the change in flow rate aimed to allow effective understanding of the behaviour of the crystalliser. Increasing the flow rate was expected to minimise the steepness of the

temperature gradient from the inlet to the mid-section of the reactor. For this purpose, an experiment was designed to obtain the temperature along the length of the crystalliser at 5°C and 40°C at flow rates of 0.25ml/min to 2ml/min. at steady state the average temperatures at the sensors are presented with respect to the position in the crystalliser at different flow rates, Figure 92.
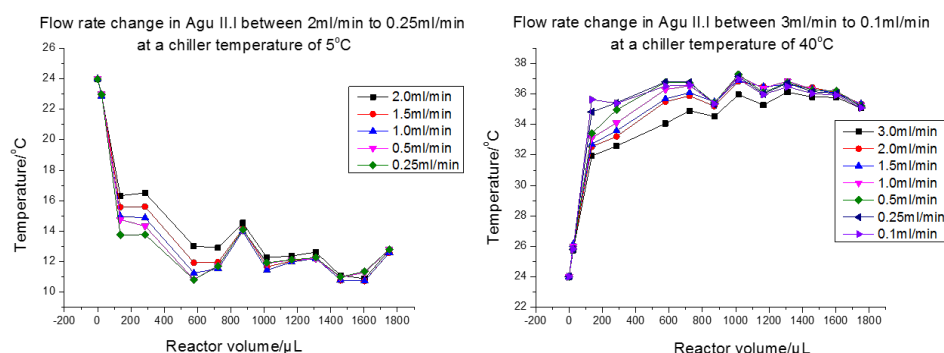


Figure 92: Temperature profile in the AM crystalliser at different flow rates, 0.25 ml/min to 2ml/min at a constant recirculating temperature of (left) 5°C and (right) 40°C.

The presented temperature profiles show a reduction in the steepness of the curves with an increase in flow rate. A similar pattern is observed at heating 40°C and cooling 5°C. If the wall of the crystalliser is assumed to be at constant temperature, specified time is taken for heat to be transferred. This phenomenon called convective heat transfer is the transfer of heat from a warmer to cooler region. With increase in flow rate, there is reduced time for heat transfer to occur between the fluid and the crystalliser wall. Similar to the previous experiment with change in the recirculating temperature, an unexpected drop in the temperature at 900 µL is also observed which bolstered the argument of an error at the sensing point. Changing the flow rate provides a method of controlling the steep drop in temperature in the crystalliser. A slow temperature drop will be beneficial in controlling crystal formation and growth.

The experimental data in this case was also modelled using the collected experimental data and presented in Figure 93. The model shows a similar trend as the experimental data. However, there are larger variations in the data. More sensing points should aid a more accurate profile prediction. A more accurate production of sensors will allow close prediction of the behaviour of the crystalliser.
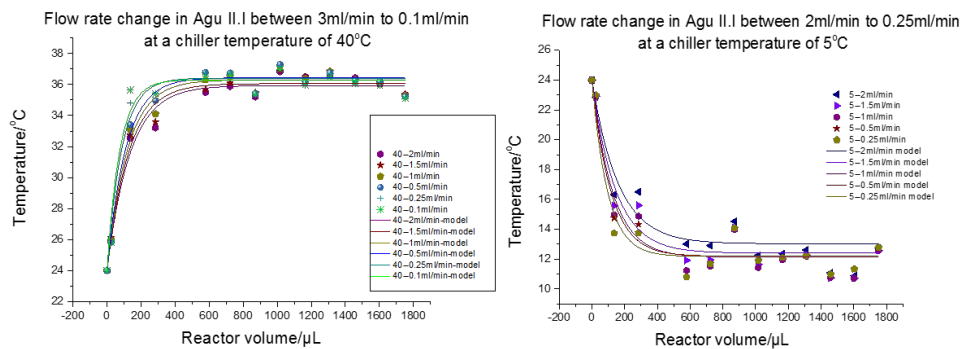


Figure 93: Temperature profile in the AM crystalliser at different flow rates, 0.25 ml/min to 2ml/min at a constant recirculating temperature of (left) 5°C and (right) 40°C with the mathematical model.

To compare the differences in temperature profile as a factor of the wall thickness the fitted models for the highest and lowest temperatures measures were used. The models for the case of the chiller temperature at 40°C (heating) and 5°C (cooling) were modelled for a wall/tube thickness of 0.45mm to 5.45mm. The thickness of the tubes used in the experiments was 3.45mm. The modelled data generated are presented for 300 µL of the crystalliser volume as at 400 µL temperature ideally flattens and remains constantly in this system. The modelled data is presented in Figure 94. Equation 4.5.3 was used in comparing the wall thickness from the change in radius.

$$Q = \frac{2\pi k}{\ln(r_2/r_1)} \cdot (T_1 - T_2) = \frac{2\pi k}{\ln(r/r_1)} \cdot (T_1 - T) \qquad \text{Equation 4.5.3}$$
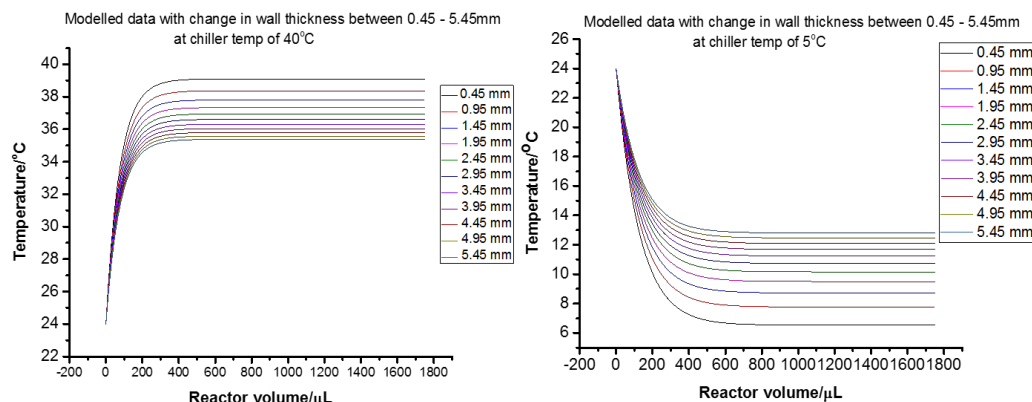


Figure 94: Modelled data for changes in wall thickness with change in thickness between 0.45-5.45mm at chiller temperature of (left) 5°C and (right) 40°C.

From the model, it was observed that increasing the thickness of the wall increases the resistance to heat transfer. Hence, a less steep temperature drop can be achieved with the increase in wall thickness and vice versa. Similar results can be seen in both cooling and heating. This however represents the case of an ideal system. In a real system, inconsistences in the fabricated material and inhomogeneous parts or faces will have an effect on the heat transfer between the fluids.

The acrylate-based AM resin poses a suitable material for studies in the recrystallization of paracetamol for several reasons. Firstly, it is found to have a good resistivity to a range of solvents including Isopropanol which is used in this work. Secondly, the material is found to have a stable thermal conductivity in the range of temperatures tested. Hence an indication that the material is stable in the range of temperatures.

Cooling crystallisation in the AM material also provides the benefit of a less steep temperature gradient compared to traditional materials used in flow reactors. Flow reactor and crystallisers are commonly manufactured in glass or metallic materials with higher thermal conductivity values. For comparison, a temperature profile of the ideal crystalliser behaviour with a measure thermal conductivity of 0.4W/mK compared with Aluminium at 205W/mK and glass at 1.05W/mK. The profiles at 40$^{\circ}$C and 5$^{\circ}$C can be seen to have a less steep gradient in the AM material. The less steep gradient of temperature in crystallisation will aid in minimising fouling and uneven crystal size distribution associated with rapid drop in temperature.
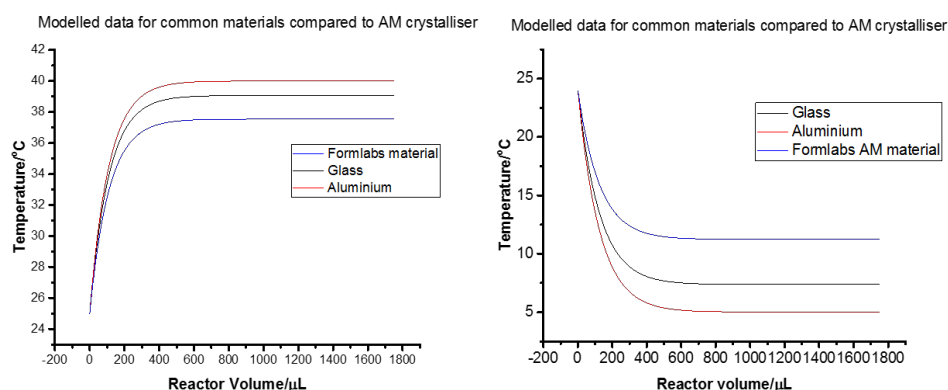


Figure 95: Modelled data for temperature profile in the crystalliser compared to a similar crystalliser fabricated in glass and aluminium at chiller temperatures of 40$^{\circ}$C (left) and 5$^{\circ}$C (right)

***Modelled temperatures for Paracetamol crystallisation***

The aim of the heat transfer study was to understand the behaviour of the crystalliser at a range of temperatures under different parameters. The crystalliser developed was to be utilised in the recrystallization of Paracetamol

(PC). It was crucial to carry out the preliminary study as the heat transfer in the crystalliser can be modelled and used in the temperature profile prediction for future experiments. For flow crystallisation processes it is important to eliminate dead zones and areas of large fluctuations in temperatures. Such areas like the temperature sensing points with dead zones and possible drop in temperature can result in the unwanted formation of crystals. In such regions the crystal could agglomerate or grow larger leading to blockages. As such, only 4 sensing ports were designed into the crystalliser for PC production. The crystalliser was also slightly longer to 0.6m with a larger inner diameter of 2.5mm. The increase in diameter was to both increase the residence time and to avoid immediate blockages. As changes were made to the crystalliser and the setup, a model was generated from the study with the previous crystalliser. Only two of the 4 temperature sensing ports were used while the rest were blocked. The two sensors were positioned at the inlet and at 0.4m into the crystalliser. The design of experiment for the PC experiment involved the dissolution of PC in aqueous IPA at 70°C and the pumping through the crystalliser. Although a jacket was added, the temperature at inlet of the crystalliser at 0.5mL was about 30°C. The collected data was used for correcting the model and the cooling profiles for the process is presented in Figure 96. The generated profiles show the drop-in temperature with increase in temperature.
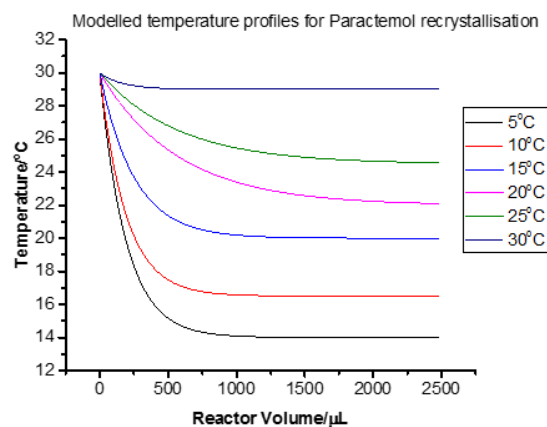
Figure 96: Modelled temperature profile for the recrystallisation of Paracetamol at a chiller temperature of 5-30°C.

### 4.5.4 Paracetamol (Acetaminophen) crystallisation in AM reactor

The syringe pump allowed for better control of the temperature using a heated jacket. At a flow rate of 0.5mL/min, with the syringe pump jacket temperature set to $60^{\circ}$C, the temperature at the inlet of the crystalliser was just above $30^{\circ}$C allowing for nucleation and crystal growth to occur in 6min. The syringe pump has some draw-backs however, due to its method of operation. It does not allow for continuous flow as time is required to extract before dispensing.
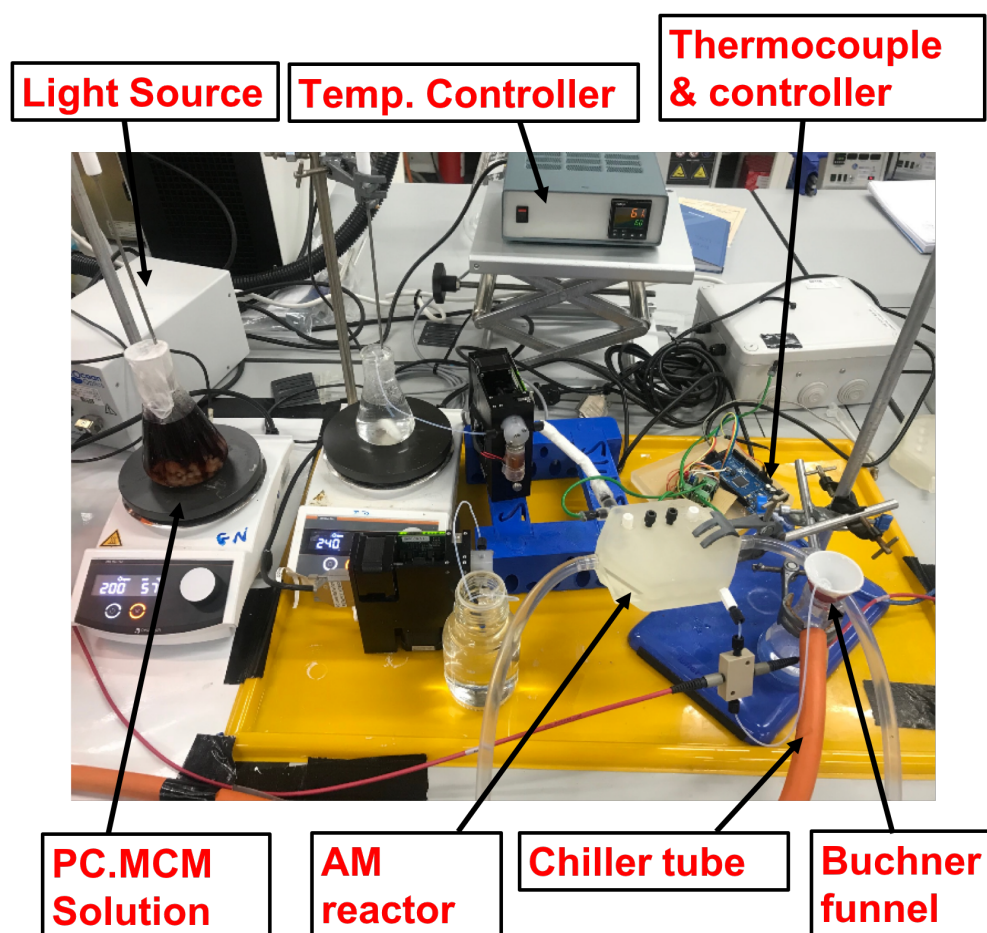


Figure 97: Actual Rig setup for cooling recrystallization of Paracetamol. This consisted of the AM fabricated device, chiller, light source, flow cell, heated PC solution, inline thermocouples connected to an Arduino microcontroller, Buchner funnel with a filter paper to collect samples

That down time leads to uneven residence time and a slight drop in the temperature during extraction. Dips in the data can be seen as the system is started from room temperature until it approaches steady state, Figure 98. The extraction was done at 15mL/min. Increasing the extraction rate further resulted in cavitation issues. Uneven residence time and excessive temperature drops will have an effect on the formation and crystal size distribution.
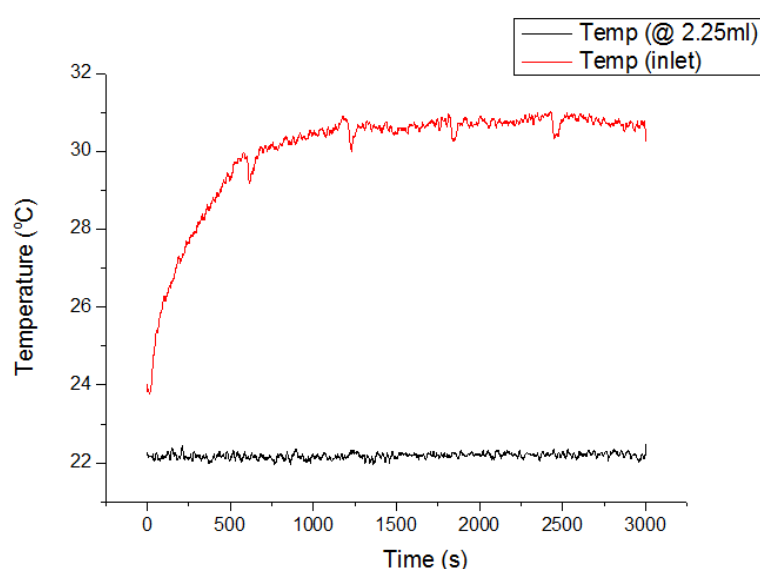


Figure 98: Temperature profile at the inlet of the (red) and at 2.25ml (black) into the crystalliser. Dips in the data can be seen at it approaches steady state. The dips relate to the drop in temperature during the fluid extraction.

Powder materials were collected for all the experiments run in filter papers coupled with a Buchner funnel and vacuum line. In all cases the crystalliser was washed by flowing aqueous IPA heated at 70°C into the crystalliser for 30min before each experiment. Fouling and blockages in the crystalliser were not observed at the first set of experiments with shorter runs of 20 min. For the longer experimental run blockages were observed. The longer runs were carried

out at 10°C, 0°C and 5°C in that sequence. The crystalliser was blocked at 60 min, 40 min and 30 min respectively. Although the residence time were equal, the blocking times recorded does not correlate to the rate of cooling. Though the crystalliser was washed before every run, the blockage time reduced with repeated use. This suggests that the cleaning process was not efficiently eradicating the build-up of fouling in the crystalliser. It also indicates that the crystalliser wall had been seeded after the first run which then speeds up the crystallisation and growth, hence increasing the time of blockage.

### 4.5.5 Inline UV-Vis spectroscopy for nucleation study

The aqueous IPA, heated to 70°C, was run through the crystalliser prior to crystallisation to ensure the conditions attained steady state before it was switched to the PC solution. In Figure 99a, the absorbance spectra at 10, 450, 800 and 1100 seconds are presented for cooling crystallisation at 20°C chiller temperature. Since the spectra collected were initialised when the PC solution was switched, at the recorded time of 10 seconds, only the water and aqueous solution is observed. As the crystalliser volume is approximately 3ml, at a flow rate of 0.5ml/min, the PC solution should be observed from 360secs. At 450 - 1100secs, a change in the spectra can be observed which seem similar and quickly saturates around 300 to 420 nm. Noise from 200 – 350nm was observed with both the PC and the aqueous IPA. Figure 99b-d shows the time series absorbance spectra, without the noisy region for 1100secs. The time at which the PC starts to leave the crystalliser can be seen around 300 to 400 secs before the spectra immediately saturates. Similar UV/Vis spectra were also observed in all the experimental conditions tested.

185

Due to the high concentration of PC and MCM which was used to ensure crystallisation before the exit of the crystalliser, the flow cell was quickly saturated. More so, with extended runs above 40 minutes, the flow cell was completely blocked due to increased fouling. As the flow cell had a small diameter and the concentration of the solution was high, the microscale UV/Vis experimentation is not suitable for this setup. Inline nucleation and crystallisation study was challenging due to characteristic encrustation during crystallisation.
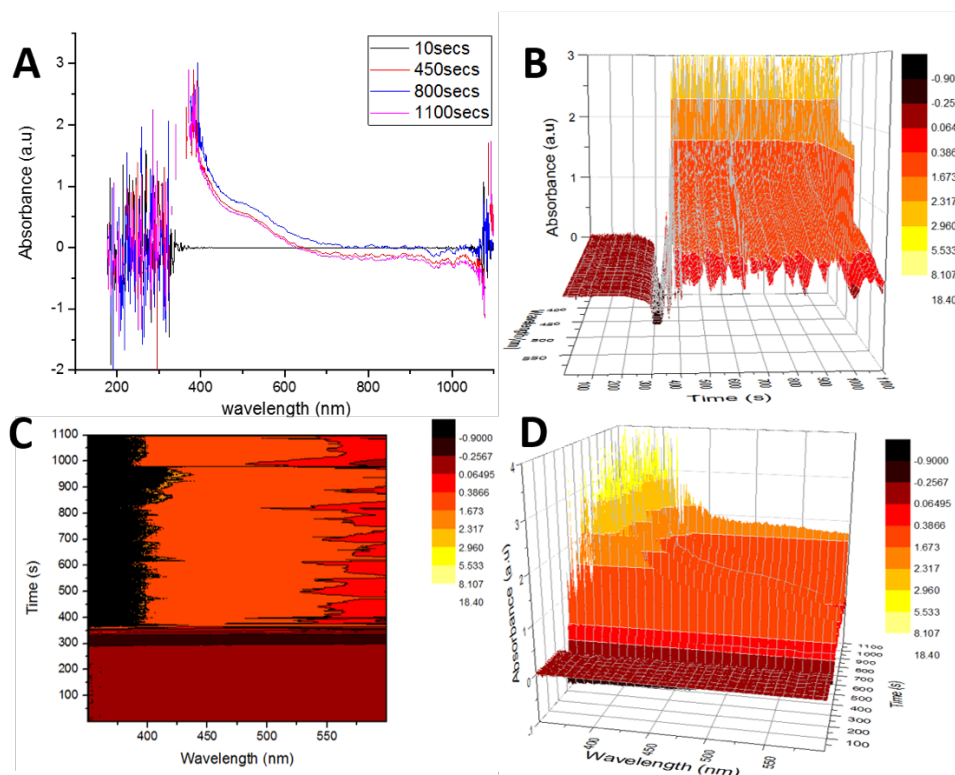


Figure 99: A) Example UV spectra obtained at a chiller temperature of 20°C at 10, 450, 800 and 1100secs. Example Absorbance vs wavelength spectra time series B) side view C) Top view D) side view.

### 4.5.6 Material characterisation

*Optical microscopy characterisation*

The images in Figure 100 and Figure 101 show a clear indication of crystal formation. Both single crystals and clusters can be observed from the images. The images collected at the higher temperatures (20°C-30°C) seem to show the formation of more needle like crystals, while a rhombic shape can be seen at the lower temperatures (5°C to 15°C). A transition of the crystal shape can be seen across the tested temperature range. The optical images do not give a clear indication of the polymorph produced or the differentiation in shape and size due to the heterogeneity of the samples. Also, clustered crystals will be difficult to quantify visually. The crystals collected could either be Paracetamol form I or II or Metacetamol, hence powder X-ray diffraction was used for further characterisation.
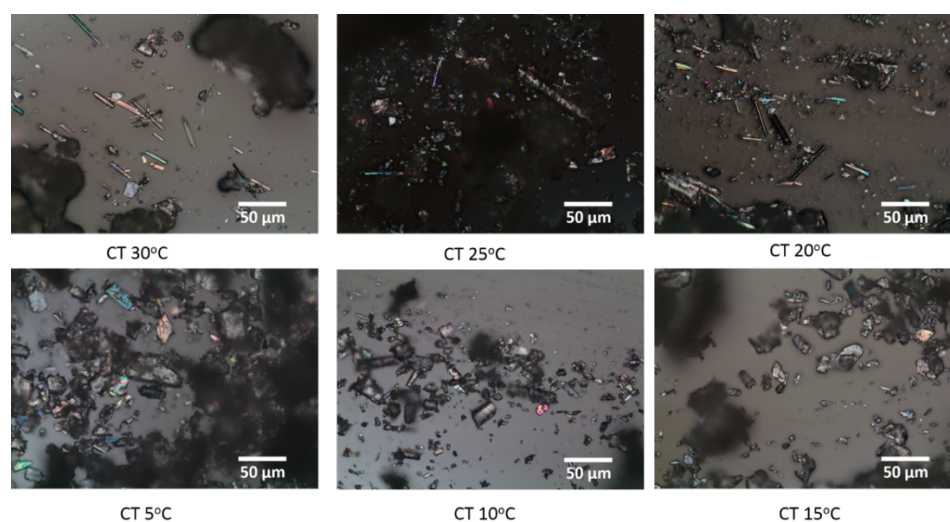


Figure 100: Optical images of collected samples at various cooling rates. Crystals can be observed in the images and the shape changes can be observed at varying chiller temperatures (CT). Images are at 5X magnification.
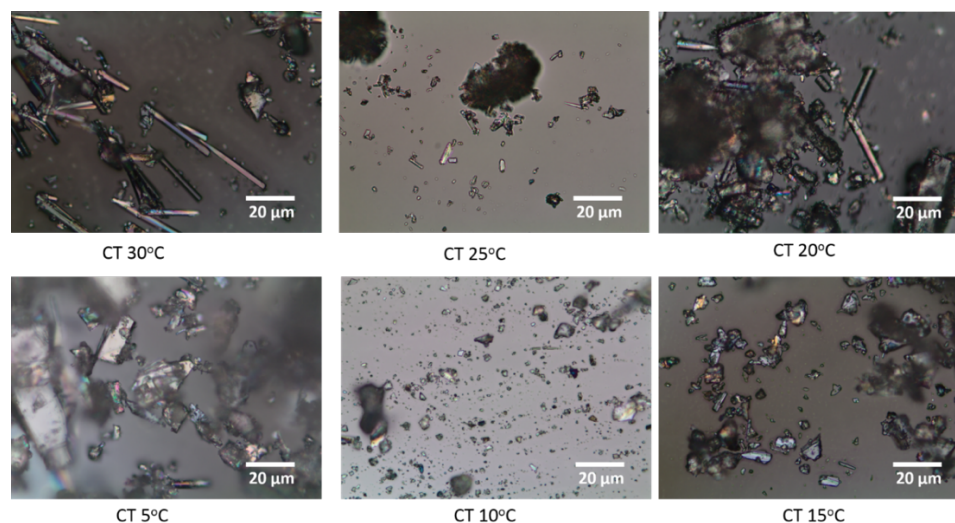
Figure 101: Optical images of collected samples at various cooling rates. Crystals can be observed in the images and the shape changes can be observed at varying chiller temperatures (CT). Images are at 10X magnification.

***Powder X-ray diffraction characterisation***

The collected samples were compiled and compared to reported reference patterns HXACAN01 – PC monoclinic form I, HXACAN26 - PC orthorhombic form II and MENSEE – MCM form I. Metacetamol hydrate (MCM.$H_2O$) reference pattern was not used in this analysis as it was not publicly available at the time of this study. PXRD serves as a valuable tool for identifying distinct polymorphic forms. In this case, it was used in distinguishing the polymorph of paracetamol produced, as well as Metacetamol. Overlaying the reference for the polymorphs of PC (I & II), Figure 102, show a clear distinction can be seen in their peaks. Several of the peaks do not match, allowing for ease of identification and comparison. The purchased paracetamol was also overlaid with the reference, Figure 103, and the peaks match, identifying the starting material is PC form I. The purchased MCM was also identified with the reference as MCM form I, Figure 104.
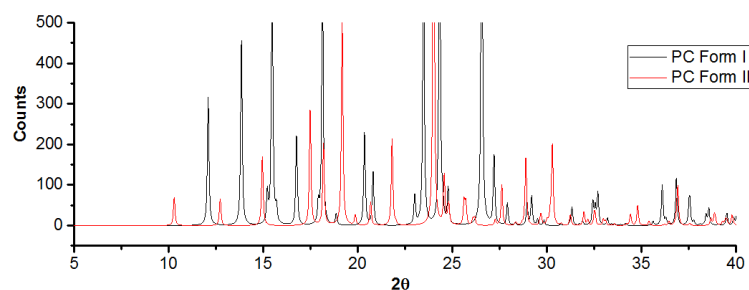
Figure 102: Reference PXRD patterns for Paracetamol form I (HXACAN01) (black) and form II (HXACAN23) (red)
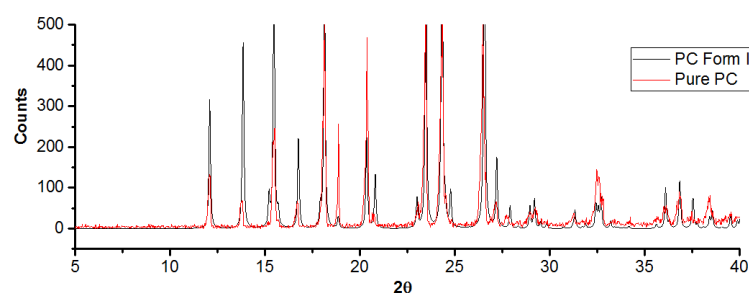


Figure 103: Overlay of the purchased Paracetamol from Sigma-Aldrich (Pure PC) (red) with the reference form I (HXACAN01) (black). This identifies the starting polymorphs as PC form I.
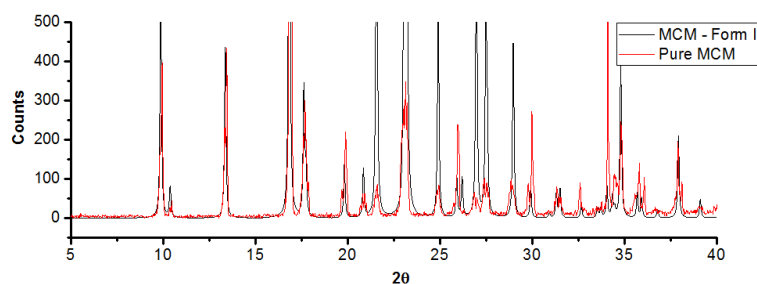


Figure 104: Overlay of the purchased Metacetamol from Sigma-Aldrich (Pure MCM) (red) with the reference form I (MENSEE) (black). This identifies the starting polymorphs as MCM form I.

Reference PC form I, PC form II and MCM patters were overlaid with the patterns obtained from the collected samples at different processing conditions (Appendix). An example of a set overlaid for an experiment carried out at chiller

temperature of 10°C and collected at 30mins after process initialisation is presented in Figure 105. As the three reference patterns have distinct peaks, this method served as a sufficient method to highlight the presence of the expected materials. The peaks were matched manually and the 2θ peak counts compiled. Though there are many factors which could lead to a misrepresentation of peaks e.g preferred orientation, instrumental error and sample preparation, this served as a relative method of comparing the samples. Higher counts of form I peaks will represent higher quantities in the tested batch. However, this method will require testing larger representative quantities under specific conditions, because the batch tested on the diffractometer may not be representative of collected samples. Also, although the temperature was allowed to achieve steady state before experiment initiation, the crystallisation process may not have attained steady state due to factors such as fouling. Hence, it is practical to question the homogeneity of the samples and treat the results as relative.
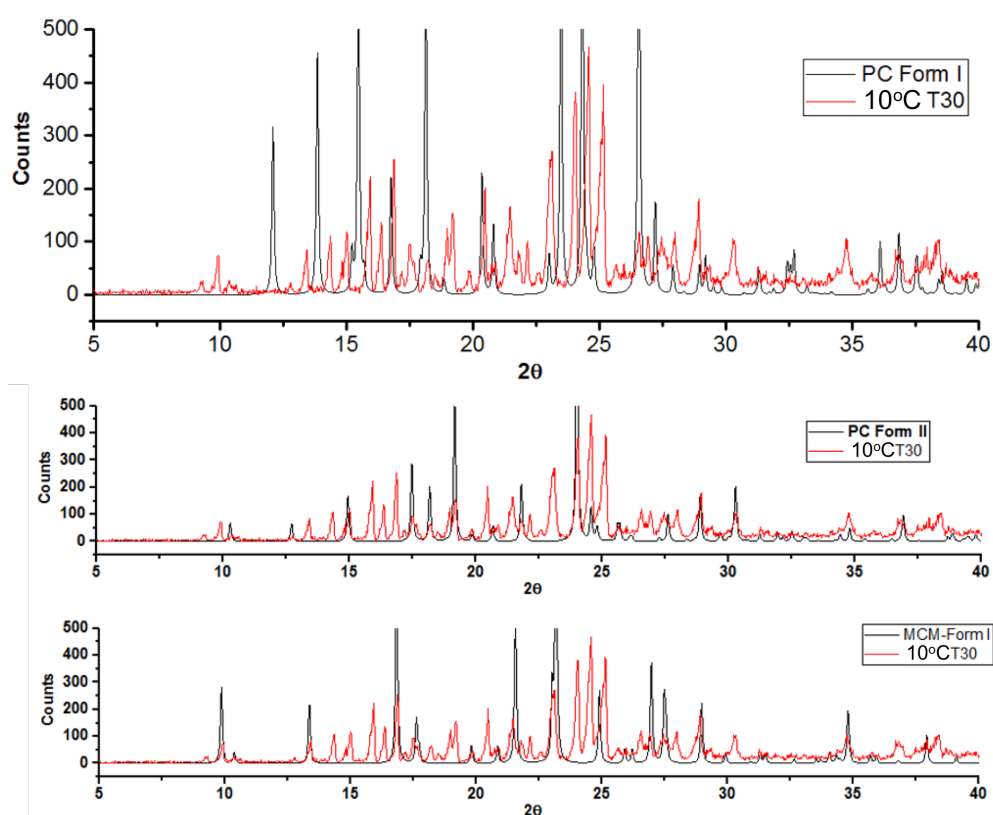
Figure 105: Example overlay of reference PC form I & form II and MCM to collected samples at CT 10ºC at 30 min from process start. All the reference PC form II peaks match with the sample peaks, while some of the form I and MCM peaks also match.

Table 18:Comparing reference PC form I, PC form II and MCM PXRD patterns to the obtained patterns of the samples collected at different processing conditions. The samples were for experiments carried out at 5ºC to 30ºC chiller temperature and a second experimentation at 0ºC to 10ºC at extended run of 60min. In the latter case, the samples were collected at 10min, 30min and 60min. Green highlighted cells represent matching peaks, while red represents unmatched peaks.

| PC (I) | 2θ | 5ºC | 10ºC | 15ºC | 30ºC | 25ºC | 10ºC T10 | 10ºC T30 | 10ºC T60 | 0ºC T10 | 0ºC T30 | 0ºC T60 | 5ºC T10 | 5ºC T30 |
|---|---|---|---|---|---|---|---|---|---|---|---|---|---|---|
| | 12.1 | R | R | R | R | R | R | R | R | R | R | R | R | R |
| | 13.8 | R | R | R | R | R | R | R | R | R | R | R | R | R |
| | 15.48 | R | R | R | R | R | R | R | R | R | R | R | R | R |
| | 16.78 | G | G | G | G | R | G | G | R | G | R | G | R | R |
| | 18.88 | G | G | G | R | G | G | G | G | G | G | G | G | G |
| | 20.36 | R | G | G | G | G | G | G | R | G | G | G | R | G |
| | 20.82 | R | G | G | G | R | G | G | R | G | G | R | G | G |
| | 23.02 | G | G | G | G | G | G | G | G | G | G | G | R | R |
| | 23.48 | R | R | R | R | R | R | R | R | R | R | R | R | R |
| | 24.33 | R | R | R | G | R | G | G | R | G | G | R | R | G |
| | 26.56 | G | G | G | G | R | G | G | G | G | G | R | R | R |
| | 27.22 | R | R | R | R | R | R | R | R | R | R | R | R | R |
| | 27.92 | G | G | G | G | G | G | G | G | G | G | G | R | R |
| | 28.96 | G | G | G | G | G | G | G | G | R | G | G | G | G |
| | 29.2 | G | G | G | G | G | G | G | G | G | G | G | G | R |
| | 31.34 | R | R | R | R | R | R | R | R | R | R | R | R | R |
| | 32.56 | R | R | R | R | R | R | R | R | R | R | R | R | R |
| | 36.1 | R | R | R | R | R | R | R | R | R | R | R | R | R |
| | 36.84 | G | G | G | R | G | G | G | G | R | R | R | G | G |
| | 37.56 | G | G | G | R | R | R | R | G | G | G | G | R | R |
| | 38.56 | R | G | G | G | G | G | G | G | G | G | G | G | G |
| | 39.52 | G | G | G | G | G | R | G | G | G | G | G | G | G |
| | % match | 45.5 | 59.1 | 59.1 | 40.9 | 36.4 | 50.0 | 45.5 | 22.7 | 40.9 | 50.0 | 45.5 | 4.5 | 22.7 |
| PC (II) | 10.3 | G | G | G | G | G | G | G | G | R | G | G | G | G |
| | 12.7 | G | G | G | R | G | G | G | G | R | G | G | R | G |
| | 14.96 | G | G | G | G | G | G | G | G | G | G | G | R | G |
| | 17.5 | G | G | G | G | G | G | G | G | G | G | G | R | G |
| | 18.2 | G | G | G | R | G | G | G | G | R | G | G | G | G |
| | 19.18 | G | G | G | G | G | G | G | G | G | G | G | G | G |
| | 19.86 | G | G | G | G | G | G | G | G | R | G | G | G | G |
| | 20.68 | R | G | G | G | G | G | G | R | G | G | G | G | G |
| | 21.82 | G | G | G | R | G | G | G | G | G | G | G | R | G |
| | 24.02 | G | G | G | R | G | G | G | G | G | G | G | G | G |
| | 24.58 | G | G | G | G | G | G | G | G | R | G | G | G | G |
| | 24.82 | G | G | G | G | G | G | G | G | R | G | G | G | G |

| | | | | | | | | | | | | | | |
|---|---|---|---|---|---|---|---|---|---|---|---|---|---|---|
| | 25.7 | | | | | | | | | | | | | |
| | 26.18 | | | | | | | | | | | | | |
| | 27.26 | | | | | | | | | | | | | |
| | 28.36 | | | | | | | | | | | | | |
| | 28.88 | | | | | | | | | | | | | |
| | 30.3 | | | | | | | | | | | | | |
| | 34.8 | | | | | | | | | | | | | |
| | 36.92 | | | | | | | | | | | | | |
| | 38.86 | | | | | | | | | | | | | |
| | % match | 95.2 | 95.2 | 95.2 | 47.6 | 95.2 | 100.0 | 100.0 | 95.2 | 38.1 | 95.2 | 90.5 | 76.2 | 100.0 |
| MCM | 8.5 | | | | | | | | | | | | | |
| | 10.4 | | | | | | | | | | | | | |
| | 13.36 | | | | | | | | | | | | | |
| | 16.84 | | | | | | | | | | | | | |
| | 17.64 | | | | | | | | | | | | | |
| | 19.82 | | | | | | | | | | | | | |
| | 20.88 | | | | | | | | | | | | | |
| | 21.58 | | | | | | | | | | | | | |
| | 23.18 | | | | | | | | | | | | | |
| | 24.92 | | | | | | | | | | | | | |
| | 25.92 | | | | | | | | | | | | | |
| | 26.22 | | | | | | | | | | | | | |
| | 26.98 | | | | | | | | | | | | | |
| | 27.5 | | | | | | | | | | | | | |
| | 28.98 | | | | | | | | | | | | | |
| | 29.92 | | | | | | | | | | | | | |
| | 31.32 | | | | | | | | | | | | | |
| | 31.5 | | | | | | | | | | | | | |
| | 32.66 | | | | | | | | | | | | | |
| | 34.06 | | | | | | | | | | | | | |
| | 34.34 | | | | | | | | | | | | | |
| | 34.8 | | | | | | | | | | | | | |
| | 35.7 | | | | | | | | | | | | | |
| | 35.94 | | | | | | | | | | | | | |
| | 36.82 | | | | | | | | | | | | | |
| | 37.94 | | | | | | | | | | | | | |
| | 39.12 | | | | | | | | | | | | | |
| | % match | 29.6 | 33.3 | 11.1 | 22.2 | 44.4 | 48.1 | 48.1 | 51.9 | 3.7 | 22.2 | 37.0 | 100.0 | 100.0 |

The peaks and comparison to collected samples are presented in Table 18. The matching peaks in the table are highlighted in green while unparalleled peaks are marked with red. From the presented data, it is evident a transformation has been observed from the starting form I to high percentage of form II being produced compared to the other two materials. However, traces of form I and MCM were also observed. More peaks of form I can be observed at 5°C to 15°C compared to that at 25°C and 30°C. The peak comparison culminated at CT of 30°C indicates that reduced crystallisation yield was obtained at this temperature as less peaks matched for both form I and form II. In most cases, form II was

observed. A reduced number of peaks were observed in the second set of experiments at 10 min compared to 30min into the run at CT 0°C and 5°C. This suggests that the process may not have achieved steady state at 10min, as samples collected at 30min and 60min matched closely. Peaks of MCM can be observed to increase with increase in process time at 10°C and 0°C. As higher quantities of MCM was observed in the collected sample, this indicates the occurrence of seeding, fouling or crystal growth in the crystalliser. As the same crystalliser was used for the second set of experiments at 10°C, 0°C and 5°C in that order, the experiments carried out at 5°C was quickly blocked in 30min. Although the crystalliser was cleaned before each run, the blockage may have been as a result of build-up of fouling. This correlates to high concentration of MCM observed at this final run. High counts of MCM and matching peaks can be seen in Table 18.

Evidently, the materials collected contained PC Form I and Form II as well as MCM to varying degrees and not a select polymorph. Improvements to the flow setup and reactor optimisation, for enhanced mass transport, will increase the purity of the materials. The major issue with the setup in this work was the lack of continuous flow using a syringe pump which resulted in the difficulty of the process to achieve steady state.


*Differential scanning calorimetry characterisation*

The compiled heat flow patterns for the untreated MCM and PC from Sigma-Aldrich are presented in Figure 106.
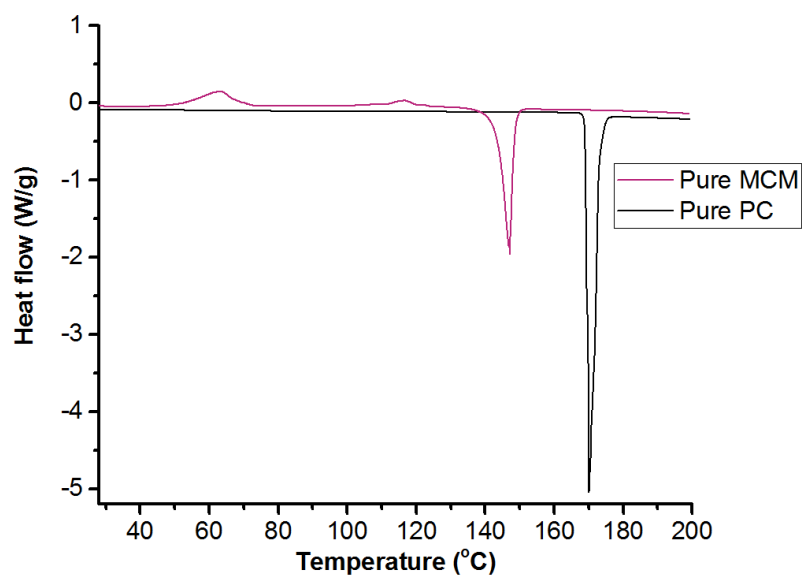
Figure 106: Differential scanning calorimetry (DSC) traces of untreated Metacetamol and Paracetamol from Sigma-Aldrich.

The DSC scan for PC shows an endothermic transition at 169.93°C, melting onset of 169.33°C and a computed enthalpy of 174.06J/g. For MCM the endothermic transition is observed at 147.07°C, melting onset of 143.47°C and enthalpy of 75.512J/g. A PC melt temperature around 170°C indicates the presence of form I while transitions at 157-160°C and 148°C, indicate presence of form II and form III polymorphs. The PC trace presented shows that the starting material is indeed form I with the absence of other polymeric forms.
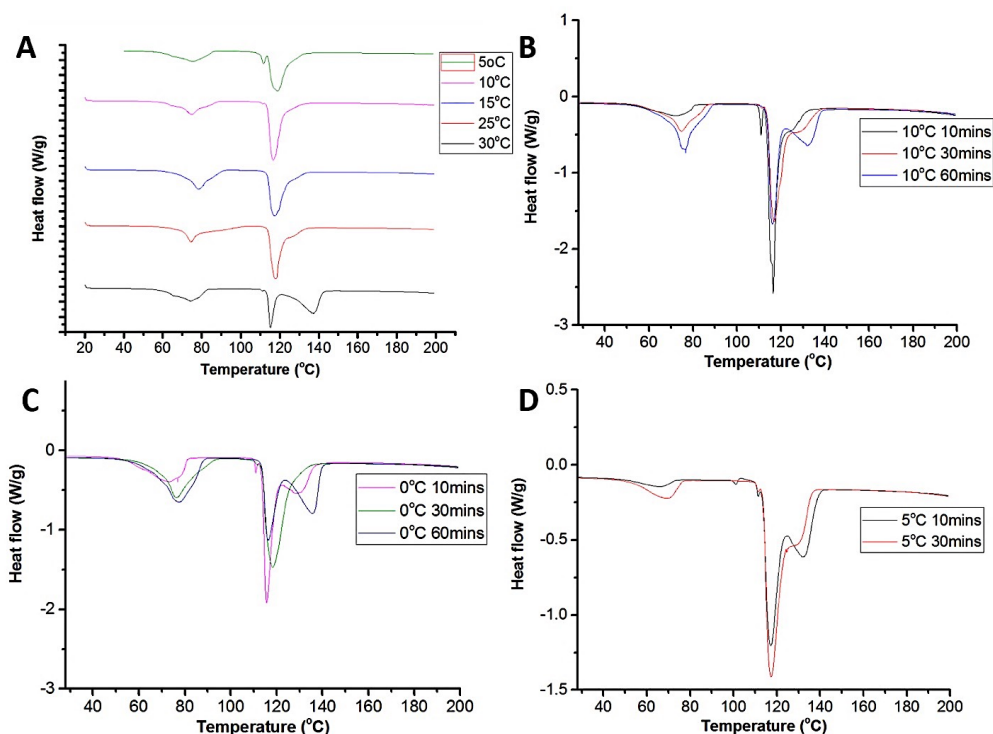
Figure 107: Differential scanning calorimetry (DSC) traces for samples collected at A) Varying cooling temperatures 5-30°C B) 10°C at 10-60min C) 0°C at 10-60min D) 5°C at 10-30min

The DSC traces collected for the samples show several distinct peaks around 70-80°C, 110-120°C and 130°C-140°C. It is interesting to observe the formation of a peak closer to 140°C in Figure 107A, which disappears with reduction in temperature from 30°C to 5°C. A similar peak can also be observed at the runs carried out up to 60min. Studying Figure 107 B&C&D, the final sample obtained before the crystalliser blocked, which is 10°C 60min, 0°C 60min and 5°C 30min, the peak around 140°C can be seen to form. This peak can be perhaps related to the collection of a higher proportion of MCM as the crystals grow in the crystalliser before the blockage occurs. This leaves a saturated higher proportion of MCM that is crystallised on leaving the crystalliser. The higher

proportion of MCM at such conditions can also be observed from the PXRD traces.

The number of superimposed peaks observed makes it complicated to quantify the proportion of a polymorphs produced or measure the proportions of crystals to amorphous materials obtained. A glaring issue with the crystallinity comparative study is the heterogeneity of the samples, which was observed in the PXRD study. The collected samples, although majorly form II, had varying quantities of form I, MCM and possibly $MCM.H_2O$. This resulted in several broad endothermic transitions which will be difficult to characterise. Hence, it is difficult to conclude that the crystallisation process achieved steady state at the concentration employed. As such, the heterogeneity of the samples did not allow for a comparative study of the crystallinity due to multiple peaks.

## 4.6 Summary

The fabrication of a mesoscale crystalliser for Paracetamol crystallisation utilising AM is presented. AM aided the fabrication of a bespoke mesoscale flow devices with near net shape geometry at studied parameters. The tubular crystalliser designed with temperature sensing ports was manufactured and utilised in the attempt to selectively obtain a desirable polymeric form of Paracetamol (PC). The PC experimentation in the AM reactor aimed to demonstrate the versatility of AM in the specialised application demonstrated. PC was selected as it has been extensively studied. Several studies into PC manufacture have been presented in literature using different approaches to produce several polymorphs. Ortho-form II PC has several benefits over form I PC. This is due to the physical structure of the polymorph, which allows for better compressibility which is advantageous for drug manufacture and enhanced bioavailability during treatment. The formation of PC in the crystalliser was studied under varying temperatures. The cooling crystallisation process carried out in the crystalliser allowed the production of PC crystals up to 60min. This will signify the first example of continuous PC crystallisation carried out in an AM crystalliser at such scale.

The scale explored however opens up several challenges. Fouling is a well-known phenomenon in chemical processes and specifically crystallisation. PC crystallisation is well known to cause fouling at the walls of reactors with more pronounced impact experienced in tubular reactors. With the narrow size of channels used (2.1-2.5mm) and a high concentration of PCM:MCM to ensure crystallisation, the reactor was susceptible to fouling. The occurrence of reactor

wall fouling prevented a lengthy stable formation of crystals. Although cleaning cycles were carried out before experimentation, it seemed the build up from subsequent runs was not eradicated. As such, this limited effective comparison for the conditions tested.

Although the channel diameter can be increased to minimise fouling, this will have a detrimental effect on the crystalliser hydrodynamics and thermodynamics. In the previous work on synthesis of Ag nanoparticle in the AM continuous oscillatory baffled flow reactor (COBR), the observed fouling was minimised compared to a tubular reactor. The COBR has been shown in the previous chapter to produce unique mixing patterns that enhance mass transport. Exploring a similar advanced reactor for cooling crystallisation will potentially provide a more stable production of materials and reduce fouling. This could be vital in the future study of added value materials crystalline molecular and advanced structured materials. The following conclusions have been drawn from the work in this chapter:

- It is possible to fabricate fully built mesoscale flow crystallisers by vat polymerisation method.

- Process conditions, in this case heat transfer, in the AM crystalliser can be monitored using off-the-shelf components and instruments for process monitoring.

- Cooling crystallisation of paracetamol by multi-component templating can be achieved in an AM fabricated crystalliser with evidence of selective formation of form II Paracetamol polymorphs.

# Chapter 5 Extrusion based AM bioreactor for transamination

## 5.1 Introduction

The development of biocatalytic processes is emerging as a new paradigm in the sustainable manufacturing of high value chemicals for the pharmaceutical industry [144, 145]. The application of biocatalysts can provide alternative synthetic approaches to those relying on more traditional chemistry, reducing the need for toxic reagents, transition-metal catalysts and avoiding costly purification steps and protecting group manipulations [146]. The immobilization of enzymes onto solid supports has facilitated the development of biocatalytic industrial processes, by simplifying the recovery and reuse of the enzymes and enabling their transition into continuous flow reactors [147-149]. However, the number of commercially available systems is currently limited, mainly due to the absence robust immobilization strategies. AM has the potential to enable the rapid assembly of complex reaction system geometries, which is often challenging using traditional manufacturing techniques [150].

Though CFRs with varying degrees of sophistication have been described in literature using AM in recent years for a variety of applications[60, 151-153], the chemical post-modification of AM fabricated devices has received much less attention [154]. The development of reliable methods for chemical modification has enormous potential to reduce cost and deliver functional devices for rapid screening of immobilized enzymes. Furthermore, the freedom of design inherent to AM allows parallelized fast screening platforms to be combined with

intensified continuous-flow reactors featuring advanced geometries and optimized mixing properties.

A key advantage of the use of AM is the ability to rapidly generate multiplexed reactors that can increase the experimental throughput, thus speeding up the discovery and optimization of new compounds or processes [155], This can be invaluable for the rapid screening of immobilization conditions, which usually relies on trial and error approach, being time and resource intensive. Furthermore, AM techniques support the utilisation of a wide range of materials. Though, each technique has its requirements for the state and physical properties of the materials that can be effectively used in fabrication.

Material extrusion AM technique, FDM, was employed in this work as it allows the cost-effective fabrication of Nylon. Nylon is a particularly convenient immobilization matrix for enzymes [156, 157]. It is inexpensive, chemically inert, non-toxic, has good mechanical properties and is commercially available in multiple formats. Several studies report the immobilization of various enzymes like proteases, glucosidases, endocellulases and laccases onto different nylon matrices [156, 158]. Various types of nylon are widely employed for AM. Powder based nylon 11&12 are commonly employed materials of choice for selective laser sintering (SLS) methods [58]. These platforms are capable of producing robust parts with highly intricate geometries and fine layer resolution of 100 μm. Therefore, there is an untapped potential to develop AM supported bioreactors fabricated in nylon. The challenge in utilisation, as discussed in the literature review, is the difficulty to clear out the flow channels of powder. This

creates the difficulty of manufacturing fully built devices, though straight section can be fabricated and assembled.

Material extrusion AM methods can be challenging to optimise depending on the selected material. Process parameters in material extrusion include, nozzle temperature, bed temperature, build orientation, extrusion rate, layer thickness, deposition speed [159, 160]. There can also be significant variability between machines, including machines with heated platform or temperature-controlled chamber. Nevertheless, when utilised for flow reactors, intersections and gaps between deposited material can cause leaks. Poor strength and weak interlayer bonds in the build direction have also been observed using material extrusion technique [161]. As mentioned in the literature review, in a split-and-recombine device produced by Capel and colleagues [52], employing FDM with ABS filament, the devices were found to leak in multiple regions at above 20 bar pressure. A flow reactor device, which was fabricated using ABS on a FDM3000 platform is demonstrated in Figure 108 [63]. Micrographs of the device in Figure 108a - c show the gaps at intersections and spaces between deposited filament and layers. These gaps resulted in the leaking and failing of the device. This shows an un-optimised fabrication of the device, as the polymer is under extruded. Nevertheless, in a recent publication, flow devices produced using PLA and ABS on a FDM machine were able to exceed the required pressure, of around 20 bar, suitable for microfluidic applications [162].
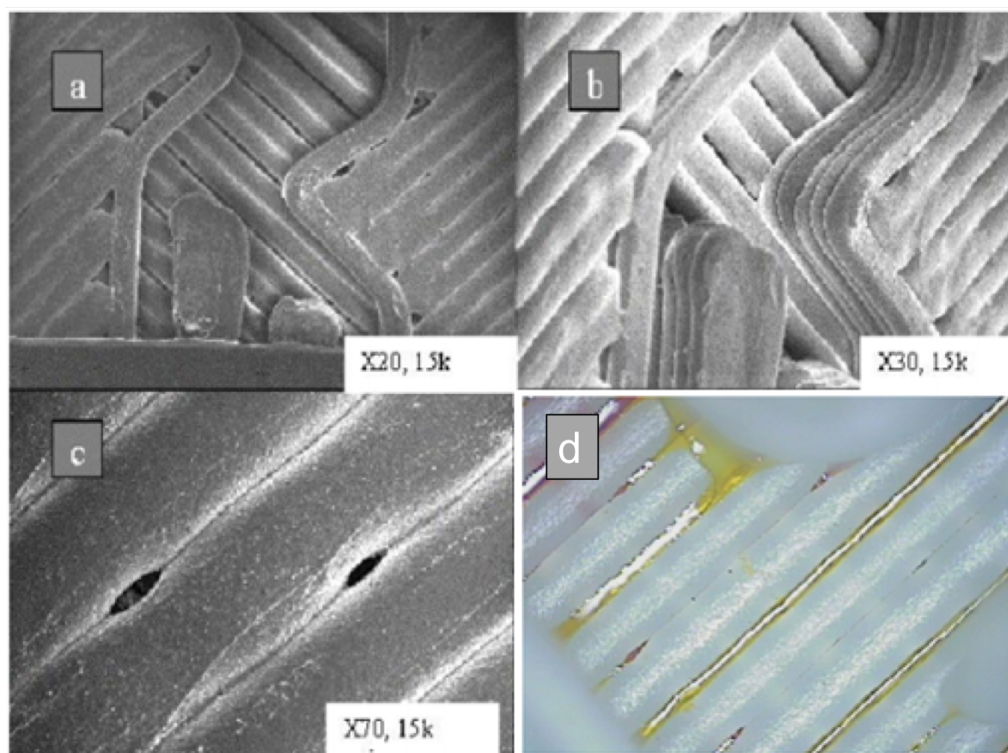
Figure 108: Magnified images of fabricated ABS flow device from FDM3000 material extrusion platform. It shows an unoptimized fabrication of a flow reactor allowing for leak to occur. (a) X20 (b) X30 (c) X70 (d) leak occurring in the device as fluid is passed through the device [63].

The application of transaminases for the synthesis of optically pure chiral amines from readily available ketones has received considerable attention from both the academic and industrial communities, due to the challenging nature of this transformation [163-168]. Additionally, there are only a handful of reports describing their successful application in continuous flow [169-172]. A commercially available (R)-ω-TA, ATA117, was selected to demonstrate the flow methodology. The enzyme was supported following a literature procedure presented in the methodology and the immobilization confirmed by ATR-FTIR. The immobilisation experiments were carried out by collaborative researchers.

## 5.2 Objectives

The overall aim of the study in this chapter was to investigate the feasibility of developing extrusion-based AM bioreactors. This encompassed experimental work using a Fused deposition modelling (FDM) extrusion-based system coupled with Nylon and Polypropylene in fabricating both test pieces and reactors. Initial trials were developed to create an understanding of the process parameters that affect reactor fabrication using this method. The learning was then applied to the aim to create a methodology for developing functional reactors for bespoke applications. The itemised objectives included:

- To study the process parameters that effect the AM-FDM fabrication of flow reactors in materials of interest i.e Nylon and Polypropylene, using a select platform.
- To develop a methodology for manufacturing leak-free Nylon bioreactors by AM material extrusion method for bio-transformation.

## 5.3 Methodology

### 5.3.1 Extrusion based manufacture of parts

To investigate the feasibility of fabricating bioreactors using FDM, experiments were designed to understand a selected extrusion-based platform and its process restrictions. Subsequently, learnings were applied to the experimental work aimed at fabricating leak free and near net shape flow reactors. Experiments were designed to understand a number of the fabrication parameters such as nozzle temperature, PEI build plate temperature, layer height and the deposition patterns, extrusion rate, deposition speed. The extrusion-based fabrication work was done with a Lulzbot Taz 5 equipped with a 0.5mm nozzle, using off the shelf, Taulman Nylon 618 and Polypropylene filaments. CAD models for the components were produced using Creo Parametric and converted to .STL (Standard triangular language) format. Cura Lulzbot software was used to generate the G-code commands for the AM platform. The G-code commands are based on programmed process parameters set for the fabrication of the components e.g layer resolution, build temperature, fill density or speed etc. On completion of the build, the parts were detached from the build base and the support structure was removed.

### 5.3.2 Fabrication of an inverse mould with a straight channel

With the intent of understanding the process parameters of the FDM platform and the characteristics of the manufactured parts, build trials were designed based on a simple CAD model. The fabrication of a simple straight channel

inverse mould model was suitable in providing an indication of the process parameters required to manufacture a flow device. The surface quality of the inverse representation of the channel can easily be measured as opposed to fabricating a channel, sectioning it before measuring. The test model was an inverse mould of a straight channel with dimension of 42x12x5mm and channel OD of 1.2mm, Figure 109. The trial parts were manufactured in Polypropylene, using the process parameters presented in Table 19. The experimental work investigated the extruder temperature and fan speed during the build.
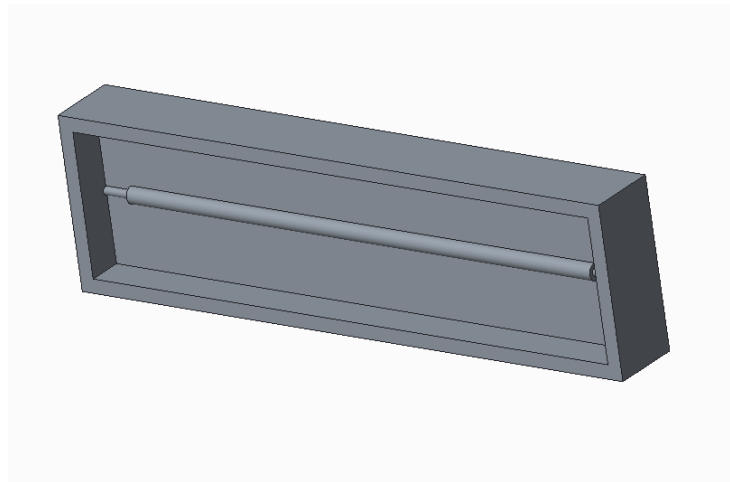


Figure 109: CAD model of an inverse mould of a straight channel

Table 19: FDM process parameters for inverse mould manufacture on Lulzbot Taz platform

| Process Parameters | Units |
|---|---|
| Print Layer height | 0.38mm |
| Initial layer height | 1.14mm |
| Fill density | 70% |
| Brim | 5 lines |
| Print speed | 15mm/s |

| Initial layer speed | 8mm/s |
|---|---|
| Nozzle diameter | 0.5mm |

*Design of experiments*

Using the fixed parameters in Table 19, experiments were designed with extruder temperature, temperature and fan speed of 200ºC to 270ºC, 120ºC to 130 ºC and 0% to 40% respectively, as in Table 20. Polypropylene

Table 20: Design of experiments for FDM inverse mould fabrication

| S/N | Nozzle temp | Bed temp | Fan speed | External Fan |
|---|---|---|---|---|
| 1 | 250 | 125 | 0 | ON |
| 2 | 250 | 125 | 0 | ON |
| 3 | 245 | 125 | 0 | ON |
| 4 | 250 | 125 | 30% | OFF |
| 5 | 270 | 130 | 0 | OFF |
| 6 | 260 | 130 | 0 | OFF |
| 7 | 250 | 125 | 0 | OFF |
| 8 | 250 | 120 | 0 | OFF |
| 9 | 240 | 125 | 0 | OFF |
| 10 | 230 | 125 | 0 | OFF |
| 11 | 220 | 125 | 0 | OFF |
| 12 | 210 | 125 | 0 | OFF |
| 13 | 200 | 125 | 0 | OFF |
| 14 | 200 | 125 | 0 | OFF |

**5.3.3 Effect of extrusion rate on part geometry**

The extrusion rate is another key process parameter which requires optimisation for the build to meet its desired intent. The extrusion rate is a factor of the

quantity of material being deposited. The extrusion rate alongside other parameters can influence the thickness of layers as well as the fill density of the parts. The fill density is particularly important in extrusion-based AM as a lower fill density is beneficial producing in light weight parts though a higher fill density is crucial to ensure reactors do not leak between layers.

### *Design of experiments*

An experiment was designed to study the effect of the extrusion rate on the fill density of the part. This was coupled with a repeatability study to ensure efficacy at the intended extrusion rate. Two layers at 0.35mm were deposited forming a cuboid of 26mm by 15mm. At a deposition speed of 22mm/sec nozzle diameter of 0.5mm and a nozzle temperature of 290ºC, the polypropylene material was deposited on 3mm polypropylene sheets, to ensure adhesion. Using a 100% fill density setting, relating to the Estep of the extrusion motor, the extrusion rate was adjusted between 20.4mm/sec to 28.1mm/sec. Other processing parameters were unchanged throughout the experiment, Table 21.

Table 21: Experimental parameters for study on an extrusion-based machine

| Parameter | 1 | 2 | 3 | 4 | 5 |
|---|---|---|---|---|---|
| Extrusion rate | 20.4 | 22 | 22.9 | 25.5 | 28.1 |
| Extrusion Temp | 290 | 290 | 290 | 290 | 290 |
| Fill density | 100% | 100% | 100% | 100% | 100% |
| layer height | 0.35 | 0.35 | 0.35 | 0.35 | 0.35 |

| Deposition speed | 22 mm/s | 23 mm/s | 24 mm/s | 25 mm/s | 26 mm/s |
|---|---|---|---|---|---|

### 5.3.4 Bioreactor manufacture

A method was developed to immobilise enzyme in an AM Nylon based flow reactor for continuous flow biocatalytic process. FDM extrusion-based AM method was utilised in developing the reactor for this study. Using the same FDM platform, Lulzbot Taz 5, Nylon 6 Taulman 618 filament was employed for the experimentation. As fabricating on the selected platform was an inexpensive process, an iterative approach was used to optimise the fabricated geometry close to the intended design. The reactor was built at a layer height of 0.3mm, bed temperature of 100°C with a layer of UHU glue stick to ensure bonding to the base and nozzle temperature 215 to 235°C. The intended reactor to be fabricated is shown in Figure 110, though supporting geometry were designed around the build, in the iterative process to achieve near net geometry. The reactor device was designed featuring a 1.5mm channel diameter with a volume of 0.8ml, channel length 44.7 mm and an all-round dimension of 110 x 60 x 11 mm.
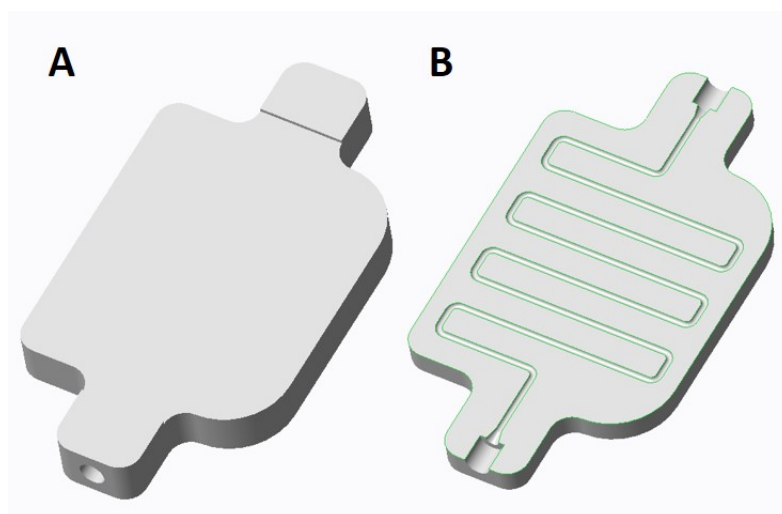
Figure 110: (A) CAD model of FDM bioreactor (B) Section of the bioreactor device, showing the inner channel

### 5.3.5 Functionalisation of a FDM reactor

The aim of fabricating the bioreactor was to enable added functionality by immobilising enzyme on the walls of the channels and utilising it for kinetic transformations. Following initial trials of immobilising enzymes in FDM fabricated Nylon wells the best conditions were applied in continuous flow using the fabricated reactor [173]. The reactor surface was treated with Hydrochloric acid HCl 5M after which the superficial amine groups were reacted with Glutaraldehyde to create covalent link points for the enzyme. The surface was then finally treated with a commercially available enzyme (R)-ω-TA, ATA117. The functionalisation process is detailed as follows:

- The reactor was filled manually with HCl 5M using a syringe. The acid solution was left inside for 10 min at room temperature.

- The HCl 5M solution was flushed out of the reactor, manually using a syringe full of air. The reactor was then washed manually with $H_2O$ using a syringe.

- The reactor was filled manually with a solution of Glutaraldehyde 25%(w/w) in $H_2O$ using a syringe. The solution was left inside for 16h at r.t.

- The Glutaraldehyde solution was flushed out of the reactor manually using a syringe full of air. Subsequently, the channel was washed with 0.1 M K phosphate buffer pH 8.0 using a HPLC pump at flow 0.01 ml/min for 5h.

- 15 mL of ATA117 enzyme 5mg/ml solution in 0.1 M K phosphate buffer ph 8.0 (with 0.1 mM PLP cofactor) was prepared (75 mg of enzyme was used) and recirculated through the reactor channel at 0.025 ml/min using a HPLC pump at r.t. during 24h.

- 0.1 M K phosphate buffer pH 8.0 was passed finally through the channel also at 0.025 ml/min using a HPLC pump at r.t. for 6h in order to flush out the enzyme solution and leave the reactor full of buffer and ready to perform bioreactions inside.
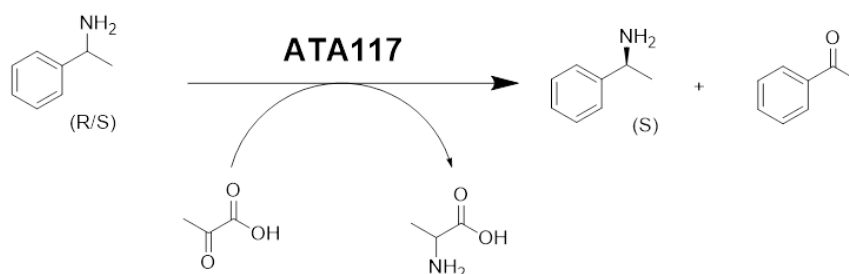


Figure 111: Benchmark reaction for the kinetic resolution of rac-methylbenzylamine. Reaction mixture: 65 µL of MBA (0.5 mmol), 36 µL of

pyruvic acid (0.5 mmol) and 2.5 mg of PLP (0.01 mmol) were solved in 100 mL of 0.1 M K phosphate buffer pH 8.0

The functionalised reactor was used in the kinetic resolution of *rac*-methyl-benzylamine into acetophenone. A solution of 5mM *rac*-methylbenzylamine, 5mM pyruvic acid and 0.1mM PLP was run through the reactor at flow rate of 25 µL·min$^{-1}$ for 5 hours after which the flow rate was dropped to 10 µL·min$^{-1}$. The solution was run for an additional 20 hours after which the reactor was flushed with buffer and stored for 48 hours at 4°C. A second cycle was run subsequently, under similar conditions (10 µL·min$^{-1}$, 5mM *rac*-methylbenzylamine, 5mM pyruvic acid, 0.1mM PLP) for a further 78hours.

## 5.4 Results and Discussion
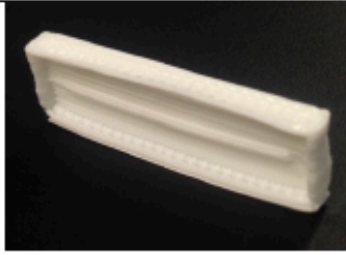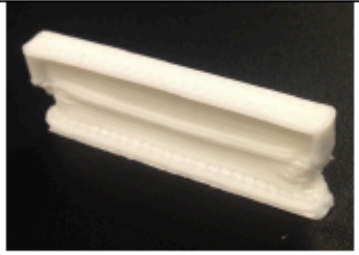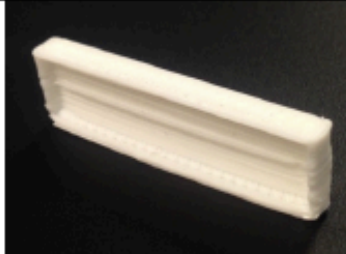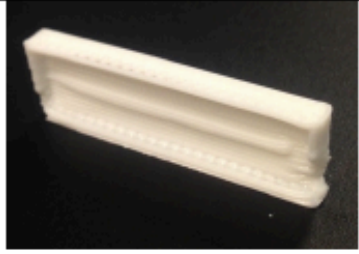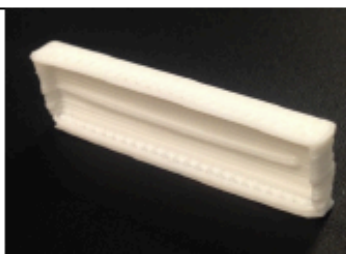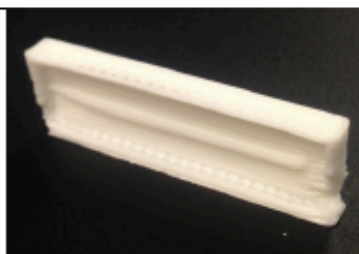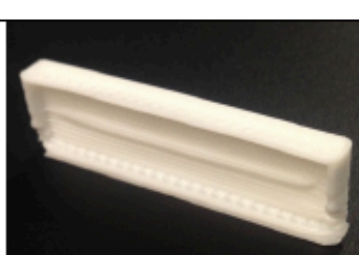
### 5.4.1 Inverse mould fabrication
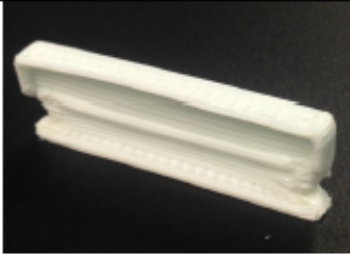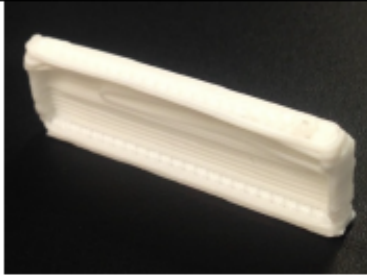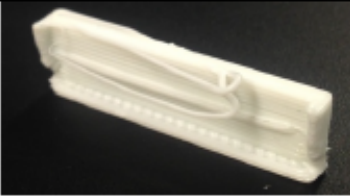
Polypropylene was utilised for the preliminary work aimed at understanding the effect of the process parameters on material extrusion parts. Polypropylene was used instead of Nylon due to its availability at the time the work was carried out. In material extrusion both materials have similar processing characteristics and provide similar challenges. This includes high extrusion temperature of greater than 250°C, as such, providing a large differential to room temperature promoting warping. Also, both materials do not adhere to common FDM surfaces such as PEI, hence layering the build surface was required. The fabrication on the reactor was carried out in Nylon. The build experiment carried out investigated a nozzle temperature range of 200°C to 270°C, a bed temperature of 125°C to 130°C and the use of an internal/external fan to cool the parts between layers, Table 19 and Table 20. The experiments can be divided into S/N 1-3, 4-8 and 9-14. For discussion, the nozzle temperature is described as low between 200°C to 240°C and high at 245°C to 270°C. S/N 1-3 parts were manufactured at high temperature with external cooling while 4-8 were fabricated in the high temperature range without external cooling. Parts 9-14 were fabricated at the low temperature without external cooling, though all the parts were built using similar bed temperature. Polypropylene (PP) showed low adhesion to the build surface, hence setting the bed temperature above 125°C was important to hold the parts to the surface during build. The melt temperature of PP is 130°C, hence temperatures lower than 125°C on the build bed led to movement of the parts during build and failures. From the images, it can be observed that some of the parts produced are closer in geometry to the intended

model. The parts 1-3 (Table 22) show the closest to the required geometry. This was as a result of the influence of the three parameters studies. The build plate temperature was higher than 125°C, which is suitable for adhesion to the base. The nozzle temperatures were at the range which allowed the polymer flow and bond with subsequent layers. Introducing a cooling fan served the purpose of reducing heat build-up. Although the temperature on the build base aided bonding, it held the temperature of the deposited polymers hindering cool down to ensure solid state bonding of the next layer.

A disfigured geometry can be seen in parts 5-11 (Table 22), which were manufactured at 220 – 270°C without a cooling fan. In these parts the bottom half closer to the plate can be seen to fold inward and not provide a distinct shape. In part 4, one of the sides was cooled with the machine's cooling fan, which is one side of the nozzle. Hence, a side can be observed to be defined leaving the other deformed. Employing lower nozzle temperatures parts 12-14 (Table 22) without a cooling fan assisted in improving the definition of the bottom layers. However, the final layers were deformed and showed signs of poor inter-layer bonding. This was because at the final few layers, the heat resulting from conduction from the heated bed was reduced and the polymer was deposited unto a cooled layer.

Table 22: Inverse mould parts fabricated by material extrusion using a Lulzbot Taz 4 machine at varying process parameters. Where NT represents nozzle temperature, BT represents base temperature, MF represents manual fan and EF represents external fan.

| 1 NT: 250°C BT: 125°C MF: OFF EF: ON |  | 8 NT: 250°C BT: 120°C MF: OFF EF: OFF |  |
|---|---|---|---|
| 2 NT: 250°C BT: 125°C MF: OFF EF: ON |  | 9 NT: 240°C BT: 125°C MF: OFF EF: OFF |  |
| 3 NT: 245°C BT: 125°C MF: OFF EF: ON |  | 10 NT: 230°C BT: 125°C MF: OFF EF: OFF |  |
| 4 NT: 250°C BT: 125°C MF: ON EF: OFF |  | 11 NT: 220°C BT: 125°C MF: OFF EF: OFF |  |
| 5 NT: 270°C BT: 130°C MF: OFF EF: OFF |  | 12 NT: 210°C BT: 125°C MF: OFF EF: OFF |  |

| 6 | | 13 | |
|---|---|---|---|
| NT: 260°C<br>BT: 130°C<br>MF: OFF<br>EF: OFF |  | NT: 200°C<br>BT: 125°C<br>MF: OFF<br>EF: OFF |  |
| 7 | | 14 | |
| NT: 250°C<br>BT: 125°C<br>MF: OFF<br>EF: OFF |  | NT: 200°C<br>BT: 125°C<br>MF: OFF<br>EF: OFF |  |

Extrusion based materials such as PLA and ABS do not require elevated temperatures to adhere the build to the PEI build plate. Hence the parts produced using such materials can provide more defined geometries without extensive optimisation, Figure 112. As polypropylene requires temperature to keep it bonded to the build plate, higher temperatures were suitable for the bottom layers with reduction in temperature towards the topmost layer of the build.
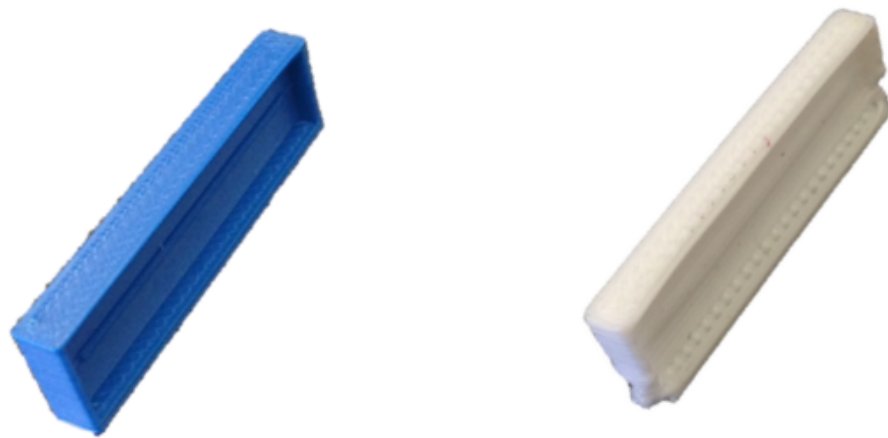
Figure 112: ABS (left) vs Polypropylene (right) in the manufacture of the inverse mould

**5.4.2 Effect of extrusion rate on part geometry**

It can be observed that at the lowest extrusion rate of 20.4mm/s, using a 0.5mm nozzle diameter, the build is observed to be the least dense, Table 23. The parts become denser with increased extrusion rate. It is crucial that the reactor is completely dense to avoid leaks. In the study, the gaps between each trace reduced with increase in extrusion rate from 20.4 mm/s to 28.1 mm/s. At 28.1 mm/s, over-lapping of the polymers is observed, without any gaps. This would be most suitable for reactor fabrication to ensure leak-free builds. With further increase in extrusion rate, the parts and base polypropylene start to deform. The effect increases with the build-up of layers. Much lower nozzle temperatures resulted in poor interlayer bonding due to reduced flow of the polymer.

Table 23: Two Polypropylene layers deposited on a polypropylene sheet using an extrusion-based machine at extrusion rate of 20.4 mm/s to 28.1 mm/s. Three repeats were carried out for at each extrusion rate, shown in the rows.



A combination of parameters affect the geometry and physical parameters of the build. An experiment was designed using a combination of the extrusion rate and nozzle temperature. This is presented in Figure 113, where two similar parts were fabricated at an extrusion rate of 22.9mm/sec. In the first build case, Figure 113 a&c, the nozzle temperature was fixed at 270°C for all the layers, while in the second case, Figure 113 b&d, the initial 3 layer were deposited at 270°C while subsequent layers were deposited at between 250°C to 240°C at the final layer.
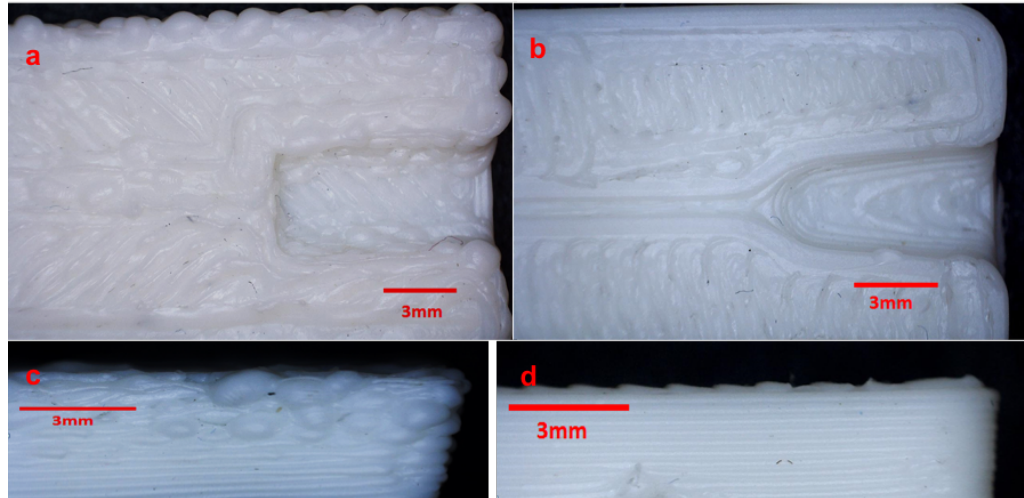
Figure 113: Images showing polypropylene parts built at an extrusion rate of 22.9mm/sec. a&c) at fixed nozzle temperature of 270°C b&d) with dynamic nozzle temperature. Initial 3 layers deposited at 270°C while subsequent layers are deposited between 250°C to 240°C at the final layer.
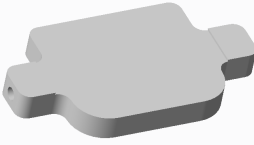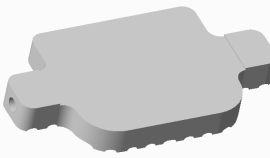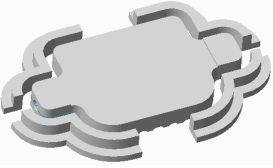
The build in both cases used a high extrusion rate to ensure sealing of the parts. The images in the first case show a deformed part compared to the later which has a defined shape similar to the design intent. The parts were built at a bed temperature of 125°C which is close to the melt temperature of PP at 130°C, whilst the deposited polymer was extruded at 270°C for the bottom layers. The higher temperature of the nozzle at the bottom layers was favourable to ensure the parts adhere to the build base. However, with several layers being deposited the layers were held at above 125°C as set. As extruded material was much higher than the melt temperature, the subsequent layers do not cool lower than the melt temperature to solidify. The FDM process requires the material to be deposited at semi-solid state whilst being bonded by a subsequent layer in its solid state. This effect is more pronounced in smaller parts and features than in build with larger surface area. This is because with a larger surface area, the time
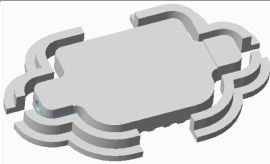
required for deposition of a layer is increased, allowing the warmer region to cool to its solid, more rigid, state before subsequent warmer deposition.

### 5.4.3 Bioreactor manufacture

The fabrication of the reactor was done by iterative method, i.e making modification to the design based on the result of a subsequent trial iteration, with the aim of achieving near net geometry to the design intent. The iterative process is described in Table 24. The initial challenge with fabricating in Nylon is the poor adhesion to the build plate. UHU glue stick was layered on the surface to enhance adhesion during the building process. Trial 1 was fabricated as designed with print conditions at 0.3mm layer height, nozzle temperature 235°C and bed temperature at 100°C. As seen in Table 24, the build warped and peeled of the bed half way through the build, giving the reactor a deformed geometry. On testing, the reactor was found to be blocked. In the next design iteration, cut outs were added to the bottom of the reactor like a track. This was aimed at breaking up the bottom layer into sections to minimise warping at the longer side of the reactor. Thus, in the fifth testing which also showed improvements to the part geometry. Three further reactors were produced using the final conditions without any blockages or leaks.

Table 24: Iterative process of modifying the process parameters to aid fabrication of an AM extrusion-based bioreactor.

| S/N | Print Conditions | CAD model | Fabricated part | Comments |
|---|---|---|---|---|
| 1 | Layer height: 0.3mm Nozzle temp: 235ºC Build temp: 100ºC | | | The designed reactor device was fabricated on the platform as designed. The build warped and went off the build bed half way before completing. (Blocked reactor) |
| 2 | Layer height: 0.3mm Nozzle temp: 230ºC Build temp: 100ºC | | | 'Tracks' were then added to the device, which aimed to break up the bottom layers and reduce warp. The build completed, however it still had a high degree of warpage causing the channels to block. (Blocked reactor) |
| 3 | Layer height: 0.3mm Nozzle temp: 230ºC Build temp: 100ºC | | | Increased the extraction flow rate of the fume cupboard to minimise build-up of temperature. This minimised warp and reduced the blistering effect see in the layers. (Blocked reactor) |
| 4 | Layer height: 0.3mm Nozzle temp: 230ºC – 215ºC Build temp: 100ºC | | | Although the heated platform at 100 °C assisted adhesion of the build, this led to an over-heated bottom layers of the part noticed in previous builds. Two tactics were employed: (a) Edge temperature controllers around the part (b) A dynamic deposition temperature reduction from bottom layers to the top to compensate for the temperature of the build bed. |

| 5 | Layer height: 0.3mm Nozzle temp: 230ºC – 215ºC Build temp: 100 ºC | | | (230-215 °C) (No blockage) Further increased the extraction flow rate of the fume cupboard with the parameters in test 4. Three further reactor devices were fabricated for experimentation using this condition without a blockages. |
|---|---|---|---|---|

The final geometry obtained from the iterative process, Test 5, was then repeated three times. The devices were found to be leak free and similar. The track on the bottom of the print allowed for adhesion to the build bed, while the blocks designed around the build in test 4 & 5, assisted the retention of heat. This led to the fabrication of a device with minimal warp. The selected conditions were a layer resolution of 0.3mm, build and nozzle temperature of 100 ºC and 230 – 215 ºC respectively.

### 5.4.4 Functionalisation of the FDM reactor

The treatment with HCl (5M), and subsequent reaction with Glutaraldehyde created a functional surface for linkage with the enzyme. This is evident in the prior functionalisation on the surface of pieces of FDM fabricated Nylon piece, which showed the presence of a characteristic aldehyde C=O band at 1719 cm$^{-1}$ in the ATR-IR spectra [173]. This modification was accompanied with a change of colour from white to light orange. The immobilisation of enzyme (R)- ω-TA on the surface of the fabricated piece was confirmed by ATR-FTIR, as the disappearance of the aldehyde band and the introduction of amide-II bands 1550cm$^{-1}$ was observed from the fully functionalised polymer [173]. It is worth noting that the volume of the reactor decreased from 0.8ml to 0.5ml after functionalisation resulting in increased pressure when flowing the solvents through the reactor. At the initial flow rate assayed 25 µL·min$^{-1}$, the solution of 5 mM rac-methylbenzylamine, 5mM pyruvic acid and 0.1mM PLP was at 20 min. After 5 h of time on stream, a conversion of the 48% of the (R) enantiomer on the amine into ketone was observed. Thus, (S)-methylbenzylamine was obtained with an enantiomeric excess of 93±2% e.e., as determined by HPLC. The low residence time of 20 min resulted in a productivity of 20.5 µmol h$^{-1}$ mg$_{enz}$. This is comparable to the batch experiment performed under similar conditions, thus indicating that the enzyme activity is retained.
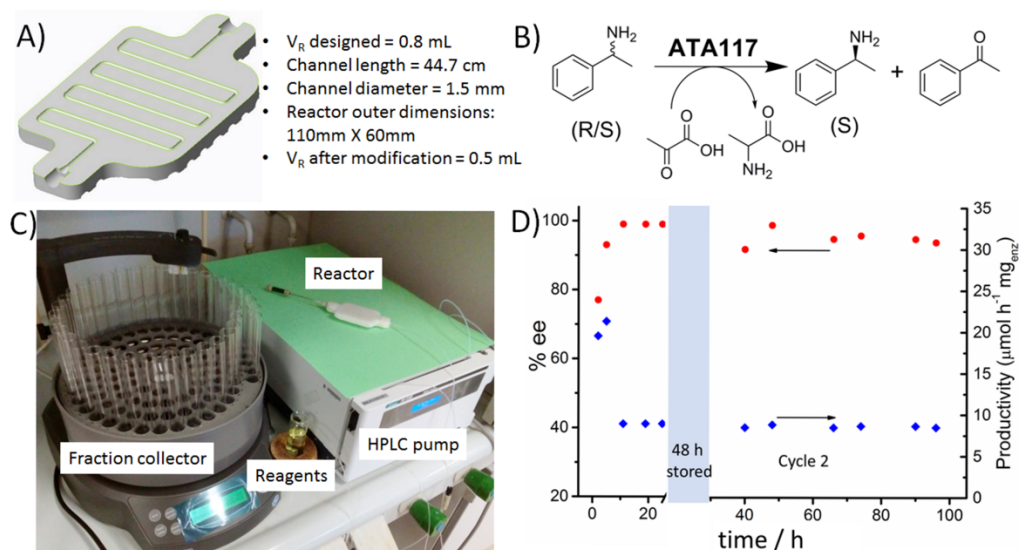
Figure 114: Continuous-flow biocatalytic reactors for the kinetic resolution of rac-methylbenzylamine. A) CAD of the bioreactor and main reactor parameters. B) Kinetic resolution of rac-methylbenzylamine employing ATA 117 supported on the 3D printed bioreactor. C) Experimental set-up employed for the continuous-flow biocatalytic transformation. D) Productivity and enantiomeric excess observed as a function of time. The first two data points correspond to experiments assayed at 25 µL·min$^{-1}$, while the rest were assayed at 10 µL·min$^{-1}$. The plot represents two separate runs under continuous-flow, the first of them for 24 h, followed by a 48h storage in fresh buffer and a subsequent run for further 78 h. The results indicate the activity and stability of the enzyme, by keeping its activity over extended periods of time (ca. 100 h) under continuous-flow streams.

Table 25: Results for the enzymatic enantiomeric resolution of MBA under continuous flow conditions.

| Time (h) | Flow (ml/min) | Conversion (%) | %ee |
|----------|---------------|----------------|-----|
| 2 | 0.025 | 87/44 | 77 |

223

| 5 | 0.025 | 96/48 | 93 |
|---|---|---|---|
| 11 | 0.01 | 99.9/49.9 | 99.9 |
| 19 | 0.01 | 99.9/49.9 | 99.9 |
| 25 | 0.01 | 99.9/49.9 | 99.9 |
| Stored in buffer at 4 °C for 48 h. | | | |
| 28 | 0.01 | 88/44 | 78 |
| 40 | 0.01 | 96/48 | 92 |
| 48 | 0.01 | 99.9/49.9 | 99.9 |
| 66 | 0.01 | 97/48 | 95 |
| 74 | 0.01 | 98/49 | 96 |
| 90 | 0.01 | 98/49 | 95 |
| 96 | 0.01 | 97/48 | 94 |

The flow rate was reduced to 10 $\mu L \cdot min^{-1}$ in order to test the temporal stability of the bioreactor and the reaction was carried out for an additional 20 hours. At this flow rate, corresponding to a residence time of 50 min, almost full conversion of the (R)-enantiomer was observed (>49 %) yielding the (S)-amine with an enantiomeric excess >99 % *e.e.* In order to evaluate the stability of the biocatalytic system, the reactor was flushed with buffer and stored at 4 °C for 48 hours. Afterwards, a second cycle was performed under the same experimental conditions (10 $\mu L \cdot min^{-1}$, 5mM *rac*-methylbenzylamine, 5mM pyruvic acid, 0.1mM PLP) and the flow system was maintained for a further 78 hours. During this period, the activity and enantioselectivity of the bioreactor was maintained with *e.e.* >94%. These results demonstrate that the enzyme can be effectively immobilized on printed flow bioreactors, and the productivity of the system is greatly enhanced by the flow conditions. A total of 105 catalytic cycles were performed with the same enzyme. This work has demonstrated the first example

of enzyme immobilization on modified 3D printed continuous flow biocatalytic reactors and paves the way for numerous applications in industrial biotechnology. The possibility of rapidly testing different immobilization mechanisms and conditions, that are easily transferred to continuous-flow bioreactors with tailored geometries will allow for the development of numerous applications. Significantly, the ω-TA enzymes tested showed a comparable activity to the free enzyme and were successfully recycled.

## 5.5 Summary

The utilisation of material extrusion AM method in the development of flow reactors was studied. Process parameters and conditions such as nozzle temperature, build bed temperature, extrusion rate and room temperature was demonstrated to significantly affect the geometry and physical properties of the build. Optimising the process parameters alongside the geometry for fabrication, aided the development of leak free reactors for a number of applications. The functionalisation of the fabricated reactor by immobilising enzymes on the internal wall surface was also carried out successfully. At a residence time of 50 min almost full conversion of the (*R*)-enantiomer was observed (>49 %) yielding the (*S*)-amine with an enantiomeric excess >99 % *e.e* for a run time of 25 h dropping slightly when run for a further 78 h. This work demonstrates the first example of modified AM devices for the immobilization and application of ω-transaminase (ω-TA) enzymes in continuous-flow.

# Chapter 6. Summary and Concluding remarks

The immense benefit of empowering researchers with cost-effective tools to manufacture bespoke mesoscale flow devices has been demonstrated in the number of applications that has been investigated. Using methods presented, flow reactors can be designed, manufactured and optimised using low cost AM machines. Three applications have been demonstrated, with the common theme being the utilisation of an additive manufacturing platform to develop mesoscale flow devices that allow enhanced mass transport, heat transfer properties and provide added functionalities. The strength of AM, which is beneficial for flow reactor manufacture, is in the ability to manufacture 3 dimensionally complex geometries specifically in flow channels. The mass transport improvements shown when utilising advanced flow reactors with static mixers, has been demonstrated in the synthesis of Silver nanoparticles in a mesoscale AM reactor. Improvements to the particle size distribution, stability of the system and fouling reduction was demonstrated. These enhancements can also potentially be translated to any other suitable process requiring fine mixing of reagents. The design freedom Additive manufacturing provides open the possibility of fabricating bespoke flow reactors with added functionalities, as well as, fit with standard fittings and laboratory instruments. This provides a valuable tool to researchers to rapidly introduce sensors, detectors and inline monitoring instruments for reaction analysis such as UV/Vis and NMR.

Though the use of additive manufacturing in flow reactor design and manufacturing presents numerous benefits, each technique requires full

consideration as they have unique properties. As each technique offers distinct equipment and processing conditions, the materials utilised, and the resulting physical properties of the devices are different. Though these techniques and available materials are constantly evolving, the ranking for the suitability of each technique for mesoscale flow reactor manufacture will largely depend on the following, in no particular order: 1. Suitability to manufacture leak free devices 2. Availability of material resistant to a wide range of solvents 3. Availability of materials with adequate thermal and mechanical properties for high temperature applications 4. Suitability to provide precision for lab-scale flow reactor applications 5. Ease of post processing, including clearing the channels of support materials 6. Adequate process reproducibility and ease of process optimisation.

Material extrusion is one of the most common and readily available AM techniques and has been utilised in a number of flow reactor application. There are a wide range of available machines from the low-cost benchtop system to more industrial units. Though higher-grade machines have the potential to provide better control of the process conditions, flow devices are still restricted to more simplistic shapes. This is due to the difficulty of reproducibly fabricating water-tight flow device whilst providing lower build resolution when compared to some powder based and vat polymerisation methods. Thus, this limits it utilisation at elevated pressures. In FDM, a common material extrusion method, the material selection for the flow devices is restricted to thermoplastics, with more solvent resistant materials such as Nylon and polypropylene being more challenging to build in and adhere to the build plate. This however limits its

utilisation in applications requiring strong solvents and elevated temperatures. Material extrusion technique is still highly beneficial for developing prototype flow devices which can later be manufactured using a different method or for the manufacture of single use devices due to the low material cost.

Vat polymerisation is another low-cost platform investigated for flow reactor manufacture. Available machines provide sufficient precision required for mesoscale reactor manufacture when working at optimum conditions. Due to the characteristic method of photopolymerising resin to subsequent layers by a light source or laser, a water-tight seal is created between layers. As such, fully dense parts can be manufactured having more complex internal structures when compared to material extrusion. The drawback to VP is in the current lack of availability of solvent resistant materials for chemical processing applications. It is also unsuitable for high temperature applications due to poor thermal conductivity of current materials. With the development of new materials specifically ones with resistance to a wide range of solvents, VP will be an excellent process for the manufacture of mesoscale flow devices.

Though not experimented in this work, powder-based methods rank excellently for mesoscale flow reactor manufacture based on the requirements. Selective laser melting meets all the requirements for the manufacture of flow reactors including precision, availability of solvent resistive materials and the unique ability to provide reactors that can be used at elevated temperatures and pressures. Laser sintering platforms can also provide adequate precision for flow reactor manufacturing as well as leak free devices. The drawback to powder

based techniques is the difficulty to clear out channels of the unfused powder. This is an issue which increases with the complexity of the flow channel path. Though powder-based methods can be more expensive than material extrusion and vat polymerisation machines, the expiration of patents and recent developments will continue to drive cost down and increase availability.

As such, future work will ideally investigate the utilisation of powder-based methods such as SLM and LS in the development of more complex flow devices which will enhance mass transport, improved heat transfer properties and provide added functionalities.

This research has built on initial work on the utilisation of AM for flow reactor manufacture with the move towards AM advanced flow reactors. This research has demonstrated the development and investigation of an advanced mesoscale flow device based on continuous oscillatory baffle reactor technology for monodispersed Ag-np formation. The combination of the static and active mixing processes provided improved mixing which translated to improved control of particle size. Secondly, an advanced flow crystalliser was investigated and developed allowing inline process monitoring to be carried out. This demonstrated the selective production of a preferential polymorph of paracetamol using a bespoke AM device. Thirdly, a modified AM device was investigated and developed, creating functionality of the reactor wall surface by immobilising enzymes that produced full conversion of a transamination reaction.

Ultimately, AM will serve as a valuable tool in research facilities for inhouse, rapid design and development of advanced flow reactors for discovery and fine tuning of new materials and processes.

# Appendix

*Paracetamol study diffractograms (Chapter 4)*

The diffractograms for the collected samples are plotted against CSD reference HXACAN01 – PC monoclinic form I, HXACAN26 - PC orthorhombic form II and MENSEE – MCM form I. The powder particles from the first run were collected after 20min, while the on the second run, they were collected at intervals of 10, 30 and 60 min (denoted as T10, T30 and T60 on the plots).
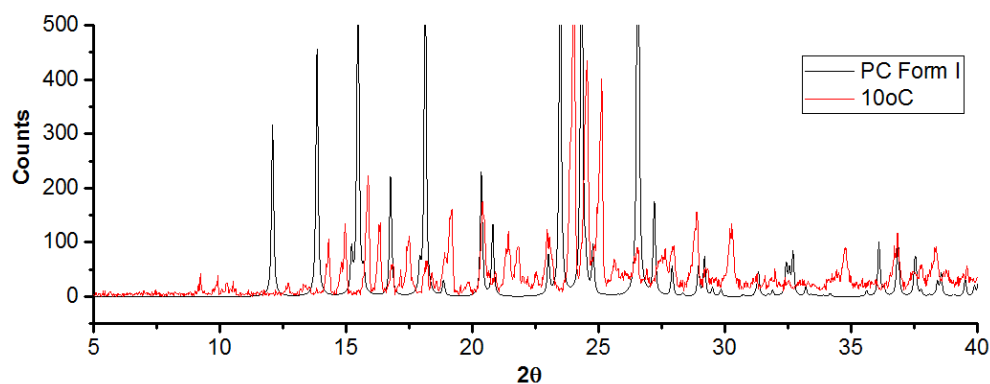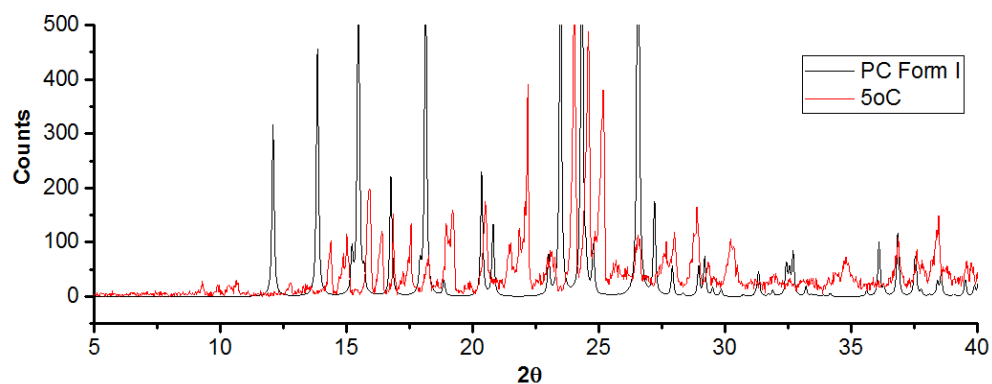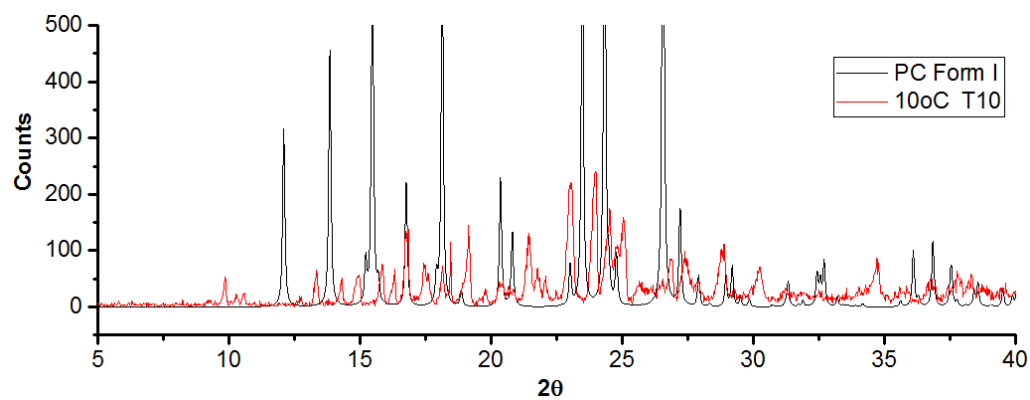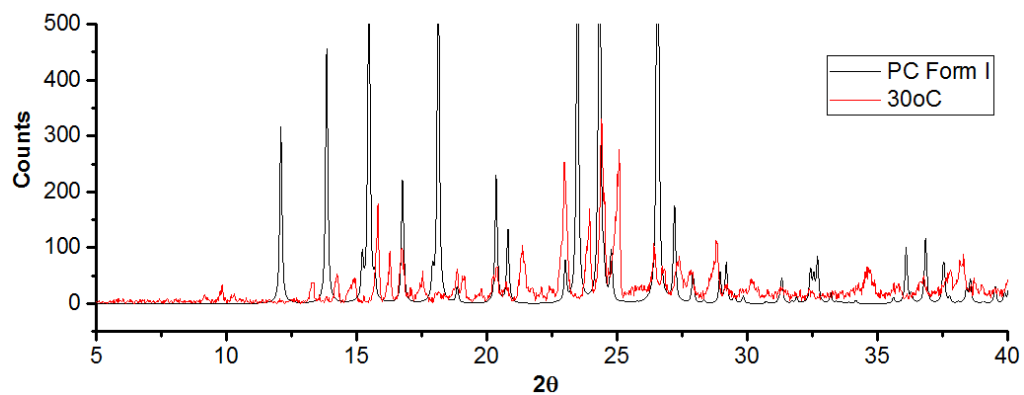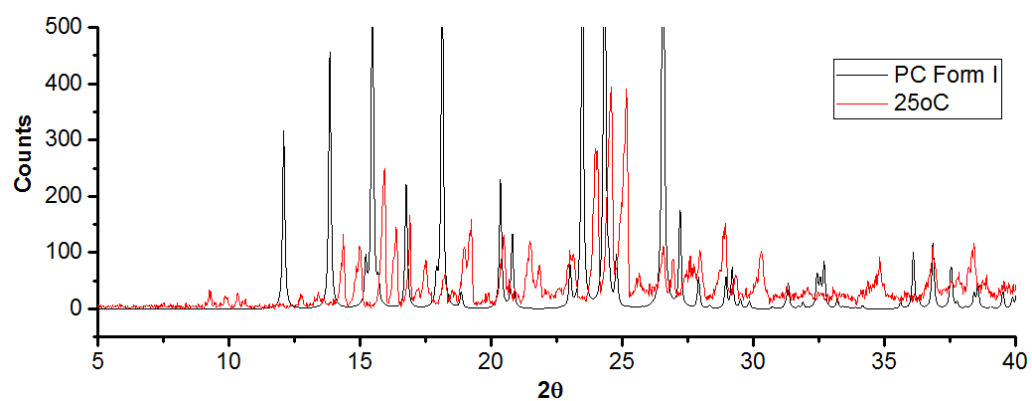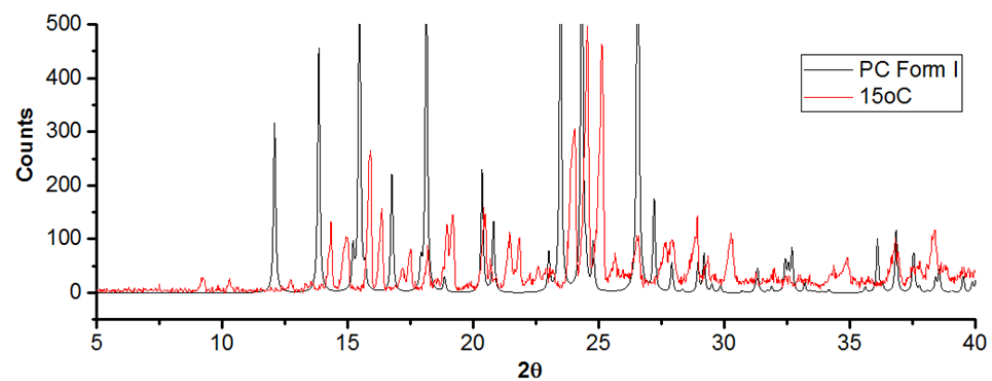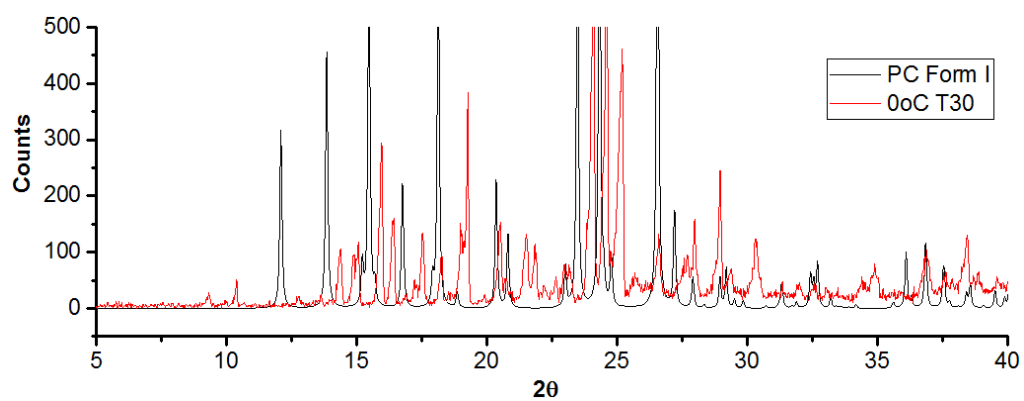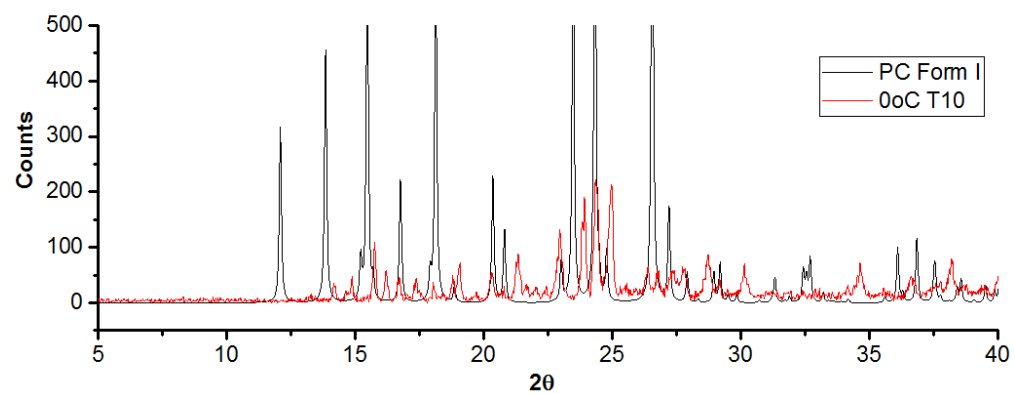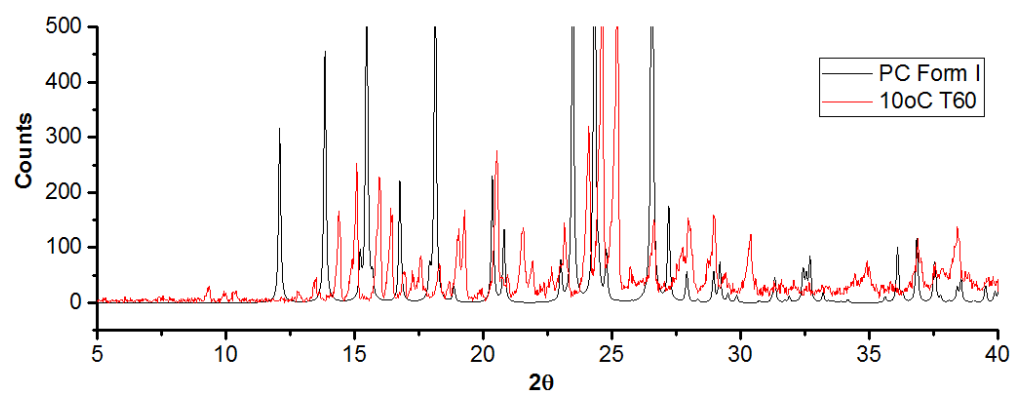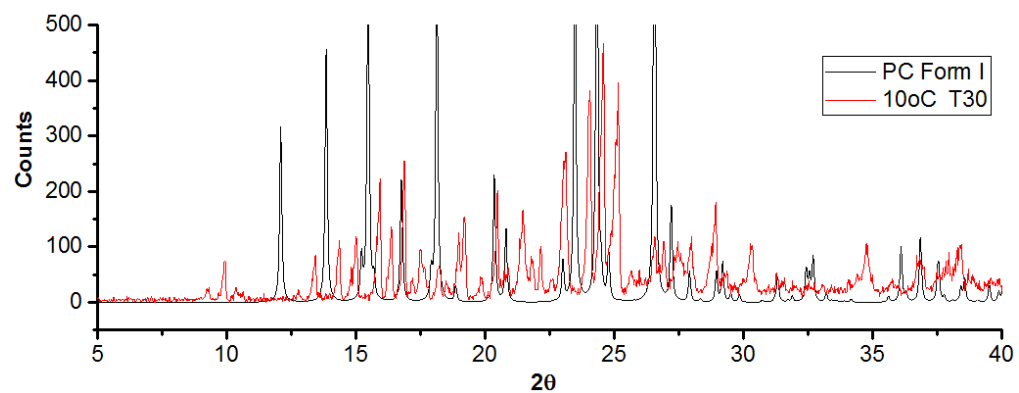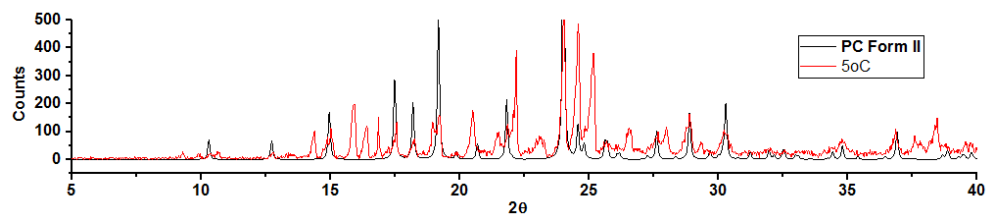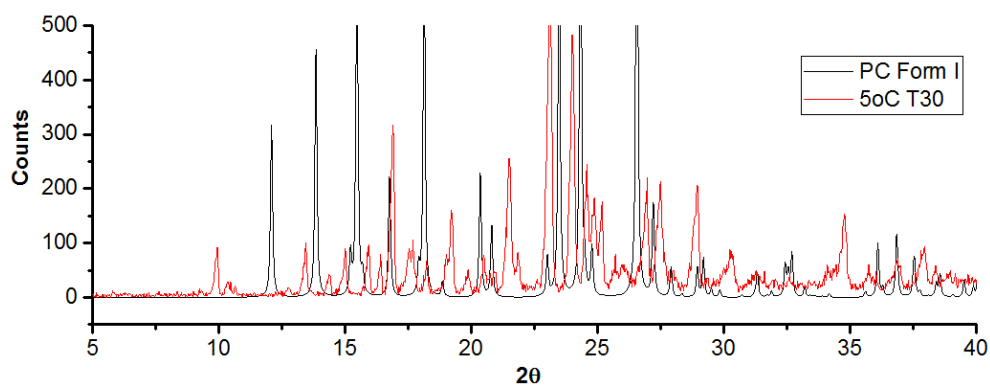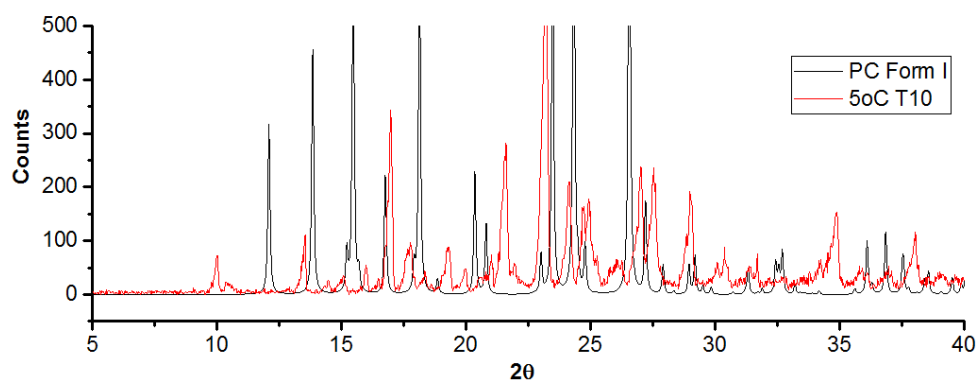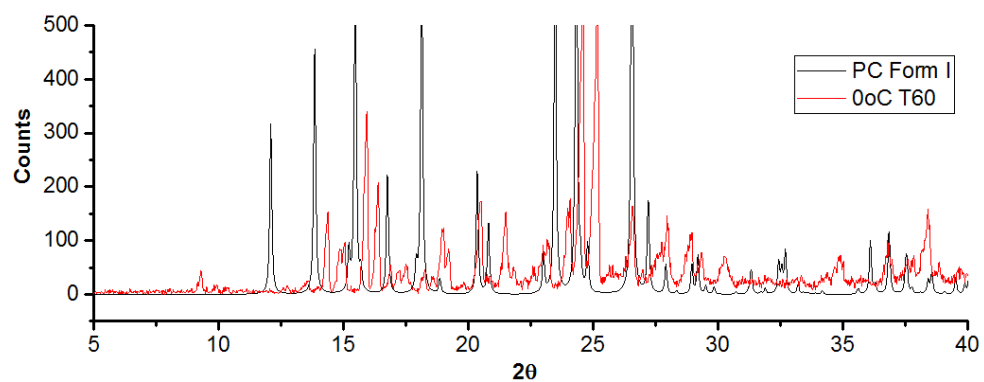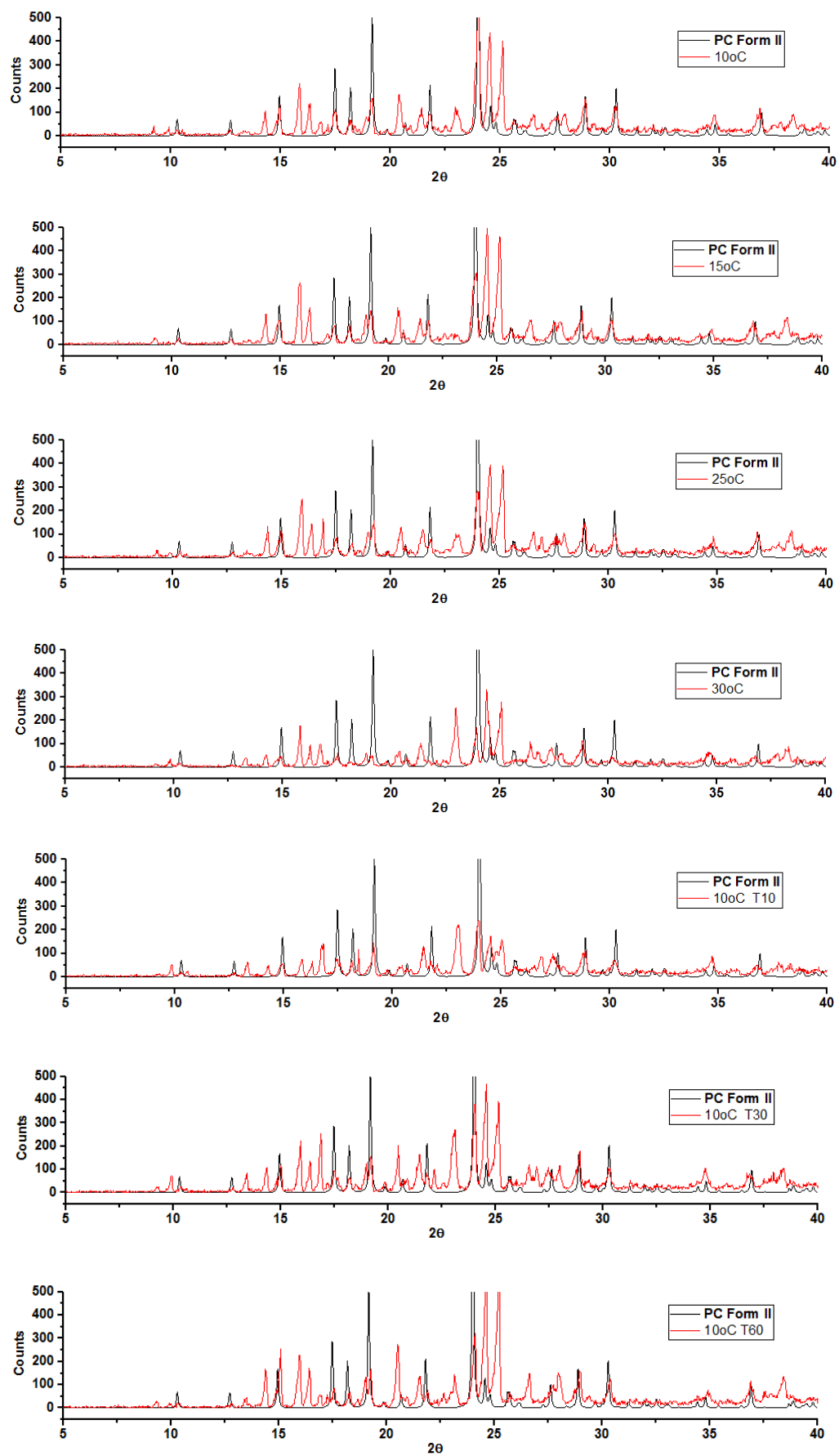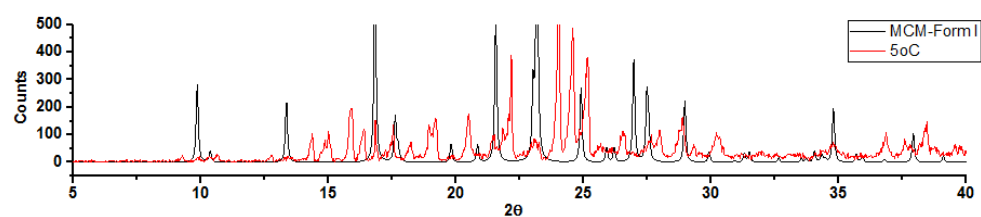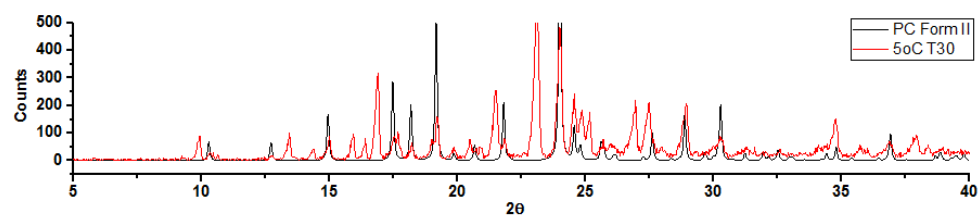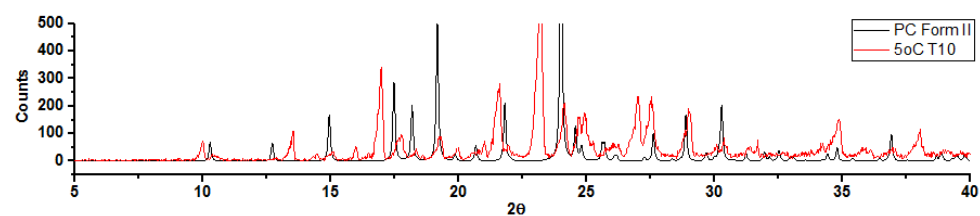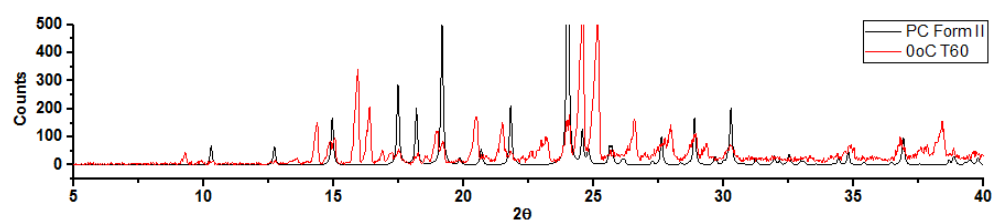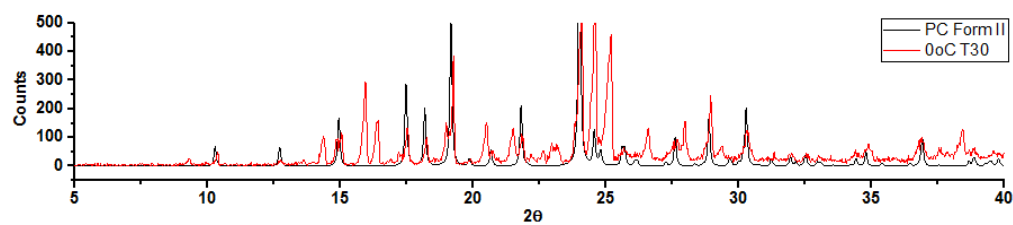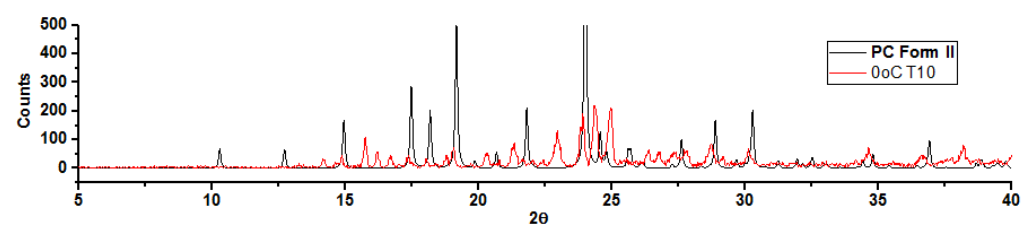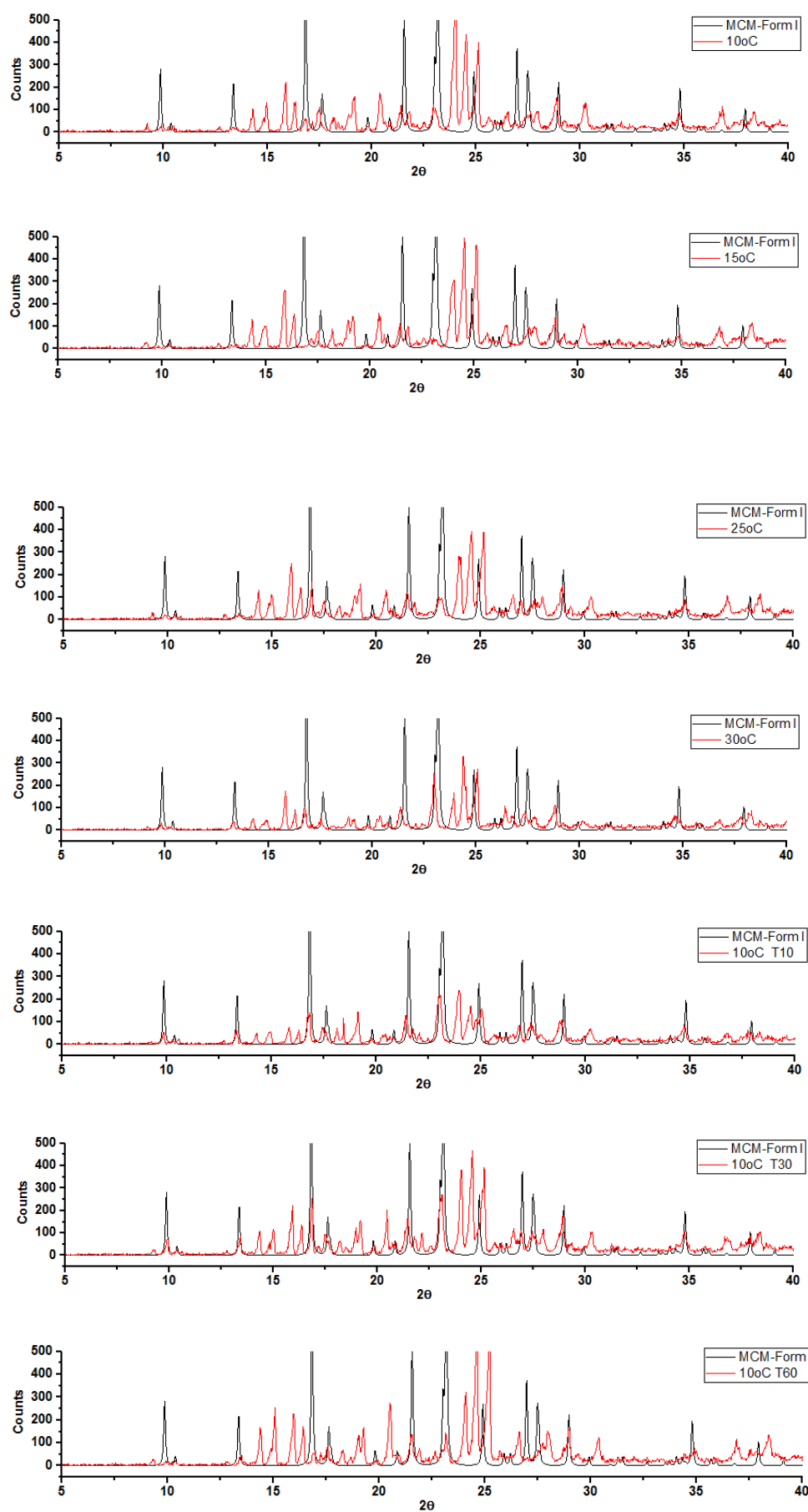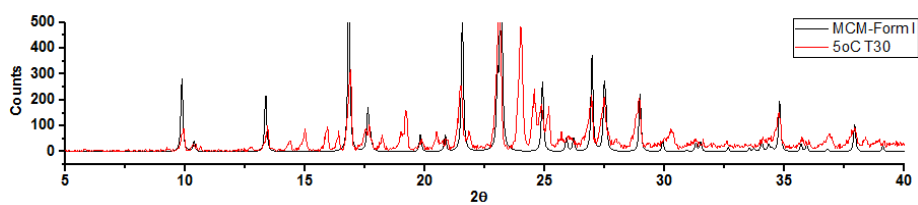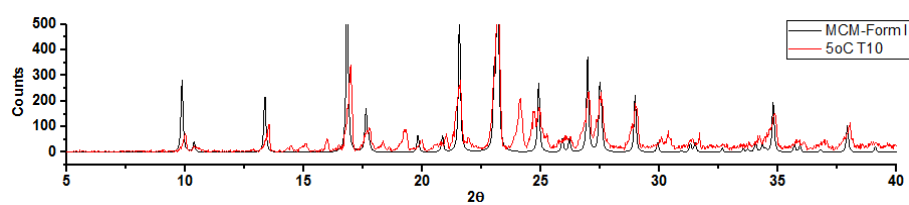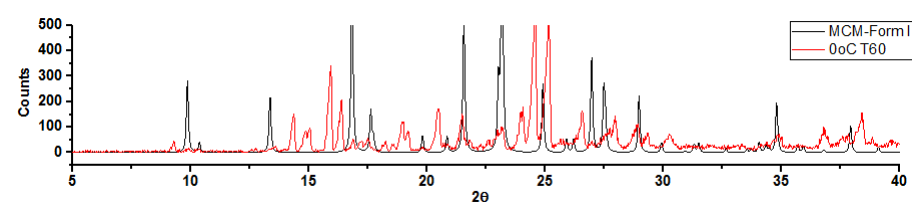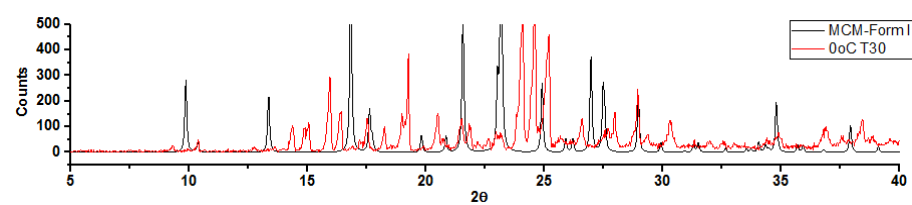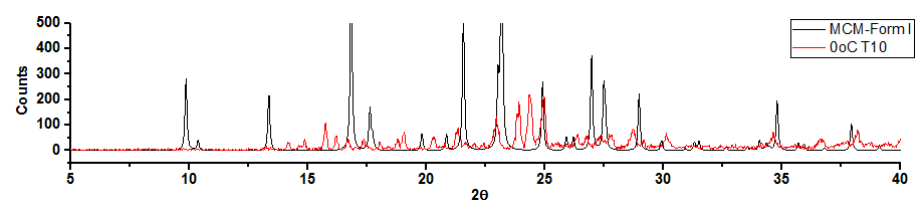
# References

1.      Hartman, R.L., J.P. McMullen, and K.F. Jensen, *Deciding whether to go with the flow: evaluating the merits of flow reactors for synthesis.* Angewandte Chemie International Edition, 2011. **50**(33): p. 7502-7519.

2.      Wiles, C. and P. Watts, *Continuous flow reactors: a perspective.* Green Chemistry, 2012. **14**(1): p. 38-54.

3.      Lawton, S., et al., *Continuous crystallization of pharmaceuticals using a continuous Oscillatory baffled Crystallizer.* Organic Process Research & Development, 2009. **13**(6): p. 1357-1363.

4.      Towler, G. and R. Sinnott, *Chemical engineering design: principles, practice and economics of plant and process design*. 2012: Elsevier.

5.      Zhou, Y., *The recent development and applications of fluidic channels by 3D printing.* J Biomed Sci, 2017. **24**(1): p. 80.

6.      Capel, A.J., et al., *3D printed fluidics with embedded analytic functionality for automated reaction optimisation.* Beilstein Journal of Organic Chemistry, 2017. **13**: p. 111-119.

7.      Stankiewicz, A.I. and J.A. Moulijn, *Process intensification: Transforming chemical engineering.* Chemical Engineering Progress, 2000. **96**(1): p. 22-34.

8.      Hessel, V., H. Löwe, and F. Schönfeld, *Micromixers—a review on passive and active mixing principles.* Chemical Engineering Science, 2005. **60**(8): p. 2479-2501.

9.      Stone, H.A., A.D. Stroock, and A. Ajdari, *Engineering flows in small devices: Microfluidics toward a lab-on-a-chip.* Annual Review of Fluid Mechanics, 2004. **36**: p. 381-411.

10.     Phan, A.N. and A. Harvey, *Development and evaluation of novel designs of continuous mesoscale oscillatory baffled reactors.* Chemical Engineering Journal, 2010. **159**(1): p. 212-219.

11.     Levenspiel, O., *Chemical reaction engineering.* 1962.

12.     Brown, C.J., et al., *Oscillatory flow reactors (OFRs) for continuous manufacturing and crystallization.* Organic Process Research & Development, 2015. **19**(9): p. 1186-1202.

13.     Jeong, G.S., et al., *Applications of micromixing technology.* Analyst, 2010. **135**(3): p. 460-473.

14.     Mansur, E.A., et al., *A state-of-the-art review of mixing in Microfluidic mixers.* Chinese Journal of Chemical Engineering, 2008. **16**(4): p. 503–516.

15.     Lee, C.-Y., et al., *Microfluidic mixing: A review.* International Journal of Molecular Sciences, 2011. **12**(5): p. 3263-3287.

16.     Campbell, C.J. and B.A. Grzybowski, *Microfluidic mixers: From microfabricated to self-assembling devices.* 2004.

17.     Tsai, J.-H. and L. Lin, *Active microfluidic mixer and gas bubble filter driven by thermal bubble micropump.* Sensors and Actuators A: Physical, 2002. **s 97–98**: p. 665–671.

18. Deshmukh, A.A., D. Liepmann, and A.P. Pisano, *Characterization of a micro-mixing, pumping, and valving system*, in *Transducers' 01 Eurosensors XV*. 2001, Springer. p. 922-925.

19. Fu, L.-M., et al., *A novel microfluidic mixer utilizing electrokinetic driving forces under low switching frequency.* Electrophoresis, 2005. **26**(9): p. 1814-1824.

20. Wen, C.-Y., et al., *Rapid magnetic microfluidic mixer utilizing AC electromagnetic field.* ELECTROPHORESIS, 2009. **30**(24): p. 4179-4186.

21. Choi, E., B. Kim, and J. Park, *High-throughput microparticle separation using gradient traveling wave dielectrophoresis.* Journal of Micromechanics and Microengineering, 2009. **19**(12): p. 125014.

22. Yang, Z., et al., *Ultrasonic micromixer for microfluidic systems.* Sensors and Actuators A: Physical, 2001. **93**(3): p. 266–272.

23. Nguyen, N.-T. and Z. Wu, *Micromixers—a review.* Journal of Micromechanics and Microengineering, 2004. **15**(2).

24. Lin, C.-H., et al., *Rapid circular microfluidic mixer utilizing unbalanced driving force.* Biomedical Microdevices, 2006. **9**(1): p. 43-50.

25. Schönfeld, F., C. Hofmann, and V. Hessel, *An optimised split-and-recombine micro-mixer with uniform 'chaotic' mixing.* Lab Chip, 2004. **4**(1): p. 65-69.

26. Hossain, S. and K.-Y. Kim, *Mixing analysis in a three-dimensional serpentine split-and-recombine micromixer.* Chemical Engineering Research and Design, 2015. **100**: p. 95–103.

27. Mason, B.P., et al., *Greener approaches to organic synthesis using Microreactor technology.* Chemical Reviews, 2007. **107**(6): p. 2300-2318.

28. Ahmed, S.M.R., A.N. Phan, and A.P. Harvey, *Mass transfer enhancement as a function of oscillatory baffled reactor design.* Chemical Engineering and Processing, 2018. **130**: p. 229-239.

29. Stroock, A.D. and G.J. McGraw, *Investigation of the staggered herringbone mixer with a simple analytical model.* Philosophical Transactions of the Royal Society of London. Series A: Mathematical, Physical and Engineering Sciences, 2004. **362**(1818): p. 971-986.

30. Lynn, N.S. and D.S. Dandy, *Geometrical optimization of helical flow in grooved micromixers.* Lab on a Chip, 2007. **7**(5): p. 580-587.

31. Kee, S.P. and A. Gavriilidis, *Design and characterisation of the staggered herringbone mixer.* Chemical Engineering Journal, 2008. **142**(1): p. 109-121.

32. Pereira, F.M., et al., *CO 2 dissolution and design aspects of a Multiorifice Oscillatory baffled column.* Industrial & Engineering Chemistry Research, 2014. **53**(44): p. 17303-17316.

33. Brunold, C.R., et al., *Experimental observations on flow patterns and energy losses for oscillatory flow in ducts containing sharp edges.* Chemical Engineering Science, 1989. **44**(5): p. 1227-1244.

34. Hobbs, D.M. and F.J. Muzzio, *Reynolds number effects on laminar mixing in the Kenics static mixer.* Chemical Engineering Journal, 1998. **70**(2): p. 93-104.

35. McDonough, J.R., et al., *Oscillatory fluid motion unlocks plug flow operation in helical tube reactors at lower Reynolds numbers (Re <= 10).* Chemical Engineering Journal, 2019. **358**: p. 643-657.

36. Thakur, R.K., et al., *Static Mixers in the Process Industries—A Review.* Chemical Engineering Research and Design, 2003. **81**(7): p. 787-826.

37. Sulzer.com. *SMX™ plus Static Mixer*. [cited 2019 24th August 2019]; Available from: https://www.sulzer.com/-/media/files/products/static-mixers/flyer_smx_plus_d.ashx.

38. Chemineer.com. *Kenics KM Mixer*. [cited 2019 24th August]; Available from: https://www.chemineer.com/products/kenics.html.

39. Gough, P., X. Ni, and K.C. Symes, *Experimental flow Visualisation in a modified pulsed baffled reactor.* Journal of Chemical Technology & Biotechnology, 1997. **69**(3): p. 321-328.

40. Okafor, O., et al., *Advanced reactor engineering with 3D printing for the continuous-flow synthesis of silver nanoparticles.* Reaction Chemistry & Engineering, 2017. **2**(2): p. 129-136.

41. Reis, N., et al., *Residence times and mixing of a novel continuous oscillatory flow screening reactor.* Chemical Engineering Science, 2004. **59**(22-23): p. 4967-4974.

42. Agnew, L.R., et al., *Continuous Crystallization of Paracetamol (Acetaminophen) Form II: Selective Access to a Metastable Solid Form.* Crystal Growth & Design, 2017. **17**(5): p. 2418-2427.

43. Ni, X., et al., *A Systematic Study of the Effect of Geometrical Parameters on Mixing Time in Oscillatory Baffled Columns.* Chemical Engineering Research and Design, 1998. **76**(5): p. 635-642.

44. Abbott, M.S.R., et al., *Biological processing in oscillatory baffled reactors: operation, advantages and potential.* Interface Focus, 2013. **3**(1): p. 20120036.

45. Erbacher, C., et al., *Towards Integrated Continuous-Flow Chemical Reactors.* Microchimica Acta, 1999. **131**(1): p. 19-24.

46. Günther, A., et al., *Transport and reaction in microscale segmented gas–liquid flow.* Lab on a Chip, 2004. **4**(4): p. 278-286.

47. Haswell, S.J., et al., *The application of micro reactors to synthetic chemistry.* Chemical Communications, 2001(5): p. 391-398.

48. Hessel, V., et al., *Handbook of Micro Reactors*. 2009, Wiley-VCH: Weinheim.

49. Inoue, T., et al., *Direct synthesis of hydrogen peroxide using glass fabricated microreactor–Multichannel operation and catalyst comparison.* Catalysis Today, 2015. **248**: p. 169-176.

50. Hwang, Y., O.H. Paydar, and R.N. Candler, *3D printed molds for non-planar PDMS microfluidic channels.* Sensors and Actuators A: Physical, 2015. **226**: p. 137–142.

51. Gutmann, B., et al., *Design and 3D printing of a stainless steel reactor for continuous difluoromethylations using fluoroform.* Reaction Chemistry & Engineering, 2017. **2**(6): p. 919-927.

52. Capel, A.J., et al., *Design and additive manufacture for flow chemistry.* Lab on a Chip, 2013. **13**(23): p. 4583-4590.

53. Monzón, M.D., et al., *Standardization in additive manufacturing: Activities carried out by international organizations and projects.* The International Journal of Advanced Manufacturing Technology, 2014. **76**(5-8): p. 1111-1121.

54. Parra-Cabrera, C., et al., *3D printing in chemical engineering and catalytic technology: structured catalysts, mixers and reactors.* Chem Soc Rev, 2018. **47**(1): p. 209-230.

55. Waheed, S., et al., *3D printed microfluidic devices: enablers and barriers.* Lab on a Chip, 2016. **16**(11): p. 1993-2013.

56. Lu, L., et al., *Origin of shrinkage, distortion and fracture of photopolymerized material.* Materials Research Bulletin, 1995. **30**(12): p. 1561-1569.

57. Derby, B., *Additive manufacture of ceramics components by inkjet printing.* Engineering, 2015. **1**(1): p. 113-123.

58. Goodridge, R.D., C.J. Tuck, and R.J.M. Hague, *Laser sintering of polyamides and other polymers.* Progress in Materials Science, 2012. **57**(2): p. 229-267.

59. Gokuldoss, P.K., S. Kolla, and J. Eckert, *Additive manufacturing processes: Selective laser melting, electron beam melting and binder jetting—Selection guidelines.* Materials, 2017. **10**(6): p. 672.

60. Kitson, P.J., et al., *Configurable 3D-Printed millifluidic and microfluidic 'lab on a chip' reactionware devices.* Lab on a Chip, 2012. **12**(18): p. 3267-3271.

61. Dragone, V., et al., *3D-printed devices for continuous-flow organic chemistry.* Beilstein journal of organic chemistry, 2013. **9**: p. 951.

62. Kitson, P.J., et al., *Digitization of multistep organic synthesis in reactionware for on-demand pharmaceuticals.* Science, 2018. **359**(6373): p. 314-319.

63. Wang, H., S. Masood, and P. Iovenitti, *Application of fused deposition modeling rapid prototyping system to the development of microchannels.* BioMEMS and Smart Nanostructures, 2001.

64. Moore, J.L., et al., *Behavior of capillary valves in centrifugal microfluidic devices prepared by three-dimensional printing.* Microfluidics and Nanofluidics, 2011. **10**(4): p. 877-888.

65. Shallan, A.I., et al., *Cost-Effective Three-Dimensional Printing of Visibly Transparent Microchips within Minutes.* Analytical Chemistry, 2014. **86**(6): p. 3124-3130.

66. Lee, W., et al., *3D-printed microfluidic device for the detection of pathogenic bacteria using size-based separation in helical channel with trapezoid cross-section.* Scientific reports, 2015. **5**: p. 7717-7717.

67. Bracconi, M., et al., *Investigation of pressure drop in 3D replicated open-cell foams: Coupling CFD with experimental data on additively manufactured foams.* Chemical Engineering Journal, 2018.

68. Avril, A., et al., *Continuous flow hydrogenations using novel catalytic static mixers inside a tubular reactor.* Reaction Chemistry & Engineering, 2017. **2**(2): p. 180-188.

69. Movsisyan, M., et al., *Taming hazardous chemistry by continuous flow technology.* Chemical Society Reviews, 2016. **45**(18): p. 4892-4928.

70. Sans, V. and L. Cronin, *Towards dial-a-molecule by integrating continuous flow, analytics and self-optimisation.* Chemical Society Reviews, 2016. **45**(8): p. 2032-2043.

71. Sans, V., et al., *A self optimizing synthetic organic reactor system using real-time in-line NMR spectroscopy.* Chemical Science, 2015. **6**(2): p. 1258-1264.

72. Harvey, A.P., M.R. Mackley, and P. Stonestreet, *Operation and optimization of an Oscillatory flow continuous reactor.* Industrial & Engineering Chemistry Research, 2001. **40**(23): p. 5371-5377.

73. Harvey, A.P., M.R. Mackley, and T. Seliger, *Process intensification of biodiesel production using a continuous oscillatory flow reactor.* Journal of Chemical Technology & Biotechnology, 2003. **78**(2-3): p. 338-341.

74. Zheng, M. and M. Mackley, *The axial dispersion performance of an oscillatory flow meso-reactor with relevance to continuous flow operation.* Chemical Engineering Science, 2008. **63**(7): p. 1788–1799.

75. Jian, H. and X. Ni, *A numerical study on the scale-up behaviour in Oscillatory baffled columns.* Chemical Engineering Research and Design, 2005. **83**(10): p. 1163–1170.

76. Phan, A.N., A.P. Harvey, and V. Eze, *Rapid production of Biodiesel in Mesoscale Oscillatory baffled reactors.* Chemical Engineering & Technology, 2012. **35**(7): p. 1214-1220.

77. Arinze, E.S., et al., *Plasmonic Nanoparticle Enhancement of Solution-Processed Solar Cells: Practical Limits and Opportunities.* ACS Photonics, 2016. **3**(2): p. 158-173.

78. Zhihai, H., et al., *Controllable Synthesis and Biomedical Applications of Silver Nanomaterials.* J. Nanosci. Nanotechnol., 2011. **11**(11): p. 9395-9408.

79. Christopher, P., H.L. Xin, and S. Linic, *Visible-light-enhanced catalytic oxidation reactions on plasmonic silver nanostructures.* Nature Chemistry, 2011. **3**(6): p. 467-472.

80. Evanoff, D.D. and G. Chumanov, *Synthesis and Optical Properties of Silver Nanoparticles and Arrays.* ChemPhysChem, 2005. **6**(7): p. 1221-1231.

81. Sarina, S., E.R. Waclawik, and H. Zhu, *Photocatalysis on supported gold and silver nanoparticles under ultraviolet and visible light irradiation.* Green Chemistry, 2013. **15**(7): p. 1814-1833.

82. László Guczi, Zoltán Pászti, and G. Peto, *Metal Nanoclusters: Electronic Aspects and Physico-Chemical Characterization.* Metal Nanoclusters in Catalysis and Materials Science, 2008. **4**: p. 77-105.

83. Knauer, A. and J.M. Koehler, *Screening of nanoparticle properties in microfluidic syntheses.* Nanotechnology Reviews, 2014. **3**(1): p. 5–26.

84. Zhang, X.-F., et al., *Silver nanoparticles: synthesis, characterization, properties, applications, and therapeutic approaches.* International journal of molecular sciences, 2016. **17**(9): p. 1534.

85. Iravani, S., et al., *Synthesis of silver nanoparticles: chemical, physical and biological methods.* Research in pharmaceutical sciences, 2014. **9**(6): p. 385-406.

86. Poe, S.L., et al., *Solving the Clogging Problem: Precipitate-Forming Reactions in Flow.* Angewandte Chemie International Edition, 2006. **45**(10): p. 1544-1548.

87. Jin, R., et al., *Atomically Precise Colloidal Metal Nanoclusters and Nanoparticles: Fundamentals and Opportunities.* Chemical Reviews, 2016. **116**(18): p. 10346-10413.

88. Fonseca, G.S., et al., *Synthesis and characterization of catalytic iridium nanoparticles in imidazolium ionic liquids.* Journal of Colloid and Interface Science, 2006. **301**(1): p. 193-204.

89. Ott, L.S. and R.G. Finke, *Transition-metal nanocluster stabilization for catalysis: A critical review of ranking methods and putative stabilizers.* Coordination Chemistry Reviews, 2007. **251**(9): p. 1075-1100.

90. de Oliveira, J.F.A. and M.B.J.L. Cardoso, *Partial aggregation of silver nanoparticles induced by capping and reducing agents competition.* 2013. **30**(17): p. 4879-4886.

91. Shin, H.S., et al., *Mechanism of growth of colloidal silver nanoparticles stabilized by polyvinyl pyrrolidone in γ-irradiated silver nitrate solution.* Journal of Colloid and Interface Science, 2004. **274**(1): p. 89-94.

92. Levenspiel, O., *Chemical reaction engineering*. 3 ed. 1999, New York: John Wiley and Sons (WIE).

93. Fogler, H.S., *Elements of chemical reaction engineering*. 1986: Prentice-Hall.

94. Adeosun, J.T. and A. Lawal, *Numerical and experimental studies of mixing characteristics in a t-junction microchannel using residence-time distribution.* Chemical Engineering Science, 2009. **64**(10): p. 2422–2432.

95. De Souza, L.R. and L. Lorenz, *Residence time distribution for tubular reactors*. 2014.

96. Michigan, U.o. *Distribution of Residence time for chemical reactors*. 2008 2016/01/18]; Available from: http://www.umich.edu/~essen/html/byconcept/chapter13.pdf.

97. Olivet, D., et al., *Application of residence time distribution technique to the study of the hydrodynamic behaviour of a full-scale wastewater treatment plant plug-flow bioreactor.* Journal of Chemical Technology & Biotechnology, 2005. **80**(4): p. 425-432.

98. Sans, V., et al., *Residence time distribution, a simple tool to understand the behaviour of polymeric mini-flow reactors.* RSC Adv., 2012. **2**(23): p. 8721-8728.

99. Kumar, C., *Microfluidic devices in Nanotechnology: Fundamental concepts*. 2010, United States: John Wiley & Sons.

100. Wolf, D. and W. Resnick, *Residence time distribution in real systems.* Industrial & Engineering Chemistry Fundamentals, 1963. **2**(4): p. 287-293.

101. Martin, A.D., *Interpretation of residence time distribution data.* Chemical Engineering Science, 2000. **55**(23): p. 5907–5917.

102. Reimer, L., *Transmission electron microscopy: physics of image formation and microanalysis.* Vol. 36. 2013: Springer.

103. Shekunov, B.Y. and P. York, *Crystallization processes in pharmaceutical technology and drug delivery design.* Journal of Crystal Growth, 2000. **211**(1-4): p. 122-136.

104. Leane, M., K. Pitt, and G. Reynolds, *A proposal for a drug product Manufacturing Classification System (MCS) for oral solid dosage forms.* Pharmaceutical Development and Technology, 2015. **20**(1): p. 12-21.

105. Karpinski, P.H., *Polymorphism of active pharmaceutical ingredients.* Chemical engineering & technology, 2006. **29**(2): p. 233-237.

106. Sudha, C. and K. Srinivasan, *Nucleation control and separation of paracetamol polymorphs through swift cooling crystallization process.* Journal of Crystal Growth, 2014. **401**: p. 248-251.

107. Bučar, D.-K., R.W. Lancaster, and J. Bernstein, *Disappearing Polymorphs Revisited.* Angewandte Chemie International Edition, 2015. **54**(24): p. 6972-6993.

108. Zhang, G.G., et al., *Phase transformation considerations during process development and manufacture of solid oral dosage forms.* Advanced drug delivery reviews, 2004. **56**(3): p. 371-390.

109. Agnew, L.R., et al., *Controlled production of the elusive metastable form II of acetaminophen (paracetamol): a fully scalable templating approach in a cooling environment.* Chemical Communications, 2016. **52**(46): p. 7368-7371.

110. Wang, I.-C., et al., *Polymorph transformation in paracetamol monitored by in-line NIR spectroscopy during a cooling crystallization process.* Aaps Pharmscitech, 2011. **12**(2): p. 764-770.

111. Fujiwara, M., et al., *Paracetamol crystallization using laser backscattering and ATR-FTIR spectroscopy: metastability, agglomeration, and control.* Crystal Growth & Design, 2002. **2**(5): p. 363-370.

112. Powell, K.A., et al., *Periodic steady-state flow crystallization of a pharmaceutical drug using MSMPR operation.* Chemical Engineering and Processing: Process Intensification, 2015. **97**: p. 195-212.

113. Hou, G., et al., *Development and Characterization of a Single Stage Mixed-Suspension, Mixed-Product-Removal Crystallization Process with a Novel Transfer Unit.* Crystal Growth & Design, 2014. **14**(4): p. 1782-1793.

114. Power, G., et al., *Design and optimization of a multistage continuous cooling mixed suspension, mixed product removal crystallizer.* Chemical Engineering Science, 2015. **133**: p. 125-139.

115. Sudha, C. and K. Srinivasan, *Supersaturation dependent nucleation control and separation of mono, ortho and unstable polymorphs of*

*paracetamol by swift cooling crystallization technique.* CrystEngComm, 2013. **15**(10): p. 1914-1921.

116. Burley, J.C., et al., *Enforcing Ostwald's rule of stages: Isolation of paracetamol forms III and II.* European Journal of Pharmaceutical Sciences, 2007. **31**(5): p. 271-276.

117. Chadwick, K., A. Myerson, and B. Trout, *Polymorphic control by heterogeneous nucleation - A new method for selecting crystalline substrates.* CrystEngComm, 2011. **13**(22): p. 6625-6627.

118. Kaialy, W., et al., *An approach to engineer paracetamol crystals by antisolvent crystallization technique in presence of various additives for direct compression.* International Journal of Pharmaceutics, 2014. **464**(1): p. 53-64.

119. Sudha, C., R. Nandhini, and K. Srinivasan, *Polymer-Induced Selective Nucleation of Mono or Ortho Polymorphs of Paracetamol through Swift Cooling of Boiled Aqueous Solution.* Crystal Growth & Design, 2014. **14**(2): p. 705-715.

120. Sudha, C., P. Parimaladevi, and K. Srinivasan, *A novel method for the separation of mono and ortho polymorphs of paracetamol in gel matrix.* Materials Science and Engineering: C, 2015. **47**: p. 150-155.

121. Thomas, L.H., et al., *Paracetamol form II: an elusive polymorph through facile multicomponent crystallization routes.* Crystal Growth & Design, 2011. **11**(5): p. 1450-1452.

122. Schaber, S.D., et al., *Economic analysis of integrated continuous and batch pharmaceutical manufacturing: A case study.* Industrial and Engineering Chemistry Research, 2011. **50**(17): p. 10083-10092.

123. McGlone, T., et al., *Oscillatory flow reactors (OFRs) for continuous manufacturing and crystallization.* Organic Process Research & Development, 2015. **19**(9): p. 1186-1202.

124. Alvarez, A.J. and A.S. Myerson, *Continuous plug flow crystallization of pharmaceutical compounds.* Crystal Growth & Design, 2010. **10**(5): p. 2219-2228.

125. Sans, V., V. Dragone, and L. Cronin, *Applications of 3D Printing in Synthetic Process and Analytical Chemistry*, in *Handbook of Green Chemistry*, P.T. Anastas, Editor. 2019.

126. Mangin, D., F. Puel, and S. Veesler, *Polymorphism in processes of crystallization in solution: a practical review.* Organic Process Research & Development, 2009. **13**(6): p. 1241-1253.

127. Raza, K., et al., *Polymorphism: The Phenomenon Affecting the Performance of Drugs. SOJ Pharm Pharm Sci, 1 (2), 10.* Polymorphism: The Phenomenon Affecting the Performance of Drugs, 2014.

128. Bauer, J., et al., *Ritonavir: an extraordinary example of conformational polymorphism.* Pharmaceutical research, 2001. **18**(6): p. 859-866.

129. Qiang, W., K. Kelley, and R. Tycko, *Polymorph-specific kinetics and thermodynamics of β-amyloid fibril growth.* Journal of the American Chemical Society, 2013. **135**(18): p. 6860-6871.

130. Saleemi, A., I. Onyemelukwe, and Z. Nagy, *Effects of a structurally related substance on the crystallization of paracetamol.* Frontiers of Chemical Science and Engineering, 2013. **7**(1): p. 79-87.

131. Fonteyne, M., et al., *Process analytical technology for continuous manufacturing of solid-dosage forms.* TrAC Trends in Analytical Chemistry, 2015. **67**: p. 159-166.

132. Barthe, S.C., M.A. Grover, and R.W. Rousseau, *Observation of Polymorphic Change through Analysis of FBRM Data: Transformation of Paracetamol from Form II to Form I.* Crystal Growth & Design, 2008. **8**(9): p. 3316-3322.

133. Janne Paaso (VTT), M.T.V., Tim Freeman, C.A.Z. (FREEMAN), Andrei Honciuc, and R.A.T.-T. (ZHAW), Frode Brakstad (TEL-TEK), *Intensified by Design© for the intensification of processes involving solids handling*, in *SPIRE 8 – 2015 – Solids handling for intensified process technology*. 2016.

134. Lee, E.H., *A practical guide to pharmaceutical polymorph screening & selection.* Asian Journal of Pharmaceutical Sciences, 2014. **9**(4): p. 163-175.

135. Ivanova, B.B., *Monoclinic and orthorhombic polymorphs of paracetamol—solid state linear dichroic infrared spectral analysis.* Journal of Molecular Structure, 2005. **738**(1): p. 233-238.

136. Leuenberger, H., *New trends in the production of pharmaceutical granules: batch versus continuous processing.* European Journal of Pharmaceutics and Biopharmaceutics, 2001. **52**(3): p. 289-296.

137. Zhang, D., et al., *Progress of Pharmaceutical Continuous Crystallization.* Engineering, 2017. **3**(3): p. 354-364.

138. Li, J., B.L. Trout, and A.S. Myerson, *Multistage Continuous Mixed-Suspension, Mixed-Product Removal (MSMPR) Crystallization with Solids Recycle.* Organic Process Research & Development, 2016. **20**(2): p. 510-516.

139. Chen, J., et al., *Pharmaceutical crystallization.* Crystal Growth and Design, 2011. **11**(4): p. 887-895.

140. Eder, R.J.P., et al., *Continuous Sonocrystallization of Acetylsalicylic Acid (ASA): Control of Crystal Size.* Crystal Growth & Design, 2012. **12**(10): p. 4733-4738.

141. Besenhard, M.O., et al., *Crystal Engineering in Continuous Plug-Flow Crystallizers.* Crystal Growth & Design, 2017. **17**(12): p. 6432-6444.

142. Jiang, M., et al., *Continuous-Flow Tubular Crystallization in Slugs Spontaneously Induced by Hydrodynamics.* Crystal Growth & Design, 2014. **14**(2): p. 851-860.

143. Behera, S., et al., *UV-visible spectrophotometric method development and validation of assay of paracetamol tablet formulation.* J Anal Bioanal Techniques, 2012. **3**(6): p. 151-7.

144. Schmid, A., et al., *Industrial biocatalysis today and tomorrow.* Nature, 2001. **409**(6817): p. 258-268.

145. Constable, D.J.C., et al., *Key green chemistry research areas-a perspective from pharmaceutical manufacturers.* Green Chemistry, 2007. **9**(5): p. 411-420.

146. Bornscheuer, U.T., et al., *Engineering the third wave of biocatalysis.* Nature, 2012. **485**(7397): p. 185-194.

147. Sheldon, R.A. and S. van Pelt, *Enzyme immobilisation in biocatalysis: why, what and how.* Chemical Society Reviews, 2013. **42**(15): p. 6223-6235.

148. Lozano, P., *Enzymes in neoteric solvents: From one-phase to multiphase systems.* Green Chemistry, 2010. **12**(4): p. 555-569.

149. Rodrigues, R.C., et al., *Modifying enzyme activity and selectivity by immobilization.* Chemical Society Reviews, 2013. **42**(15): p. 6290-6307.

150. Gibson, I., D.W. Rosen, and B. Stucker, *Additive Manufacturing Technologies: Rapid Prototyping to Direct Digital Manufacturing.* Additive Manufacturing Technologies: Rapid Prototyping to Direct Digital Manufacturing. 2010, Berlin: Springer-Verlag Berlin. 1-459.

151. Symes, M.D., et al., *Integrated 3D-printed reactionware for chemical synthesis and analysis.* Nature Chemistry, 2012. **4**(5): p. 349-354.

152. Rossi, S., et al., *Stereoselective Catalytic Synthesis of Active Pharmaceutical Ingredients in Homemade 3D-Printed Mesoreactors.* Angewandte Chemie-International Edition, 2017. **56**(15): p. 4290-4294.

153. Au, A.K., et al., *3D-Printed Microfluidics.* Angewandte Chemie-International Edition, 2016. **55**(12): p. 3862-3881.

154. Guo, Q., et al., *"Paintable" 3D printed structures via a post-ATRP process with antimicrobial function for biomedical applications.* Journal of Materials Chemistry B, 2013. **1**(48): p. 6644-6649.

155. Kitson, P.J., et al., *3D Printed High-Throughput Hydrothermal Reactionware for Discovery, Optimization, and Scale-Up.* Angewandte Chemie-International Edition, 2014. **53**(47): p. 12723-12728.

156. Fatarella, E., et al., *Nylon 6 film and nanofiber carriers: Preparation and laccase immobilization performance.* Journal of Molecular Catalysis B: Enzymatic, 2014. **102**: p. 41-47.

157. Lozano, P. and J.L. Iborra, *Enzyme Immobilization on Nylon*, in *Immobilization of Enzymes and Cells*, G.F. Bickerstaff, Editor. 1997, Humana Press: Totowa, NJ. p. 27-40.

158. Isgrove, F.H., et al., *Enzyme immobilization on nylon–optimization and the steps used to prevent enzyme leakage from the support.* Enzyme and Microbial Technology, 2001. **28**(2–3): p. 225-232.

159. Wang, T.-M., X. Jun-Tong, and J. Ye, *A model research for prototype warp deformation in the FDM process.* Int J Adv Manuf Technol, 2006.

160. Vasudevarao, B., D.P. Natarajan, and M. Henderson, *Sensitivity of rp surface finish to process parameter variation*. 2000.

161. Bhattacharjee, N., et al., *The upcoming 3D-printing revolution in microfluidics.* Lab on a Chip, 2016. **16**(10): p. 1720-1742.

162. Morgan, A.J.L., et al., *Simple and versatile 3D printed Microfluidics using fused filament fabrication.* PLOS ONE, 2016. **11**(4): p. e0152023.

163. Green, A.P., N.J. Turner, and E. O'Reilly, *Chiral Amine Synthesis Using omega-Transaminases: An Amine Donor that Displaces Equilibria and Enables High-Throughput Screening.* Angewandte Chemie-International Edition, 2014. **53**(40): p. 10714-10717.

164. O'Reilly, E., C. Iglesias, and N.J. Turner, *Monoamine Oxidase- w-Transaminase Cascade for the Deracemisation and Dealkylation of Amines.* Chemcatchem, 2014. **6**(4): p. 992-995.

165. O'Reilly, E., et al., *A Regio-and Stereoselective w-Transaminase/ Monoamine Oxidase Cascade for the Synthesis of Chiral 2,5-Disubstituted Pyrrolidines**.* Angewandte Chemie-International Edition, 2014. **53**(9): p. 2447-2450.

166. Martinez-Montero, L., et al., *Stereoselective amination of racemic sec-alcohols through sequential application of laccases and transaminases.* Green Chemistry, 2017. **19**(2): p. 474-480.

167. Lopez-Iglesias, M., et al., *Biocatalytic Transamination for the Asymmetric Synthesis of Pyridylalkylamines. Structural and Activity Features in the Reactivity of Transaminases.* Acs Catalysis, 2016. **6**(6): p. 4003-4009.

168. Guo, F. and P. Berglund, *Transaminase biocatalysis: optimization and application.* Green Chemistry, 2017. **19**(2): p. 333-360.

169. Planchestainer, M., et al., *Continuous flow biocatalysis: production and in-line purification of amines by immobilised transaminase from Halomonas elongata.* Green Chemistry, 2017. **19**(2): p. 372-375.

170. Miložič, N., et al., *Theoretical and experimental study of enzyme kinetics in a microreactor system with surface-immobilized biocatalyst.* Chemical Engineering Journal, 2017. **313**: p. 374-381.

171. Neto, W., et al., *Immobilisation of ω-transaminase for industrial application: Screening and characterisation of commercial ready to use enzyme carriers.* Journal of Molecular Catalysis B: Enzymatic, 2015. **117**: p. 54-61.

172. Andrade, L.H., W. Kroutil, and T.F. Jamison, *Continuous Flow Synthesis of Chiral Amines in Organic Solvents: Immobilization of E. coli Cells Containing Both ω-Transaminase and PLP.* Organic Letters, 2014. **16**(23): p. 6092-6095.

173. Peris, E., et al., *Tuneable 3D printed bioreactors for transaminations under continuous-flow.* Green Chemistry, 2017. **19**(22): p. 5345-5349.